Development of an Integrated Free Surface and Groundwater Flow Model

KUMARS EBRAHIMI

Ph.D. 2004

ProQuest LLC
789 East Eisenhower Parkway
P.O. Box 1346
Ann Arbor, MI 48106-1346

Development of an Integrated Free Surface and Groundwater Flow Model

A thesis submitted to the Cardiff University
In candidature for the degree of
Doctor of Philosophy

by

Kumars Ebrahimi

B.Sc., M.Sc.

Division of Civil Engineering, Cardiff School of Engineering
Cardiff University

February 2004

Development of an Integrated Free Surface and Groundwater Flow Model

Kumars Ebrahimi
PhD Thesis Abstract, Cardiff University, UK, 2004

Keywords: *Numerical Modelling, 2-D Free Surface/Groundwater flow modelling, Solute Transport, Physical Modelling, Dye Tracer*

An integrated novel, two-dimensional, numerical groundwater-surface flow model has been developed to simulate hydro-environmental interactions between wetland areas, the neighbouring coastal waters and the groundwater passages. The main target in this research was to prepare a general linked model, which could be applied to different applications.

For free surface flow modelling, an existing widely used two-dimensional, unsteady mathematical model, named the DIVAST model (Depth Integrated Velocities And Solute Transport model, developed originally by Falconer 1976) has been refined. However, in order to simulate the flow and solute transport in porous media, a two-dimensional model namely the GWK (Ground Water Key) has been developed to include an aquifer influenced by tidal currents.

The GWK model is based on the transient flow *Boussinesq* equation as the governing equation for groundwater flow, and the advection-diffusion equation is used as the governing equation for contaminant transport. The model predicts the water table, the velocity components in the horizontal plane, the recharge/discharge levels for source/sink on the water table and solute tracer levels across the domain. The finite difference scheme used in this model is based upon the Alternating Direction Implicit (ADI) technique and using orthogonal grids. The structure of the GWK model is based on having a good relationship with the free surface flow model. The two sub-models (DIVAST-GWK) are linked by an interface, and flow and pollutants are able to pass across the interface in both directions, depending on the relative height of the water levels.

A physical scale model has been constructed to provide experimental data of the groundwater transport between an idealised wetland and the adjacent coastal waters. However, in the dimensional analysis and designing of the physical model the Fleet Lagoon and adjacent coastal waters, in Dorset just west of Weymouth and the Isle of Portland UK, was chosen as a typical prototype. In the physical model the aim has been to study seepage behavior through the sand embankment by recording water levels on both sides of the sand, point velocity measurements, and the studies of a conservative dye tracer for constant water levels on one side of the embankment while running tidal cycle on the other side of the sand ridge.

The integrated model has been verified using the laboratory data. Comparison between the experimental data and the simulated physical model, involving numerical linked model, showed that the integrated model was capable of simulating both phenomena, groundwater and free surface water, with a high level of accuracy.

Acknowledgements

I would like to express my appreciation to Professor Roger A. Falconer for his constant help and guidance while this research was being done. His valuable advice, encouragement and support are sincerely appreciated.

Special thanks go to Dr Binliang Lin, for his honest guidance and help throughout this project.

I am so grateful to the Ministry of Science, Research and Technology of the Islamic Republic of Iran for funding this research project.

In addition, I wish to express my deepest gratitude to colleagues and all members and staff of the Hydroenvironmental Research Centre (HRC), Division of Civil Engineering and the "ELS" (the English Language Service) at Cardiff University. In particular I express my sincere gratitude to Mr Paul Leach for his support during the design and construction of the laboratory model.

Most importantly, I recognize a great personal debt to my family and my respected parents for their patience, understanding and support during this research programme.

Above all, I give thanks to *God* for giving me the opportunity, ability and stamina to do this research course.

Dedicated to;

My wife: Firozeh, who has been very patient,
My children: Maedeh and Mostafa
And
My dear parents

TABLE OF CONTENTS

Page

CHAPTER 1

INTRODUCTION

CHAPTER 2

TWO DIMENSIONAL FREE SURFACE AND GROUNDWATER HYDRODYNAMIC EQUATIONS AND SOLUTE TRANSPORT PROCESSES

CHAPTER 3

NUMERICAL MODELLING OF POROUS MEDIA AND THE LINKED APPROACH

CHAPTER 4

POROUS MEDIA NUMERICAL MODEL TESTS

CHAPTER 5

PHYSICAL MODELLING OF WETLANDS AND ADJACENT COASTAL WATERS

CHAPTER 6

APPLICATION OF LINKED NUMERICAL MODEL TO PHYSICAL MODEL AND LABORATORY RESULTS

CHAPTER 7

CONCLUSIONS AND RECOMMENDATIONS

LIST OF FIGURES

CHAPTER 1

CHAPTER 2

CHAPTER 3

CHAPTER 4

CHAPTER 5

CHAPTER 6

APPENDIX A

APPENDIX B

LIST OF TABLES

NOTATIONS

a_L	longitudinal dispersivity of porous media
a_T	transverse dispersivity of porous media
A, A_o	cross sectional area of flow
b	aquifer thickness
C	Chezy roughness coefficient
C	solute concentration of porous media
C_D	drag coefficient
C_e	eddy viscosity coefficient
C_f	Courant number
C_w	air-water resistance coefficient
d	some representative length of porous matrix
D_L	longitudinal dispersion coefficient
D_T	transverse dispersion coefficient
$D_{xx}, D_{xy}, D_{yx}, D_{yy}$	depth averaged dispersion-diffusion coefficients
f	Coriolis parameter (Chapter 2, part one)
f	dispersive mass flux in porous media
g	acceleration of gravity
h	bed level below datum (Chapter 2, part one)
h	piezometric head
H	total depth of water

i, j	discretised grid points
J	hydraulic gradient
J^*	mass flux (mass per unit area per unit time)
k	von Karman's constant
k_l	depth averaged longitudinal dispersion coefficient
k_t	lateral turbulent diffusion coefficient
K	mortality coefficient for coliform bacteria (Chapter 2, part one)
K	hydraulic conductivity
K_s	saturated hydraulic conductivity
m	mass
n	porosity or number of row or column
n	time step index (as a superscript, Chapter 3)
N	source and sinks
p	discharge per unit width in x direction
P	pressure
q	discharge per unit width in y direction or depth-integrated fluid flux (Chapter 2, part one)
q	specific discharge; Darcy velocity
q_m	source discharge per unit horizontal area
Q	discharge rate
Q_o	out-fall discharge rate
R	recharge rate
R_e	Reynolds number

S	depth average solute concentration (Chapter 2, part one)
S	storage coefficient, sink/source
S_o	out-fall discharge concentration
S_s	specific storage
S_y	specific yield
t	time
T	transmissivity
U, V	depth averaged velocity components in x-,y- direction
v	pore velocity; average linear velocity
x, y, z	Cartesian co-ordinates
β	momentum correction factor for a non-uniform vertical velocity profile
$\Delta x, \Delta y$	grid spacing in x-, and y- direction
$\Delta t, dt$	time step or time interval
ε	depth average turbulent eddy viscosity
η	water surface elevation above datum
ν	kinematic viscosity of fluid
ρ	density of water
ρ_a	density of air
τ_e	mean shear stress
ϕ	total head (i.e. elevation above datum level plus static pressure head)
Φ_s	source and sink (Chapter 2, part one)

ABBREVIATIONS

ADI	Alternating Direction Implicit
ADV	Acoustic Doppler Velocimeter
CFD	Computational Fluid Dynamics
DIVAST	Depth Integrated Velocities And Solute Transport
GWK	Ground Water Key
HWL	High Water Level
LWL	Low Water Level
ME	Mid-Ebb
MF	Mid-Flood
MWL	Mean Water Level
WS	Water Surface
WT	Water Table

CHAPTER 1

INTRODUCTION

1.1 OVERVIEW

Aquatic pollution has been one of the most important topics of concern to society during recent decades. To-date most effort in preventing this problem has been targeted at the control of point-source effluent discharges, such as domestic and industrial effluents. The importance of pollution arising from land-use activities that are dispersed across a catchment, namely diffuse pollution, has only been recognized recently and the current capability of predicting the impact of diffuse pollution on the aquatic environment is limited. Since land pollutants, in general, are ultimately transported to the catchment receiving waters, pollution from diffuse sources is essentially transported by precipitation through pathways governed by the physical characteristics of the catchment. Diffuse pollution is often closely associated with storm events, which mobilise many pollutants from urban and rural surfaces to rivers, estuaries and coastal waters. Some soluble material may be leached into the groundwater, which may rejoin streams or rivers at a later stage (Stapleton et al., 2000).

As mentioned above, diffuse pollution loads from agriculture and urban runoff are frequently attributed to the pollution of aquifers, which can have significant implications for potable water quality and the use of environmental waters for recreation. High nutrient concentrations are typical of the catchments and the lower reaches of major rivers in many countries. Episodic peak concentrations can be very high and are especially noticeable after periods of prolonged drought. Eutrophication problems involve ecological change and damage to natural ecosystems. In most surface waters, phosphorus is the limiting element controlling the occurrence and severity of eutrophication. However, nitrogen (N) can play an important role in hyper-eutrophic situations, and flowing surface waters may well be N limited and therefore responsive to any additional N (Edwards et al., 2000). Shallow groundwater systems are particularly susceptible to contamination. While conceptually, and in terms of regulation, it is probably easier to consider surface and groundwater bodies separately. The continuum that exists between these environmental components in real catchment systems must be appreciated and integrated approaches developed. These require an understanding of the hydrodynamics and critical hydrological and hydro-geological pathways within a catchment.

Although groundwater and surface water systems are physically inseparable, they have traditionally been considered as separate systems and managed independently. With population growth and increase in land development, comprehensive management of sustainable water resources related to water supply, water quality, wetlands, and recreational issues have become increasingly important. To address these issues, an integrated approach (combining planning and rule making with technological development) to manage water resources seems to be more critical than hitherto. The water resources management plans should integrate these two systems to effectively solve problems in the areas of aquifer storage and recovery systems, artificial recharge, stormwater management systems, water quality studies, watershed planning and management, and modelling (see Panigrahi, 2001).

Since decision making in environmental management has become increasingly dependent on predictions generated by numerical models, time dependent (dynamic) mathematical models are therefore very useful for gaining a more detailed comprehension of the flow and solute pathways in combined surface (both wetland and coastal waters) and subsurface environments.

1.2 OBJECTIVES OF THESIS

The main objective of this research study was therefore to develop a scientific understanding of diffuse pollution and to develop such a process based generic model, with which to gain a more detailed comprehension of water and solute transport processes in combined surface and subsurface environments. Therefore, in other words the main objectives of the study were to develop *an integrated free surface-groundwater flow model*, to describe more accurately the concentration distributions and the recharge and discharge interaction processes between wetland and coastal waters through the groundwater system. In the numerical modelling studies undertaken in this research programme, the development, integration and verification of an innovative subsurface/free surface flow and solute transport model have been considered to create an advanced comprehensive wetland-groundwater and coastal water simulation model. The aims, objectives and achievements of this study can therefore be summarised in more detail as follows:

1.2.1 New Representation of Interaction between Wetland Areas, Coastal Waters and Groundwater passages

In recent decades, increased attention has been paid to the environmental issues of interaction between beach groundwater tables and adjacent shallow coastal waters. For example; Numerical Modelling of Tide-Induced Beach Water Table Fluctuations was studied by Li et al. (1997). The Chemical Effects of Beach Groundwater on Coastal Water was also another title of this subject which was considered by the same author later, as he mentioned:

> *groundwater tables in a coastal aquifer fluctuate with oceanic tides. These fluctuations have been found to affect coastal processes such as beach sediment transport and chemical transfer from the aquifer to the ocean. One-dimensional models based on the Boussinesq equation are often used to help understand and analyse coastal aquifers' behaviour, e.g., to predict the water table fluctuations. The tidal forcing occurs over the beach slope, creating a moving boundary condition at the shore* (Li et al., 2000).

Larabi and Smedt (1997) also studied seawater intrusion into unconfined aquifers, and also some other cases like: the rainfall-runoff process and interaction between surface/subsurface flow components were focused on and described by Morita and Yen (2002). On the other hand wetlands and mangroves have been studied extensively, because of their important roles and influences on the aquatic ecosystem. For instance, as mentioned by Westwater (2001), wetlands are still one of the most complex and poorly understood ecosystems in terms of water management, with engineers and environmental managers historically tending simply to drain these areas, and use the land more productively for agricultural or industrial purposes. Also Franks and Falconer (1999) noted that "Recognising the values and functions of wetlands such as mangroves presents a direct challenge to the traditional objectives of water management for specific sectoral purposes, and raises questions about the meaning of better water management".

To-date a large number of different physical and mathematical models have been developed and deployed for predicting these processes in different types of schemes. However, interaction between wetlands and coastal waters through shallow groundwater is a completely novel, complex and poorly understood ecosystem issue and needs to be studied in more detail. Because of the complexity of this subject, our knowledge of this phenomenon is still limited in terms of describing the whole process accurately. In this

Figure 1.1: An example of wetland area, the neighbouring coastal waters (Allen, 2004)

study a new representation of integrated modelling of subsurface/free surface flows has been carried out. A general view of an example of the above mentioned combined environments is indicated in Figure 1.1. The figure shows the Fleet lagoon and the adjacent coastal area (Dorset, UK), which will be described in Chapter 5.

1.2.2 Flow and Solute Transport Modelling in Shallow Waters

As highlighted in the abstract, this research has focused primarily upon achieving a wider scientific understanding of interactions between wetland areas and coastal waters via groundwater flow paths. This means that the study had to integrate the simulations of two completely separate aspects of flow and solute transport including; shallow waters (for both the coastal and wetland areas) and groundwater zones.

However, for the free surface flow modelling of this study, an existing, widely used, two dimensional (2-D) numerical model, named DIVAST (Depth Integrated Velocities And Solute Transport) has been used, which was originally developed by Falconer (1976), and refined considerably by Lin and Falconer (1997). In order to simulate the flow and solute transport in porous media a new 2-D model namely, **GWK** (**G**round **W**ater **K**ey), was developed to include an aquifer influenced by tidal currents.

For numerical model studies, the approach generally adopted for two-dimensional studies is to solve the governing differential equations of mass (or continuity) and momentum in two orthogonal directions in the horizontal plane for hydrodynamic modelling, with the solute transport equation then being solved for each individual water quality parameter, as described by Falconer (1992). The DIVAST model is a two-dimensional, depth-integrated time-variant model, which primarily has been developed for estuarine and coastal modelling and was refined later to predict hydrodynamic and shallow water processes through wetlands (see Westwater et al., 1999). This model is suitable for water bodies that are dominated by horizontal, unsteady flow and do not display significant vertical stratification. The model simulates two-dimensional current distributions, water surface elevations and various water quality parameters within the modelling domain and as functions of time, taking into account the hydraulic characteristics governed by the bed topography and boundary conditions. It has been developed using the FORTRAN 77 programming language (DIVAST model reference manual - Falconer et al., 2000).

1.2.3 Flow and Solute Transport Modelling in Porous Media

For simulating the flow and solute transport progresses in porous media within this study, a new two-dimensional time-variant model namely GWK (Ground Water Key) was developed. The model predicts the flow and contaminant transport in a porous media. A brief description of the 2-D numerical model (GWK) and its characteristics could be presented as follows:

The GWK model predicts the hydraulic head (water table), the velocity components in the horizontal plane, the recharge/discharge levels for source/sink on the water table and solute tracer levels across the domain as functions of time. Numerical modelling of the fluid flow was based on mass conservation and Darcy's law (Boussinesq equation) within the aquifer to be modelled. To simulate the solute transport phenomenon in the porous media the governing two-dimensional advection-diffusion equation was developed and solved. The finite difference scheme used in this model is based upon the Alternating Direction

Implicit (ADI) technique, which involves the sub-division of each time step into two half time steps. The model was developed using FORTRAN 77 and the structure of the GWK model was based on having a dynamic linked with the free surface flow model. The model has been developed in two different versions. In the first version the simulation results are listed in tabular form and in a beneficial format for visual investigation of the results. In the second version the results are generated and transported to a Tecplot software package for post processing to create graphical plots and animation files of the simulations.

1.2.4 Linking the two 2-D Numerical Sub-Models

In aquatic pollution processes, interaction between surface and subsurface flow components plays an important role. Therefore, coupling of surface and subsurface flow sub-models is necessary for advanced comprehensive and sophisticated wetlands-groundwater and coastal flow simulation.

Generally a numerical linked model consists of two or more sub-models. In the current study the two-dimensional GWK model has been dynamically linked to the two-dimensional DIVAST model, and the resulting single model has been calibrated and verified against experimental data. These data were acquired from a constructed physical model of a wetland basin and an adjacent coastal basin.

For the initial and boundary conditions in the linked model, at the start of the simulation period a number of settings were made. The initial velocities and solute concentrations were first set to zero across the domain. The water elevations were set horizontally, near high water level. However, depending on the direction of flow, the water and solute concentration levels along the shoreline of the coastal waters, wetland and groundwater zone were all used as boundary conditions at any timestep for both the GWK and DIVAST models.

1.2.5 Performance of Experiments Using the Physical Model

For the purposes of this research, a physical scale model of an idealised-design wetland and adjacent coastal waters area was constructed. Physical models can be used as a source of providing controlled data for describing the main groundwater/free surface flow processes. Scale modelling has been shown to provide valuable information of complex flow systems (Sellin et al., 2001). This model has provided the required experimental data of the transport processes between the idealised wetland and the adjacent coastal waters. It enabled the integrated model to be calibrated and verified and has also provided an understanding of the interaction processes between these two water bodies. The aim was to study seepage behaviour through the sand embankment, by studying the water fluctuation on both sides of the sandy ridge and also to study the contaminant distribution by a conservative tracer for constant water levels on one side of the embankment, while running various tidal cycles on the other side of the sand embankment. The process of distributing and advecting the dye tracer through the sand embankment was filmed so that time series simulation and measured results would be compared, with the details being described in Chapter 6. In the physical model, the time series of point velocities within the free surface domain were also measured. These processes are described in some detail in Chapter 5.

1.2.6 Calibration and Verification of the Integrated Model

The data set which was collected from the physical model has been used to calibrate and verify the numerical linked model. To achieve this aim the main parameters which were used included: point velocity measurements, and time series wave elevations either side of the sand embankment. These parameters were related to the recharge and discharge through the sand, and dye tracer distribution patterns within the surface flow domain.

1.3 OUTLINE OF THE THESIS

In the first chapter, the project has been introduced and a review of different aspects of this research study is presented. The motivation and aims of the research are also discussed. The remainder of thesis is detailed as follows:

- Chapter 2 firstly presents the governing equations of hydrodynamics, including the continuity and momentum equations for a two-dimensional framework in a free surface flow. Secondly, details are given of the mass conservation and Darcy's law (Boussinesq equation) for fluid flow within an aquifer, and the governing two-dimensional advection-diffusion equation used to simulate the solute transport phenomenon in the porous media.
- The numerical solutions and discretisation of the governing partial differential equations for groundwater, and the approach to linking the two sub-models: i.e. the groundwater and free surface flow models, are discussed in chapter 3.
- The new porous media numerical model is applied for three test cases and the related results are discussed in Chapter 4.
- Chapter 5 describes the physical modelling set-up and programme for a wetland and a neighbouring coastal basin with a groundwater embankment.

- The integrated model has been applied to the physical model. The details of this application are given in Chapter 6. This chapter provides the laboratory results and the linked model calibration and verification data.
- The results of the analyses which were carried out within this research project are discussed and summarised in Chapter 7, with some future research recommendations being given in the same chapter.

CHAPTER 2

TWO DIMENSIONAL FREE SURFACE AND GROUNDWATER HYDRODYNAMIC EQUATIONS AND SOLUTE TRANSPORT PROCESSES

2.1 Introduction

In recent years hydro-environmental modelling has become one of the key topics for research in the field of aquatic pollution. With recent progress in computing science and numerical techniques, many researchers have focused on developing individual numerical models to predict the levels of diffuse pollution in surface waters, for instance: rivers, estuaries and coastal waters, and in groundwater basins. These models, which have usually been verified and validated against experimental or field data, are able to predict different required variables in space and time, according to different boundary inputs and basin criteria. However, in predicting the flow and distribution of solute concentrations, it is essential to derive the relevant governing partial differential equations to formulate either the free surface or groundwater processes according to their limitations. Then by using a suitable numerical method, such as: finite difference, finite element or finite volume, a numerical solution procedure can be developed to solve the above mentioned equations. However, to complete the solution procedure various experimental parameters need to be included, which appear in the mathematical equations and it is so important to estimate and include these different parameters as accurately as possible.

In this study, in order to model dynamically the interactions between wetland areas, coastal waters and groundwater basins, it was first necessary to link two basic different sub-models. One sub-model was to be used to simulate the flow and solute transport processes in shallow waters and the second sub-model was to be used to simulate the same processes in porous media. As mentioned before, the basic DIVAST model was chosen for simulation of the free surface flow processes, and for the groundwater flow a new two-dimensional model, GWK, was developed.

It was not the purpose of this research study to undertake a detailed analysis of free surface modelling. However, it is important to discuss briefly the DIVAST model and some of the background to the theory on this subject, due to the significance of this phenomenon on the governing flow and solute transport equations. Hence, in the first part of this chapter, a brief introduction is given to the governing equations of the free surface flow sub-model, DIVAST. Then, in part two, firstly an overview is given of groundwater flow, followed by a review of the basic laws of groundwater and Dupuit assumptions for phreatic surface flow. Finally, the governing partial differential equations of groundwater flow and hydrodynamic and solute transport modelling are derived.

2.2 Governing Two Dimensional Free Surface Flow Equations

2.2.1 History and Overview of the DIVAST Model

The model DIVAST (Depth Integrated Velocities And Solute Transport) is based on a finite difference model for predicting time varying water elevations, velocity components in the horizontal plane and depth averaged solute concentration distributions. The model first was developed as part of a PhD programme by Falconer (1976). The model has subsequently been extensively developed and refined, considerably by Lin and Falconer (1997), with particular emphasis being focused on the treatment of the advective accelerations, wind effects, bottom friction, turbulence, high concentration gradients, dispersion, water quality indicators, sediment transport processes and the complex hydrodynamic phenomenon of flooding and drying. The model is structured into one main program, which includes a hydrodynamic module and a water quality and sediment transport module, with each being solved for each half time step. The programme of the model is supported by 39 subroutines, with most of these subroutines being written in a general format.

The model has also been calibrated and verified extensively against laboratory and field measured data, with details of the model refinements and verification tests being reported in over 70 publications by the original model author. The model has been successfully applied to well over 50 site specific studies by various consulting engineering firms research institutions and is now widely used within the UK and overseas.

DIVAST is a comprehensive and versatile model for predicting the water elevations and depth averaged velocity components and up to eight user specified water quality constituents and sediment transport fluxes. The model is applicable to well mixed coastal, estuarine and inland water bodies and includes an improved wind stress distribution through the use of an assumed second order parabolic velocity profile. The hydrodynamic module is based on the solution of the depth integrated Navier-Stokes equations and includes the effects of:- local and advective accelerations, the earth's rotation, barotropic and free surface pressure gradients, wind action, bed resistance and a simple mixing length turbulence model. The differential equations are written in their pure differential form, thereby allowing for momentum conservation in the finite difference sense.

The governing differential equations are solved using the finite difference technique and using a scheme based on the alternating direction implicit formulation. The advective accelerations are written in a time centred form for stability, with these terms and the turbulent diffusion terms being centred by iteration. Whilst the model has no stability constraints, there is a Courant number restriction for accuracy in the hydrodynamic module. The finite difference equations are formulated on a space staggered grid scheme, with the water surface elevations and x-direction velocity components being initially solved during the first half timestep by using the method of Gauss elimination and back substitution. The water quality indicators and sediment flux distributions are then evaluated, before proceeding to the second half time step and repeating the process for the implicit description of the y-direction variable derivatives.

In the water quality and sediment transport modules the advection terms are treated using a higher order accurate third order upwind difference formulation, with this scheme reducing considerably the introduction of artificial diffusion and under- and over- shoot in regions of high concentration gradients. The advective-diffusion equation is solved for a range of water quality indicators, including: salinity, total coliforms, faecal coliforms, biochemical oxygen demand, ammonia, nitrate and nitrite nitrogen and dissolved oxygen. The general depth integrated equations include: local and advective effects, turbulent dispersion and diffusion: including wind effects where appropriate, source and sink inputs, and decay and kinetic transformation processes. For the sediment transport module, the equilibrium suspended flux is included in the model using the van Rijn formulation (van Rijn, 1984a and b). However, other formulations are available, including formulae proposed by: (i) Engelund and Hansen (1967), and (ii) Bijker (1967).

At the beginning of the program a list of key variables are first specified, including such variables as the gird size, timestep, open boundary specifications, coefficient values for the governing hydrodynamic equations and dispersion and decay rates etc for the solute transport equation. For the water quality and sediment transport equations, the open boundary conditions are fed in either as water elevations or depth averaged velocity (or discharge per unit width) components for the hydrodynamic module and solute concentration levels for the corresponding water quality or sediment transport equations. The domain is specified in terms of a prescribed integer code, wherein zero represents dry land and unity represents an active interior grid square, and with the depths below datum generally being obtained from the appropriate Admiralty Chart and specified at the appropriate grid square location using a digitising package, namely DGM3. In general a constant roughness coefficient is specified across the domain in the absence of extensive field data, although the option of including a spatially varying roughness coefficient exists if required. The eddy viscosity and dispersion-diffusion terms are represented in a spatially varying manner and are related to the shear velocity and the water column depth in a similar manner to the functional relationship obtained for a traditional logarithmic velocity profile.

In terms of the output, user defined flags allow numerical and graphical output to be produced of the water elevations, velocity fields and distributions of all the specified water quality constituents. For the sediment transport simulations, depth averaged tidal residual velocity and bed shear stress distributions are also reproduced, thereby enabling a more comprehensive interpretation of the results and, in particular, enabling the user to identify more precisely regions of relatively high erosion and deposition. Apart from reproducing the individual variable distributions, other useful data are specified such as the mean and standard deviations of each specified variable across the domain. All of these data can be obtained at any time during a simulation, with the printout and plot times being specified by the user.

The DIVAST model has been developed using the FORTRAN 77 programming language and it is compatible with any mainframe and personal computer systems which support this language.

2.2.2 Governing Equations

2.2.2.1 Hydrodynamic Equations

Numerical modelling of fluid flow is based on the principles of continuity of mass and conservation of momentum within the body of fluid to be modelled. In many cases, the flow is defined by the Reynolds equations, which describes the three-dimensional turbulent motion of an incompressible fluid. For flows which show little variation in the vertical direction, it is appropriate to integrate these equations over the depth of water, resulting in simplified or 'two-dimensional' equations of motion.

When integrated over depth, the equations governing fluid motion can be written as:

Conservation of mass:

$$\frac{\partial \eta}{\partial t} + \frac{\partial p}{\partial x} + \frac{\partial q}{\partial y} = q_m \tag{2.1}$$

Conservation of momentum:

$$\begin{aligned} \frac{\partial p}{\partial t} + \frac{\beta \partial p U}{\partial x} + \frac{\beta \partial p V}{\partial y} &= fq - gH\frac{\partial \eta}{\partial x} + \frac{\rho_a}{\rho} C_w W_x \sqrt{W_x^2 + W_y^2} \\ &- \frac{gp\sqrt{p^2+q^2}}{H^2C^2} + \varepsilon\left[2\frac{\partial^2 p}{\partial x^2} + \frac{\partial^2 p}{\partial y^2} + \frac{\partial^2 q}{\partial x \partial y}\right] \end{aligned} \tag{2.2}$$

$$\begin{aligned} \frac{\partial q}{\partial t} + \frac{\partial \beta q U}{\partial x} + \frac{\partial \beta q V}{\partial y} &= -fp - gH\frac{\partial \eta}{\partial y} + \frac{\rho_a}{\rho} C_w W_y \sqrt{W_x^2 + W_y^2} \\ &- \frac{gq\sqrt{p^2+q^2}}{H^2C^2} + \varepsilon\left[\frac{\partial^2 q}{\partial x^2} + 2\frac{\partial^2 q}{\partial y^2} + \frac{\partial^2 p}{\partial x \partial y}\right] \end{aligned} \tag{2.3}$$

where:

$p(=UH)$, $q(=VH)$	discharges per unit width in the x and y directions respectively $(m^3/s/m)$;
q_m	source discharge per unit plan-surface area $(m^3/s/m^2)$;
U, V	depth average velocity components in the x and y directions respectively (m/s);
β	momentum correction factor for a non-uniform vertical velocity profile;
f	Coriolis parameter due to the earth's rotation (=2ω Sinϕ, with ω = angular rotation speed of the earth and ϕ = geographical angle of latitude; $\omega = 2\pi/(24\times3600) = 7.27 \times 10^{-5}$ radians/s);
g	gravitational acceleration (= 9.8076 m/s^2);
H	total water column depth ($= \eta + h$);
η	water surface elevation above or below datum;
h	bed elevation below datum;
ρ_a	density of air ($\cong$ 1.292 kg/m^3);
ρ	density of fluid (kg/m^3);
C	Chezy roughness coefficient ($m^{1/2}/s$);
C_w	air/fluid resistance coefficient
ε	depth averaged turbulent eddy viscosity (m^2/s);
x, y	co-ordinate axes in the horizontal plane (m)

2.2.2.1.1 Momentum Correction Factor

According to Falconer et al. (2000), for an assumed logarithmic vertical velocity profile, the momentum correction factors may be calculated according to the following relationship:

$$\beta = 1 + \frac{g}{C^2 k^2} \tag{2.4}$$

where k = von Karman's constant (= 0.4). For an assumed seventh power law velocity profile the value of β is 1.016 and 1.20 for an assumed quadratic velocity profile (Falconer and Chen, 1991).

2.2.2.1.2 Wind stress Effects

The wind exerts a drag force as it flows over the water surface. The shear stress at the air-water interface is calculated by assuming that it is proportional to the square of the wind speed at a particular height above the water surface. Various empirical formulae have been proposed to calculate an air-water resistance coefficient, similar to the drag coefficient in turbulent flow field. In DIVAST, Wilson's (Weiyan, 1992) value is used, which refers to the resistance height at z = 10 m above the water surface. In water bodies with strong currents such as estuaries and rivers, the wind stress is often small compared to bottom shear stress. However, the wind generally plays a more important role in the open sea and in lakes.

2.2.2.1.3 Bottom Friction

Bottom friction has a non-linear, retarding effect on the flow. The Chezy coefficient is a semi-empirical bottom friction coefficient, which was originally developed to describe uniform flow in open channels. Under rough turbulent flow conditions, i.e., Reynolds number Re > > 1000 and an assumed logarithmic velocity-depth profile, the Chezy bottom friction coefficient is assumed to be independent of the flow and varies only with the relative roughness of the bed:

$$C = -18 \times \log_{10}\left(\frac{k}{H \times 12.0}\right) \tag{2.5}$$

Under transitional flow conditions, i.e., if Re 2000 – 4000, the Chezy coefficient varies with the flow conditions. The user can decide to switch to a different mode of calculating the Chezy coefficient by setting the corresponding flag in the data file. Under transitional flow conditions, the Chezy coefficient is dependent upon the relative roughness and the Reynolds number and may be written as:

$$C = -18 \times \log_{10}\left(\frac{k}{H \times 12.0} + \frac{5}{Re \times 18.0} \times C\right) \tag{2.6}$$

k = roughness length (data file)

Re = Reynolds number

Within DIVAST, the Chezy coefficient is recalculated every few time steps, where the duration is specified by the user in the data file. The Chezy coefficient may typically vary between 20-70 $(m^{0.5}/s)$ for floodplains and rivers (Weiyan, 1992).

2.2.2.1.4 Turbulence

The turbulent shear stress refers to the flow resistance associated with the random motion of the fluid in space and time. The momentum exchange brought about by the turbulence causes the velocity-depth distribution to be more uniform than under laminar flow conditions. DIVAST only considers turbulent shear stress near the bed. The turbulence model in DIVAST relates to Boussinesq's approximation for the mean shear stress τ_e in turbulent flow giving:

$$\tau_e = \varepsilon \frac{dv}{dy} \tag{2.7}$$

where ε is the eddy viscosity, which is dependent on the turbulence characteristics of the flow and is generally several orders of magnitude greater than the molecular viscosity. If the turbulent shear stress is dominated by bottom friction, a relationship between the Chezy coefficient and the eddy viscosity exists. In DIVAST, the depth-integrated eddy viscosity is calculated (after Fischer, 1979) from:

$$\varepsilon = C_e \frac{H}{C} \sqrt{g(U^2 + V^2)} \tag{2.8}$$

where

C_e = eddy viscosity (constant specified in the data file)

Fischer's (1979) suggested typical values for C_e of 0.15, based upon laboratory data. For actual tidal flows in estuaries and coastal areas, the value of C_e is frequently much larger and in this study $C_e \approx 1.0$ is used (see Falconer et al., 2000).

2.2.2.2 Solute Transport Equations

When a cloud of dissolved or suspended material is released into a receiving water, the cloud will propagate, dilute and spread as it moves with the flow due to the effects of advective, diffusive and dispersive transport processes. The advection refers to the transport of the material by an imposed current system, such as that due to a tide in estuarine and coastal waters. Diffusion includes the scattering of particles by molecular and turbulent motion. The dispersion, as distinct from diffusion, is the dilution process associated with the stretching out and distortion of a cloud of solute in a non-uniform flow, by the effect of velocity shear and consequential averaging of the flow distribution over depth for two-dimensional models (Smith, 1992).

For a horizontal or quasi-horizontal flow, the three-dimensional solute mass balance equation can be integrated over the water column depth to give the two-dimensional depth integrated advective-diffusion equation according to the DIVAST model reference manual (2000) as:

$$\begin{aligned}&\frac{\partial HS}{\partial t}+\frac{\partial HUS}{\partial x}+\frac{\partial HVS}{\partial y}=\frac{\partial}{\partial x}\left[D_{xx}H\frac{\partial S}{\partial x}+D_{xy}H\frac{\partial S}{\partial y}\right]\\&+\frac{\partial}{\partial y}\left[D_{yx}H\frac{\partial S}{\partial x}+D_{yy}H\frac{\partial S}{\partial y}\right]+\phi_s\end{aligned} \tag{2.9}$$

where; S = depth averaged solute concentration (mass/unit volume) or temperature (°C), $D_{xx}, D_{xy}, D_{yx}, D_{yy}$ = depth averaged dispersion-diffusion coefficients in the x and y directions respectively (m^2/s), which have been shown (Preston, 1985, Holly, 1984) to be of the form:

$$\left.\begin{aligned}D_{xx}&=\frac{(k_l p^2+k_t q^2)\sqrt{g}}{C\sqrt{p^2+q^2}}\\D_{yy}&=\frac{(k_t p^2+k_l q^2)\sqrt{g}}{C\sqrt{p^2+q^2}}\\D_{yx}=D_{yx}&=\frac{(k_l-k_t)pq\sqrt{g}}{C\sqrt{p^2+q^2}}\end{aligned}\right\} \tag{2.10}$$

in which, k_l and k_t are the depth averaged longitudinal dispersion and lateral turbulent diffusion coefficients respectively, and have typical values of 5.93 for k_l and 0.23 for k_t after Elder (1959).

2.2.2.2.1 Water Quality Processes

Φ_s summarises all other sources and sinks of solute. Sources and sinks include discharges from outfalls and rivers as well as chemical and biological kinetic transformations.

In DIVAST all solutes may enter the modelling domain via outfalls. The discharge from the outfalls can be constant or varying. An initial concentration of each pollutant in the cell containing the outfall is calculated by assuming that the discharged material is immediately and homogeneously distributed over that particular cell.

(a) For outfalls:

$$\phi_s = \frac{Q_o}{A_o} S_o \tag{2.11}$$

where

Q_o = outfall discharge rate (m^3/s)

A_o = horizontal outfall discharge area (m^2), corresponding to Δx^2, where Δx^2 is the grid size.

S_o = outfall discharge concentration (mass/unit volume)

(b) For a non-conservative solute the source term may be written as:

$$\phi_s = -KSH \tag{2.12}$$

where, K = mortality rate, as in the case of coliform bacteria, or a kinetic transformation rate. The transformation may be biological or chemical and has different values and a different theoretical background for each water quality variable. In water quality models like DIVAST, K is typically assumed to be constant, making the equation analogous to radioactive decay or may be set to vary between day time and night time. Nonetheless, the underlying processes can be fundamentally different. Although first order decay is often appropriate, it should be born in mind that biological processes such as substrate uptake can be more complex, i.e., because bacterial populations adapt to high substrate concentrations. Such adaptations can play a role in the vicinity of sewage outfalls etc. The Transformation and decay of specific pollutants is discussed in more detail later.

As mentioned at the start of this chapter it is not the purpose of this research to undertake a detailed analysis of free surface flow modelling. Therefore, for further details of the water quality sub-models of DIVAST including: bacteria, BOD and dissolved oxygen, nitrogen and phosphorus etc, the reader is referred to the DIVAST model reference manual (Falconer et al., 2000).

2.2.2.3 Finite Difference Schemes

The finite difference scheme used in the DIVAST model is based upon the Alternating Direction Implicit, or ADI, technique which involves the sub-division of each timestep into two half time steps. Thus a two-dimensional implicit scheme can be applied but considering only one dimension implicitly for each half timestep, without the solution of a full two-dimensional matrix. For the first half timestep the water elevation, U velocity component (or the unit width discharge p) and the solute concentration are solved implicitly in the x-direction, whilst the other variables are represented explicitly. Similarly, for the second half timestep, the water elevation, V velocity component (or the unit width discharge q) and the solute concentration are solved implicitly in the y-direction, with the other variables being represented explicitly. With the boundary conditions included, the resulting finite difference equations for each half timestep are solved using the method of Gauss elimination and back substitution. In the DIVAST model, a space staggered grid system is used to enable the boundary conditions to be included in a more straightforward manual (see Falconer et al., 2000 for details).

The ADI scheme, which is used in the DIVAST model, is basically second order accurate both in time and space and with no stability constraints due to the time centred implicit character of the ADI technique. However, it has been recognised that the time step needs to be restricted so that a reasonable level of computational accuracy can be achieved (Chen, 1992). A maximum Courant number (C_f) has been suggested by Stelling (1982) as given by:

$$C_f = 2\Delta t\sqrt{gH\left(\frac{1}{\Delta x^2}+\frac{1}{\Delta y^2}\right)} \le 4\sqrt{2} \qquad (2.14)$$

with an average depth being used in the cited examples. When the 2-D solute transport equation is also solved for each timestep, then the choice of the time step should also consider the stability requirements for the solute transport equation.

A refined and highly accurate finite difference scheme has been used to solve the solute transport or advective-diffusion equation, namely the ULTIMATE QUICKEST scheme. This scheme reduces considerably the introduction of numerical (or artificial) diffusion and eliminates undershoot or overshoot in regions of high concentration gradients. This factor is particularly useful for the simulation of point sources, such as long sea outfall discharges and random episodic discharges from combined sewer overflows. For more details of the DIVAST model, regarding the initial and boundary conditions and solution strategy, see Falconer et al. (2000).

2.3 Governing Two Dimensional Groundwater Flow Equations

2.3.1 History and Overview of the Groundwater

As one of the main aims of this study was to develop a 2-D groundwater model, it is essential to present more details about this area. Therefore, in part two, firstly a brief history of groundwater flow is given and then the governing partial differential equations are derived.

The birth of groundwater hydrology as a quantitative science can be traced back to the year 1856. It was in that year that a French hydraulic engineer, named *Henry Darcy,* published his report on the water supply of the city of Dijon, France. In the report Darcy described a laboratory experiment that he had carried out to analyse the flow of water through sands. The results of his experiment can be generalised into the empirical law that now bears his name (see Freeze and Cherry, 1979).

The water law governing groundwater flow is less advanced than that for surface water flow because of: the complexity of the mechanics within groundwater movement, the lack of specific information on the physical features of groundwater basins, and the relatively limited use of groundwater prior to 50 years ago (Fredericks et al., 1998).

2.3.2 Governing Equations

2.3.2.1 Groundwater Flow

Water in a porous medium may be found in various compositions. To a small degree, it is absorbed by soil grains (hygroscopic water); with increasing moisture, it begins to cover the soil grains under the form of a thin film; with a further increase in the moisture content, it fills the narrow pores in the form of menisci; and finally, water may fill all the pores (with the exclusion of isolated parts, filled with air bubbles). In the latter state, water acquires the property to move under the influence of gravity. It is called gravitational or groundwater flow. Laws are applicable to this kind of flow, that are related to the laws of hydrodynamics (see Polubarinova-Kochina, 1962).

In this study, only saturated flow is considered. As mentioned above, in saturated flows, water completely fills the void spaces of the considered porous medium. The basic equation governing the fluid motion through a porous medium is developed from first principles, of a homogeneous fluid, with the basic assumptions being reviewed, and starting from the experiments of Darcy in 1856. However, further details of this derivation may be found elsewhere and in a variety of textbooks such as Freeze and Cherry (1979), Bear (1979), Hunt (1983) and Spitz and Moreno (1996).

2.3.2.1.1 Darcy's Law

According to Bear (1979), in 1856 Henry Darcy investigated the flow of water in vertical homogeneous sand filters in connection with the fountains of the city of Dijon, France. He measured the discharge and the head drop through the sand. From his experiments, Darcy concluded that the rate of flow Q, i.e., volume of water per unit time, was proportional to the constant cross-sectional area A, to the differential head $(\varphi_2 - \varphi_1)$ across the filter, of length L, and inversely proportional to the length L (see figure 2.1). When combined, these conclusions gave the basic form of Darcy's law for an incompressible fluid as follows:

$$Q = -KA\frac{(\varphi_2 - \varphi_1)}{L} \tag{2.15}$$

where K is the hydraulic conductivity of the porous medium, φ_1 and φ_2 are the inlet and outlet Piezometric heads, respectively.

In the formula above the piezometric head, described in terms of the head of water, the sum pressure and potential energies of the fluid per unit weight give the hydraulic gradient.

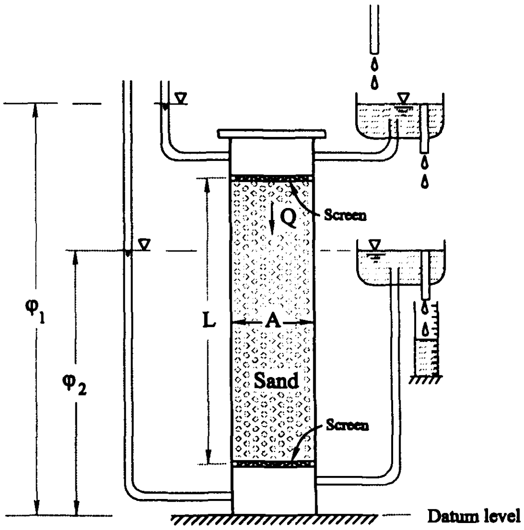

Figure 2.1: Darcy's experiment (Bear, 1972).

The hydraulic gradient is denoted by J, where $J = (\varphi_1 - \varphi_2)/L$. Therefore, the specific discharge, q, could be defined as the volume of water flowing per unit time through a unit cross-sectional area, which in the direction of flow is given as:

$$q = -KJ \tag{2.16}$$

i.e. this is another form of Darcy's formula, where $q = Q/A$.

For the case of an inclined homogeneous porous medium column, Figure 2.2, Darcy's formula can be re-written as:

$$Q = KA(\phi_1 - \phi_2)/L; \qquad q = K(\phi_1 - \phi_2)/L = KJ \tag{2.17}$$

where $\phi = z + \frac{p}{\gamma}$ is the total head (i.e. elevation above datum level plus static pressure head), p is the pressure and γ is the specific weight of water. Also the energy loss, which is denoted by $\Delta\phi = \phi_1 - \phi_2$, is due to friction in the flow through the narrow tortuous paths of the porous medium. In Darcy's law since changes in the piezometric head along the flow path are much larger than changes in the kinetic energy, the latter is generally neglected.

2.3.2.1.2 Extensions of Darcy's Law

The above mentioned Darcy's law is limited to one-dimensional flow of a homogeneous

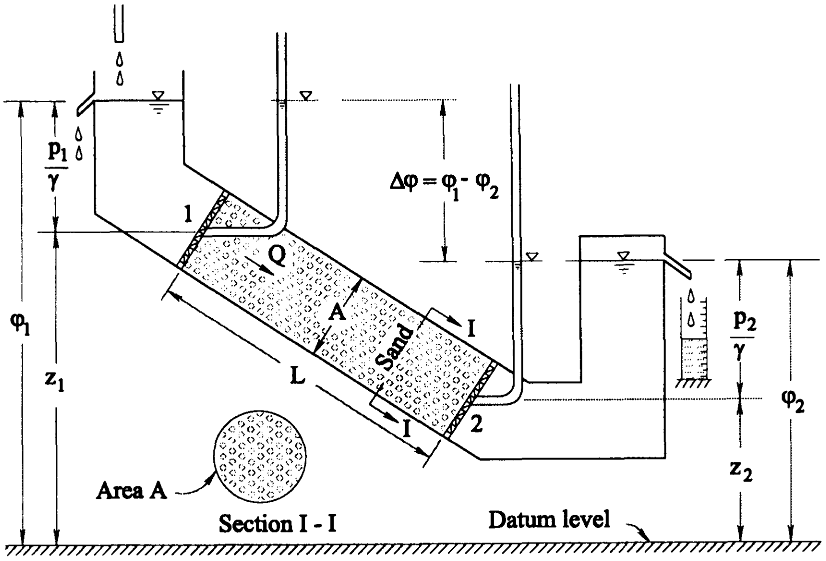

Figure 2.2: Darcy's experiment, inclined sand filter (Bear, 1972).

incompressible fluid. For a three-dimensional flow analysis the equation can be extended to give:

$$q = KJ = -Kgrad\phi \tag{2.18}$$

where q is the specific discharge vector with components q_x, q_y, q_z in the, x, y, z, co-ordinate directions respectively, and $J = -grad\phi$ (or $-\nabla\phi$), i.e. the hydraulic gradient, with components $J_x = -\partial\phi/\partial x$, $J_y = -\partial\phi/\partial y$, $J_z = -\partial\phi/\partial z$ in the x, y, z, directions, respectively. For a homogeneous isotropic medium the coefficient K is a constant scalar and the above mentioned formula can be written as follow:

$$\left.\begin{aligned} q_x &= KJ_x = -K\partial\phi/\partial x \\ q_y &= KJ_y = -K\partial\phi/\partial y \\ q_z &= KJ_z = -K\partial\phi/\partial z \end{aligned}\right\} \tag{2.19}$$

Therefore, for a homogeneous isotropic medium, it is possible to write:

$$q = -grad(K\phi) = -grad\varphi, \quad \varphi = K\phi, \quad [\varphi] = L^2/T \tag{2.20}$$

In these formulae the parameters have the same meaning as before.

2.3.2.1.3 *Range of Validity of Darcy's Law*

In the current research study the numerical model developed herein has been calibrated and verified using supplied data from a physical model. Therefore, it was important to control the validation limits of Darcy's law in the physical model. This criterion is now discussed briefly.

Research so far has shown that as the specific discharge, q, increases, the relationship between the specific discharge and the hydraulic gradient, J, gradually deviates from the linear relationship expressed by Darcy's law. Figure 2.3 shows typical experimental results leading to this conclusion. In practically all cases, Darcy's law is valid as long as the Reynolds number does not exceed a value of between about 1 and 10 (Bear, 1972). In flow through conduits, the Reynolds number, Re, which is a dimensionless number expressing the ratio of inertial to viscous forces acting on the fluid, is used as a criterion to distinguish between laminar flow occurring at low velocities and turbulent flow occurring at higher velocities. The critical value of Re between laminar and turbulent flow in pipes is around 2000. By analogy, a Reynolds number is defined also for flow through porous media, $\mathrm{Re} = qd/\nu$, where d is some representative length of the porous matrix, and ν is the kinematic viscosity of the fluid. Often the mean grain diameter is taken as the length dimension d in the formula. Sometimes d_{10}, that is, the diameter such that 10 percent by weight of the grains are smaller than that diameter, is mentioned in the literature as a representative grain diameter. According to Bear (1972), also it is suggested that,

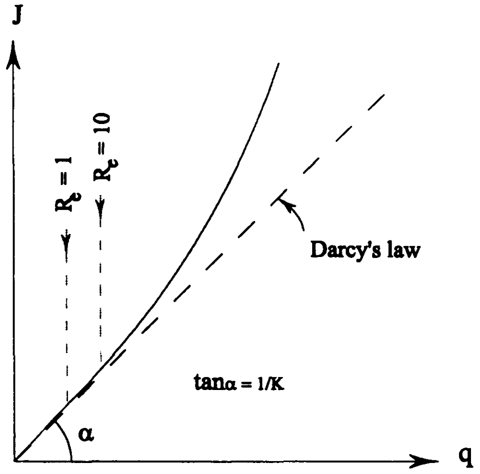

Figure 2.3: Range of validity of Darcy's law (Bear, 1979).

$d = (k/n)^{1/2}$, where k is permeability and n is porosity, as the representative length d, also it is suggested as $d = k^{1/2}$. This will be reviewed again briefly in Chapter 5.

2.3.2.1.4 Hydraulic Conductivity

The saturated hydraulic conductivity (K_s) of soils is an important factor affecting soil water infiltrability and is often required as an input parameter for hydrological models (Ebrahimi and Fardad, 1999). The hydraulic conductivity of an isotropic porous medium is a scalar (dimensions L/T) that expresses the ease with which a fluid is transported through a porous matrix. It appears in various forms in Darcy's law and is also called the coefficient of permeability. In an isotropic porous medium it may be defined, using $q = KJ = -Kgrad\phi$, as the specific discharge per unit, hydraulic gradient. The hydraulic conductivity depends on the properties both of the porous matrix and the fluid. The relevant fluid properties are density, ρ, and viscosity, μ, and the relevant solid matrix properties are mainly the grain size distribution, shape of grains, tortuosity, specific surface and porosity, Bear (1972).

However, some other factors such as: the structure of porous medium, the percentage of organic materials in a soil, and the joints and cracks in different soils could affect the rate of this coefficient dramatically, the affects of these factors have been investigated by the author in detail, see Ebrahimi (1994). Several field and laboratory methods are available for the determination of the hydraulic conductivity, e.g., Auger hole method (Ernst), Inverse auger hole method (Porchet), Shallow well pump in test and Guelph permeameter are some of field methods. On the other hand the Falling head and the Constant head methods are two laboratory methods which are generally used for this purpose. In this study determination of the hydraulic conductivity of the sand, which was used in the physical model, has involved the Constant head method. This will be reviewed briefly in Chapter 5.

2.3.2.1.5 *Aquifer Transmissivity and Specific Storage*

In the study of transient groundwater flow, we are directly concerned with gain or loss of water from storage. The amount of water released from storage per unit surface area of an aquifer, per unit change in head is referred to as the *specific storage coefficient*. The specific storage coefficient in an unconfined aquifer is equivalent to the specific yield, S_y, or effective porosity n_e and it may range from 1% to 30%. In a confined aquifer, storage, S_s, is attributed to compression of both the aquifer and the water, and storage coefficient is comparatively small as noted by Spitz and Moreno (1996).

For a confined aquifer of thickness b, the transmissivity (or transmissibility) T, is defined as:

$$T = Kb \tag{2.21}$$

and the storativity (or storage coefficient) S, is defined as

$$S = S_s b \tag{2.22}$$

The storativity of a saturated confined aquifer, of thickness b, can be defined as the volume of water that an aquifer releases from storage per unit surface area of aquifer, per unit decline in the component of hydraulic head, normal to that surface (Freeze and Cherry, 1979). In an unconfined aquifer, the transmissivity is not as well defined as in a confined aquifer, but it can nevertheless be used. It is defined by the same equation, but b is now the saturated thickness of the aquifer, or the height of the water table above the top of the underlying layer that bounds the aquifer.

2.3.2.1.6 Mass Conservation and Continuity Equation

In order to derive the mass conservation equation, consider a control volume, figure 2.4,

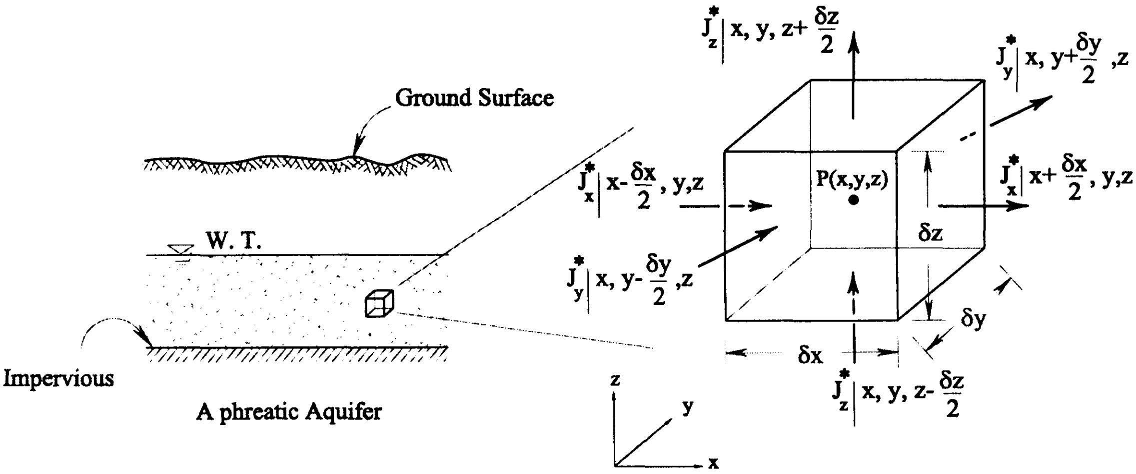

Figure 2.4: Conservation of mass for a control volume (Bear, 1979).

with the shape of a rectangular box of dimensions $\partial x, \partial y, \partial z$ centred at some point *p(x,y,z)* inside the flow domain. The aim is to write a balance, according to the Eulerian approach, of conservation for the mass of water entering, leaving and being stored in the control volume. In the Eulerian approach, contrary to the Lagrangian approach, the mass of water which follows as it moves in the porous medium, it is not fixed.

In figure (2.4) the vector J^* denotes the mass flux (mass per unit area per unit time) of water of density ρ at the point *P(x,y,z)* and therefore we can write:

$$J^* = \rho q \tag{2.23}$$

where, ρ is the density of water and q is specific discharge (flow per unit area per unit time). According to the above information, for different dimensions the excess of inflow over outflow of mass in the control volume, and during a short time interval ∂t, in the x-direction, and similarly for the y and z-directions, can be written as:

$$\left.\begin{matrix} \left[J^*_x\big|_{x-\partial x/2,y,z} - J^*_x\big|_{x+\partial x/2,y,z} \right]\partial y\partial z\partial t \\ \left[J^*_y\big|_{x,y-\partial y/2,z} - J^*_y\big|_{x,y+\partial y/2,z} \right]\partial x\partial z\partial t \\ \left[J^*_z\big|_{x,y,z-\partial z/2} - J^*_z\big|_{x,y,z+\partial z/2} \right]\partial x\partial y\partial t \end{matrix}\right\} \tag{2.24}$$

By adding these expressions, the total increase of mass inside the control volume during ∂t will be equal to:

$$\left[\frac{\left[J^*_x\big|_{x-\partial x/2,y,z} - J^*_x\big|_{x+\partial x/2,y,z} \right]}{\partial x} + \frac{\left[J^*_y\big|_{x,y-\partial y/2,z} - J^*_y\big|_{x,y+\partial y/2,z} \right]}{\partial y} + \frac{\left[J^*_z\big|_{x,y,z-\partial z/2} - J^*_z\big|_{x,y,z+\partial z/2} \right]}{\partial z} \right]\partial x\partial y\partial z\partial t \tag{2.25}$$

where, $\partial x\partial y\partial z = \partial u$, or the volume of the control volume. By dividing equation 2.25 by ∂u and ∂t, and assuming that the box converges at the point p, (*i.e.* $\partial u \to 0$), then the increase of mass per unit volume of a porous medium and per unit time is given as:

$$-\left(\frac{\partial J^*_x}{\partial x} + \frac{\partial J^*_y}{\partial y} + \frac{\partial J^*_z}{\partial z}\right) = -divJ^*, \quad J^* = \rho q \tag{2.26}$$

On the other hand, according to the principle of mass conservation, the rate of increase of mass inside the element must be equal to the change of mass, m, during ∂t, within the element giving:

$$-(\frac{\partial J^*_x}{\partial x}+\frac{\partial J^*_y}{\partial y}+\frac{\partial J^*_z}{\partial z})=\frac{\partial \rho n}{\partial t} \text{ or } -div(\rho q)=\partial \rho n/\partial t \qquad (2.27)$$

where, n, is the porosity of the porous medium. Equation (2.27) is a form of mass conservation for porous media and each side of the equation expresses the net added mass of water per unit time and unit volume of porous media around point p.

For the case of steady state flow $(\partial \varphi/\partial t)=0$ and/or when both fluid and solid matrix are incompressible (*i.e.* $\partial S/\partial t=0$) and $\rho = const.$ then the equation reduces to:

$$divq=0 \qquad (2.28)$$

which actually defines a conservation of volume. Previously, for a homogeneous and isotropic medium the following form of Darcy's law; $q=KJ^* = -Kgrad\phi$ was obtained the specific discharge. By considering equation (2.27) for a compressible medium the equation can be rewritten as:

$$K\ div(grad\varphi)=K\left(\frac{\partial^2\varphi}{\partial x^2}+\frac{\partial^2\varphi}{\partial y^2}+\frac{\partial^2\varphi}{\partial z^2}\right)=S\frac{\partial\varphi}{\partial t} \qquad (2.29)$$

in the equation 2.29, S is the storage coefficient of an aquifer and is a function of the total head, φ.

Again, for a steady state flow and/or when both the water and solid matrix are assumed to be incompressible, the right hand side of the equation (2.29) vanishes and it reduces to the Laplace equation for a three dimensional domain:

$$\nabla^2\varphi=\frac{\partial^2\varphi}{\partial x^2}+\frac{\partial^2\varphi}{\partial y^2}+\frac{\partial^2\varphi}{\partial z^2}=0 \qquad (2.30)$$

2.3.2.1.7 Flow in a Confined Aquifer

In considering figure (2.5) for a confined aquifer and for the control volume of $b\partial x\partial y$ the continuity of flow (on balance of volume) can be written as follows:

$$\left\{\begin{array}{l} \partial y\left[Q_x\left(x-\frac{\partial x}{2},y\right)-Q_x\left(x+\frac{\partial x}{2},y\right)\right]+\\ \partial x\left[Q_y\left(x,y-\frac{\partial y}{2}\right)-Q_y\left(x,y+\frac{\partial y}{2}\right)\right]\end{array}\right\}\partial t = S(\partial x\partial y)\left[\varphi(t+\partial t)-\varphi(t)\right] \tag{2.31}$$

where $Q = -Kb.grad\varphi$, is the discharge within the aquifer. Each side of the above equation expresses the rate of increase of water (in terms of volume) inside the element during time ∂t. Dividing equation (2.31) by $\partial x\partial y\partial t$, and assuming that $\partial x, \partial y, \partial t \to 0$, then in the limit equation (2.31) reduces to:

$$div(Tgrad\varphi) = S\frac{\partial\varphi}{\partial t} \tag{2.32}$$

where $T = b.K$ and S is the specific storage of an aquifer.

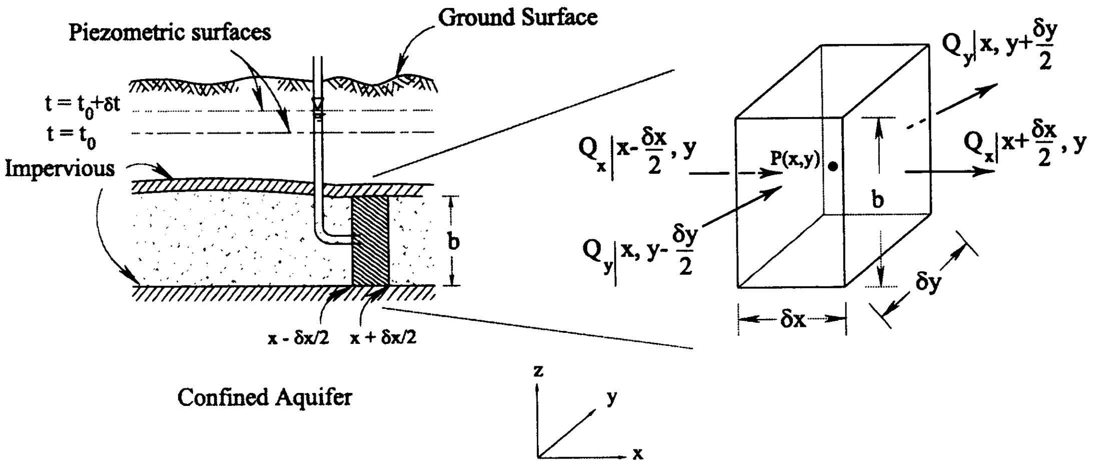

Figure 2.5: Continuity of flow for a confined aquifer (Bear, 1979).

In equation (2.32) it is essential to regard the effect of distributed source and sinks, $N(x,y,t)$, and as well point sources and sinks (e.g., recharging and pumping wells, respectively). As a final result, for a homogeneous isotropic aquifer, T=const., equation (2.32) can be written as:

$$T\left(\frac{\partial^2\varphi}{\partial x^2}+\frac{\partial^2\varphi}{\partial y^2}\right)+N(x,y,t)=S\frac{\partial\varphi}{\partial t} \qquad (2.33)$$

and again for a steady state flow and no source/sink inputs, the above equation reduces to the Laplace equation:

$$\nabla^2\varphi,\ \frac{\partial^2\varphi}{\partial x^2}+\frac{\partial^2\varphi}{\partial y^2}=0 \qquad (2.34)$$

2.3.2.1.8 Dupuit Assumptions for a Phreatic Aquifer

A phreatic aquifer, unconfined aquifer system, is defined as one in which a water table (phreatic surface) serves as its upper boundary. In fact, a phreatic surface is an imaginary surface, at all points of which the pressure is atmospheric. According to Freeze and Cherry (1979), for flow in a phreatic aquifer, an approach pioneered by Dupuit (1863) and advanced by Forchheimer (1930) is often invoked. This approach is based on two assumptions: (i) flow-lines are assumed to be horizontal and equipotentials vertical, and (ii) the hydraulic gradient is assumed to be equal to the slope of the free surface and invariant with depth. In fact this assumption neglects the vertical flow components. Therefore, a three-dimensional unconfined flow field is reduced to a two-dimensional *xy* horizontal flow field by invocation of the Dupuit-Forchheimer theory. The Dupuit assumptions are probably the most powerful tool for treating unconfined flows (Bear 1972). Also Bear (1972) has included a very lengthy theoretical treatment of the Dupuit-Forchheimer theory.

2.3.2.1.9 Flow for a Phreatic Aquifer

Numerical modelling of fluid flow in a porous media, in the case of transient flow, is based on mass conservation and Darcy's laws (Boussinesq equation). In order to achieve this aim we need to derive the equation by considering a control volume within a phreatic aquifer, as shown in the figure 2.6.

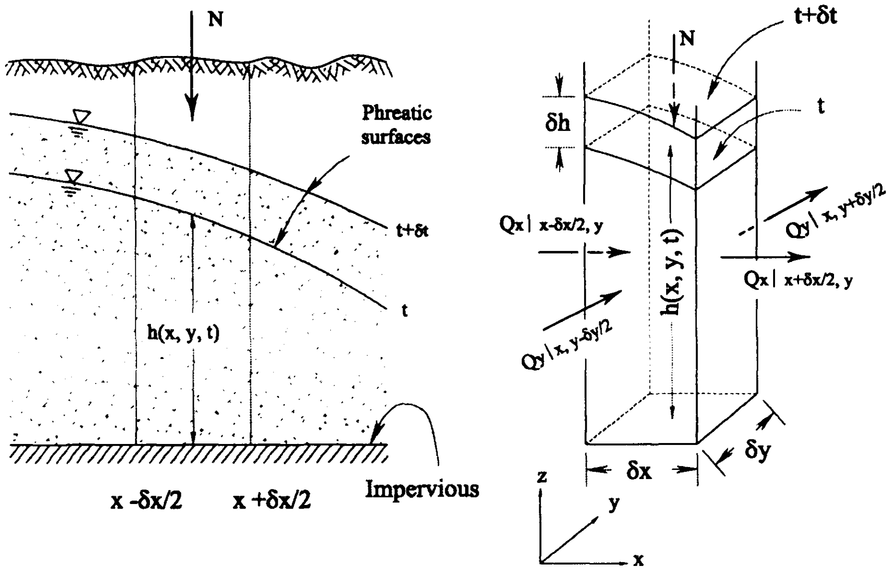

Figure 2.6: Flow in a phreatic aquifer (Bear, 1979).

In the figure (2.6) the net effect of natural replenishment, artificial recharge and pumping is shown as a rate of accretion, N or point sources/sinks. It is positive when vertically downward. Also all the inputs/outputs, i.e., recharging and pumping wells, respectively, can be introduced as distributed sources and sinks.

Therefore, we may express the net inflow as:

$$N(x,y,t)=\sum_{(i)} N(x_i,y_i,t)\partial(x-x_i,y-y_i) \tag{2.35}$$

where N is the rate of net inflow at a point (x_i,y_i) and time t. Note that the dimensions of $N(x,y,t)$ are L/T while those of $N(x_i,y_i,t)$ are L^3/T.

The balance equation based on the Dupuit assumption of horizontal flow and with no internal sources/sinks could be written as follows:

$$\left\{\begin{aligned} &\partial y\left[Q_x\left(x-\frac{\partial x}{2},y\right)-Q_x\left(x+\frac{\partial x}{2},y\right)\right]+\\ &\partial x\left[Q_y\left(x,y-\frac{\partial y}{2}\right)-Q_y\left(x,y+\frac{\partial y}{2}\right)\right]\end{aligned}\right\}\partial t = S(\partial x\partial y)\left[h(t+\partial t)-h(t)\right] \tag{2.36}$$

where, S is the specific yield of the phreatic aquifer.

Again, by dividing the equation (2.36) by $\partial x\partial y\partial t$, and letting $\partial x,\partial y,\partial t \rightarrow 0$, then a homogeneous isotropic phreatic aquifer, K=const., maybe assumed giving:

$$\frac{\partial}{\partial x}\left(h\frac{\partial h}{\partial x}\right)+\frac{\partial}{\partial y}\left(h\frac{\partial h}{\partial y}\right)+\frac{N}{K}=\frac{S}{K}\frac{\partial h}{\partial t} \tag{2.37}$$

This is the basic continuity equation for groundwater flow in a phreatic aquifer with a horizontal impervious base. It is often referred to as the *Boussinesq equation.* This equation can be rearranged and simplified to give:

$$\left(\frac{\partial^2 h^2}{\partial x^2}+\frac{\partial^2 h^2}{\partial y^2}\right)+\frac{2N}{K}=\frac{S}{T}\frac{\partial h^2}{\partial t}, \quad \text{or} \quad \frac{\partial h}{\partial t}=\frac{T}{S}\left(\frac{\partial^2 h}{\partial x^2}+\frac{\partial^2 h}{\partial y^2}\right)-\frac{N}{S} \tag{2.38}$$

where:

h	total hydraulic head;
S	specific yield of the phreatic aquifer;
T	transmissivity of the aquifer;
N	sources/sinks

2.3.2.2 Solute Transport Processes

2.3.2.2.1 Introduction

Groundwater rarely constitutes “pure water”. It generally contains dissolved elements and suspended particles. Water quality can also be affected by bacteria, viruses, gases etc. The type and concentration of dissolved elements depends upon the chemical composition of the rock formations in which groundwater flow occurs and on the travel time of the fluid mass within these rocks.

Contaminants may reach the groundwater either dissolved in the water column (miscible) or as a liquid phase that may be immiscible in water. Some contaminants, such as heavy metals, may also be absorbed on fine particles and transported in suspension. Miscible liquids (or dissolved contaminants) migrate through the aquifer differently from immiscible fluids. Miscible fluids and the natural groundwater form one phase whose movement can be expressed by Darcy’s law, and is often referred to as single-phase flow. Immiscible liquids flow in separate phases through the pore space (giving multiphase flow). Modelling of multiphase flow is far more complex than simulating single-phase flow. Multiphase flow occurs for example in the unsaturated zone or in hydrocarbon or chlorinated solvent spills (i.e., hydrocarbon-water or chlorinated solvent-water phases).

Solutes that remain stable in groundwater and do not change due to physical, biological, or chemical processes are described as conservative. Typical examples of conservative solutes are fluorescin, which is widely used in migration tests, and chloride. The purpose of discussing transport mechanisms is to understand the processes that most strongly influence the migration of dissolved contaminants in saturated flow in a granular aquifer. The most general transport mechanisms are; Advection, Diffusion, Dispersion, Sorption and Decay.

As the concentration of current research has been placed on the simulation of the conservative migration of dissolved contaminates in the complex flow system of wetlands and the adjacent coastal waters through groundwater, it is necessary here to mention the related governing equations of advection and diffusion. Further details may be found elsewhere in a variety of textbooks such as Spitz and Moreno (1996) or Wang and Anderson (1982).

2.3.2.2.2 Basic Concepts

The transport of dissolved solids with the local groundwater flow field is called *advective* transport. The simulation of the advection process and the movement of dissolved contaminants in groundwater is a particularly active area of research. Movement of contaminants in groundwater occurs not only by advection but also by *dispersion.* Dispersion refers to mixing and spreading caused in part by molecular diffusion and, in part, by variations in velocity within the porous medium, see Wang and Anderson, (1982).

Consider a flow field in which the average linear velocity has components v_x and v_y. The tracer is carried along by the flow field and is dispersed. The microscopic velocity at any point in the aquifer may vary from the average linear velocity. Let v_x^* and v_y^* be the microscopic velocity components relative to the average velocity components, i.e., v_x and

v_y; that is, v_x^* and v_y^* represent the dispersive tracer movement. Their definition incorporates the idea that point-to-point statistical fluctuations of velocity exist relative to the average.

A *mass flux* is the amount of mass crossing a unit cross-sectional area per unit time. The dispersive mass flux is the mass flux which results from the relative velocity components v_x^* and v_y^*. In the infinitesimally small volume surrounding a point in the aquifer, the groundwater specific discharge through a face perpendicular to the x direction is nv^*_x where n is the porosity. If C is the solute concentration expressed as a mass per unit volume of water, then the dispersive mass flux in the x direction is given as:

$$f_x^* = nCv_x^* \tag{2.39}$$

Similarly, the dispersive flux in the y direction can be written as

$$f_y^* = nCv_y^* \tag{2.40}$$

For the case of a uniform flow field the longitudinal and transverse components of the dispersion coefficient in the x direction, where $v_x = \bar{v}_x$ and $v_y = 0$, need to be defined. The longitudinal component D_L [of units L^2/T], of the dispersion coefficient is defined by analogy to Fick's law of diffusion. Specifically, the dispersive flux is assumed to be proportional to the product of the concentration gradient in the flow direction and the porosity giving:

$$nCv_x^* = -nD_L \frac{\partial C}{\partial x} \tag{2.41}$$

Dividing through out by n gives;

$$Cv_x^* = -D_L \frac{\partial C}{\partial x} \tag{2.42}$$

Likewise, the transverse component D_T of the dispersion coefficient is defined such that the dispersive flux perpendicular to the flow direction is proportional to the product of the porosity and the concentration gradient in the y direction, giving:

$$nCv_y^* = -nD_T \frac{\partial C}{\partial y} \tag{2.43}$$

Dividing Eq. (2.43) by n gives

$$Cv_y^* = -D_T \frac{\partial C}{\partial y} \tag{2.44}$$

Equations (2.42) and (2.44) are similar to Fick's law of diffusion, since the distribution of a concentration about the mean at a point in groundwater flow field is assumed to be analogous to the distribution of molecular diffusion of a concentration about the mean concentration in a diffusing gas.

Experiments have demonstrated that, in an isotropic medium, the longitudinal and transverse components of dispersion in equations 2.42 and 2.44 are linearly dependent upon the average velocity magnitude of the groundwater flow. For a uniform flow field with an average linear velocity equal to $\bar{v}_x$ then:

$$D_L = a_L \bar{v}_x \tag{2.45}$$

and

$$D_T = a_T \bar{v}_x \tag{2.46}$$

where the parameters a_L and a_T are the longitudinal and transverse dispersivities, respectively. The dispersivities are intended to be an intrinsic physical property of the porous medium and have units of length. One would expect the dispersivities to vary spatially with changes in the lithology of the porous medium. However, dispersivities generally have been assumed to be constants in such models.

2.3.2.2.3 *Governing Equations of Solute Transport*

The assumed law that the dispersive mass flux is proportional to the concentration gradient (i.e., equations 2.42 and 2.44 for a uniform flow field) is known as the Fickian model. This law plays the same role in obtaining a governing equation for advective-dispersive mass transport as does Darcy's law in obtaining the governing equation for groundwater flow. The other law used in the derivation is the continuity or conservation of mass principle. The derivation of the time dependent governing equation for the case of steady-state uniform flow in the x direction could be as follows:

The total mass flux in the x direction is the sum of the advective and dispersive fluxes, giving:

$$f_x = n(C\overline{v}_x + Cv_x^*) \tag{2.47}$$

The assumption of uniform flow in the *x-direction* means that the total mass flux in the y direction is just the dispersive flux giving:

$$f_y = nCv_y^* \tag{2.48}$$

The advective term in equation 2.47 is $nC\overline{v}_x$, and the dispersive terms in equations 2.47 and 2.48 are nCv_x^* and nCv_y^*, respectively. Continuity requires that the divergence of the flux, that is the net outward flow of mass per unit volume of the aquifer per unit time, is equal to the rate of decrease of solute concentration per unit volume of aquifer, which can be expressed as:

$$\frac{\partial f_x}{\partial x}+\frac{\partial f_y}{\partial y}=-n\frac{\partial C}{\partial t} \tag{2.49}$$

The time derivative of the solute concentration is multiplied by the porosity, so that the right-hand side of equation 2.49 represents the change in solute mass per unit aquifer volume, rather than per unit water volume. In recalling that the concentration is defined as solute mass per unit water volume, then equations 2.42, 2.44, 2.47, 2.48 and 2.49 can be combined to give:

$$\frac{\partial}{\partial x}\left(nD_L\frac{\partial C}{\partial x}\right)+\frac{\partial}{\partial y}\left(nD_T\frac{\partial C}{\partial y}\right)-\frac{\partial}{\partial x}\left(nC\bar{v}_x\right)=n\frac{\partial C}{\partial t} \tag{2.50}$$

By replacing the components of the average velocity in the x and y direction, v_x and v_y or U and V, instead of $\bar{v}_x$ and rearranging equation (2.50) gives:

$$\frac{\partial C}{\partial t}+\frac{\partial (UC)}{\partial x}+\frac{\partial (VC)}{\partial y}=\frac{\partial}{\partial x}(D_L\frac{\partial C}{\partial x})+\frac{\partial}{\partial y}(D_T\frac{\partial C}{\partial y})-S \tag{2.51}$$

where S is the sink or source representation of the solutes. For the case of an incompressible fluid, if it is assumed that the aquifer is homogenous, then $\left(\frac{\partial U}{\partial x}+\frac{\partial V}{\partial y}\right)=0$ and $\frac{\partial D_L}{\partial x}=\frac{\partial D_T}{\partial y}=0$, with equation (2.51) being re-written to give:

$$\frac{\partial C}{\partial t}=D_L\frac{\partial^2 C}{\partial x^2}+D_T\frac{\partial^2 C}{\partial y^2}-U\frac{\partial C}{\partial x}-V\frac{\partial C}{\partial y}-S \tag{2.52}$$

where $\frac{\partial C}{\partial t}$ is the change in storage, $U\frac{\partial C}{\partial x}$ and $V\frac{\partial C}{\partial y}$ are the advective flow components and $D_L\frac{\partial^2 C}{\partial x^2}$ and $D_T\frac{\partial^2 C}{\partial y^2}$ are the diffusive fluxes.

Research so far has showed that dispersion is more pronounced in the longitudinal direction than in the transverse direction. Hence, the dispersion coefficients in both directions were defined as follows:

(i) Longitudinal dispersion coefficient:

$$D_L = \alpha_L v \tag{2.53}$$

(ii) Transverse dispersion coefficient:

$$D_T = \alpha_T v \tag{2.54}$$

where

α_L = longitudinal dispersivity [L]

α_T = transverse dispersivity [L]

v = transport velocity [L/T]

The magnitude of the dispersivities for homogeneous sands has traditionally been obtained from hydraulic models by fitting the appropriate solution of the advection-dispersion equation with the observed concentration pattern. Typical values for the dispersivities at the pore-grain scale are:

$$\alpha_L \approx \text{average grain diameter} \tag{2.55}$$

and

$$\alpha_T \approx \frac{1}{10}\alpha_L \tag{2.56}$$

According to Spitz and Moreno (1996) the ratio of the longitudinal and transverse dispersivities typically ranges from 10 to 100. Generally, dispersive spreading in nature appears to be significantly stronger than dispersion observed in hydraulic laboratory tanks or calculated in theory. Dispersion coefficients are calculated to be several orders of magnitude larger than those found for theoretical dispersion with ($\alpha_L \leq 20$ m in controlled field experiments, and $\alpha_L \leq 100\,\mathrm{m}$ obtained from plume studies). Also they suggested that; as a rule of thumb, longitudinal dispersivity is about 0.1 of the travel distance, that is:

$$\alpha_L \approx 0.1 \text{ travel distance} \tag{2.57}$$

However, the actual value may differ significantly from this simple approximation.

In the current study, the value of $\alpha_L \approx$ *average grain diameter* and $\alpha_T \approx \frac{1}{10}\alpha_L$ have been used.

2.4 Summary

In the first part of this chapter a brief introduction has been given regarding the governing equations used for free surface flow modelling in models such as DIVAST. In the second part of the chapter, the history, background and the principles of flow through porous media have been reviewed. Some hydrodynamic characteristics of porous media; such as the hydraulic conductivity, aquifer transmissivity and specific storage, have then been described in some detail. This is followed by a derivation of the governing partial differential equations of groundwater flow, for confined and phreatic aquifers (based upon Dupuit assumptions), and using both mass conservation and Darcy's laws. The above mentioned equations have been derived for an orthogonal Cartesian co-ordinate system assuming an incompressible fluid and homogeneous aquifers. Finally, a conservative form of the solute transport equation for groundwater modelling in a two-dimensional field has been derived and the corresponding coefficients for dispersion and diffusion have been discussed.

CHAPTER 3

NUMERICAL MODELLING OF POROUS MEDIA AND LINKED APPROACH

3.1 Introduction

In chapter two the governing equations of flow and solute transport in porous media are derived and presented. As mentioned in chapter two, the derived equations for porous media, like many other physical processes, appear in the form of partial differential mathematical equations. Furthermore, for these equations there are no analytical solutions. However, it is important to note that for the governing partial differential equations of porous media usually there are analytical solutions, which are limited just up to two-dimensional steady state flows. Therefore, it is essential to use the numerical (approximation) methods to achieve algebraic difference forms of the derived equations. The most frequently used numerical methods include; the finite difference, the finite element and finite volume methods, which have their own advantages and disadvantages (see Falconer, 1992). "The finite difference method is one of the oldest, most generally applicable and most easily understood methods for obtaining numerical solutions to steady and unsteady groundwater flow problems" (Hunt, 1983).

This chapter presents some general basic concepts of numerical solutions and also the numerical solution of the hydrodynamic and solute transport equations for porous media, for a two dimensional transit model, GWK, involving the finite difference method. It is worth mentioning here that the DIVAST model (Falconer, 1976), which is used to simulate the free surface phenomenon part, is based on the finite difference method too.

3.2 Basic Concepts

3.2.1 Different Types of Partial Differential Equations

The formulation of most scientific phenomena involve quantifying rates of change with respect to two or more independent variables, e.g. time, length or angle, which lead to either a partial differential equation or a set of such equations. A general form of two-dimensional second-order partial differential equations may be written as follows:

$$a\frac{\partial^2 f}{\partial x^2}+b\frac{\partial^2 f}{\partial x\partial y}+c\frac{\partial^2 f}{\partial y^2}=d(x,y,f,\frac{\partial f}{\partial x},\frac{\partial f}{\partial y}) \tag{3.1}$$

where, a, b, c and d may be functions of the independent variables x and y and of the dependent variable f.

Basically, there are three types of partial differential equations including; *Elliptic*, *Parabolic* and *Hyperbolic*. There are some special, numerical solutions for any type of the above mentioned equations; therefore, it is important to recognise the type of equations. To achieve this aim, a criterion is defined as follows:

$$\Delta = b^2 - 4ac \tag{3.2}$$

where:

a, b and c have the same meaning as before, see equation (3.1). If an equation is; $\Delta < 0$, then the equation is Elliptic, however for $\Delta = 0$ the equation is Parabolic and finally if it is bigger than zero, then the equation is Hyperbolic. For instance, the Laplace equation, $\frac{\partial^2 f}{\partial x^2} + \frac{\partial^2 f}{\partial y^2} = 0$, or Poisson's equation, $\frac{\partial^2 f}{\partial x^2} + \frac{\partial^2 f}{\partial y^2} = g$, are both two dimensional *Elliptic* equations, which are generally associated with equilibrium or steady-state problems. When the Poisson equation is derived for a case such as groundwater, *g* shows a constant rate for a source/sink. Problems involving time *t* as one independent variable usually lead to the parabolic or hyperbolic equations. For example, the simplest *Parabolic* equation, which derives from the theory of heat condition, is: $\frac{\partial u}{\partial t} - D\frac{\partial^2 u}{\partial x^2} = 0$ and the solution of this equation generates, the temperature *u* in the *x*-co-ordinate direction. Finally, hyperbolic equations generally originate from vibration problems. In other words, they originate from problems where discontinuities can persist in time, such as shock waves, across which there are discontinuities in speed, pressure and density. The simplest example of a hyperbolic equation is the one-dimensional wave equation; $\frac{\partial^2 u}{\partial t^2} - C^2\frac{\partial^2 u}{\partial x^2} = 0$. The solution of this gives, the transverse displacement *u* in the x-direction equation after a time *t,* in this case more details can be found in variety of textbooks such as Smith (1985). Similarly, there are different types of sets of partial differential equations, which are determined by evaluating the parameter *A*. By considering the following set of equations:

$$\left.\begin{aligned} a_1\frac{\partial f}{\partial x} + b_1\frac{\partial f}{\partial y} + c_1\frac{\partial g}{\partial x} + d_1\frac{\partial g}{\partial y} = e_1 \\ a_2\frac{\partial f}{\partial x} + b_2\frac{\partial f}{\partial y} + c_2\frac{\partial g}{\partial x} + d_2\frac{\partial g}{\partial y} = e_2 \end{aligned}\right\} \qquad (3.3)$$

The parameter, *A*, is defined as follows:

$$A = (a_1 d_2 - a_2 d_1 + b_1 c_2 - b_2 c_1)^2 - 4(a_1 c_2 - a_2 c_1)(b_1 d_2 - d_2 d_1) \tag{3.4}$$

and it is evaluated as:

$$\begin{cases} if, A < 0 \Rightarrow Elliptic, \\ if, A = 0 \Rightarrow Parabolic, \\ if, A > 0 \Rightarrow Hyperbolic \end{cases}$$

The famous system of two first-order Cauchy-Riemann equations, is a good example of such a system of equations, for more details see Tannehill et al. (1997).

Basically, the derivation of governing partial differential equations of scientific phenomena is the first step in the simulation of the phenomena. However, changes to the shape of the area of integration or to the boundary and initial conditions of partial differential equations often make their analytical solutions impossible. Such changes do not fundamentally affect finite difference methods, although they sometimes necessitate rather complicated modifications to the methods (see Smith, 1985).

When a set of differential equations is derived, it is essential to choose a suitable scheme to discretise them. In the case of an elliptic equation, using the central, forward or backward sub-methods of the finite difference method, which will be explained later in this chapter, the differential equation is discretised over defined grid points and converted to numerical difference equations. Then, by solving the set of algebraic equations, the unknown variables will be obtained in space. However, for the time dependent parabolic and hyperbolic equations it is necessary to discretise the derivative terms of an equation in space and time; e.g. using the finite difference method. The well known *Explicit* and *Implicit* methods could be used to achieve this aim. The semi-implicit, fully implicit and

Crank-Nicholson methods are some sub-methods of the implicit scheme, which will be reviewed later.

It worth noting that whereas numerical development of the parabolic and hyperbolic equations involving the *explicit* finite difference method are not often encountered in solving a system of non-linear equations; i.e. there is often a direct solution for them, the same development of the elliptic equations in space, and also development of the parabolic/hyperbolic equations involving *implicit* methods in space and time, are encountered in solving a system of non-linear equations. On the other hand no general algebraic method is available for solving all non-linear algebraic equations. Hence, different solution techniques exist for solving linear and non-linear systems of equations, with varying degrees of accuracy and rates of convergence being available. The degree of accuracy of results is directly related to the amount of computational effort and the method being used.

3.2.2 Finite Difference Approximations

The most common method to approximate the derivatives of a function in the case of partial differential equation in space and time is the finite difference method, which involves using Taylor's series. In the finite difference procedure, for solving partial differential equations, the continuous domain is replaced by a finite difference mesh or grid. As mentioned above, Taylor's series is then used to develop the finite difference method and is expressed below.

When a function $f(x)$ and its derivatives are finite and continuous with x and single valued, then for Δx, an increment of x, according to the Taylor's theorem the value of the function at the location of $(x+\Delta x)$ is given by:

$$f(x+\Delta x)=f(x)+\frac{\Delta x}{1!}\frac{\partial f(x)}{\partial x}+\frac{\Delta x^2}{2!}\frac{\partial^2 f(x)}{\partial x^2}+\frac{\Delta x^3}{3!}\frac{\partial^3 f(x)}{\partial x^3}+\cdots \tag{3.5}$$

similarly for $(x-\Delta x)$, see Figure 3.1, Taylor's series gives:

$$f(x-\Delta x)=f(x)-\frac{\Delta x}{1!}\frac{\partial f(x)}{\partial x}+\frac{\Delta x^2}{2!}\frac{\partial^2 f(x)}{\partial x^2}-\frac{\Delta x^3}{3!}\frac{\partial^3 f(x)}{\partial x^3}+\cdots \tag{3.6}$$

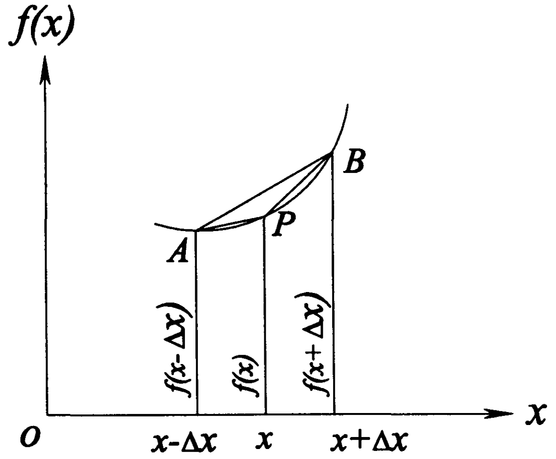

Figure 3.1: Taylor's theorem and finite difference approximations

Addition of equations (3.5) and (3.6) yields:

$$f(x+\Delta x)+f(x-\Delta x)=2f(x)+\Delta x^2\frac{\partial^2 f(x)}{\partial x^2}+O(\Delta x^4) \tag{3.7}$$

where the last term, i.e. $O(\Delta x^4)$, denotes terms containing fourth and higher powers of Δx. Assuming that the value of these terms, i.e. $O(\Delta x^4)$, is negligible in contrast with lower powers of Δx and then at the location x the truncated error is higher order from the right-hand side and can be written as:

$$\frac{\partial^2 f(x)}{\partial x^2} = (\frac{d^2 f}{dx^2})_{x=x} \approx \frac{1}{(\Delta x^2)} \{f(x+\Delta x) - 2f(x) + f(x-\Delta x)\} \tag{3.8}$$

Subtraction of Equations (3.6) from (3.5) and neglecting terms of order Δx^2, or second order truncation error, leads to the following equation:

$$\frac{\partial f(x)}{\partial x} = (\frac{df}{dx})_{x=x} \approx \frac{1}{2(\Delta x)} \{f(x+\Delta x) - f(x-\Delta x)\} \tag{3.9}$$

which is a *central-difference* approximation and approximates the slope of the tangent at the point *P* by the slope of the chord *AB*. Also according to Figure 3.1, the *forward-difference* and *backward-difference* formulae (i.e. equations 3.10 and 3.11) can also be approximated by the slope of the tangent at P of the chord PB and the chord AP, respectively.

$$\frac{\partial f(x)}{\partial x} \approx \frac{1}{(\Delta x)} \{f(x+\Delta x) - f(x)\} \tag{3.10}$$

$$\frac{\partial f(x)}{\partial x} \approx \frac{1}{(\Delta x)} \{f(x) - f(x-\Delta x)\} \tag{3.11}$$

By establishing a grid of nodal points the finite difference approximations respectively for forward and backward methods in space derivatives can be written as:

$$\left.\begin{aligned} \frac{\partial f(x)}{\partial x} &\approx \frac{f_{i+1,j} - f_{i,j}}{\Delta x}, \\ \frac{\partial f(x)}{\partial x} &\approx \frac{f_{i,j} - f_{i-1,j}}{\Delta x} \end{aligned}\right\} \tag{3.12}$$

with a leading truncation error of order (Δx^2). Similarly, for a central difference approximation it could be written as:

$$\frac{\partial f(x)}{\partial x} \approx \frac{f_{i+1,j} - f_{i-1,j}}{2\Delta x} \tag{3.13}$$

with an error of order (Δx^2).

With using the same approach, Equation (3.8) could be written as:

$$\frac{\partial^2 f(x)}{\partial x^2} \approx \frac{f_{i+1,j} - 2f_{i,j} + f_{i-1,j}}{(\Delta x)^2} \tag{3.14}$$

Also, the finite difference approximation of a time derivative $\partial f / \partial t$ at each nodal point, for the forward and backward approximations can be written as given in Equation (3.15). It should be noted that the term $\partial f / \partial t$ needs to be divided in terms of time just as in terms of space. Therefore, for the time level (n), where ($n+1$) represents one time step later and ($n-1$) represents one time step earlier, then at time (n) the derivation can be written as:

$$\left.\begin{aligned} \frac{\partial f}{\partial t} &\approx \frac{f_{i,j}^{n+1} - f_{i,j}^{n}}{\Delta t}, \\ \frac{\partial f}{\partial t} &\approx \frac{f_{i,j}^{n} - f_{i,j}^{n-1}}{\Delta t} \end{aligned}\right\} \tag{3.15}$$

where Δt is the length of the time step. The use of the central difference approximation;

$$\frac{\partial f}{\partial t} \approx \frac{f_{i,j}^{n+1} - f_{i,j}^{n-1}}{2\Delta t} \tag{3.16}$$

should be avoided because this approximation is unconditionally unstable (see Wang and Anderson, 1982). In the current study, the forward difference approximation has been used to write the finite difference form of the time derivative term.

3.2.3 Explicit and Implicit Schemes

In using Equations (3.14) and (3.15), the related finite difference approximation to the equation $a\frac{\partial f}{\partial t} = \frac{\partial^2 f}{\partial x^2}$ can be written as:

$$a\frac{f_i^{n+1} - f_i^{n}}{(\Delta t)} = \frac{f_{i+1}^{n} - 2f_i^{n} + f_{i-1}^{n}}{(\Delta x)^2} \tag{3.17}$$

where f is the exact solution of the approximation difference equations.

Equation (3.17) could be written as:

$$f_i^{n+1} = \frac{\Delta t}{a(\Delta x)^2}\left[f_{i-1}^n - 2f_i^n + f_{i+1}^n\right] + f_i^n \tag{3.18}$$

Hence, the unknown pivotal values of *f* can be calculated along the first time-row, $t = \Delta t$, in terms of known boundary and initial values along $t = 0$, then the unknown pivotal values along the second time-row in terms of the calculated pivotal values along the first, etc. A formula such as (3.18) which expresses *one* unknown pivotal value directly in terms of known pivotal values is called an *Explicit* formula. Although the explicit method is computationally simple it has one serious drawback. The convergence and stability condition of the explicit methods is as follows, for more details see Abbott and Basco (1997).

$$\lambda = \frac{\Delta t}{a(\Delta x)^2} \leq 1/2 \tag{3.19}$$

Therefore, the time step is necessarily very small because the process is valid only for $0 < \lambda \leq 0.5$, i.e. $\Delta t \leq 0.5(\Delta x^2)$, and Δx must be kept relatively small in order to attain reasonable accuracy.

In order to optimise the calculations and remove the limitations of explicit methods, *Implicit* methods are often used. The general form of an implicit finite difference approximation to the equation $a\frac{\partial f}{\partial t} = \frac{\partial^2 f}{\partial x^2}$ is given as:

$$\frac{a(\Delta x)^2}{\Delta t}(f_i^{n+1} - f_i^n) = \sigma(f_{i-1}^{n+1} - 2f_i^{n+1} + f_{i+1}^{n+1}) + (1-\sigma)(f_{i-1}^n - 2f_i^n + f_{i+1}^n) \tag{3.20}$$

As can be seen for the above equation in implicit methods the differences are done at both time-step levels, i.e. *n* and *n+1*. The limitation of implicit methods is governed by, $0 \leq \sigma \leq 1$. In the case of; $\sigma = 1$, the method is called *fully implicit* and has its own limitations. If $\sigma = 0$, then equation (3.20) will revert to the explicit method. For the case of $\sigma = 1/2$, then equation (3.20) may be written as:

$$f_i^{n+1} - f_i^n = \frac{\lambda}{2}\left[f_{i-1}^{n+1} - 2f_i^{n+1} + f_{i+1}^{n+1} + f_{i-1}^n - 2f_i^n + f_{i+1}^n\right] \tag{3.21}$$

which was first proposed by Crank and Nicolson (1947) and it is referred to as the *Crank-Nicolson implicit method.* In fact they considered the partial differential equation as being satisfied at the midpoint $\{i(\Delta x),(n+1/2(\Delta t)\}$ and replaced $\frac{\partial^2 f}{\partial x^2}$ by the mean of its finite-difference approximations at the n^{th} and $(n+1)^{th}$ time-levels. Although the Crank-Nicolson method is valid for all finite values of λ, a large value will yield an inaccurate approximation for $\partial f/\partial t$. A suitable value for λ is proposed equal to *1*, to make the coefficient of f_i^n zero in (3.21). On the other hand, however, the method for $\partial f/\partial t = \partial^2 f/\partial x^2$ is stable for all positive values of λ in the sense that the solution and all errors eventually tend to zero as *n* tends to infinity, it has been shown that large values for λ, such as 40, can introduce unwanted finite oscillations into the numerical solution. Such oscillations die away only very slowly with increasing *n,* and usually occur in the neighbourhood of points of discontinuity in the initial values or between initial values and boundary values.

3.3 Choosing a Suitable Scheme

As derived in chapter two the governing partial differential equation of groundwater flow within a phreatic aquifer and for a horizontal impervious base, i.e. equation (2.38), is given as:

$$\frac{\partial h}{\partial t} = \frac{T}{S}\left(\frac{\partial^2 h}{\partial x^2} + \frac{\partial^2 h}{\partial y^2}\right) - \frac{N}{S}$$

In the above mentioned formula the parameters have been defined previously. Since this 2-D equation is different from its 1-D equivalent, caution must be exercised when attempting to apply the finite-difference methods to this equation. This is explained below.

3.3.1 Explicit Methods

If a simple explicit method is applied to equation (2.38), then the following algorithm results:

$$\frac{h_{i,j}^{n+1}-h_{i,j}^{n}}{\Delta t}=\frac{T}{S}\left[\frac{h_{i+1,j}^{n}-2h_{i,j}^{n}+h_{i-1,j}^{n}}{(\Delta x)^2}+\frac{h_{i,j+1}^{n}-2h_{i,j}^{n}+h_{i,j-1}^{n}}{(\Delta y)^2}\right]-\frac{N}{S} \tag{3.22}$$

where $x = i\Delta x$ etc. As discussed earlier in this chapter, according to Wang and Anderson (1982), regarding the validity of the explicit solution in a one-dimensional case, the parameter $\lambda = \frac{T\Delta t}{S(\Delta x)^2}$ must be less than or equal to 0.5. For a two-dimensional case where $\Delta x = \Delta y$, then the stability condition, $\lambda = \frac{T\Delta t}{S(\Delta x)^2}$, must be less than or equal to 0.25. This is twice as restrictive as the 1-D constraint and this makes this method even more impractical.

3.3.2 Implicit Methods

The application of the Crank-Nicolson scheme to equation (2.38) yields:

$$\frac{h_{i,j}^{n+1}-h_{i,j}^{n}}{\Delta t}=\frac{T}{2S}\left(\partial_x^2+\partial_y^2\right)\left(h_{i,j}^{n+1}+h_{i,j}^{n}\right)-\frac{N}{S} \tag{3.23}$$

where the 2-D central-difference operators ∂_x^2 and ∂_y^2, are $\frac{u_{i+1,j}^{n}-2u_{i,j}^{n}+u_{i-1,j}^{n}}{(\Delta x)^2}$ and $\frac{u_{i,j+1}^{n}-2u_{i,j}^{n}+u_{i,j-1}^{n}}{(\Delta y)^2}$, respectively. As mentioned before the Crank-Nicolson scheme for a

1-D formulation is unconditionally stable when applied to the 2-D above mentioned equation with periodic boundary conditions. Unfortunately, the resulting system of linear algebraic equations is no longer tridiagonal because of the five unknowns $h_{i,j}^{n+1}, h_{i+1,j}^{n+1}, h_{i-1}^{n+1}, h_{i,j+1}^{n+1}$ and $h_{i,j-1}^{n+1}$, with the same difficulties arising for all types of implicit schemes. In other words, equation (3.23) can be written as:

$$a h_{i,j-1}^{n+1} + b h_{i-1,j}^{n+1} + c h_{i,j}^{n+1} + b h_{i+1,j}^{n+1} + a h_{i,j+1}^{n+1} = d_{i,j}^{n} \tag{3.24}$$

where

$$a = -\frac{T\Delta t}{2S(\Delta y)^2} = -\frac{1}{2}\lambda_y,\ b = -\frac{T\Delta t}{2S(\Delta x)^2} = -\frac{1}{2}\lambda_x,\ c = 1 + \lambda_x + \lambda_y,$$

$$d_{i,j}^{n} = h_{i,j}^{n} + \frac{T\Delta t}{2S}\left(\hat{\partial}_x^2 + \hat{\partial}_y^2\right)h_{i,j}^{n}$$

then applying, for example, equation (3.24) to a 2-D $(n \times n)$ computational mesh, the result will be a system of non-tridiagonal linear algebraic equations which must be solved at each *(n+1)* time-step and this system requires substantially more computer time to solve than does a tri-diagonal system. In fact, equations of this type are often best solved using iterative methods, for more details see Tannehill et al. (1997).

3.3.3 ADI Method

The difficulties described above, which occur when attempting to solve a 2-D time dependent equation by conventional algorithms, led to the development of alternating-direction implicit (ADI) methods by Peaceman and Rachford (1955) and Douglas (1955). The ADI method is a two-step method involving the solution of tri-diagonal sets of equations along lines parallel to the x and y-directions, at the first step (time level n to *n+1/2*) and second step (time level *n+1/2* to *n+1*), respectively. In other words, it decomposes the computation into two separate parts. The conventional ADI method is expressed as:

$$\left.\begin{aligned}
&Step1:\ \frac{f_{i,j}^{n+1/2}-f_{i,j}^{n}}{\Delta t/2}=\left(\begin{aligned}&\alpha_x\sigma\frac{f_{i-1,j}^{n+1/2}-2f_{i,j}^{n+1/2}+f_{i+1,j}^{n+1/2}}{(\Delta x)^2}+\alpha_x(1-\sigma)\frac{f_{i-1,j}^{n}-2f_{i,j}^{n}+f_{i+1,j}^{n}}{(\Delta x)^2}+\\&\alpha_y\frac{f_{i,j-1}^{n}-2f_{i,j}^{n}+f_{i,j+1}^{n}}{(\Delta y)^2}\end{aligned}\right)\\
&Step\,2:\ \frac{f_{i,j}^{n+1}-f_{i,j}^{n+1/2}}{\Delta t/2}=\left(\begin{aligned}&\alpha_y\sigma\frac{f_{i,j-1}^{n+1}-2f_{i,j}^{n+1}+f_{i,j+1}^{n+1}}{(\Delta y)^2}+\alpha_y(1-\sigma)\frac{f_{i,j+1}^{n+1/2}-2f_{i,j}^{n+1/2}+f_{i,j-1}^{n+1/2}}{(\Delta y)^2}+\\&\alpha_x\frac{f_{i-1,j}^{n+1/2}-2f_{i,j}^{n+1/2}+f_{i+1,j}^{n+1/2}}{(\Delta x)^2}\end{aligned}\right)
\end{aligned}\right\}\quad(3.25)$$

This procedure is illustrated in Figure (3.2). In a word, the ADI method is a two-stage scheme, second-order accurate, and with a truncation error of $O[(\Delta t)^2,(\Delta x)^2,(\Delta y)^2]$, when $\sigma=\frac{1}{2}$, for more details the reader is referred to Abbott and Basco (1997).

In the first stage of the computation, i.e. from $n \to n+1/2$, the double-sweep technique is used along the *x-axis* to calculate values of $f_{i,j}^{n+1/2}$ for all *i*, where *i=1,...ii,* at a fixed *j*. This is repeated successively for all other *y*-positions, each time holding the new *j* constant during the *x-axis* sweep for all *i*. As a result of this first stage, $f_{i,j}^{n+1/2}$ is known for all *i*, *j* grid points. The second half of the computation, i.e. from $n+1/2 \to n+1$, is completely analogous to the first stage. However, in this stage the double-sweep is made along the *y-axis* to calculate $f_{i,j}^{n+1}$ values for all *j*, where *j=1,...,jj*, at a fixed *i*. The sweeps are again

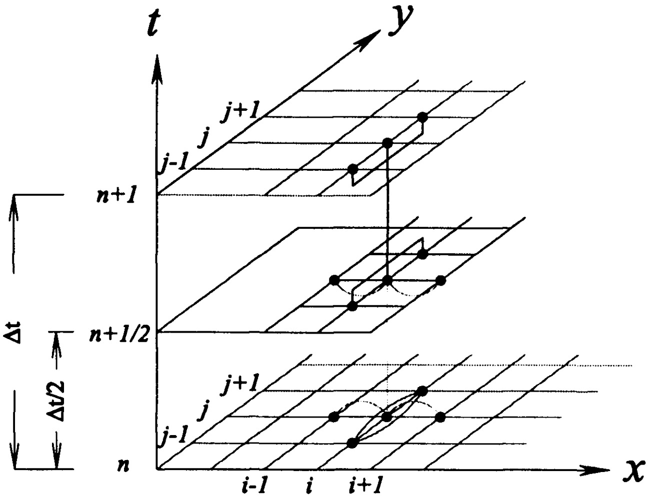

Figure 3.2: ADI calculation procedure

repeated until all *x-axis* positions have been covered, each time holding the new *i* value constant during the *y-axis* sweep over all *j*. Finally, $f_{i,j}^{n+1}$ is known for all *i,j* and the entire two-stage cycle can be repeated again for $n+1 \to n+1\frac{1}{2}$ *and* $n+1\frac{1}{2} \to n+2$, etc. The directions of the implicit calculation are altered in this fashion, thus giving the *alternating-direction implicit* (ADI) method. Of course, what is taken as the 'first' direction and 'second' direction is arbitrary. According to Tannehill et al. (1997), this method is unconditionally stable and as stated by Abbott and Basco (1997) "in general, implicit 2-D schemes do not have time-step stability limitations, so that they have corresponding economic advantages".

In the current study, the discretisation of the governing equations has been done involving the ADI method.

3.4 Numerical Solutions and Discretisation of the Governing Groundwater Equations

3.4.1 Numerical Solution and Discretisation of the Groundwater Flow Equation

As demonstrated in chapter two the governing 2-D transient partial differential equation of groundwater flow, known as the *Boussinesq* equation (2.38) is given as:

$$\frac{\partial h}{\partial t}=\frac{T}{S}\left(\frac{\partial^2 h}{\partial x^2}+\frac{\partial^2 h}{\partial y^2}\right)-\frac{N}{S}$$

where

h total hydraulic head

S specific yield of the phreatic aquifer

T transmissivity of the aquifer

N source/sink

To approximate the above equation using a basic implicit method, by making use of the forward finite difference approximation for time to advance from time level *n* to *n+1* and using a centred finite difference approximation in space, the following difference equation can be obtained:

$$\begin{aligned}\frac{h_{i,j}^{n+1}-h_{i,j}^{n}}{\Delta t}=&\frac{T}{S}(\sigma\frac{h_{i-1,j}^{n+1}-2h_{i,j}^{n+1}+h_{i+1,j}^{n+1}}{(\Delta x)^2}+(1-\sigma)\frac{h_{i-1,j}^{n}-2h_{i,j}^{n}+h_{i+1,j}^{n}}{(\Delta x)^2})+\\&\frac{T}{S}(\sigma\frac{h_{i,j-1}^{n+1}-2h_{i,j}^{n+1}+h_{i,j+1}^{n+1}}{(\Delta y)^2}+(1-\sigma)\frac{h_{i,j-1}^{n}-2h_{i,j}^{n}+h_{i,j+1}^{n}}{(\Delta y)^2})-\frac{N}{S}\end{aligned} \qquad (3.26)$$

where $0<\sigma<1$. When $\sigma=1$, the scheme is fully implicit, when $\sigma=0$ the scheme is explicit and in between the scheme is said to be semi-implicit. In order to apply the ADI or alternating direction implicit method to equation (3.26), a variety of values for σ should be substituted for reference terms of the above equation. Therefore, for the first half time step, $n \rightarrow n+1/2$, the value of $\sigma=1$ is applied for terms which are differenced in the *x-direction* to produce a fully implicit scheme for those terms, for a value of $\sigma=0$ the terms which are differenced in the y-direction are written in an explicit form. For the second half of the computation, i.e. from $n+1/2 \rightarrow n+1$, the scheme is completely analogous. This time the value of $\sigma=1$ is used for terms which are differenced in the *y-direction* creating a fully implicit scheme and a value of $\sigma=0$ is applied to terms which are differenced in the *x-direction* to produce an explicit form.

Step 1, $n \rightarrow n+1/2$ (x-direction):

By substituting the above mentioned values for σ, the *x-direction* flow equation discretisation takes the following form:

$$\begin{aligned}\frac{h_{i,j}^{n+1/2}-h_{i,j}^{n}}{\Delta t/2}=\frac{T}{S}&\left(1\times\frac{h_{i-1,j}^{n+1/2}-2h_{i,j}^{n+1/2}+h_{i+1,j}^{n+1/2}}{(\Delta x)^2}+(1-1)\frac{h_{i-1,j}^{n}-2h_{i,j}^{n}+h_{i+1,j}^{n}}{(\Delta x)^2}\right)+\\ &\frac{T}{S}\left(0\times\frac{h_{i,j-1}^{n+1/2}-2h_{i,j}^{n+1/2}+h_{i,j+1}^{n+1/2}}{(\Delta y)^2}+(1-0)\frac{h_{i,j-1}^{n}-2h_{i,j}^{n}+h_{i,j+1}^{n}}{(\Delta y)^2}\right)-\frac{N}{S}\end{aligned} \tag{3.27}$$

where Δx *and* Δy are the mesh spacing. Rearranging equation (3.27) gives:

$$\frac{h_{i,j}^{n+1/2}-h_{i,j}^{n}}{\Delta t/2}=\frac{T}{S}\left(\frac{h_{i-1,j}^{n+1/2}-2h_{i,j}^{n+1/2}+h_{i+1,j}^{n+1/2}}{(\Delta x)^2}\right)+\frac{T}{S}\left(\frac{h_{i,j-1}^{n}-2h_{i,j}^{n}+h_{i,j+1}^{n}}{(\Delta y)^2}\right)-\frac{N}{S} \tag{3.28}$$

Multiplying equation (3.28) by $\Delta t/2$ yields:

$$h_{i,j}^{n+1/2}-h_{i,j}^{n}=\frac{T\Delta t}{2S(\Delta x)^2}\left(h_{i-1,j}^{n+1/2}-2h_{i,j}^{n+1/2}+h_{i+1,j}^{n+1/2}\right)+\frac{T\Delta t}{2S(\Delta y)^2}\left(h_{i,j-1}^{n}-2h_{i,j}^{n}+h_{i,j+1}^{n}\right)-\frac{N\Delta t}{2S} \tag{3.29}$$

By assuming,

$(\Delta x) = (\Delta y)$ and $\dfrac{-T\Delta t}{2S(\Delta x)^2} = A$

then equation (3.29) can be written as:

$$h_{i,j}^{n+1/2} - h_{i,j}^{n} = -Ah_{i-1,j}^{n+1/2} + 2Ah_{i,j}^{n+1/2} - Ah_{i+1,j}^{n+1/2} - Ah_{i,j-1}^{n} + 2Ah_{i,j}^{n} - Ah_{i,j+1}^{n} - \frac{N\Delta t}{2S} \tag{3.30}$$

Equation (3.30) could now be written in a simpler form to give:

$$h_{i,j}^{n+1/2} + Ah_{i-1,j}^{n+1/2} - 2Ah_{i,j}^{n+1/2} + Ah_{i+1,j}^{n+1/2} = h_{i,j}^{n} - Ah_{i,j-1}^{n} + 2Ah_{i,j}^{n} - Ah_{i,j+1}^{n} - \frac{N\Delta t}{2S}$$

or

$$Ah_{i-1,j}^{n+1/2} + (1-2A)h_{i,j}^{n+1/2} + Ah_{i+1,j}^{n+1/2} = (1+2A)h_{i,j}^{n} - Ah_{i,j-1}^{n} - Ah_{i,j+1}^{n} - \frac{N\Delta t}{2S} \tag{3.31}$$

Finally, the main equation in the *x-direction* for flow model can be expressed as:

$$Ah_{i-1,j}^{n+1/2} + Bh_{i,j}^{n+1/2} + Ch_{i+1,j}^{n+1/2} = D \tag{3.32}$$

where

$A = \dfrac{-T\Delta t}{2S(\Delta x)^2}$,

$B = 1 - 2A$,

$C = A$

$D = -Ah_{i,j-1}^{n} + (1+2A)h_{i,j}^{n} - Ah_{i,j+1}^{n} + (\dfrac{N}{S}\Delta t)$

It should be recalled that, in the above mentioned equations T is the transmissivity of the aquifer, S is the specific yield and Δt is the whole time-step for both steps 1 and 2.

Equation (3.32), with the unknown total hydraulics heads, $h_{i-1,j}^{n+1/2}$, $h_{i,j}^{n+1/2}$ *and* $h_{i+1,j}^{n+1/2}$, being specified over the entire computational mesh, has to be solved at each first half time-step to determine values of the field variables from the given initial data. The equation constitutes a linear three diagonal system of equations for $h_{i,j}^{n+1/2}$. This is similar to the equation $A_{i'}X_{i-1} + B_{i'}X_i + C_{i'}X_{i+1} = D_{i'}$, where $X_i = h_{i,j}^{n+1/2}$ and i' is the row number of the related matrix and i is the row number of the grid space. The related matrix is symmetric and strictly diagonally dominant. This set of equations can be written in a matrix form as illustrated below (3.33). In the current study the Thomas algorithm (see Wang and Anderson, 1982) has been used to solve this system of equations.

$$\begin{bmatrix} B_1\ C_1\ 0\ \cdots\ 0\,0\,0 \\ A_2\ B_2\ C_2\ 0 \cdots\ 0\,0 \\ \vdots \\ 0\,0 \cdots 0 A_{n-1}\ B_{n-1}\ C_{n-1} \\ 0\,0\,0\ \cdots 0\ A_n\ \ B_n \end{bmatrix} \begin{bmatrix} X_1 \\ X_2 \\ \vdots \\ X_{n-1} \\ X_n \end{bmatrix} = \begin{bmatrix} D_1 \\ D_2 \\ \vdots \\ D_{n-1} \\ D_n \end{bmatrix} \tag{3.33}$$

In general, a matrix equation such as equation (3.33) can be solved by a technique known as Gaussian elimination. However, except for special types of coefficient matrices, Gaussian elimination requires a great deal of computer storage and time. As mentioned above, the Thomas Algorithm is a particularly efficient form of Gaussian elimination, in that it can be used to solve matrix equations which have a tridiagonal coefficient matrix. Using the notation given in equation (3.33), the development of the Thomas algorithm for tridiagonal matrices by systematically solving the linear equations by row operations can be summarised as follows:

$$\begin{cases} \begin{cases} P_1 = \dfrac{C_1}{B_1} \\ Q_1 = \dfrac{D_1}{B_1} \end{cases} \\ \begin{cases} P_{i'} = \dfrac{C_{i'}}{B_{i'} - P_{i'-1} A_{i'}} \\ Q_{i'} = \dfrac{P_{i'}(D_{i'} - A_{i'} Q_{i'})}{C_{i'}}, or \\ Q_{i'} = \dfrac{P_{i'}(D_{i'} - A_{i'} Q_{i'-1})}{P_{i'}(B_{i'} - A_{i'} P_{i'-1})} \end{cases} \\ \begin{cases} X_n = Q_n \\ X_{i'} = Q_{i'} - P_{i'} X_{i'+1} \end{cases} \end{cases} \tag{3.34}$$

where, $2 \le i' \le n$, $i' = 1,2,\cdots,n$ and P *and* Q are two vectors as defined above (see Pipes and Hovanessian, (1969) and Wang and Anderson, (1982) for more details).

Step 2, $n+1/2 \to n+1$ (y-direction):

By substituting for the values of σ, which are relevant for the second half time step, as discussed previously regarding equation (3.26), then the *y-direction* flow equation discretisation takes the following form:

$$\frac{h_{i,j}^{n+1} - h_{i,j}^{n+1/2}}{\Delta t/2} = \frac{T}{S}\left(0 \times \frac{h_{i-1,j}^{n+1} - 2h_{i,j}^{n+1} + h_{i+1,j}^{n+1}}{(\Delta x)^2} + (1-0)\frac{h_{i-1,j}^{n+1/2} - 2h_{i,j}^{n+1/2} + h_{i+1,j}^{n+1/2}}{(\Delta x)^2}\right) +$$

$$\frac{T}{S}\left(1 \times \frac{h_{i,j-1}^{n+1} - 2h_{i,j}^{n+1} + h_{i,j+1}^{n+1}}{(\Delta y)^2} + (1-1)\frac{h_{i,j-1}^{n+1/2} - 2h_{i,j}^{n+1/2} + h_{i,j+1}^{n+1/2}}{(\Delta y)^2}\right) - \frac{N}{S}$$

or

$$\frac{h_{i,j}^{n+1} - h_{i,j}^{n+1/2}}{\Delta t/2} = \frac{T}{S}\left(\frac{h_{i-1,j}^{n+1/2} - 2h_{i,j}^{n+1/2} + h_{i+1,j}^{n+1/2}}{(\Delta x)^2}\right) + \frac{T}{S}\left(\frac{h_{i,j-1}^{n+1} - 2h_{i,j}^{n+1} + h_{i,j+1}^{n+1}}{(\Delta y)^2}\right) - \frac{N}{S} \tag{3.35}$$

Multiplying equation (3.35) by $\Delta t/2$ yields:

$$h_{i,j}^{n+1} - h_{i,j}^{n+1/2} = \frac{T\Delta t}{2S(\Delta x)^2}\left(h_{i-1,j}^{n+1/2} - 2h_{i,j}^{n+1/2} + h_{i+1,j}^{n+1/2}\right) + \frac{T\Delta t}{2S(\Delta y)^2}\left(h_{i,j-1}^{n+1} - 2h_{i,j}^{n+1} + h_{i,j+1}^{n+1}\right) - \frac{N\Delta t}{2S} \quad (3.36)$$

with the assumption of

$$(\Delta x) = (\Delta y) \text{ and } \frac{-T\Delta t}{2S(\Delta x)^2} = A$$

Rewriting equation (3.36) in terms of A gives:

$$h_{i,j}^{n+1} + Ah_{i,j-1}^{n+1} - 2Ah_{i,j}^{n+1} + Ah_{i,j+1}^{n+1} = h_{i,j}^{n+1/2} - Ah_{i-1,j}^{n+1/2} + 2Ah_{i,j}^{n+1/2} - Ah_{i+1,j}^{n+1/2} - \frac{N\Delta t}{2S} \quad (3.37)$$

or

$$Ah_{i,j-1}^{n+1} + (1-2A)h_{i,j}^{n+1} + Ah_{i,j+1}^{n+1} = -Ah_{i-1,j}^{n+1/2} + 2Ah_{i,j}^{n+1/2} - Ah_{i+1,j}^{n+1/2} + h_{i,j}^{n+1/2} - \frac{N\Delta t}{2S} \quad (3.38)$$

Finally, the main flow equation in the *y-direction* can be written as:

$$Ah_{i,j-1}^{n+1} + Bh_{i,j}^{n+1} + Ch_{i,j+1}^{n+1} = D \quad (3.39)$$

where

$$A = \frac{-T\Delta t}{2S(\Delta x)^2}$$

$$B = 1 - 2A$$

$$C = A$$

$$D = -Ah_{i-1,j}^{n+1/2} + (1+2A)h_{i,j}^{n+1/2} - Ah_{i+1,j}^{n+1/2} - (\frac{N}{2S}\Delta t)$$

As for step 1, equation (3.39) and the unknown total hydraulic heads $h_{i,j-1}^{n+1}$, $h_{i,j}^{n+1}$ *and* $h_{i,j+1}^{n+1}$, which are specified over the entire computational mesh, needs to be solved at each second half time-step to determine values of the field variables from the given first half time-step. In the second step the equation constitution is exactly the same as for the first step, except that the direction of calculations is changed from the x to y-direction.

3.4.2 Numerical Solution and Discretisation of the Groundwater Advective-Diffusion Equation

This section is concerned with the numerical solution of the groundwater advective-diffusion equation to simulate solute transport phenomenon in porous media. As derived in chapter two, the governing 2-D partial differential equation of solute transport in porous media is as follows:

$$\frac{\partial C}{\partial t} = D_L \frac{\partial^2 C}{\partial x^2} + D_T \frac{\partial^2 C}{\partial y^2} - U \frac{\partial C}{\partial x} - V \frac{\partial C}{\partial y} - S$$

where C is the solute concentration as a mass per unit volume of water, D_L *and* D_T are longitudinal and transverse components of the dispersion coefficient for flow, respectively. Also, U and V are the average velocity components in the x and y-directions, respectively and S is a source/sink input.

The same basic implicit approach, as used in the development of the governing groundwater flow equation in the current chapter, could be applied to develop the advective-diffusion equation. Therefore, using the forward finite difference approximation for time to advance from time level n to $n+1$ and a centred finite difference approximation for space yields:

$$\begin{aligned}\frac{C_{i,j}^{n+1} - C_{i,j}^{n}}{\Delta t} = {} & D_L \left(\sigma \frac{C_{i-1,j}^{n+1} - 2C_{i,j}^{n+1} + C_{i+1,j}^{n+1}}{(\Delta x)^2} + (1-\sigma) \frac{C_{i-1,j}^{n} - 2C_{i,j}^{n} + C_{i+1,j}^{n}}{(\Delta x)^2} \right) + \\ & D_T \left(\sigma \frac{C_{i,j-1}^{n+1} - 2C_{i,j}^{n+1} + C_{i,j+1}^{n+1}}{(\Delta y)^2} + (1-\sigma) \frac{C_{i,j-1}^{n} - 2C_{i,j}^{n} + C_{i,j+1}^{n}}{(\Delta y)^2} \right) - \\ & U \left(\sigma \frac{C_{i+1,j}^{n+1} - C_{i-1,j}^{n+1}}{2(\Delta x)} + (1-\sigma) \frac{C_{i+1,j}^{n} - C_{i-1,j}^{n}}{2(\Delta x)} \right) - \\ & V \left(\sigma \frac{C_{i,j+1}^{n+1} - C_{i,j-1}^{n+1}}{2(\Delta y)} + (1-\sigma) \frac{C_{i,j+1}^{n} - C_{i,j-1}^{n}}{2(\Delta y)} \right) - S\end{aligned} \qquad (3.40)$$

where, Δx and Δy are the mesh spacing and Δt is the time-step, with the same explanation as before for $0<\sigma<1$. When $\sigma=1$ the scheme is fully implicit, when $\sigma=0$ the scheme is explicit and in between the scheme is termed semi-implicit. Application of the ADI method to equation (3.40) needs a variety of values for σ to be substituted for reference terms of the last mentioned equation. Therefore, in the first half time step, $n \to n+1/2$, the value of $\sigma=1$ is applied for terms which are differenced in the x-direction to produce a fully implicit scheme for these terms and a value of $\sigma=0$ is applied to terms which are differenced in the y-direction to create an explicit scheme for these terms. The second half of the computation, from $n+1/2 \to n+1$, is completely analogous to the first. For this case the value of $\sigma=1$ for terms which are differenced in the *y-direction* is applied to create a fully implicit scheme for these terms and a value of $\sigma=0$ is applied for terms which are differenced in the *x-direction* to produce an explicit scheme for them.

Step 1, $n \to n+1/2$ (x-direction):

By substituting the above mentioned values for σ, the *x-direction* advection-diffusion equation discretisation takes the following form:

$$\begin{aligned}
\frac{C_{i,j}^{n+1/2}-C_{i,j}^{n}}{\Delta t/2} = {} & D_L\left(1\times\frac{C_{i-1,j}^{n+1/2}-2C_{i,j}^{n+1/2}+C_{i+1,j}^{n+1/2}}{(\Delta x)^2}+(1-1)\frac{C_{i-1,j}^{n}-2C_{i,j}^{n}+C_{i+1,j}^{n}}{(\Delta x)^2}\right)+\\
& D_T\left(0\times\frac{C_{i,j-1}^{n+1/2}-2C_{i,j}^{n+1/2}+C_{i,j+1}^{n+1/2}}{(\Delta y)^2}+(1-0)\frac{C_{i,j-1}^{n}-2C_{i,j}^{n}+C_{i,j+1}^{n}}{(\Delta y)^2}\right)-\\
& U\left(1\times\frac{C_{i+1,j}^{n+1/2}-C_{i-1,j}^{n+1/2}}{2(\Delta x)}+(1-1)\frac{C_{i+1,j}^{n}-C_{i-1,j}^{n}}{2(\Delta x)}\right)-\\
& V\left(0\times\frac{C_{i,j+1}^{n+1/2}-C_{i,j-1}^{n+1/2}}{2(\Delta y)}+(1-0)\frac{C_{i,j+1}^{n}-C_{i,j-1}^{n}}{2(\Delta y)}\right)-S
\end{aligned}$$

or

$$\frac{C_{i,j}^{n+1/2}-C_{i,j}^{n}}{\Delta t/2}=D_L\frac{C_{i-1,j}^{n+1/2}-2C_{i,j}^{n+1/2}+C_{i+1,j}^{n+1/2}}{(\Delta x)^2}+D_T\frac{C_{i,j-1}^{n}-2C_{i,j}^{n}+C_{i,j+1}^{n}}{(\Delta y)^2}- \\ U\frac{C_{i+1,j}^{n+1/2}-C_{i-1,j}^{n+1/2}}{2(\Delta x)}-V\frac{C_{i,j+1}^{n}-C_{i,j-1}^{n}}{2(\Delta y)}-S \tag{3.41}$$

multiplying throughout by $\Delta t/2$ and rearranging gives:

$$C_{i,j}^{n+1/2}-C_{i,j}^{n}=\frac{D_L\Delta t}{2(\Delta x)^2}(C_{i-1,j}^{n+1/2}-2C_{i,j}^{n+1/2}+C_{i+1,j}^{n+1/2})+\frac{D_T\Delta t}{2(\Delta y)^2}(C_{i,j-1}^{n}-2C_{i,j}^{n}+C_{i,j+1}^{n})- \\ \frac{U\Delta t}{4(\Delta x)}(C_{i+1,j}^{n+1/2}-C_{i-1,j}^{n+1/2})-\frac{V\Delta t}{4(\Delta y)}(C_{i,j+1}^{n}-C_{i,j-1}^{n})-\frac{S\Delta t}{2} \tag{3.42}$$

the assumption of

$$\frac{D_L\Delta t}{2(\Delta x)^2}=A$$

$$\frac{D_T\Delta t}{2(\Delta y)^2}=B$$

$$\frac{U\Delta t}{4\Delta x}=c$$

$$\frac{V\Delta t}{4\Delta y}=e_c$$

changes equation (3.42) to

$$C_{i,j}^{n+1/2}-C_{i,j}^{n}=A(C_{i-1,j}^{n+1/2}-2C_{i,j}^{n+1/2}+C_{i+1,j}^{n+1/2})+B(C_{i,j-1}^{n}-2C_{i,j}^{n}+C_{i,j+1}^{n})- \\ c(C_{i+1,j}^{n+1/2}-C_{i-1,j}^{n+1/2})-e_c(C_{i,j+1}^{n}-C_{i,j-1}^{n})-\frac{S\Delta t}{2}$$

or

$$C_{i,j}^{n+1/2}-AC_{i-1,j}^{n+1/2}+2AC_{i,j}^{n+1/2}-AC_{i+1,j}^{n+1/2}+cC_{i+1,j}^{n+1/2}-cC_{i-1,j}^{n+1/2}=C_{i,j}^{n}+BC_{i,j-1}^{n}-2BC_{i,j}^{n}+ \\ BC_{i,j+1}^{n}-e_cC_{i,j+1}^{n}+e_cC_{i,j-1}^{n}-\frac{S\Delta t}{2}$$

A simpler form of the above equation can be written to give:

$$(1+2A)C_{i,j}^{n+1/2}+(-c-A)C_{i-1,j}^{n+1/2}+(c-A)C_{i+1,j}^{n+1/2}=(1-2B)C_{i,j}^{n}+(B+e_c)C_{i,j-1}^{n}+$$
$$(B-e_c)C_{i,j+1}^{n}-\frac{S\Delta t}{2}$$

Finally, the main equation in the *x-direction* for solute transport can be written as:

$$aC_{i-1,j}^{n+1/2}+bC_{i,j}^{n+1/2}+dC_{i+1,j}^{n+1/2}=D_c \tag{3.43}$$

where

$a=-c-A$

$b=1+2A$

$d=c-A$ and

$$D_c=(B+e_c)C_{i,j-1}^{n}+(1-2B)C_{i,j}^{n}+(B-e_c)C_{i,j+1}^{n}-\frac{S\Delta t}{2}$$

Equation (3.43), with the unknown solute concentrations, $C_{i-1,j}^{n+1/2}$, $C_{i,j}^{n+1/2}$ *and* $C_{i+1,j}^{n+1/2}$, being specified over the entire computational mesh, has to be solved at each first half time-step to determine values of the field variables from the given initial data or previous time-step results. The equation is solved using the Thomas algorithm as explained before.

Step 2, $n+1/2 \rightarrow n+1$ (y-direction):

Using the same procedure and substituting for σ values for the second half time step, as discussed previously regarding equation (3.40), the discretised y-direction advective-diffusion equation can be written as follows:

$$\frac{C_{i,j}^{n+1}-C_{i,j}^{n+1/2}}{\Delta t/2}=D_L\left(0\times\frac{C_{i-1,j}^{n+1}-2C_{i,j}^{n+1}+C_{i+1,j}^{n+1}}{(\Delta x)^2}+(1-0)\frac{C_{i-1,j}^{n+1/2}-2C_{i,j}^{n+1/2}+C_{i+1,j}^{n+1/2}}{(\Delta x)^2}\right)+$$
$$D_T\left(1\times\frac{C_{i,j-1}^{n+1}-2C_{i,j}^{n+1}+C_{i,j+1}^{n+1}}{(\Delta y)^2}+(1-1)\frac{C_{i,j-1}^{n+1/2}-2C_{i,j}^{n+1/2}+C_{i,j+1}^{n+1/2}}{(\Delta y)^2}\right)-$$
$$U\left(0\times\frac{C_{i+1,j}^{n+1}-C_{i-1,j}^{n+1}}{2(\Delta x)}+(1-0)\frac{C_{i+1,j}^{n+1/2}-C_{i-1,j}^{n+1/2}}{2(\Delta x)}\right)-$$
$$V\left(1\times\frac{C_{i,j+1}^{n+1}-C_{i,j-1}^{n+1}}{2(\Delta y)}+(1-1)\frac{C_{i,j+1}^{n+1/2}-C_{i,j-1}^{n+1/2}}{2(\Delta y)}\right)-S$$

so that

$$\begin{aligned}\frac{C_{i,j}^{n+1}-C_{i,j}^{n+1/2}}{\Delta t/2}&=D_L\frac{C_{i-1,j}^{n+1/2}-2C_{i,j}^{n+1/2}+C_{i+1,j}^{n+1/2}}{(\Delta x)^2}+D_T\frac{C_{i,j-1}^{n+1}-2C_{i,j}^{n+1}+C_{i,j+1}^{n+1}}{(\Delta y)^2}-\\&U\frac{C_{i+1,j}^{n+1/2}-C_{i-1,j}^{n+1/2}}{2(\Delta x)}-V\frac{C_{i,j+1}^{n+1}-C_{i,j-1}^{n+1}}{2(\Delta y)}-S\end{aligned}\tag{3.44}$$

This equation can be multiplied by $\Delta t/2$ and rearranged to give:

$$\begin{aligned}C_{i,j}^{n+1}-C_{i,j}^{n+1/2}&=\frac{D_L\Delta t}{2(\Delta x)^2}(C_{i-1,j}^{n+1/2}-2C_{i,j}^{n+1/2}+C_{i+1,j}^{n+1/2})+\frac{D_T\Delta t}{2(\Delta y)^2}(C_{i,j-1}^{n+1}-2C_{i,j}^{n+1}+C_{i,j+1}^{n+1})-\\&\frac{U\Delta t}{4(\Delta x)}(C_{i+1,j}^{n+1/2}-C_{i-1,j}^{n+1/2})-\frac{V\Delta t}{4(\Delta y)}(C_{i,j+1}^{n+1}-C_{i,j-1}^{n+1})-\frac{S\Delta t}{2}\end{aligned}\tag{3.45}$$

The following assumptions provide Equation (3.46), which is a simplified form of Equation (3.45).

$$\frac{D_L\Delta t}{2(\Delta x)^2}=A_c$$

$$\frac{D_T\Delta t}{2(\Delta y)^2}=B_c$$

$$\frac{U\Delta t}{4\Delta x}=c_c$$

$$\frac{V\Delta t}{4\Delta y}=e_c$$

$$C_{i,j}^{n+1} - C_{i,j}^{n+1/2} = A_c(C_{i-1,j}^{n+1/2} - 2C_{i,j}^{n+1/2} + C_{i+1,j}^{n+1/2}) + B_c(C_{i,j-1}^{n+1} - 2C_{i,j}^{n+1} + C_{i,j+1}^{n+1}) - \\ c_c(C_{i+1,j}^{n+1/2} - C_{i-1,j}^{n+1/2}) - e_c(C_{i,j+1}^{n+1} - C_{i,j-1}^{n+1}) - \frac{S\Delta t}{2} \tag{3.46}$$

or

$$C_{i,j}^{n+1} - B_c C_{i,j-1}^{n+1} + 2B_c C_{i,j}^{n+1} - B_c C_{i,j+1}^{n+1} + e_c C_{i,j+1}^{n+1} - e_c C_{i,j-1}^{n+1} = C_{i,j}^{n+1/2} + A_c C_{i-1,j}^{n+1/2} - 2A_c C_{i,j}^{n+1/2} + \\ A_c C_{i+1,j}^{n+1/2} - c_c C_{i+1,j}^{n+1/2} + c_c C_{i-1,j}^{n+1/2} - \frac{S\Delta t}{2}$$

so that

$$(1 + 2B_c)C_{i,j}^{n+1} + (-B_c - e_c)C_{i,j-1}^{n+1} + (e_c - B_c)C_{i,j+1}^{n+1} = (1 - 2A_c)C_{i,j}^{n+1/2} + (A_c + c_c)C_{i-1,j}^{n+1/2} + \\ (A_c - c_c)C_{i+1,j}^{n+1/2} - \frac{S\Delta t}{2}$$

Finally, the main equation for the solute transport model in the y-direction can be written as:

$$a'C_{i,j-1}^{n+1} + b'C_{i,j}^{n+1} + d'C_{i,j+1}^{n+1} = D'_c \tag{3.47}$$

where

$a' = -B_c - e_c$

$b' = 1 + 2B_c$

$d' = e_c - B_c$

$$D'_c = (1 - 2A_c)C_{i,j}^{n+1/2} + (A_c + c_c)C_{i-1,j}^{n+1/2} + (A_c - c_c)C_{i+1,j}^{n+1/2} - \frac{S\Delta t}{2}$$

Equation (3.47), with the unknown solute concentrations, $C_{i-1,j}^{n+1}, C_{i,j}^{n+1}$ *and* $C_{i+1,j}^{n+1}$, being specified over the entire computational mesh, has to be solved at each second half time-step to determine values of the field variables from the given previous first half time-step. Equation (3.47) again has been solved using the Thomas algorithm.

3.4.3 Initial and Boundary Conditions

At the start of the simulation period, the initial values of the velocities and the solute concentrations were set to zero and the water surface elevations set to be horizontal and usually equated to the high water level, on the both sides of the sand embankment (e.g., see Figure 3.3, physical model). The figure also shows the location of the open and closed boundaries for the porous medium computational domain.

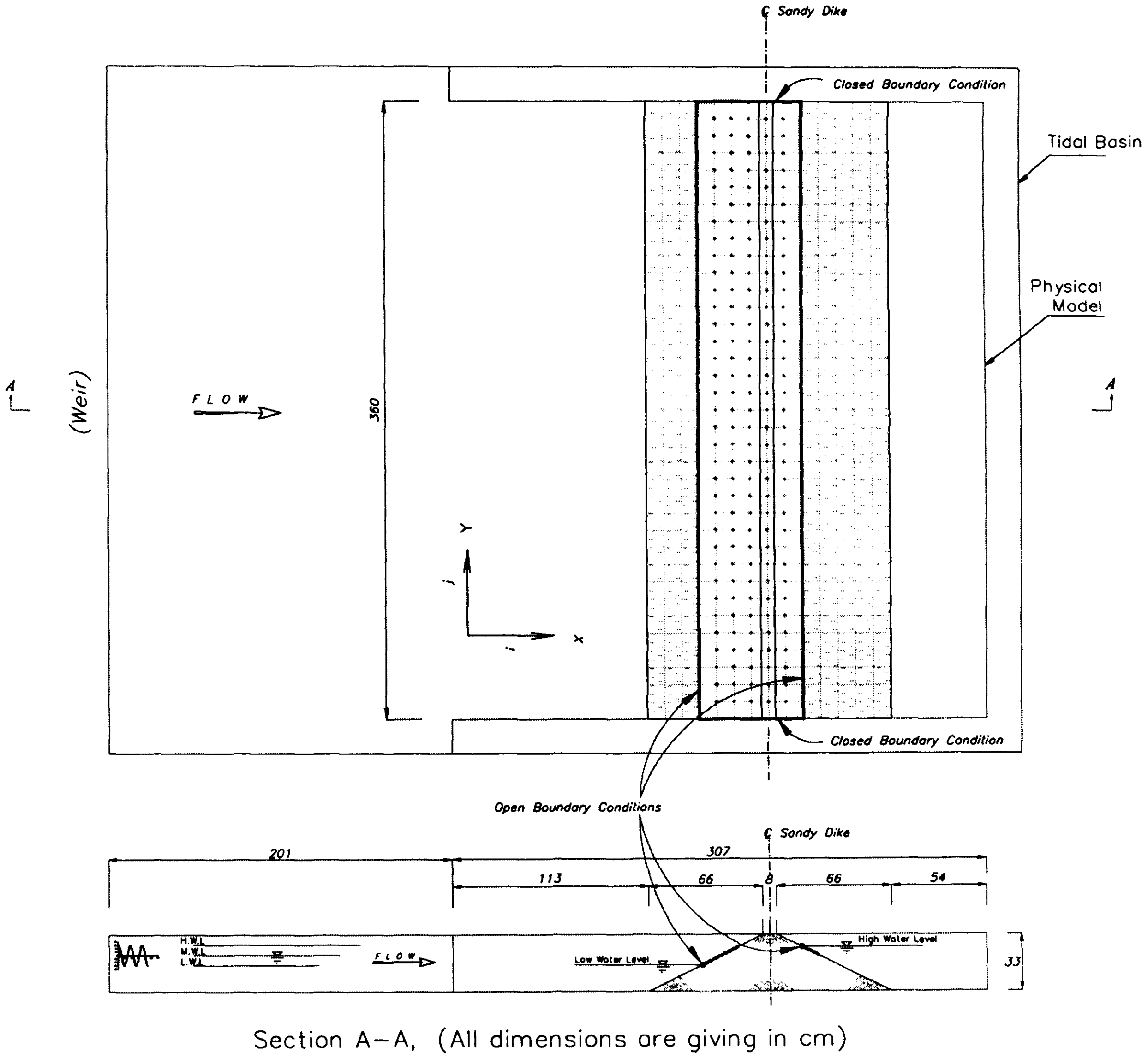

Figure 3.3: Computational domain and boundary conditions of the porous medium

Once the new hydraulic heads $h_{i,j}^{n+1}$ are determined, the intermediate velocities $U_{i+1/2,j}^{n+1}$ and $V_{i,j+1/2}^{n+1}$ are found from equation (2.15, Darcy equation), also see Figure A.1 of Appendix A. The open boundary conditions must be specified through the simulation time at the extremities of the computational domain, when the hydrodynamic and solute transport equations are being solved. For the physical model study of this research the open boundary conditions, as illustrated in Figure 3.3, were obviously normal to the direction of tidal flow, since the groundwater domain is rectangular in shape. Both upstream and downstream boundary conditions were specified as water elevation boundaries. However, the rate of leaked water is measured along the boundaries at any time step in any direction.

The description of the boundary conditions, which have been used within the development of the GWK program, as noted by Falconer et al. (2000) is presented below. There are generally two types of boundary conditions, the first being the closed boundary and the second the open boundary. For the identification of boundary values it is important to note that velocity components in the x and y directions are not specified at the same points for the staggered grid, and solving equations parallel to the boundary requires the use of values of variables just outside the boundary. The treatment of these two boundary conditions is explained in detail below, with grid cells b1-b4 in Figures 3.4 – 3.6 being just outside the boundary.

3.4.3.1 Closed Boundary Condition

A closed boundary can be regarded as a 'wall' boundary so that no flow or solute fluxes are permitted to cross the closed boundary. This type of boundary occurs along coastlines or adjacent to structures. Values outside the modelling domain are obtained by assuming a 'no slip' condition (or zero flow velocity at the wall) parallel to the boundary and zero flow perpendicular to the boundary, which are illustrated in Figure 3.4 using Equation 3.49.

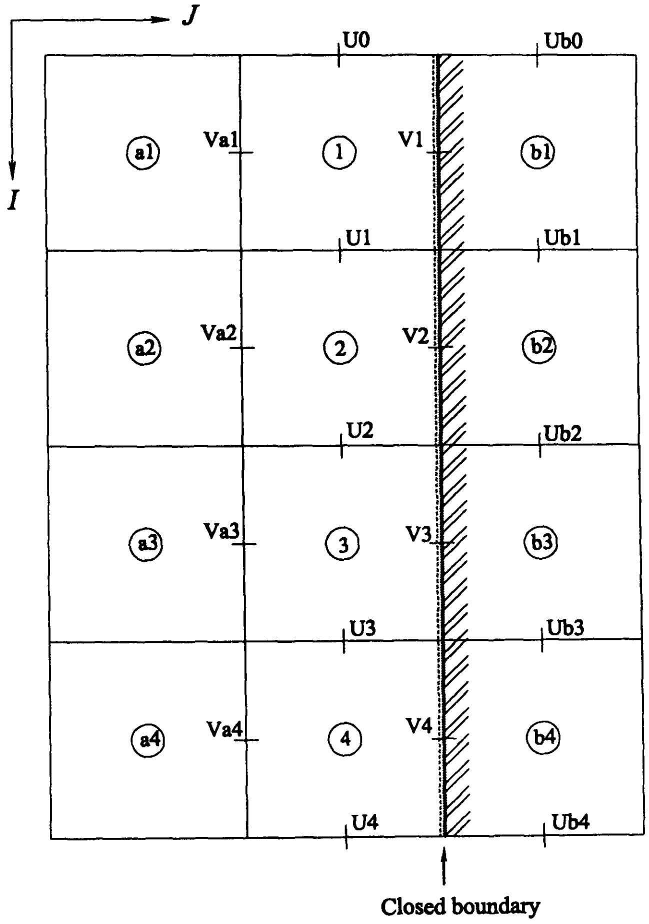

Figure 3.4: Wall boundary

$$V_1 = V_2 = V_3 = V_4 = 0 \tag{3.48}$$

$$U_i = -U_{bi} \qquad (i = 0,1,2,3,\cdots)$$

Hence all velocities parallel to the wall are set to zero, whereas the velocities outside the boundary are assigned the same value as the corresponding velocity inside the domain, but with a negative sign. So as to satisfy the condition of zero tangential velocity at the boundary.

The closed boundary condition for the solute is:

$$\left.\frac{\partial C}{\partial y}\right|_w = 0 \ and \ \left.\frac{\partial^2 C}{\partial y^2}\right|_w = 0 \tag{3.49}$$

meaning that there is no concentration flux through the closed boundary. The subscript *w* indicates that the value is taken at the wall boundary.

3.4.3.2 Open Boundary Condition

Unlike a closed boundary, flow and solute fluxes are allowed to cross an open boundary. Appropriate hydrodynamic and solute conditions need to be specified, such as measured water surface elevations, velocities and solute values. A free slip boundary condition is used by assuming zero gradient of a variable perpendicular to the open boundary.

If the open boundary is a flow boundary and the velocities at the boundary can be defined as shown in Figure 3.5, then the following boundary conditions can be obtained for the hydrodynamic module:

$$\left.\begin{array}{ll} V_i = V_{bi}; & (i = 1,2,3,4) \\ U_{bi} = U_i, & (i = 0,1,\cdots,4) \end{array}\right\} \tag{3.50}$$

meaning that the V velocity at the wall is given by the boundary and the corresponding U velocity outside the domain is set equal to the boundary value.

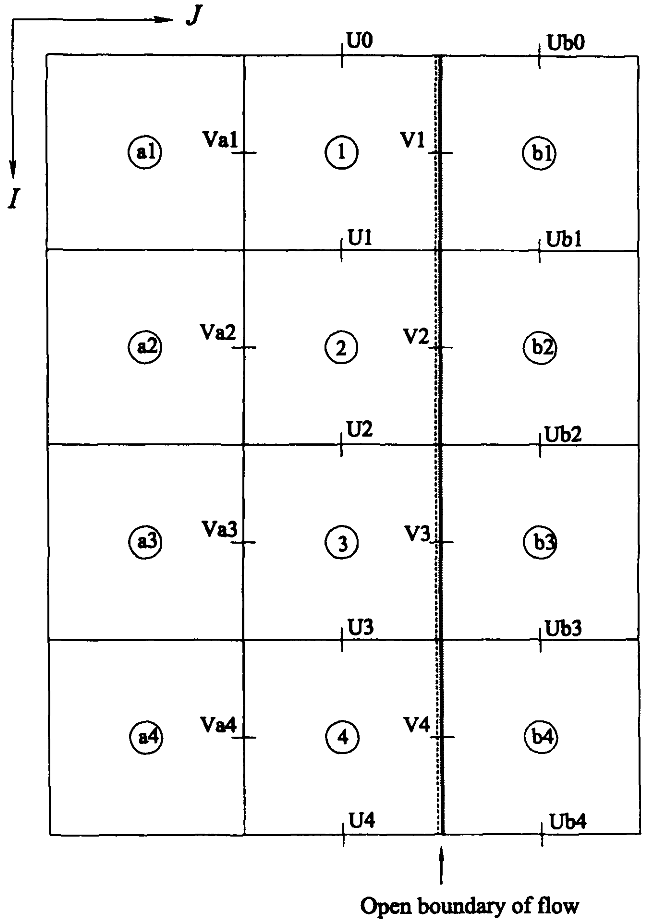

Figure 3.5: Flow boundary

If the open boundary condition is of a water elevation type, as shown in Figure 3.6, then the following boundary condition can be obtained for the hydrodynamic module:

$$\left.\begin{array}{ll} U_i = U_{ai}; & (i = 0,1,\cdots,4) \\ V_i = V_{bi}; & (i = 1,\cdots,4) \\ h_i = h_{bi}, & (i = 1,\cdots,4) \end{array}\right\} \tag{3.51}$$

where *hbi* is the known water elevation values at the open boundary. The solute values at the open boundary are described by known boundary values C*bi* giving:

$$C_i = C_{bi} \tag{3.52}$$

If the flows at the boundary are leaving the domain, then solute values outside the boundary are not needed. However, if the flows at the open boundary are entering the domain, then the solute values immediately outside the boundary are required. A simple extrapolation relationship is used such as:

$$C_{bi} = C_i (i = 1,2,3,4 \text{ at the open boundary}) \tag{3.53}$$

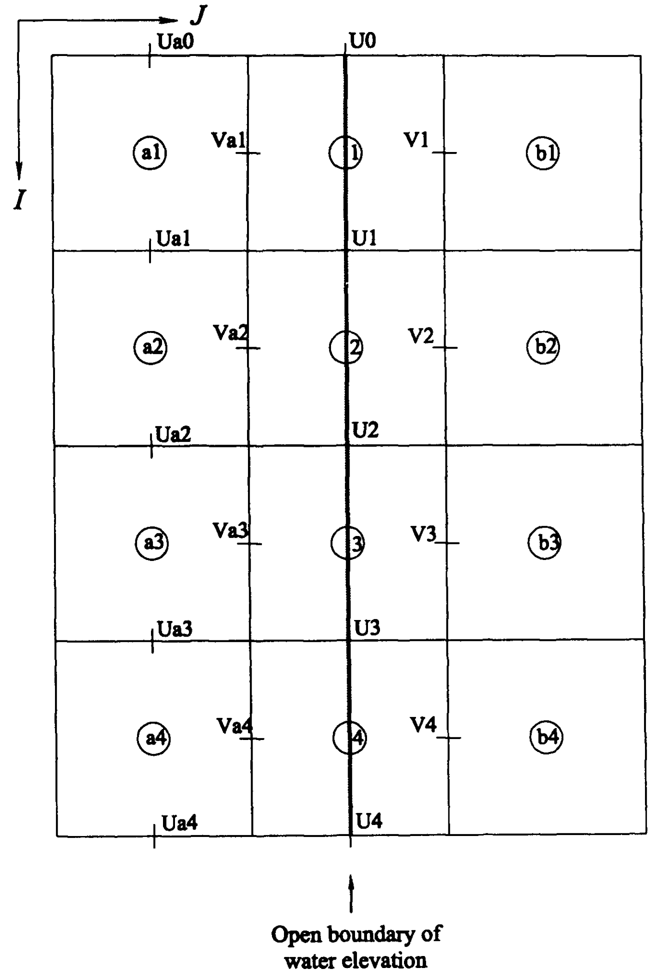

Figure 3.6: Water elevation boundary

Similarly, the boundary conditions along the y direction can also be obtained in the same way as those described above along the x direction.

With the boundary conditions being included, the finite difference equations for the hydrodynamic and solute transport modules are solved for each half time step using the efficient method of Gauss elimination, i.e. the Thomas algorithm. After establishing the hydrodynamic field within the model domain, including the water surface elevations, the flow depths and the velocity distributions, and the solute concentration distributions are computed for each half time step.

3.4.4 Structure of the GWK Model and Summary of Numerical Implementation

As mentioned in chapter one, in this research study the main effort has been focused on achieving a wider scientific understanding of interactions between wetland areas, coastal waters and aquifers. Therefore, the structure of the GWK model has been arranged to give a good relationship with a free surface phenomena. Generally speaking, the GWK model is capable of simulating both the hydrodynamic and solute transport processes in porous media. The model predicts the hydraulic heads (or water table), the velocity components (U, V) in the horizontal plane, the recharge and discharge levels of an aquifer in a tidal regime, the recharge/discharge levels for sources (such as discharge wells) on the water table and solute tracer levels across the domain.

The model has two dependent separate time steps, the main and sub-time steps. The first time step has been used to simulate the water elevation boundary condition of tide levels either side of the sand embankment, the discharge/recharge and volume of water that leaks through the embankment in either direction during the current time step. The second time step has been used in the implicit numerical solution scheme (ADI scheme) to simulate the head, the components of velocity and the flux of a solute. Note that the first time step must be chosen as an integral multiple of the second one. The numerical solution is run inside the first time step and these two procedures are not independent and therefore they are both involved for different information. However, choosing equal values for these two time steps is possible. In the current example the numerical solution is explicit. This is

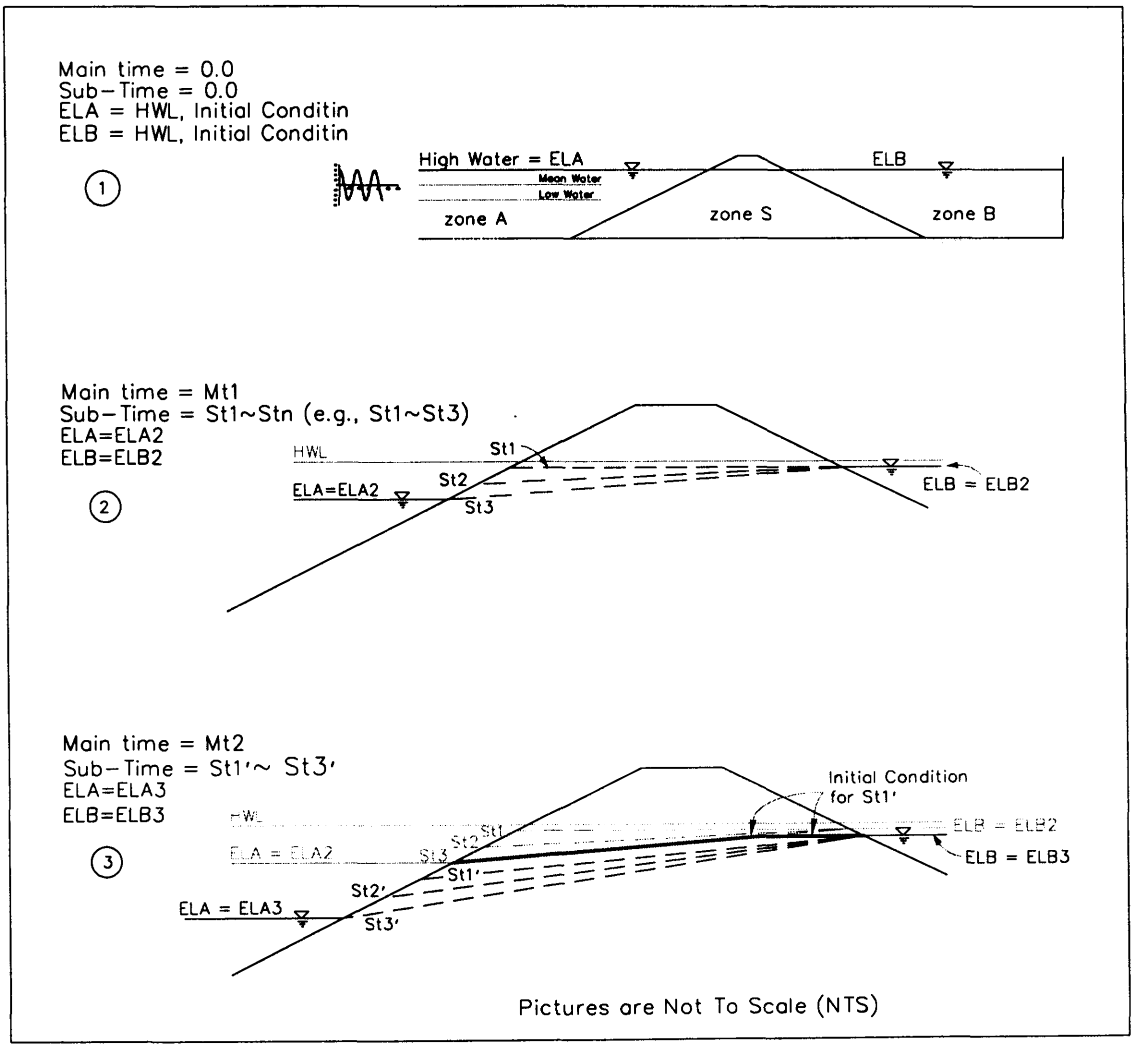

Figure 3.7: The Solution Procedure of the GWK model, e.g., calculation and simulation of the water levels in a successive procedure of the physical model

illustrated in Figure 3.7, where it is seen that tide is running in the front of the sandy dike, zone A, and because of discharge/recharge through the sand, zone S, other tidal levels occur behind the embankment, zone B. It should be noted that Figure 3.7 is related to the physical modelling of this study which will be discussed in chapters five and six.

In this study an alternative direction implicit numerical model has been used to model flow and solute transport phenomena. The solution procedure of a complete *Main Time Step* according to Figures 3.3, 3.7 and 3.8 can be summarised as follows:

1. The initial values for total hydraulic heads and solute concentration are initialised at the start of the main time step.
2. The Main and Sub-main time steps according to the tide characteristics and the input parameters are calculated.
3. The water elevation boundary condition tide level in front of the sand embankment is calculated.
4. The discharge/recharge and volume of water that seeped through the embankment during the current main time step in any direction is computed and the water elevation boundary condition behind the sand embankment is updated.
5. The porous media flow Equations (3.32) and (3.39) are solved to obtain the heads through the sand domain.
6. The velocity field is calculated using Equation (2.15).
7. The solute concentration field is obtained from Equations (3.43) and (3.47).
8. The simulation times are checked and the required print outs are prepared.

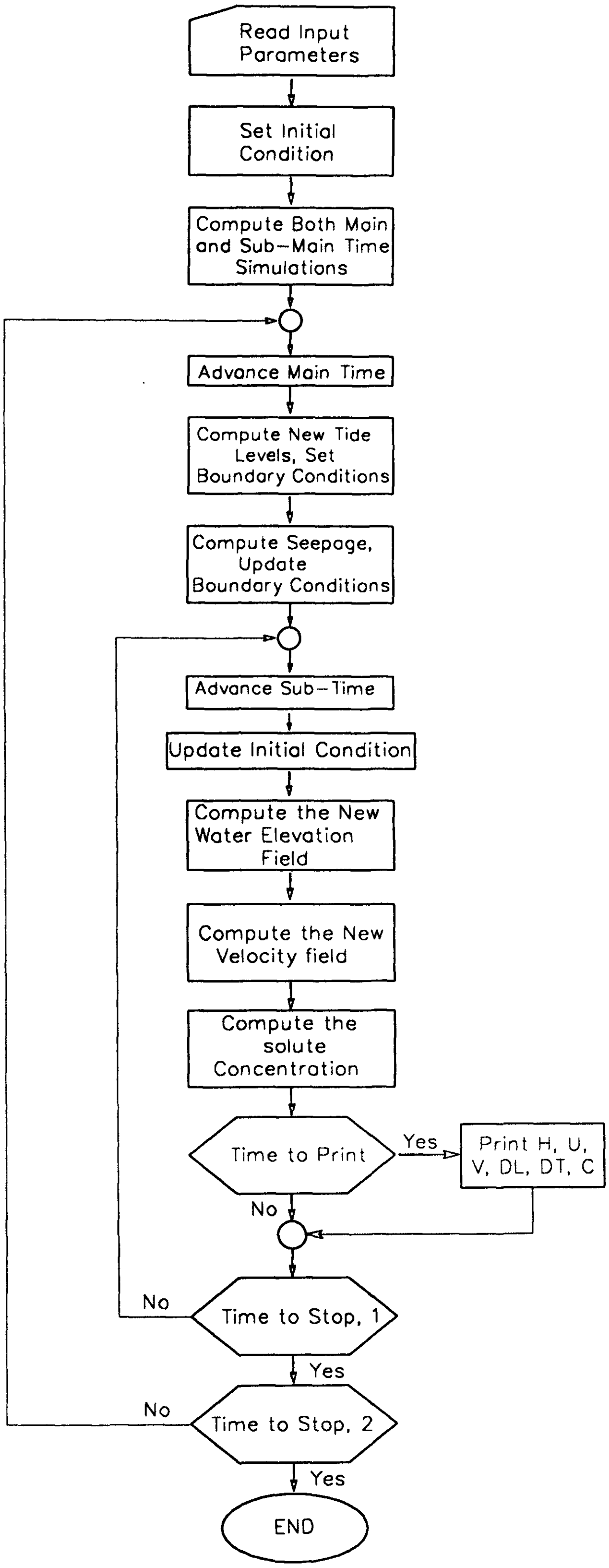

Figure 3.8: Flow-chart of the GWK program

3.5 Dynamic Linked Model Approach

In order to acquire a combined groundwater-surface flow and solute transport model, the GWK and DIVAST models have been dynamically linked. The integrated model is capable of investigating hydro-environmental interactions between the surface and subsurface waters. It is based on physical processes and is able to describe more accurately the pollutant pathways and concentration distributions of a tracer, and the recharge and discharge interaction processes between the above mentioned water systems. The linked model includes; shared time controller, shared mobile boundaries of flow (water elevation and discharge-recharge), shared mobile boundaries of solute concentrations and shared output files. Hence, flow and tracer are able to pass across the shared boundaries in both directions, depending on the relative height of the water table. As the Integrated (DIVAST-GWK) model has been applied to a physical model, the application is used as an example to explain the simulation procedure of the linked model. It should be noted that the results of the application are given in detail in chapter six.

The shared boundaries of both phenomena in the application of the physical model are shown in Figure 3.9. As illustrated in the picture there are two shared boundaries for both sub-models, boundaries; *II* and *III*.

The simulation procedure of the integrated numerical model for a complete time-step can be summarised as follows:

1. The initial water elevations are set horizontally near high water level, the initial velocities are set to zero and the solute concentrations are set to a constant value, if

① Location of the boundaries

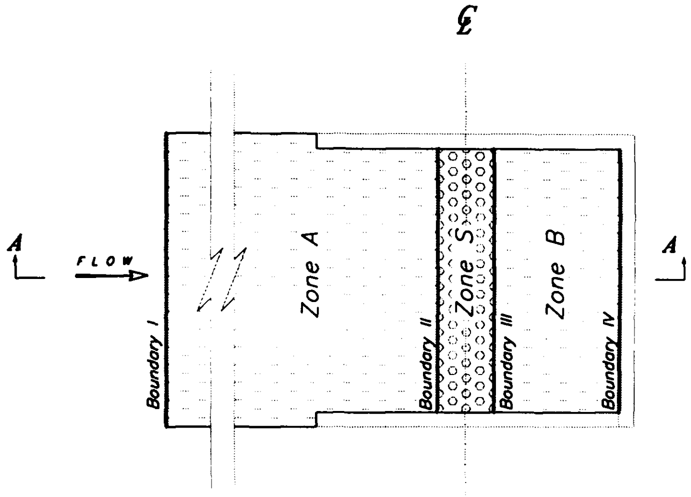

② Section A–A

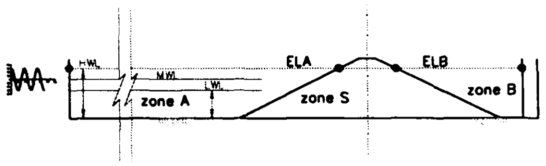

(Pictures are not to scale)

③ Open Boundaries:

Zone A:
I; water elevation open boundary for Free Surface Model.
II; flow or velocity open boundary for Free Surface Model.

Zone S:
II; water elevation open boundary for Porous Media Model.
III; water elevation open boundary for Porous Media Model.

Zone B:
III; flow or velocity open boundary for Free Surface Model.
IV; closed boundary for Free Surface Model.

Figure 3.9: The boundary conditions, for the physical model

the solute distribution is uniform initially, across the domain.

2. The input data files of the DIVAST and GWK models are read, respectively.
3. The water elevation open boundary condition *I* is updated to simulate the water elevation, velocities and solute concentration distribution fields for *zone A* (see Figure 3.9). Also the open boundary *II* is updated. Simultaneously using the initial condition, *zone B* is simulated.
4. The discharge and volume of water that seeped through the embankment during the current time step is computed and the water elevation open boundary condition *III* is updated.
5. The groundwater domain is simulated to predict the total hydraulic heads, the velocity field and the solute concentration distribution. The open boundaries *II* and *III* for flow and solute concentrations are updated.

The following figure shows above mentioned procedure for the linked model.

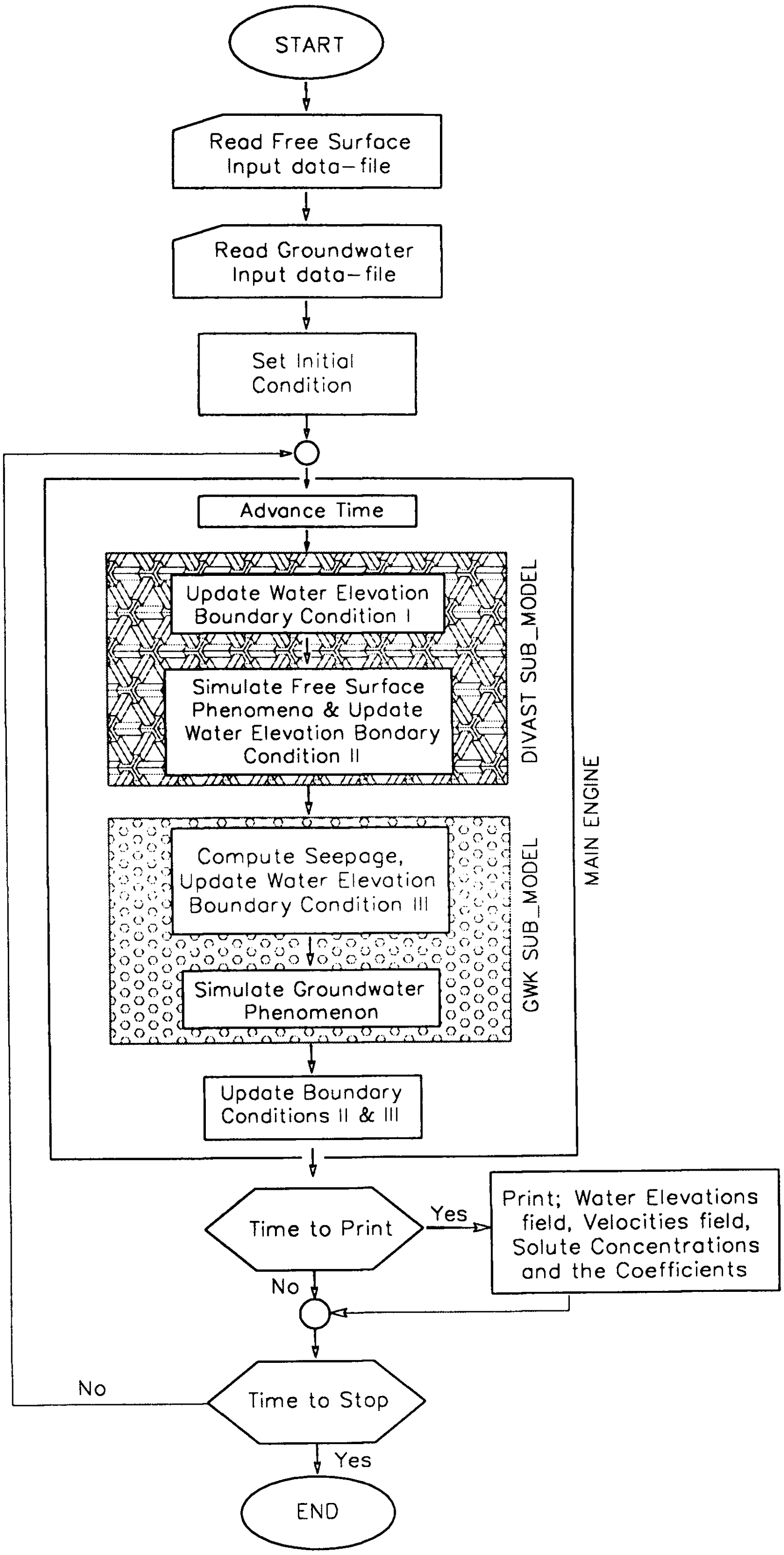

Figure 3.10: Flow-chart of the linked models, GWK-DIVAST

3.6 Summary

In this chapter the background of different types of partial differential equations is presented, followed by a review of basic finite difference methods. The details of the discretisation and solution procedure for groundwater flow and a conservative form of the advective-diffusion equation are described, in order to predict the hydrodynamic and solute transport processes. Also, the stability of the different finite difference methods has been discussed, in discretising the Boussinesq equation (Equation 2.38). The structure of the GWK model is defined, together with a description of its numerical implementation. Finally, a dynamic linked approach is outlined, which was used to create an integrated model of groundwater-surface flow involving the GWK and the DIVAST model.

CHAPTER 4

POROUS MEDIA NUMERICAL MODEL TESTS

4.1 Introduction

In this chapter numerical simulations of the porous media sub-model, GWK, have been performed for various situations. For this purpose the GWK numerical model was first set up to simulate the hydrodynamic field of an idealized porous medium domain for different conditions, to assess the computational capability of the model. Then the solute transport phenomena was tested and applied to this case, in the form of a conservative dye tracer contaminant. Input parameters and flow conditions of the test cases are given in this chapter, together with the predictions of the hydrodynamic parameters, contaminate distributions and the related discussion.

It should be noted that later in this thesis (i.e. Chapter 6) the linked numerical model has been applied to the whole physical model, i.e. both for porous medium and free surface flow phenomenon, and the simulation results have been compared to the experimental data, to investigate the accuracy of the linked numerical model predictions.

4.2 Idealized Test Case Application

The above mentioned idealized domain was based on the porous medium domain of the physical model as shown in Figure 4.1. Figure 4.1-a illustrates a plan and longitudinal section of the physical model, which will be described in more detail in Chapter 5. As can be seen from Figure 4.1-a, the porous medium domain of the physical model is highlighted by the *ABCD* cadre. The sides *AB* and *DC* of this domain are two mobile boundaries, with these boundaries being shared between the free surface phenomenon and the porous medium domain. At this stage it is assumed that these two boundaries are fixed. However, in Chapter 6 the effects of tides, and the wetting and drying of cells, will be included in the simulations. Figure 4.1-b shows the idealized computational domain for the test cases with the grid overlain. The length of the domain was chosen to be three times that of the porous medium region shown in Figure 4.1-a, see *BC and BE* sides. This extension provided enough of a run-in to evaluate the capability of the new 2-D model for different situations. The model has been constructed with a square grid, of size 5cm x 5cm. The origin, and the longitudinal and transverse axes can be seen in Figure 4.1-b.

Therefore, the computational domain which was used for model testing comprised a rectangular symmetric domain, of constant dimensions of 360cm by 180cm, as shown in Figure 4.1-b.

4.3 Model Application for Test Cases

Three test cases were chosen to evaluate the accuracy of the porous media sub-model predictions. Both up-stream and down-stream open boundaries were set as water elevation boundaries. The depth of water on the down-stream boundary, i.e. the *EF* boundary, was

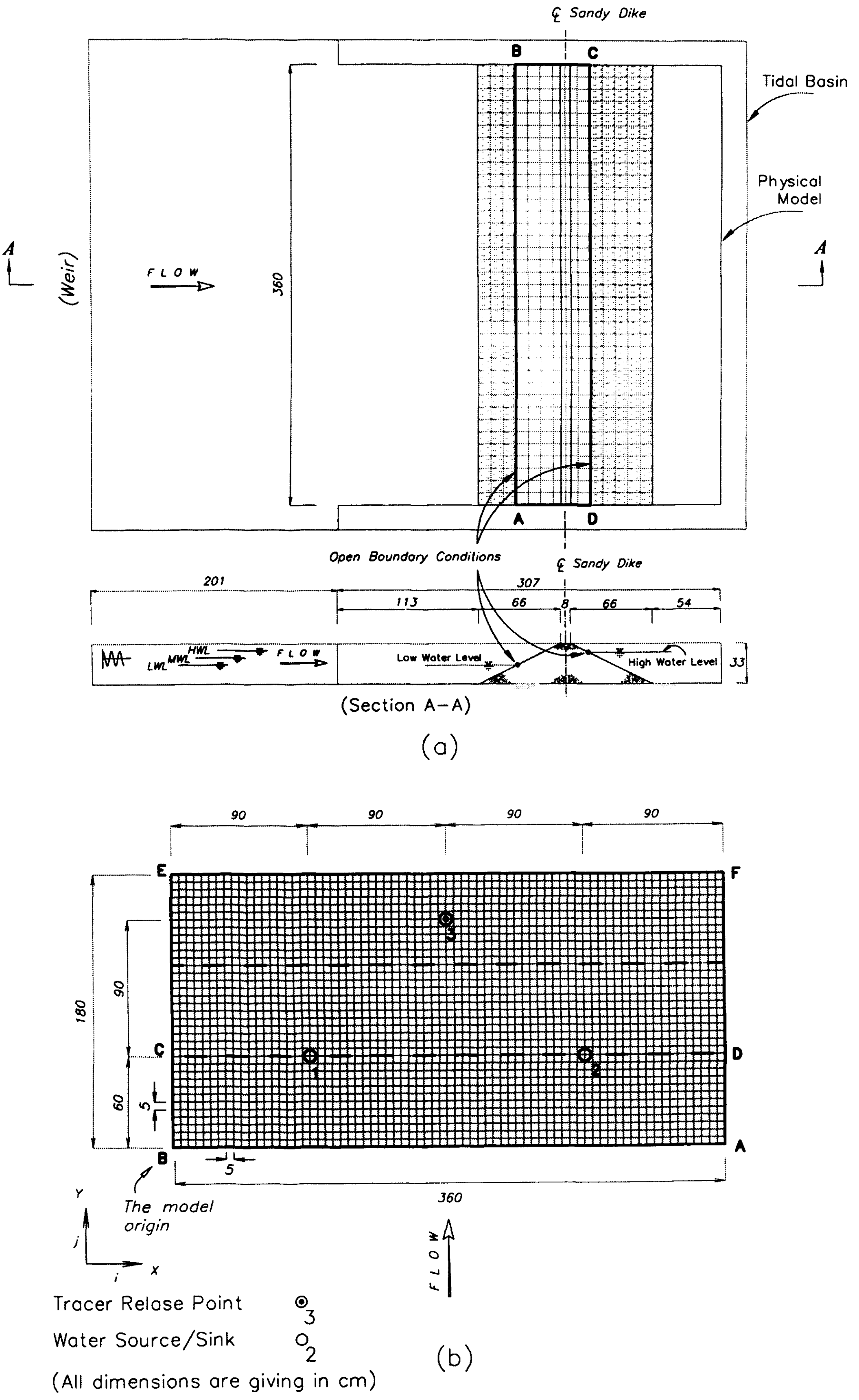

Figure 4.1: Idealized porous media test case domain

assumed to be constant at high-water-level. However, a fluctuating tidal elevation was chosen as the forward open boundary, i.e. the *AB* open boundary. The tidal flow was generated by a sinusoidally varying water elevation, with a period of 355 s, an amplitude of 12 cm and mean water level equal to 21 cm. The time-step used in the model was 4 s and the simulation period for each test case was undertaken for 10 repetitive tidal cycles. For each individual simulation, the water levels throughout the domain were initially fixed at high tide at the beginning of the simulation. Therefore, all simulations were started with the same horizontal high tide water level throughout the model. For all tests the initial solute concentration level across the domain was set to zero and then a conservative dye tracer, of concentration 50 mg/l was introduced at the beginning of the ninth tide, i.e. at the time when the water elevation at the forward boundary of the domain was at high water, see Figure 4.1-b point 3. Also, the solute input from the open boundaries was assumed to be zero. Therefore, a steep gradient in the solute level was simulated, especially at the upstream open boundary, i.e. boundary *AB*.

The first test undertaken was the simulation of both hydrodynamic and solute transport phenomena throughout the computational domain while the tracer was released over the two last tides of the simulation period. In this test no source/sink of water was considered in the domain. It should be noted that the graphical outputs and related discussion of these tests are given later in this chapter.

The second test case was undertaken to establish further the scope of the newly developed numerical model. In a similar procedure to the first test case, and with the same concentration of dye tracer and the same open boundary conditions as given for the first test, in the second test case the hydrodynamic and solute transport fields were again simulated. However, in this test case, in order to establish the configuration of the water table, velocity field and tracer contaminant distributions, two water sinks, were included at the discharge points 1 and 2, as illustrated in Figure 4.1-b. Each sink had a constant discharge rate of 20 l/s throughout the simulation time. As can be seen from Figure 4.1-b, in order to create symmetric simulations the co-ordinates of these two sinks were selected in symmetrical positions, and in both sides of the computational domain.

The final test case undertaken was to repeat the second test case, but including two sources instead of sinks, with the sources located at the same positions and with the same recharge rate of 20 l/s. This test case provided further evidence of the response of the newly developed 2-D numerical model to the boundary and initial conditions.

It should be noted that in the simulation of the above mentioned test cases, the values used for the longitudinal and transverse dispersivity coefficients were, 1.5 and 0.1 respectively, and the coefficients of hydraulic conductivity, 0.95cm/s, and specific yield, 30%, were based on the calibrated values obtained from the physical model results. Details of the calibration of these coefficients will be outlined in Chapter 6.

4.3.1 Test Case One

As mentioned previously the first test case was undertaken for the simplest setup, to investigate the initial accuracy criteria of the numerical model predictions. Graphical plots of the velocity field, solute distribution and equi-potential lines are produced at mid-ebb, high, mid-flood and low water elevations of tide 9, involving the Tecplot software package, and are presented in Figures 4.2 to 4.6.

As can be seen from the figures, each figure comprises both a tracer contaminate distribution, including scaled velocity vectors, and equi-potential lines, including velocities which –for convenience- have not been reproduced to the same scale.

Figure 4.2-a illustrates the appearance of the tracer on top of the computational domain and Figure 4.2-b shows the related hydraulic heads. It should be noted that these two figures have not produced at the exact high water level, but are shown at close to high water in order to show the appearance of the tracer. However, these plots did not show considerable differences from the tracer distribution at high water. The overall concentration of the tracer at this stage is less than 5 mg/l and the water elevations across the domain at this time varies between 0.27 m, i.e. fixed high water at the top of the domain, and 0.257 m which was calculated in the middle of the domain, where y = 0.85 m. This is a mirror image of the velocity vectors and along the line where the velocities cross.

Figures 4.3 to 4.6 show the progression of the simulation for the different time stages. In Figure 4.3 the water elevation along the upper boundary is at mid-ebb tide and the tracer is spreading uniformly while the flow is discharging from the upper boundary. As can be seen from Figure 4.3-a, the velocities at this stage are very low.

The highest velocities can be seen in Figure 4.4, where they are approximately equal to 1 mm/s and are simulated close to the upper boundary. At this phase the upper boundary is at low water level and therefore the maximum gradient occurs in the water table. Although at this stage the tracer plume has greatly expanded compared with the last figure, the diffusion occurs more along the y axes than along the x axes. This is because for this test case the magnitude of the u component of velocities were zero. Also, the maximum tracer concentration at this stage, which is related to the centre of the tracer plume, was approximately 700mg/l.

The zero velocity magnitude contour can be seen along $y = 0.25$ m in Figure 4.5-a, where the two stream flows cross. The water elevation along this line is about 0.20 m. At this stage the contaminant plume is being advected towards the far boundary. A comparison of this figure with the next figure, i.e. Figure 4.6, proves this observation. The simulated water elevation field shown in Figure 4.6-b is exactly the same as that in Figure 4.2-b, which again proves the accuracy of the simulations.

In order to show the time variations in water levels for test case 1, 2 and 3, typically two points across the domain are chosen, points 1 and 2 of Figure 4.1, and the relevant plots are presented in Appendix B, Figures B.1 to B.6 to give an indication of sink/source effects of water table.

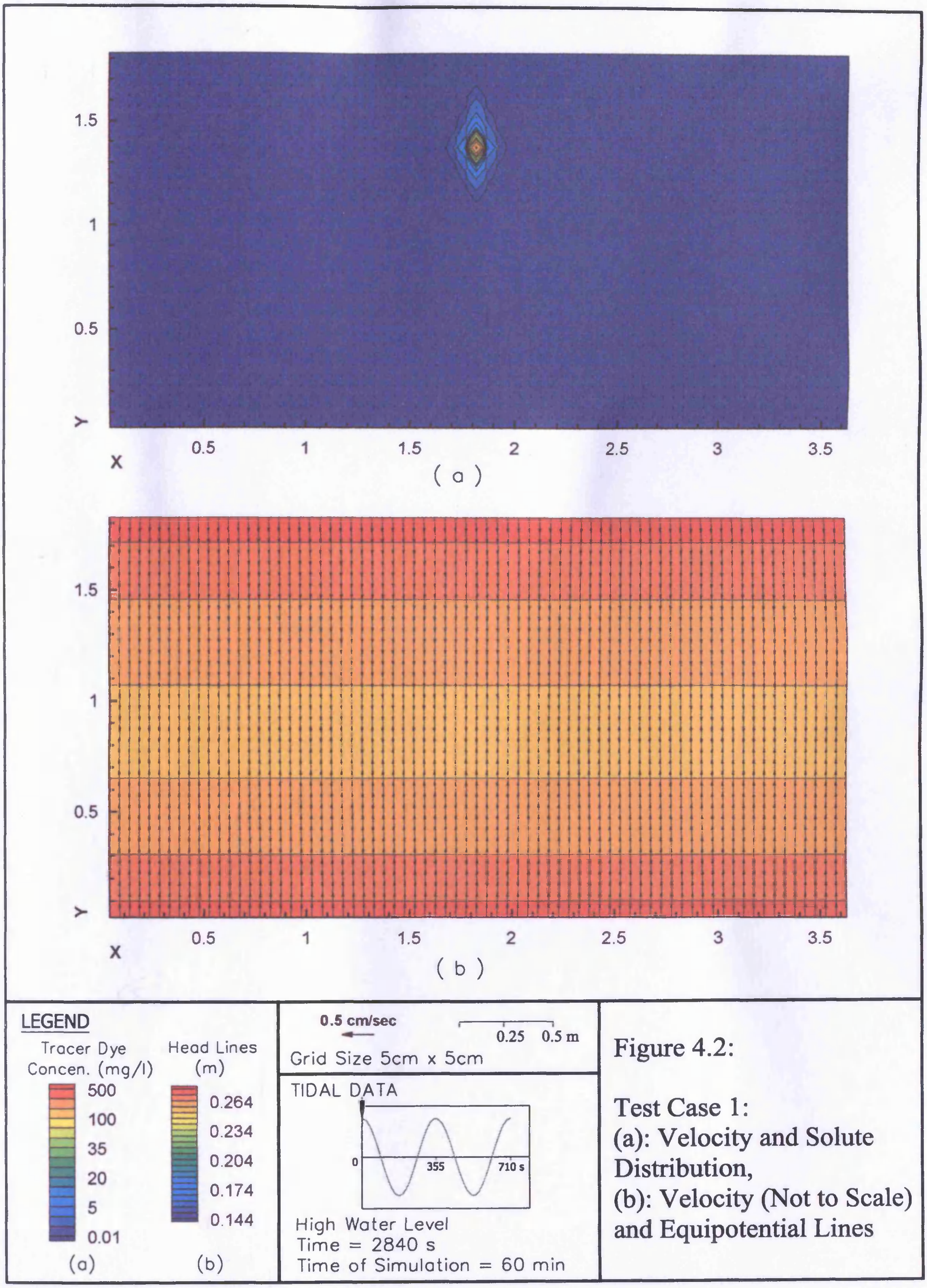

Figure 4.2:

Test Case 1:
(a): Velocity and Solute Distribution,
(b): Velocity (Not to Scale) and Equipotential Lines

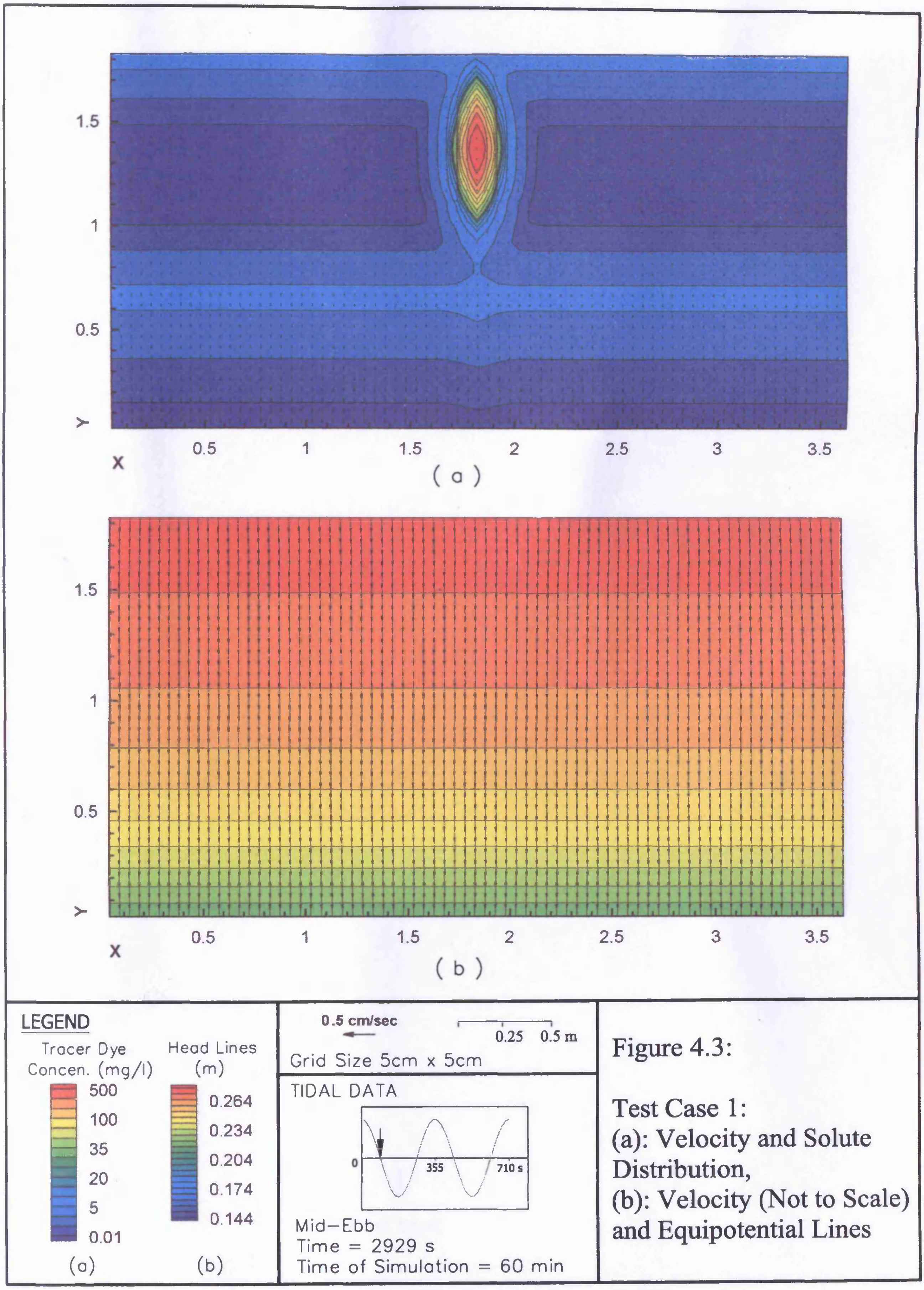

Figure 4.3:

Test Case 1:
(a): Velocity and Solute Distribution,
(b): Velocity (Not to Scale) and Equipotential Lines

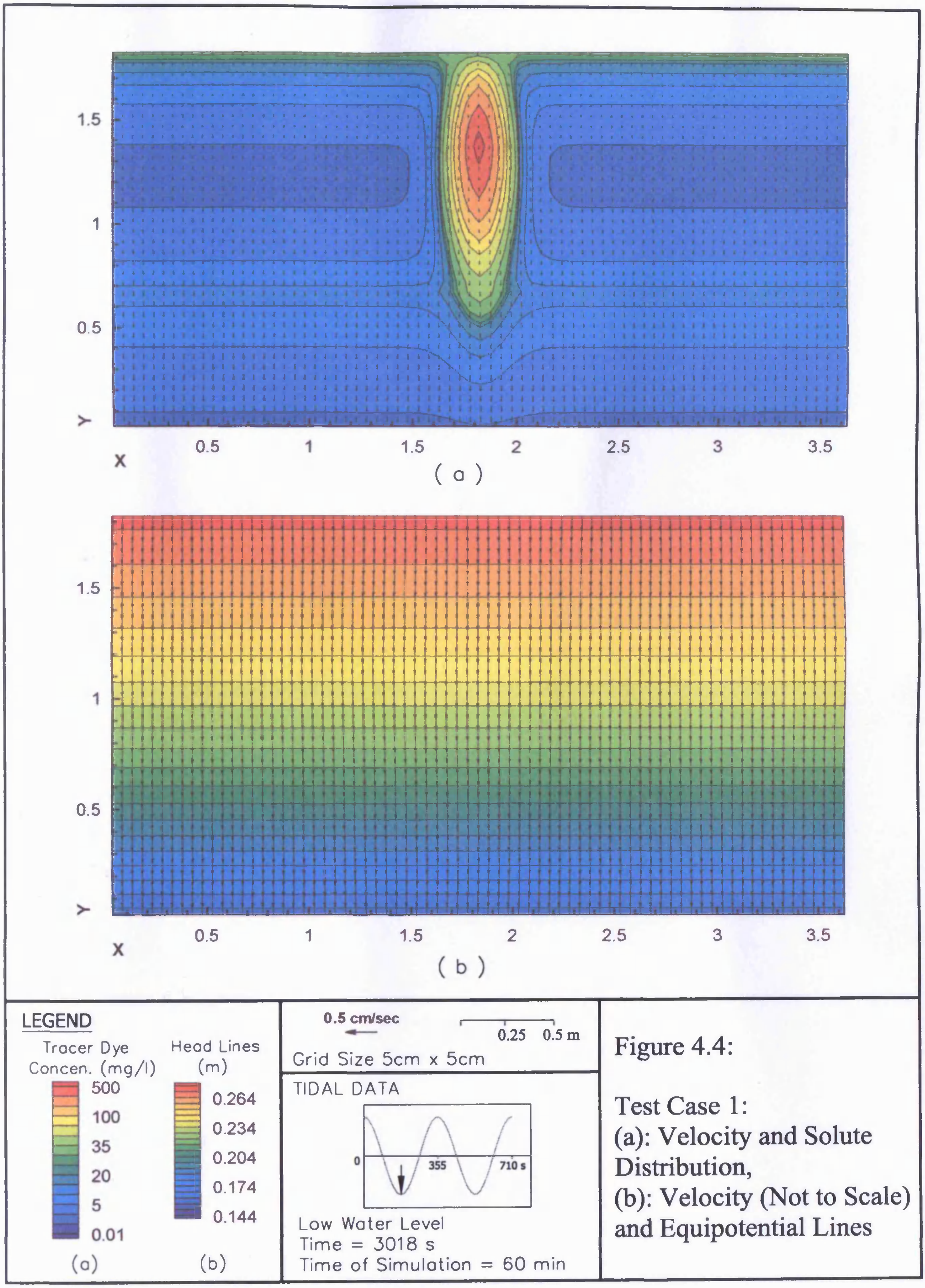

Figure 4.4:

Test Case 1:
(a): Velocity and Solute Distribution,
(b): Velocity (Not to Scale) and Equipotential Lines

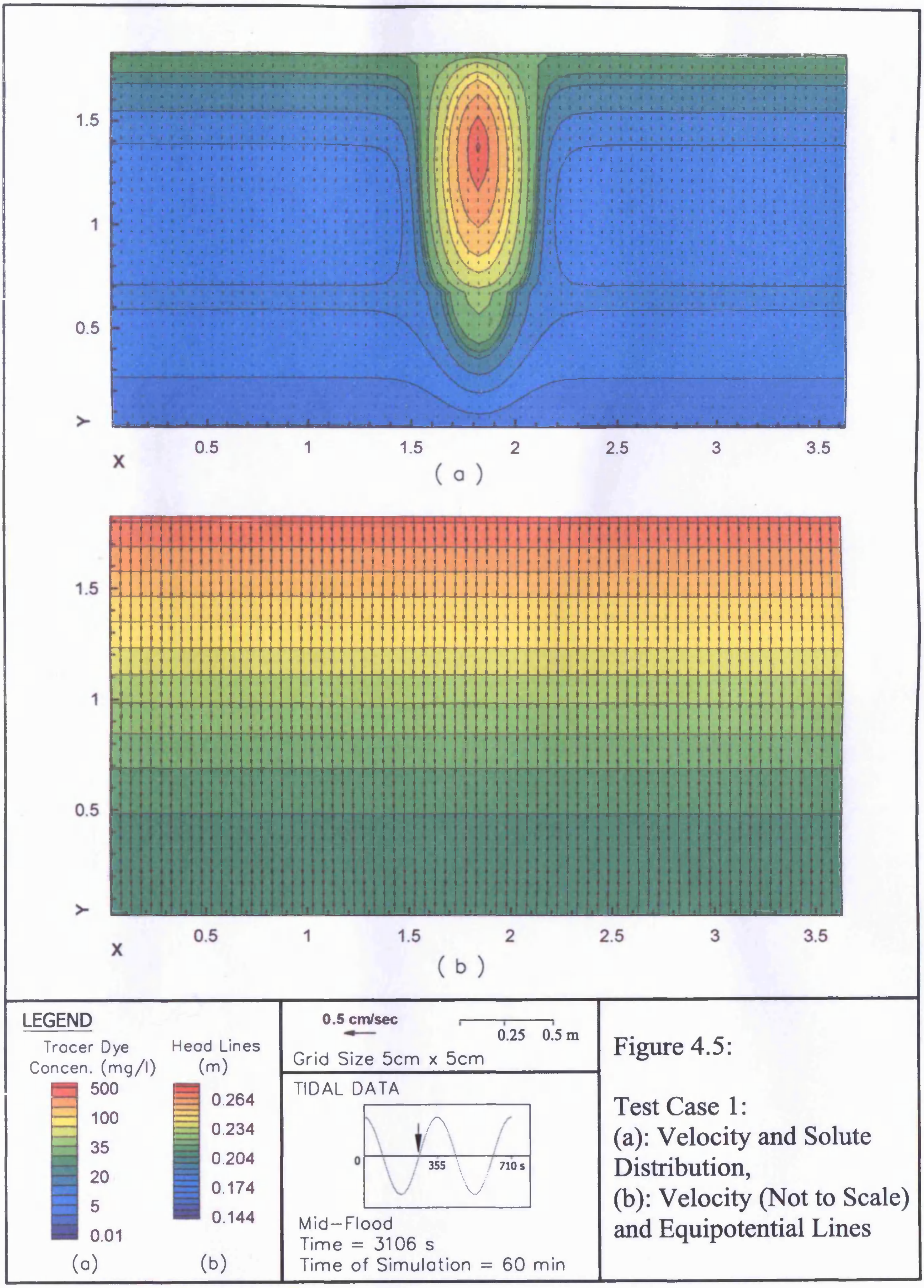

Figure 4.5:

Test Case 1:
(a): Velocity and Solute Distribution,
(b): Velocity (Not to Scale) and Equipotential Lines

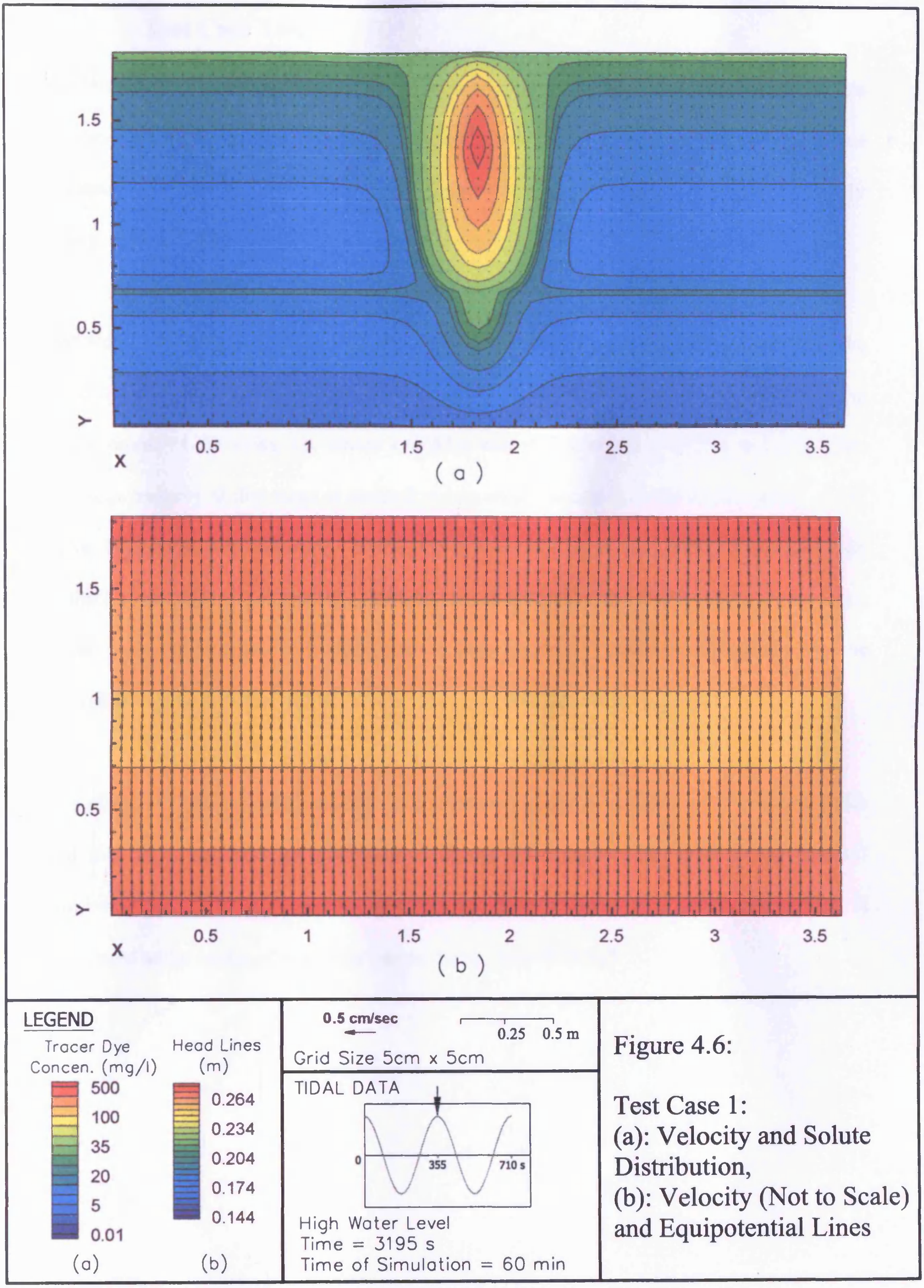

Figure 4.6:

Test Case 1:
(a): Velocity and Solute Distribution,
(b): Velocity (Not to Scale) and Equipotential Lines

4.3.2 Test Case Two

The two dimensional behaviour of the GWK model output is demonstrated more so by this test case rather than the first test. The graphical results of the second test case are indicated in Figures 4.7 to 4.11. The location of the sinks in the computational domain can be clearly seen in Figure 4.7-b.

The water elevation across the domain at this stage varies between 0.27 m, which is the fixed water level at the top of the domain, and 0.24 m which is the simulated head at the centre points of the sinks, i.e. where $x=0.95m$ and $y=0.65m$ and $x=2.75m$ and $y=0.65m$. The peak velocity at this stage is about 2 mm/s, which occurs near the centre points of the sinks. Therefore, at this stage the lowest water level is 0.017m less than at the same stage of the last test case, i.e. Figure 4.2, and this result highlights the effect of the sinks on the water table. Also, Figure 4.7-b shows that at high water level the tide progresses along the *y-direction* up to $y=0.85m$ and at this location it is the same as in Figure 4.2.

The effect of these two sinks on the configuration of equi-potential curves, velocity fields and the tracer contaminant distributions at the other time-levels created symmetrical similar to as Figure 4.7. The highest concentration is given in Figure 4.11, which is calculated at the centre of the tracer plume, to be about 860mg/l.

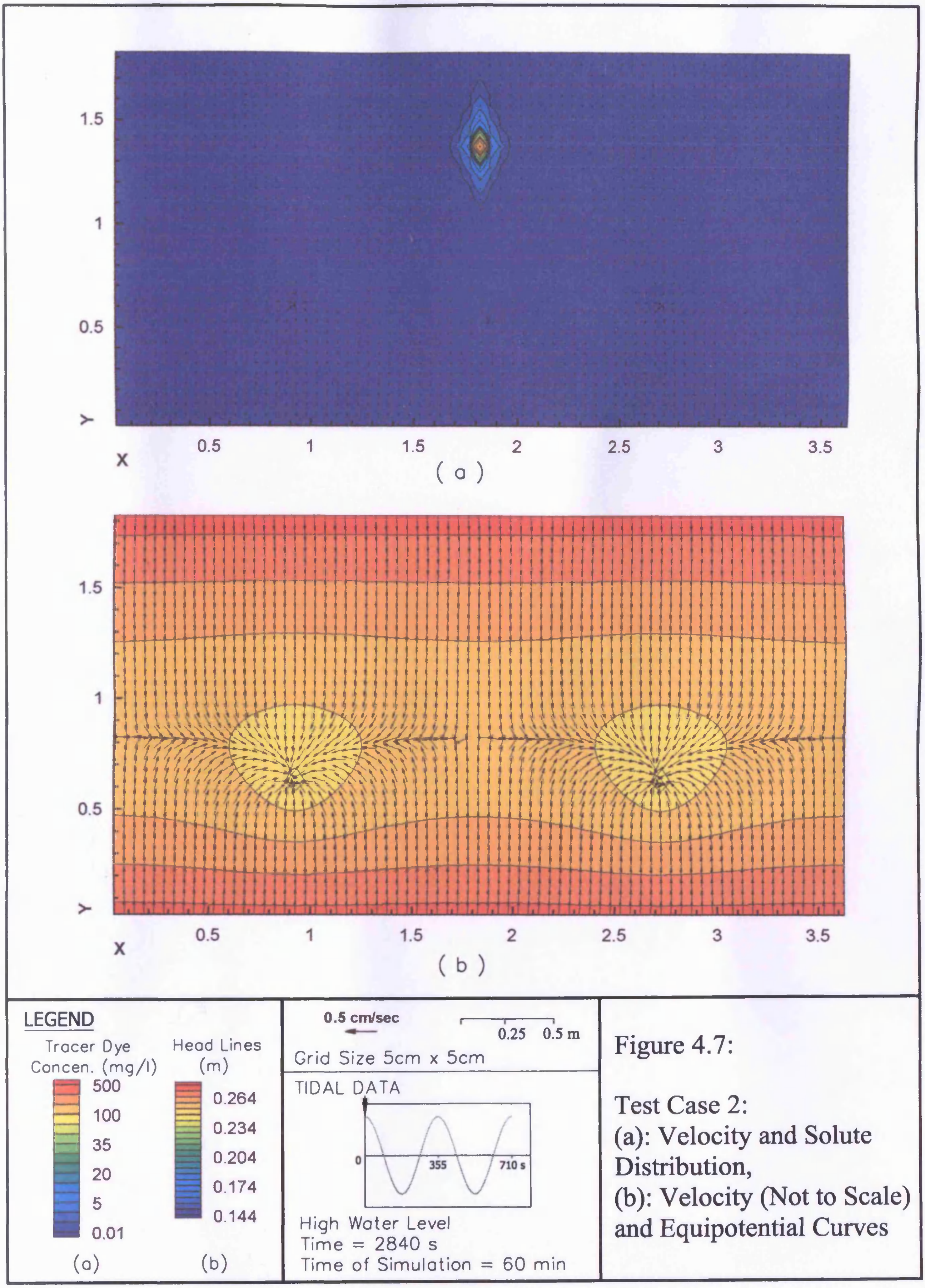

Figure 4.7:

Test Case 2:
(a): Velocity and Solute Distribution,
(b): Velocity (Not to Scale) and Equipotential Curves

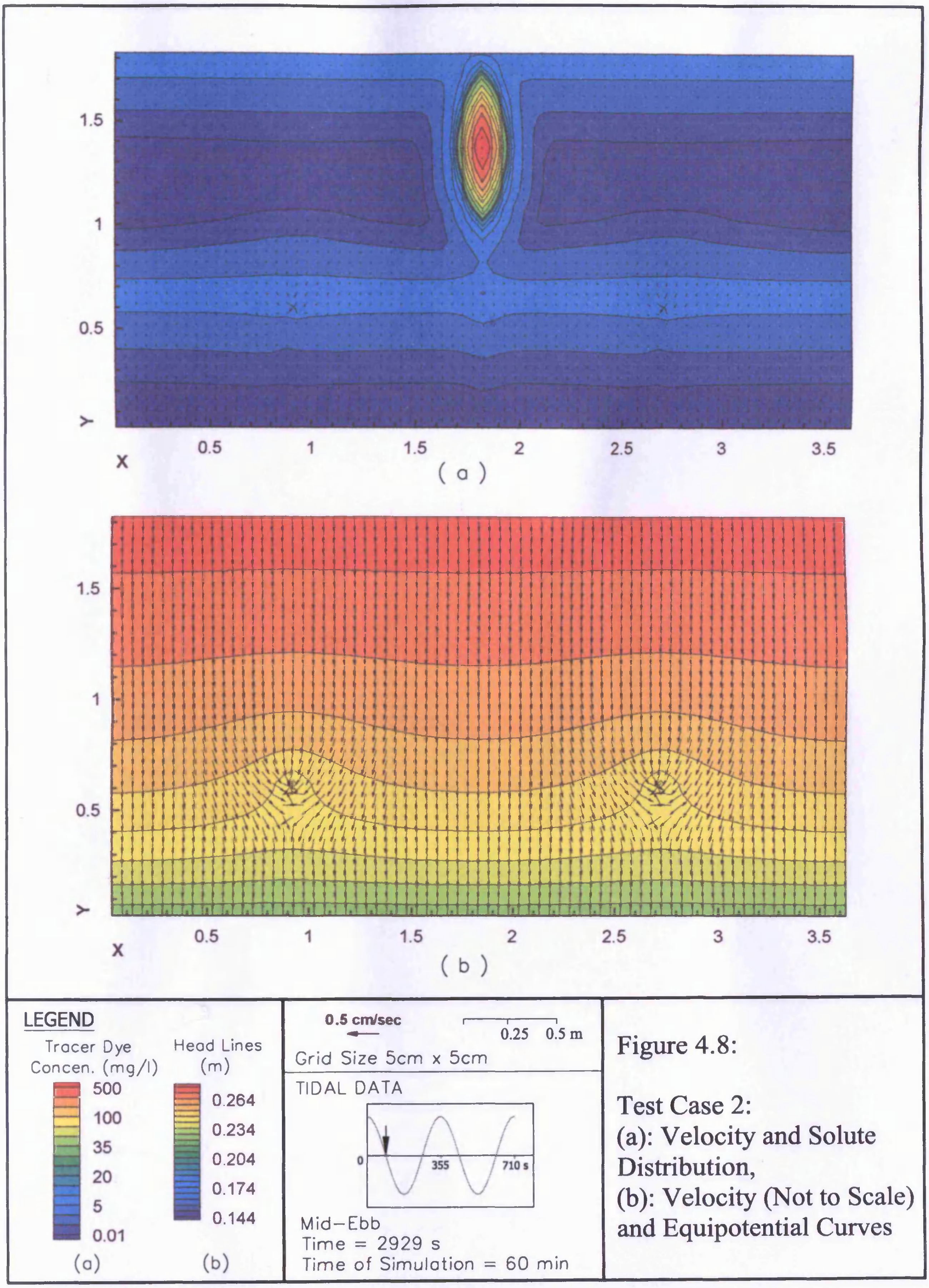

Figure 4.8:

Test Case 2:
(a): Velocity and Solute Distribution,
(b): Velocity (Not to Scale) and Equipotential Curves

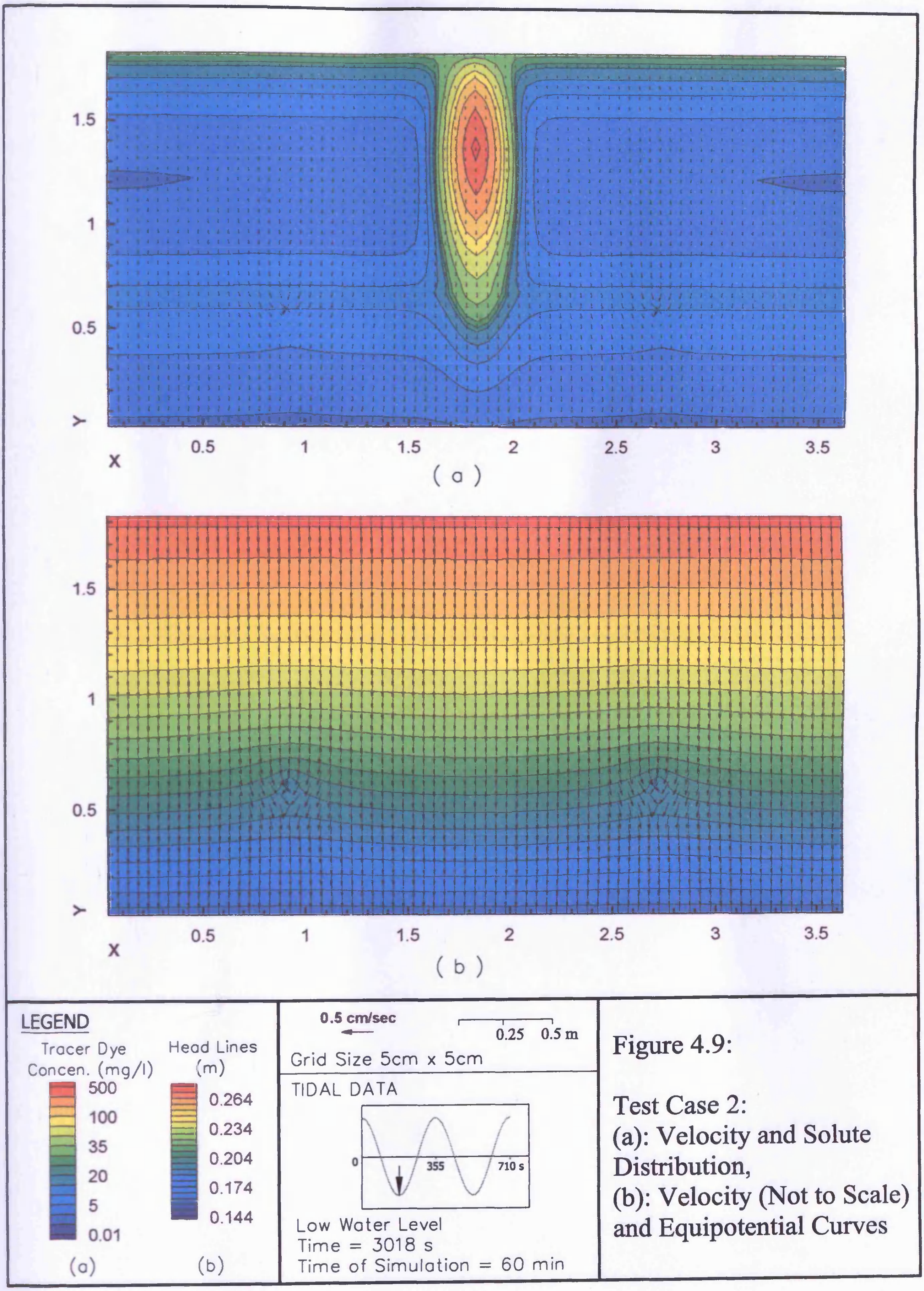

Figure 4.9:

Test Case 2:
(a): Velocity and Solute Distribution,
(b): Velocity (Not to Scale) and Equipotential Curves

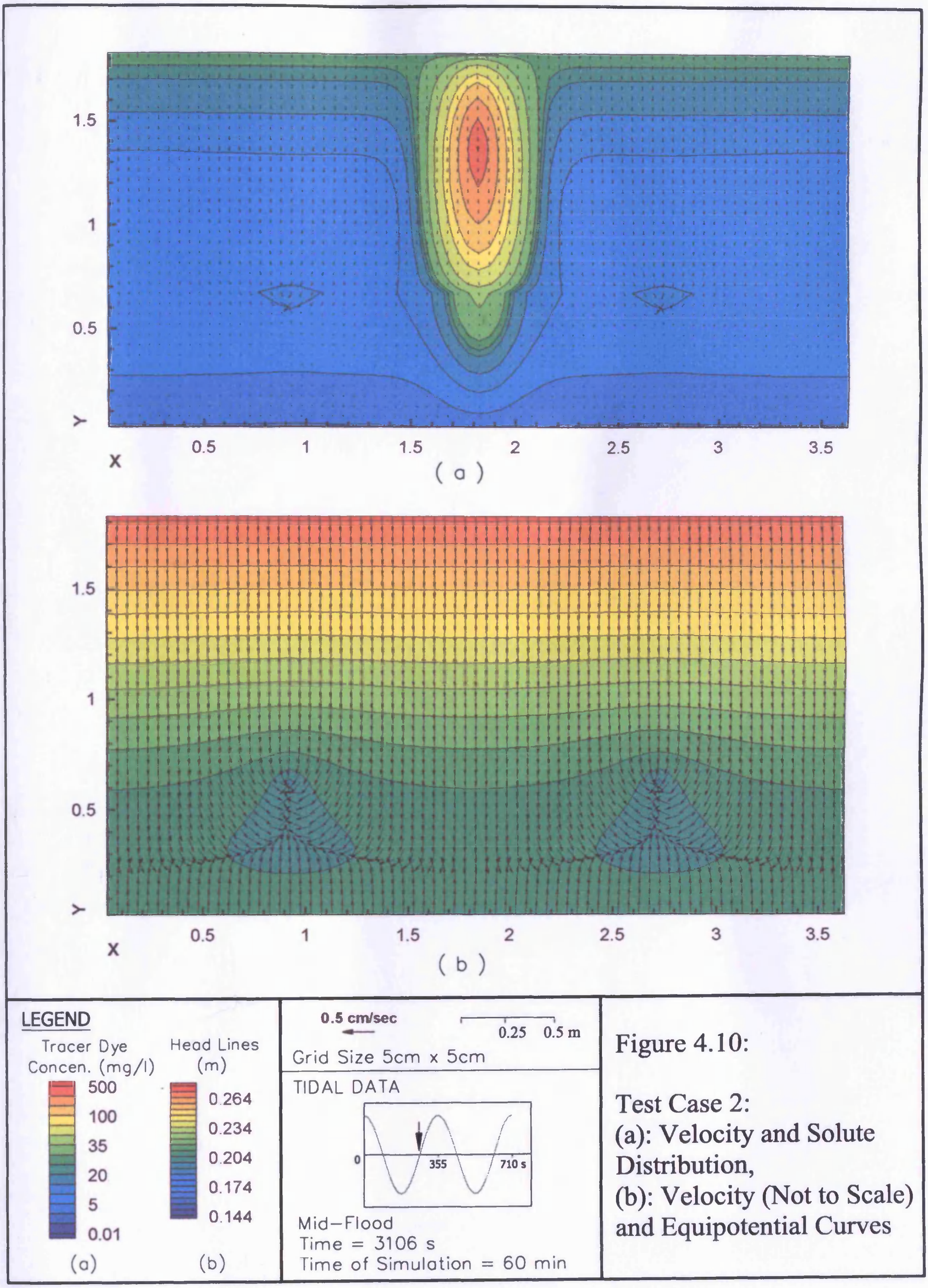

Figure 4.10:

Test Case 2:
(a): Velocity and Solute Distribution,
(b): Velocity (Not to Scale) and Equipotential Curves

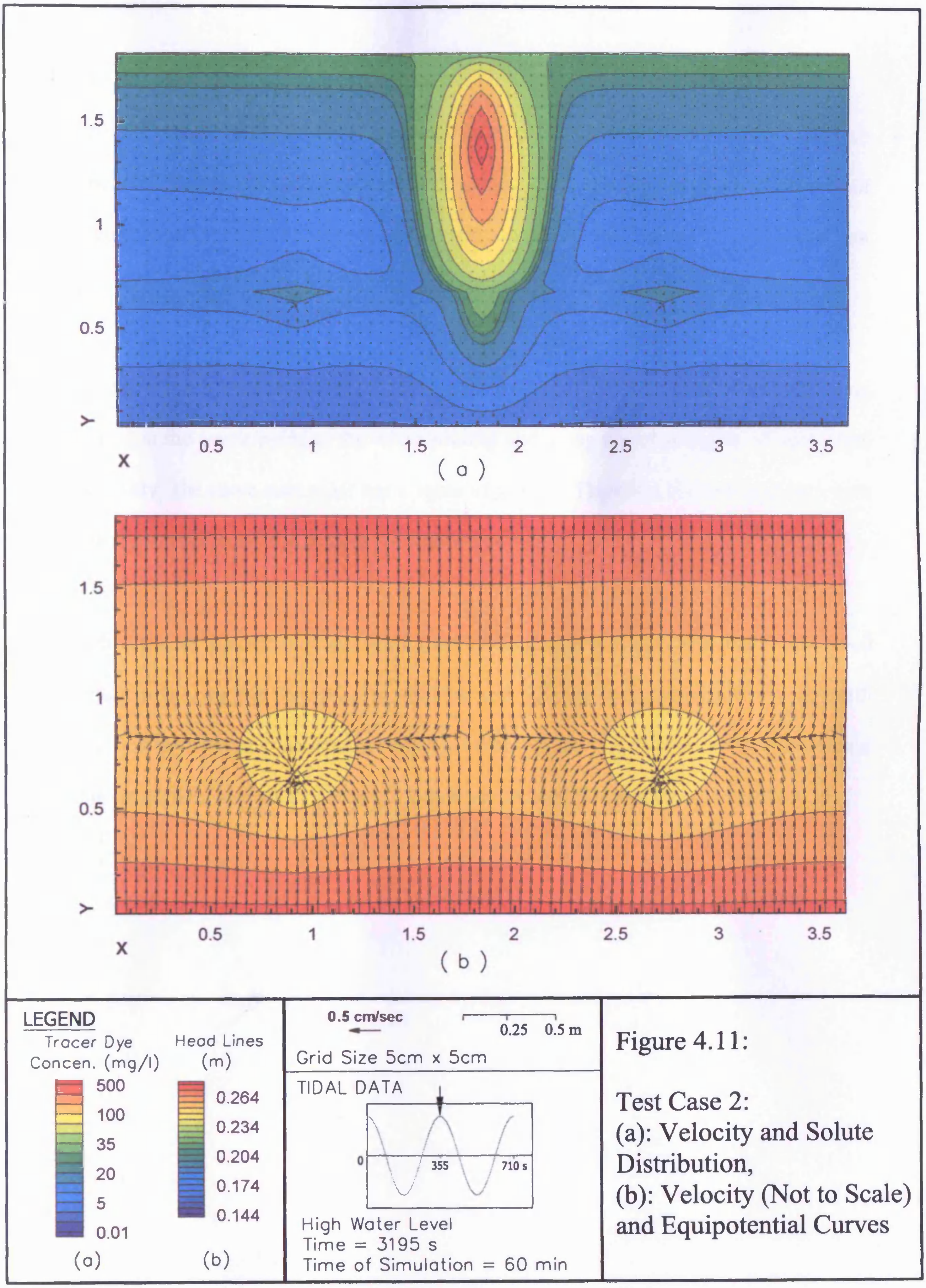

Figure 4.11:

Test Case 2:
(a): Velocity and Solute Distribution,
(b): Velocity (Not to Scale) and Equipotential Curves

4.3.3 Test Case Three

The results of the last test case are illustrated in Figures 4.12 to 4.16. The recharges which are included in this test case affected the direction of the velocity vectors and the overall configuration of the output plots in a different way from those given in the second test case.

The variation in the water elevations illustrated in Figure 4.12 is from 0.276 m to 0.26 m, occurring at the centre point of the water sources and along the cross curves of velocities, respectively. The curve start point has a value of $y=0.85$. Therefore, the two highest points in this figure are 0.06m higher than the high water level.

The elevation of the centre of sources for next time stages: mid-ebb, low water, mid-flood and high water, are 0.273m, 0.229m, 0.230m and 0.276m, respectively. Also it is worth noting that the highest concentration among the above mentioned time-sections according to this simulation is equal to 1080mg/l, which occurs at high water level in Figure 4.16.

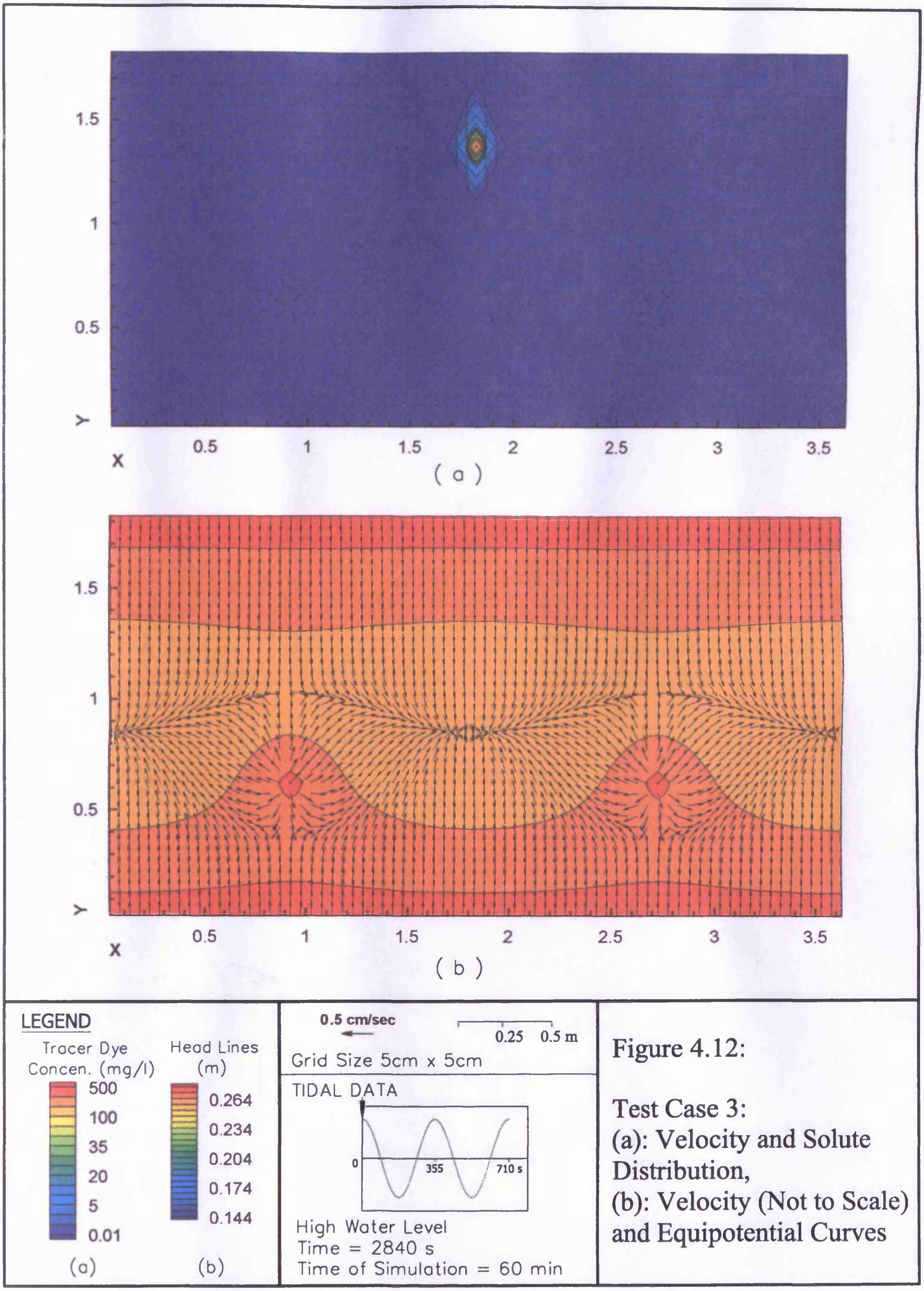

Figure 4.12:

Test Case 3:
(a): Velocity and Solute Distribution,
(b): Velocity (Not to Scale) and Equipotential Curves

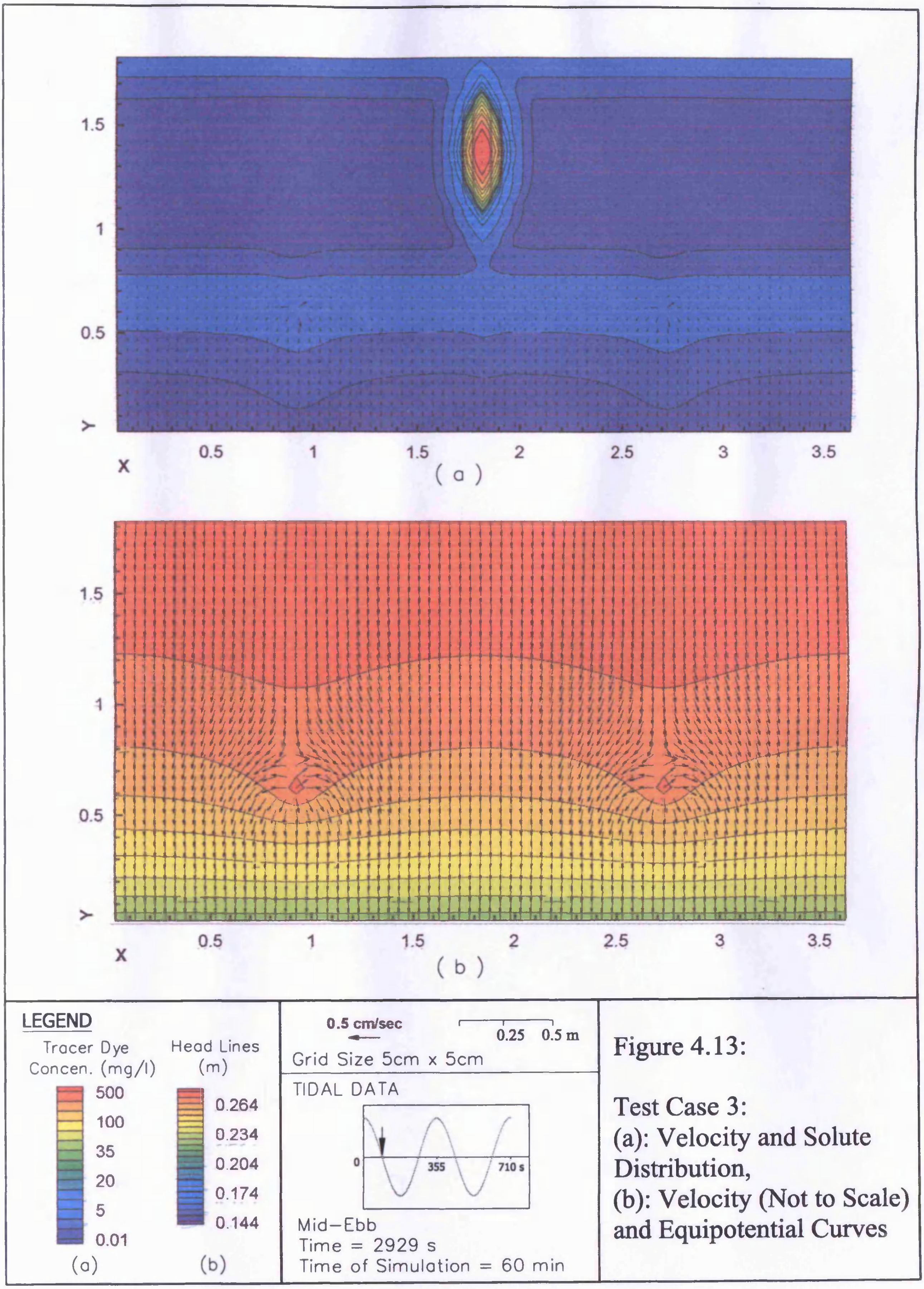

Figure 4.13:

Test Case 3:
(a): Velocity and Solute Distribution,
(b): Velocity (Not to Scale) and Equipotential Curves

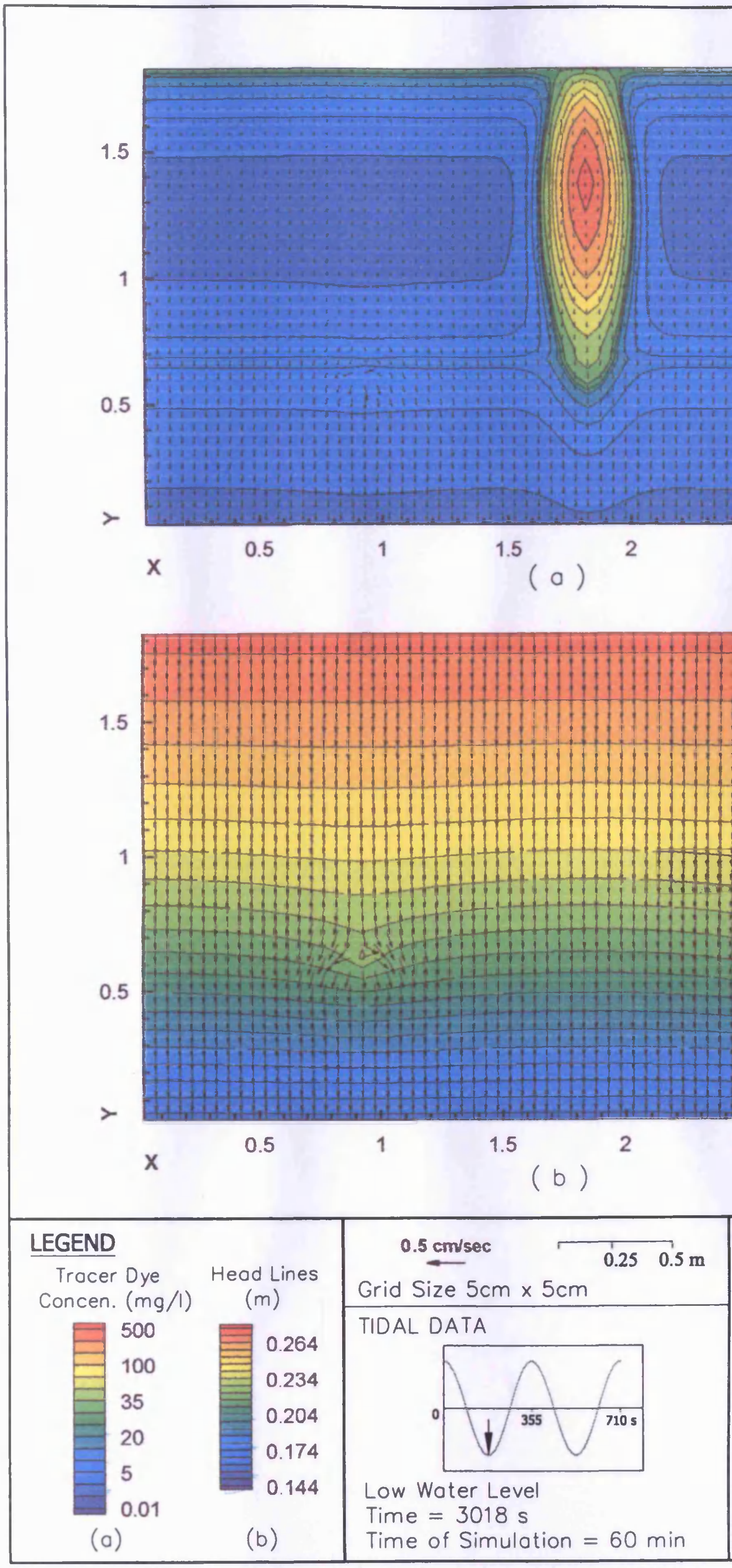

Figure 4.14:

Test Case 3:
(a): Velocity and Solute Distribution,
(b): Velocity (Not to Scale) and Equipotential Curves

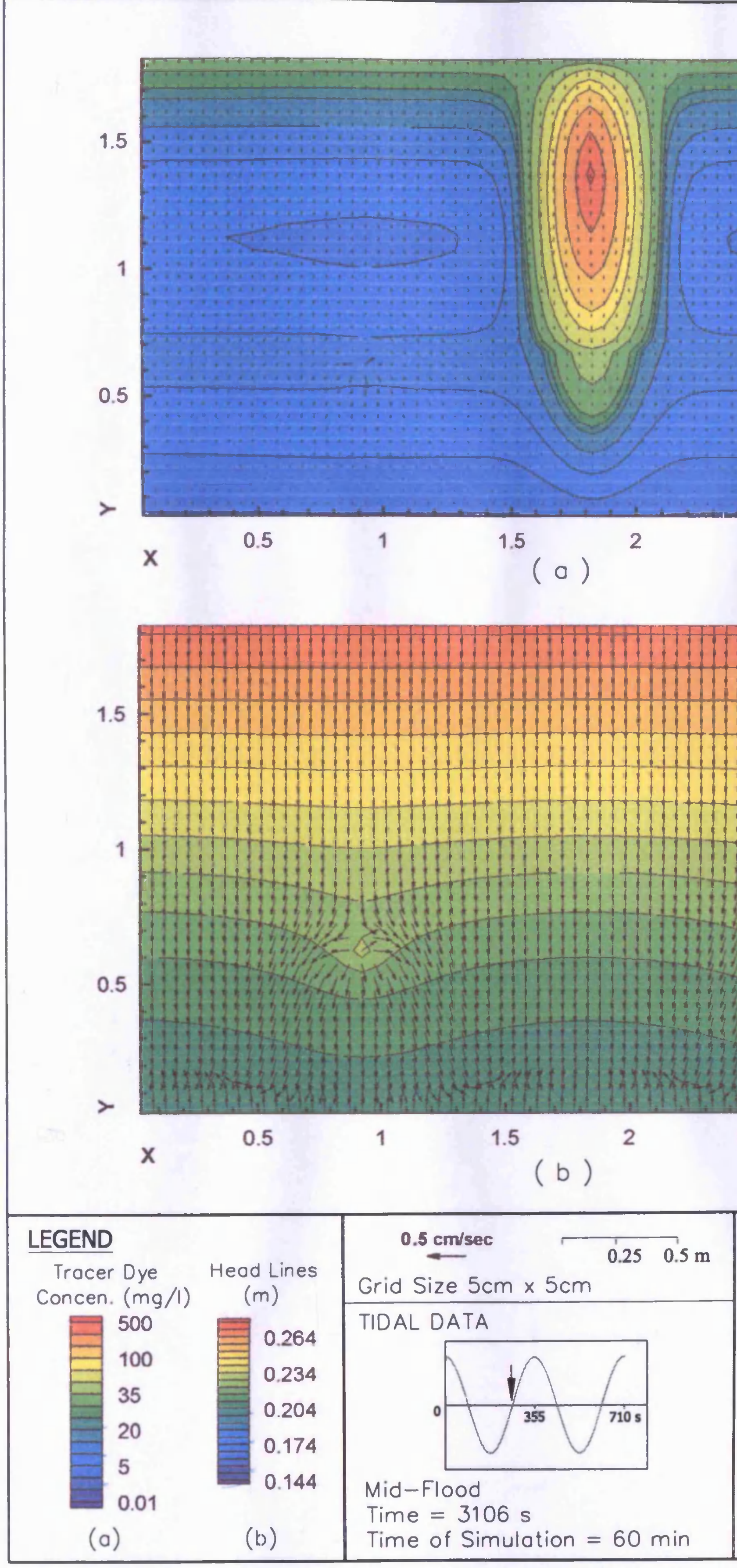

Figure 4.15:

Test Case 3:
(a): Velocity and Solute Distribution,
(b): Velocity (Not to Scale) and Equipotential Curves

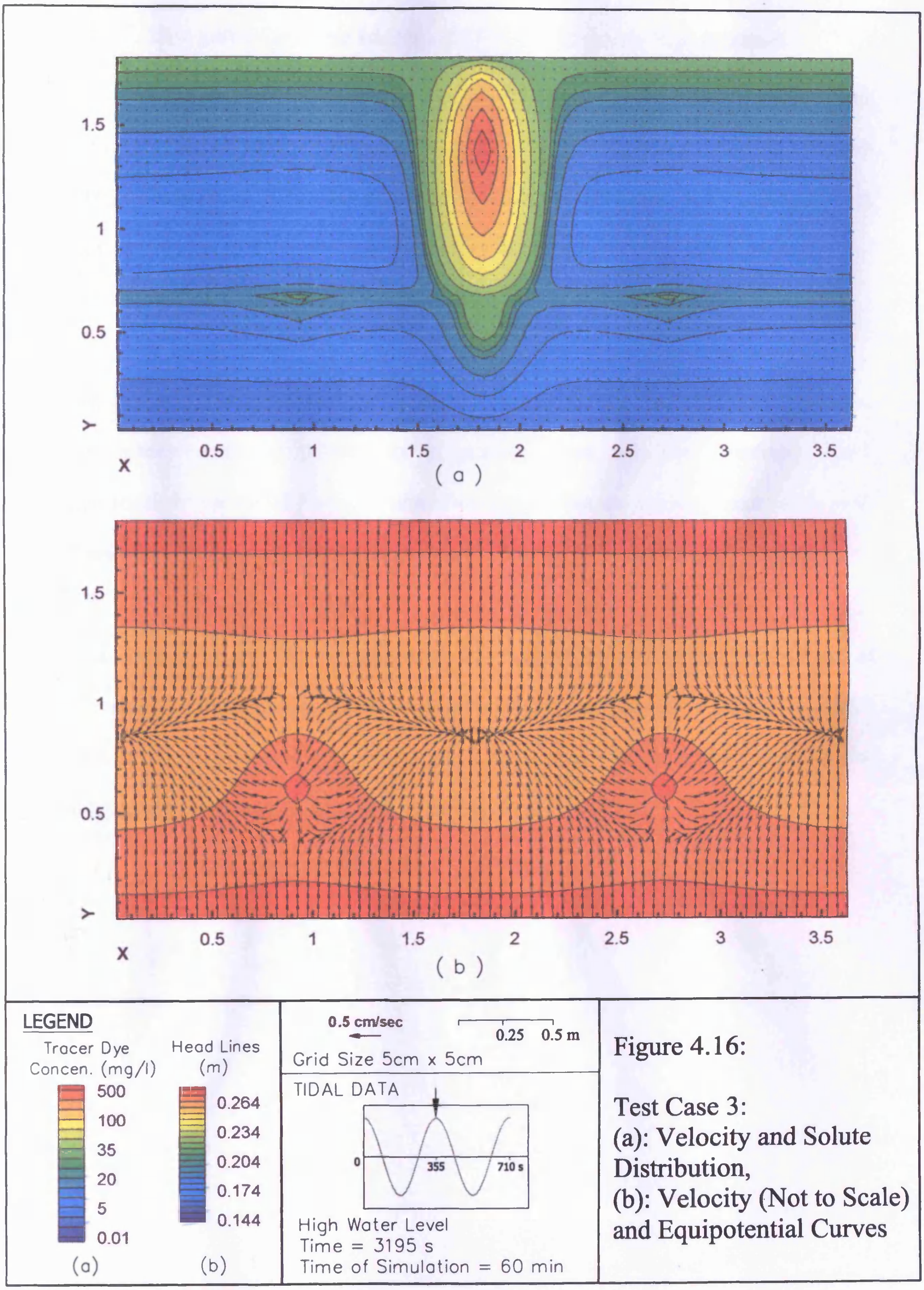

Figure 4.16:

Test Case 3:
(a): Velocity and Solute Distribution,
(b): Velocity (Not to Scale) and Equipotential Curves

4.3.4 Discussion for the Idealized Porous Medium Application

The numerical model was applied to an idealized porous medium domain. A constant water level and a sinusoidal tide were used as the two open boundary conditions. For two mirror positions along both sides of the computational domain two source/sinks of fluid were considered to evaluate the 2-D and sharp water level gradients, and the velocity and solute concentration distribution.

In the set up of this application, all modelling parameters such as physical dimensions, tracer release position, source/sinks co-ordinates and boundary conditions were symmetrical. It was found from the simulation results that the hydrodynamic parameters and the tracer contaminant distribution across the domain were symmetrical, as expected.

In conclusion, it can be said that the overall comparison between the graphical outputs of these three test cases proves the accuracy prediction of the new 2-D numerical model. However, as mentioned earlier, in Chapter 6 more investigation will be made in the validation of this model linked to the free surface DIVAST model.

4.4 Summary

In this chapter, the newly developed 2-D numerical model, GWK, was first applied to an idealized porous medium test case to demonstrate the capability of its predictions. To achieve this aim, three test cases were evaluated. The water elevation, equi-potential curves, and velocity fields for the idealized test case were simulated for three different cases, and their changes due to tidal action were examined. It was found that the numerical model was capable of the numerically simulating these scenarios in a stable manner. The distribution of a conservative dye tracer was also investigated for the idealized test cases and it was found that the numerical model was also capable of numerically simulating the solute concentration changes in a stable manner. The effects of a discharge and recharge, i.e. source/sinks of fluid mass, on the water table, velocity field and tracer contaminant levels were investigated and the model demonstrated that it was able to predict the effects of the presence of any source/sink on the configuration of these variables.

CHAPTER 5

PHYSICAL MODELLING OF WETLANDS AND ADJACENT COASTAL WATERS

5.1 Laboratory Study

5.1.1 Introduction

Basically, there are three approaches or methods that can be used to solve a problem in fluid mechanics including; experimental, theoretical and computational methods (Tannehill et al. 1997). Hughes (1995) also noted that coastal engineers rely on three complementary techniques to deal with the complex fluid flow regimes typical of many coastal projects. These techniques are field measurements and observations, laboratory measurements and observations, and mathematical or numerical calculations.

According to Hughes (1995), field studies provide the best data, but they are usually expensive and too many of nature's variables are present, making data interpolation difficult. In contrast, physical models are smaller, less expensive, easily studied, and simpler than nature, yet they may include the more important aspects of the problem. In addition, physical and numerical model input conditions can be controlled and systematically varied, whereas field studies have no such control. Regarding the advantages of physical models for nearshore processes, the same reference mentioned two advantages as follows:

(i): The physical model integrates the appropriate equations governing the processes without simplifying assumptions that have to be made for analytical or numerical models.

(ii): The small size of the model permits easier data collection throughout the regime at a reduced cost, whereas field data collection is much more expensive and difficult, and simultaneous field measurements are hard to achieve.

Also, Hughes (1995) added that a third advantage of physical models is the degree of experimental control that allows simulation of varied, or sometimes rare, environmental conditions at the convenience of the researcher, and a fourth advantage is the ability to get a visual feedback from the model. It is stated that, watching a physical model in operation often gives the experimentalist an immediate qualitative impression of the physical processes, which in turn can help to focus the study and reduce the planned testing (Hughes, 1995). Hughes also described a Physical Model as a physical system reproduced (usually at a reduced size) so that the major dominant forces acting on the system are represented in the model in correct proportion to the actual physical system. Falconer (1992) not only noted that physical models are generally used as an additional engineering design tools but he also added that:

> *In the case of physical model studies, the coastal region to be modelled is generally scaled down, both vertically and horizontally, and constructed and located within a large tidal basin. Tidal currents are generally measured by means of*

> *drogues or mini-current meters, and pollution surveys are regularly undertaken using dye tracer studies. One disadvantage with physical models in connection with pollution model surveys is a technical constraint in terms of scaling.*

Regarding physical modelling of solute transport in porous media, Harris et al. (2000) pointed out that physical modelling of contaminant transport problems offers major time-scaling advantages. Thus, pore fluid seepage at prototype scale over a period of years can be simulated in the model in a matter of hours. Esposito et al. (2000) described that predicting the transport of liquids containing hazardous chemical substances in the soil and groundwater has proven to be an extremely challenging exercise. They added that both mathematical and physical models have been developed to quantify such movements. However, Khalifa et al. (2000) emphasised that the observation of identical phenomena for a full-scale structure (i.e. the prototype) and the corresponding observations for small-scale models requires consideration of different conditions of similitude for the different physical units.

Physical models are broadly classified into what could be considered two "goal-related" categories. The first type are those physical models used to verify (or extend) numerical models. These models may not resemble anything in the real world because they are often idealized and simplified to minimize scale effects and provide a test case that more closely fits the assumptions inherent in the numerical model. Physical models of this type could be referred to as validation models. An example of a validation model would be an idealized, rectangular harbour constructed with perfectly reflecting vertical side walls. The second type of physical model has the goal of attempting to predict prototype behaviour by reproducing as far as possible all the features and forces of an actual prototype situation. This type of physical model is termed as a design model. Also, a third type of "goal-related" model is provided that is referred to as the process model. This is a physical model designed to study a physical process in detail, in order to develop a new understanding about the physics (for more detail see Hughes, 1995).

According to the last mentioned reference the future of physical modelling will be directed towards the process based models because they are unique research tools that will yield valuable insight into the details of very complex hydrodynamic processes. These models allow systematic investigation of both steady-state or transient flow phenomena, and they are the key for advancing numerical modelling capabilities. Also two key rules in the same reference are given to help guide us while evaluating physical model results: (i) if there is a discrepancy between a theory and the experiments undertaken, then it is likely that the inaccuracies are in the experiments, and (ii) it is far more difficult to set up accurate experimental facilities than it is to develop accurate theories. From these statements it can be seen that physical modelling provides a valuable tool for complementing fluid dynamics problems. Details of the physical model, experimental procedures and the equipment used in the current research study are presented in this chapter.

5.1.2 Objectives

The main aim of the current research study has been to develop and verify an integrated numerical model to simulate interactions between wetland areas and adjacent coastal waters through groundwater flow. Therefore, the purpose of undertaking the physical model was to obtain data that could be used: (i) to understand the interaction processes between free surface and groundwater bodies, and (ii) to calibrate and validate the newly developed 2-D numerical model, GWK, and also the linked model, DIVAST-GWK, as discussed in the previous chapters.

The constructed physical model has provided extensive experimental data of the seepage behaviour through sand embankments, by monitoring the tide levels on both sides of the embankment, velocity point measurements and also the behaviour of a dye tracer for constant water levels on one side of the embankment and a model on the other side of the sand ridge. Therefore, the main parameters that needed to be measured included: water levels, point velocity measurements and monitoring the behaviour of the dye tracer.

5.1.3 Scope

Initially, the purpose of this laboratory analysis was to construct an idealized physical model, similar to the characteristics of the west part of the Fleet Lagoon (Dorset, UK) and the adjacent coastal areas. Therefore, this part of the study was focused on creating a scale version of an *Idealized-Design Model* of wetland areas and the adjacent coastal waters for the purpose of reproducing a numerical simulation of this scale model.

5.2 Laboratory Setup

This section includes details of the laboratory physical model configuration, measurement devices, tidal specifications, sand embankment properties and the experimental setup. All experimental data were collected using the newly constructed facilities in the Hyder Hydraulics Laboratory at the Cardiff School of Engineering.

5.2.1 Tidal Basin

5.2.1.1 Initial Evaluations

A tidal basin of length 5.3m, width 4m and depth 0.40m was available and the physical model was designed to set up within the basin. Constant amplitude and period tides were produced in the tidal basin by a vertically oscillating weir, located just inside the tidal basin and opposite the physical model. The basin was fed by a water supply at a constant rate entering the basin through a perforated manifold. To minimise the lateral variation in the velocity and to reduce turbulence and artificial circulation in the model area, a 30mm thick honeycomb baffle was located near the weir (Figure 5.1a and b).

As mentioned in section 5.1.3, firstly an idealized model of wetland areas adjacent to neighbouring coastal waters was planned. Figure 5.1-a shows the general location and the plan of the initial model in the tidal basin, while Figure 5.1-b illustrates the longitudinal section of the basin. The sandy embankment and the enclosed idealised wetland cited behind the embankment can be seen in the plan and section. Also in the corner of the wetland area a sluice gate was included to control the water surface level in the wetland area and also for purposes of the creating a flushing discharge, (see Figure 5.1, details *a* and *b*). The model was not finally constructed as originally planned due to the reasons explained below. As the construction of the physical model progressed it became apparent

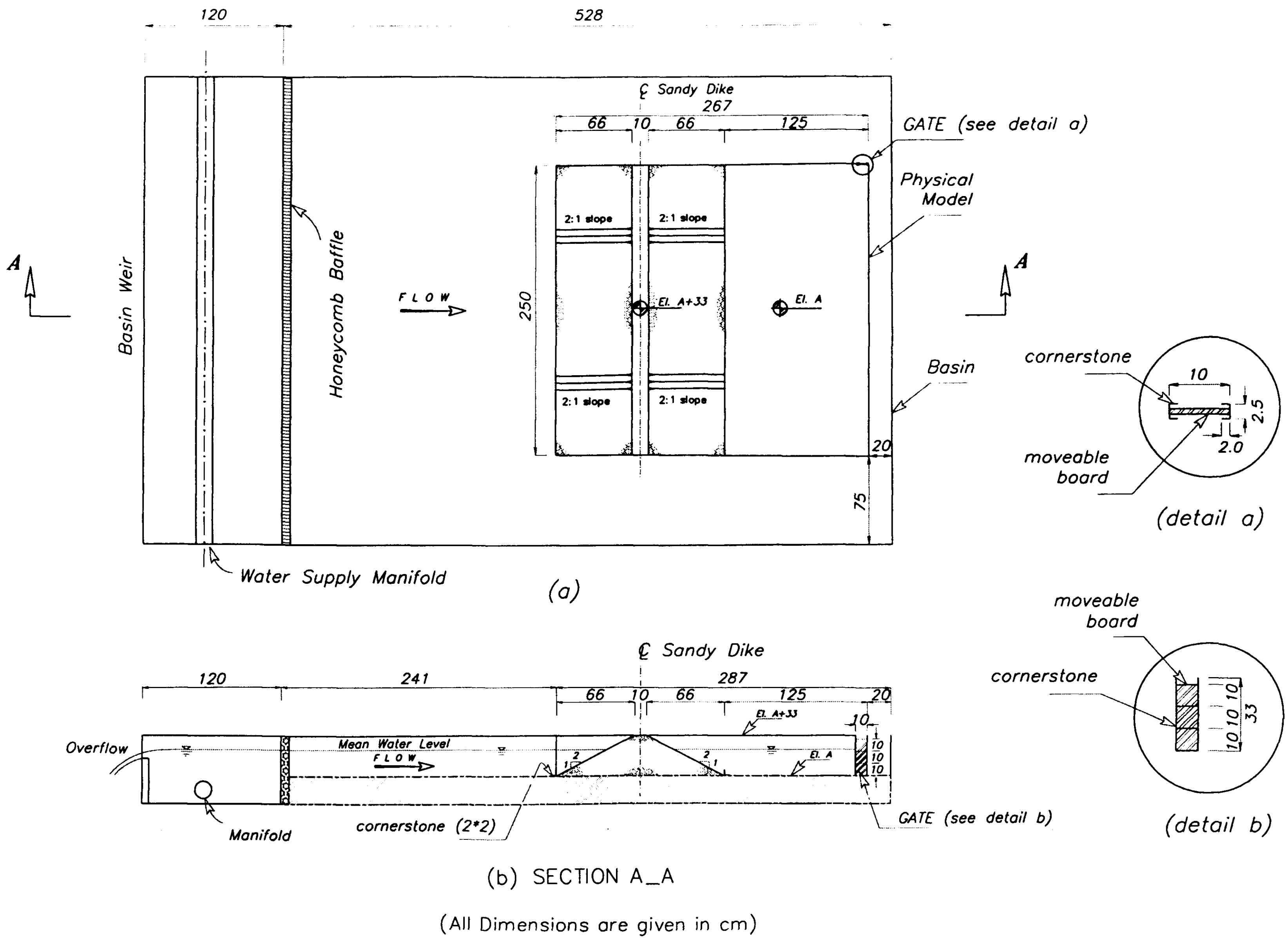

Figure 5.1: General plan and details of idealized physical model

that the tidal basin had to be refined, so some preliminary tests were performed for this purpose.

Figures 5.2 and 5.3 show two views of the initial tests. It should be noted that as this type of laboratory study is naturally very sensitive to any uncontrolled leaks, in order to test the isolation of the system initially the surrounding plywood walls of the physical model were built up to be completely closed. This was completed before arranging the sand embankment. As shown in Figure 5.3, at an early stage of the laboratory programme it became apparent that the existing tidal basin did not satisfy these appropriate conditions. Some simple tests were carried out under variable hydraulic loads to check for the stability and leakage of the basin floor. It was established that there were considerable uncontrolled leaks from different joints of the floor plates, and in addition the floor base structure was found to be too weak to bear the sand load. Moreover, as the analysis of this model was not

Figure 5.2: Surrounding walls of initial model and tidal basin testing

Figure 5.3: Overall condition of existing tidal basin with uncontrolled leaks

based on any particular case study it did not have any clear dynamic and geometric similarities. In order to remove the difficulties mentioned above regarding the physical model and the tidal basin the following refinements were undertaken.

5.2.1.2 Tidal Basin Refinements and Specification

The tidal basin had two main problems:

(i) the floor base structure was too weak to support the extra sand loading, and

(ii) uncontrolled leaks occurred through the deformed floor plates.

Therefore, it was necessary to increase the foundation beams and change the floor plates.

The strengthening process of the foundation is illustrated in Figure 5.4. As shown in the figure, the old floor cover was removed and new grid support floor foundation beams were installed. This was done to ensure structural rigidity under both sand loading and water pressure when the tidal basin was in operation. Also, these changes were included to maintain the rigidity of the basin floor and thereby reduce the uplift stresses experienced on the floor when the initial tests on the basin were operational. Figure 5.5 below shows a view of the finished grid beam.

Figure 5.6 shows the new floor covered by with PVC (Polyvinyl chloride) plates. The new floor was covered by ten 2m by 1m plates, with all of the PVC plates being 12mm thick, and the joints being waterproofed with PVC solvent cement. The mobile access platform

Figure 5.4: Strengthening of basin foundation

Figure 5.5: New basin floor base structure

Figure 5.6: New basin floor

provided suitable access for different experimental purposes, see Figure 5.6, and the instrumentation beam provided the required base for installation of the ADV or/and the wave monitor, see Figure 5.3.

5.2.2 Physical Model Specifications and Construction

Following the previous calculations and design regarding the physical model characteristics, and according to the initial experimental results which were undertaken to evaluate the hydrodynamic behaviour of the basin, it was decided to improve the physical model design and dimensions. To achieve this aim, however, the scope of this laboratory analysis was not to recreate a particular case study to scale, but as mentioned above in order to improve the hydrodynamic and geometric similarities of the model. The west part of Fleet lagoon and the adjacent coastal waters (Dorset, UK) were chosen as a typical prototype. Figure 5.7 shows the general location and Figure 5.8 illustrates the general map of the prototype.

5.2.2.1 Prototype Properties

The Fleet is a shallow coastal lagoon trapped behind ‘Chesil Beach’ north west of Portland Bill on the south coast of England. The lagoon is influenced by tidal currents in neighbouring the coastal waters, which are linked by a groundwater passage through the 120m wide and approximately 12.5km long sandy ‘Chesil Beach’ ridge (see Robinson et al., 1983). A general view of the prototype is shown in Figure 5.9.

The Fleet in Dorset is one of the largest and best studied lagoons in the UK and has been identified as an SAC (Special Areas of Conservation) for this feature. It is considered to be one of the finest examples of its physio-graphic type in the UK, and one of the most important in Europe. The Fleet is of considerable importance for its biological communities and presence of a number of specialist lagoonal invertebrate species. It is also of conservation importance for its wildfowl, in particular for the number of wintering wildfowl, with a number of species of terrestrial importance being found along Chesil beach, which forms a barrier between the lagoon and the sea. The basin is of additional interest due to the presence of the Abbotsbury swannery in the western Fleet – the only colonial breeding site for mute swans in the UK; for more details see Johnston and Gilliland (2000).

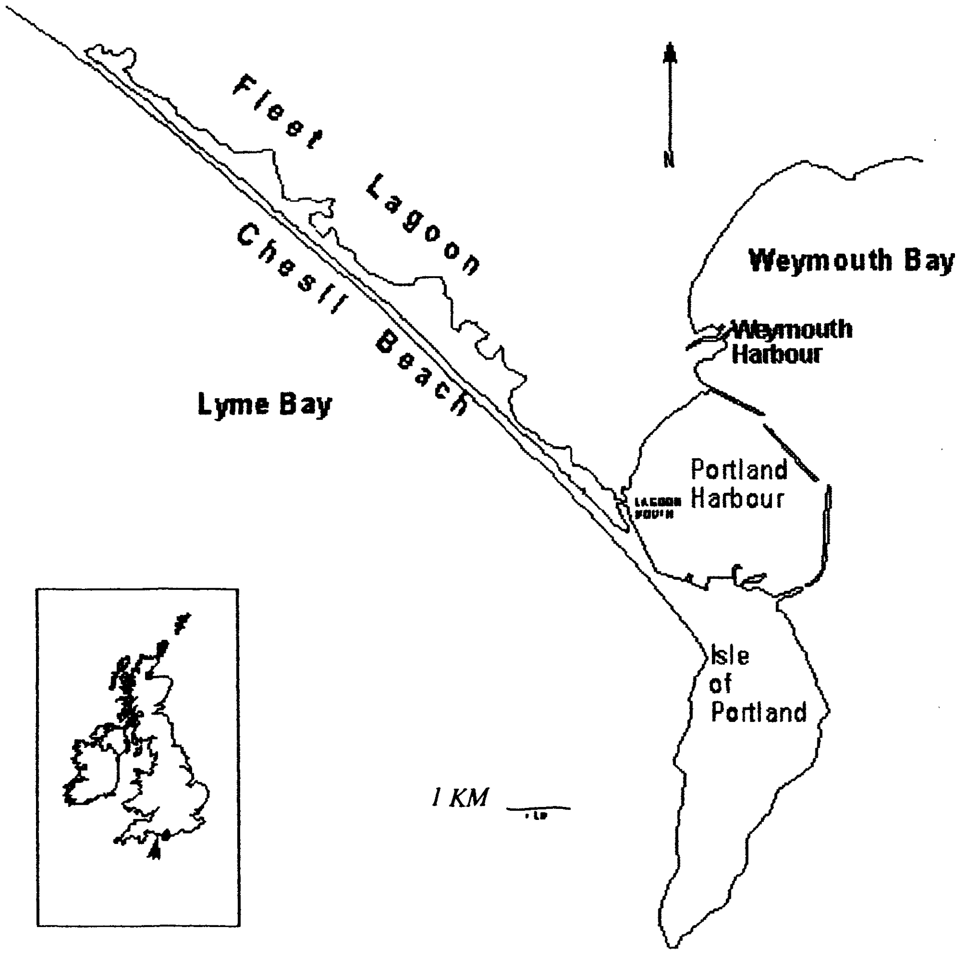

Figure 5.7: General location of the prototype (UK Marine, 2003)

Figure 5.8: General map of the prototype (UK Marine, 2003)

Figure 5.9: General view of the prototype (UK Marine, 2003)

Generally speaking, Fleet Lagoon consists of two separate parts, namely East and West Fleet (see Figure 5.8). There is no opening to West Bay through the beach, but the Fleet is connected to the English Channel at its south eastern end through Portland Harbour. It is therefore tidal and saline. A few streams drain into the lagoon from a small catchment area of about 50 km^2, although seepage through the ground into the Fleet may drain from a wider area.

It is also very shallow, varying in depth from 3 to 5m in the first 2km between the tidal entrance at Smallmouth and The Narrows. Here the lagoon is marine in character, with a strong tidal exchange to the sea. It then widens out to 2.5km in the area known as Littlesea, where the depth is between 0 and 1.2m below chart datum, intersected by a narrow channel of up to 4m deep. The tide is strongly attenuated in this region and penetrates only weakly into the remaining 8km of the lagoon, known as West Fleet which has a depth of between 0 and 1.2m (Robinson, 1983).

West Fleet has demonstrated a significant lack of flushing and circulation characteristics as compared with those observed from the East Fleet. Large areas of stagnant zones of water, particularly at the Abbotsbury end of the Fleet, lead to the West Fleet acting principally as a dead zone, with little exchange with East Fleet and seawards (Westwater et al. 1999).

5.2.2.2 Physical Model Specifications

As mentioned previously, the hydrodynamic and geometric simulation of the physical model was based on the characteristics of West Fleet lagoon and the adjacent coastal area. However, according to the final results it was decided to have an *Idealised-design* model, which is described here. In the geometric similarity, both undistorted and distorted scale models were considered. The distorted model was used to compute the physical model dimensions, because undistorted models generated unacceptable results, especially due to the complex shape of the prototype. The In other words, in order to obtain reasonable practical results it was necessary to choose different scales in the vertical and horizontal directions. Therefore in order to select the final characteristics of the physical model, not only were the calculated results used, but the practical criteria and initial experimental results were also considered.

In dimension scaling the physical model was developed upon the basis of dynamic similarity through the Froude law, in order to maintain similar gravitational characteristics to those found in the prototype. From studies undertaken by Westwater et al. (1999), Johnston and Gilliland (2000) and Kennedy (2001) on the Fleet Lagoon, typical values for the prototype characteristics were chosen and were used in the calculations.

According to the above mentioned references, the length of the West Fleet is about 7,000m and the average width of the Chesil beach is 150m. Also, the average velocity of the tidal currents in the prototype is 0.6m/s and also, according to the initial experiments the same velocity for the tidal basin was found to be 0.014m/s, using those values in a manner of undistorted modelling, yield a length of 3.80m for the model. As. the angle steel bracket supports, which were used in construction of surrounding walls, needed 0.20m of space at any side of the model. Therefore, the model's length was reduced to 3.60m and the scale modelling found to be 1/1900 and, also the top width of the embankment was calculated to be 0.08cm. The results for the average depth of water, vertical scaling, was unacceptable and therefore the distorted approach as follow was considered.

The construction results according to the distorted manner for the physical model simulations are illustrated in Figure 5.10. As shown in Figure 5.10-a, the physical model had a length of 3.07m, a width of 3.60m and a depth of 0.33m, and was sited in the tidal basin of total length 6.48m, width 4.00m and total depth 0.40m. Figure 5.10-b illustrates a longitudinal section of the model. An embankment of length 3.60m, top-width 0.08m, bed-width 1.40m, total height 0.33m, including 0.06m free board, and side slopes of 1:2 (vertical : horizontal), separated the model wetland from the idealised coastal waters. The wetland dimensions were 0.54m bed-width and 1.20m top-width. As mentioned previously, a sluice gate was located in the corner of the model, to control the constant water level behind the model embankment and also generally for the purpose of flushing (see Figure 5.10, details *a* and *b*).

As a part of the experiments, it was planned to study the behaviour of a conservative dye tracer for constant water levels on one side of the embankment and with a tide operating on the other side of the sand ridge. In order to create this condition, a sluice gate and a horizontal slotted pipe were installed behind the sand, see Figure 5.11a. This is described briefly below. However, the procedure of the dye tracer experiments will be explained in much greater detail later in this chapter and a comparison of the experimental results and the numerical outputs will be discussed in chapter 6.

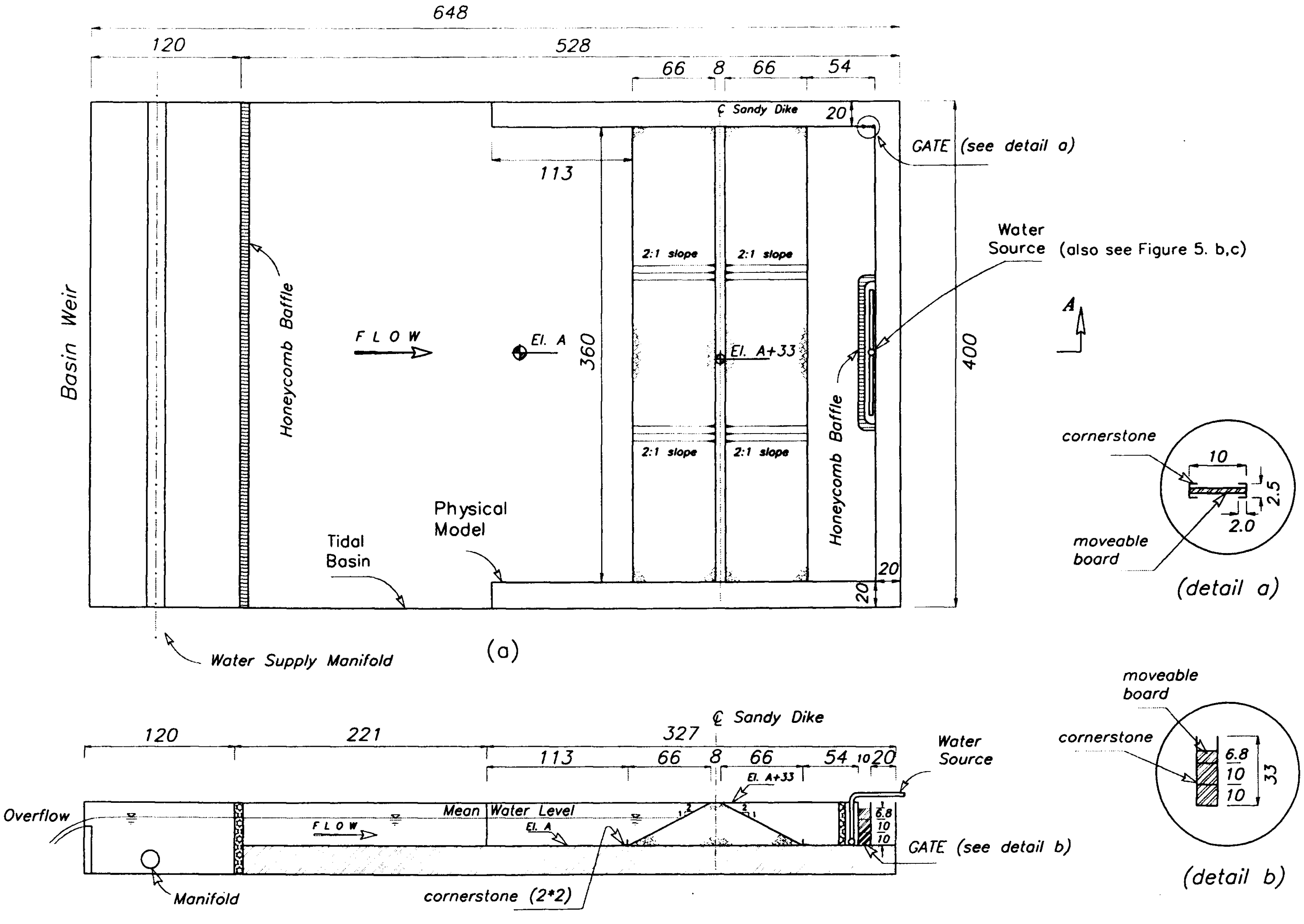

(b) SECTION A_A

(All Dimensions are given in cm)

Figure 5.10: Physical model construction details

The sluice gate consisted of three pieces with a total height of 300mm and width 100mm. However, this height was then changed to 268mm in order for the water level to remain at a high water level of 27cm. A simple water source was installed on the far side of the model behind the sand embankment. In order to control any circulation of water behind the sand, the slotted pipe was covered by a layer of porous abrasive matting. This acted to diffuse the jet created by the water exiting the slotted inlet tube (Figure 5.11b and c). Tube slots were oriented to the back wall of the model and a 30mm thick honeycomb baffle was inserted in front of the pipe to reduce turbulence in the area between the pipe and the sand embankment (Figure 5.11a). The water flow was operated manually through the use of an uncalibrated valve, and was adjusted by trial and error for the experiments.

The combination of the source-sink and overflow-gate kept the water level constant during times of seepage and extra water respectively. However, a fluctuation of about 4mm on the water levels was experienced in the area.

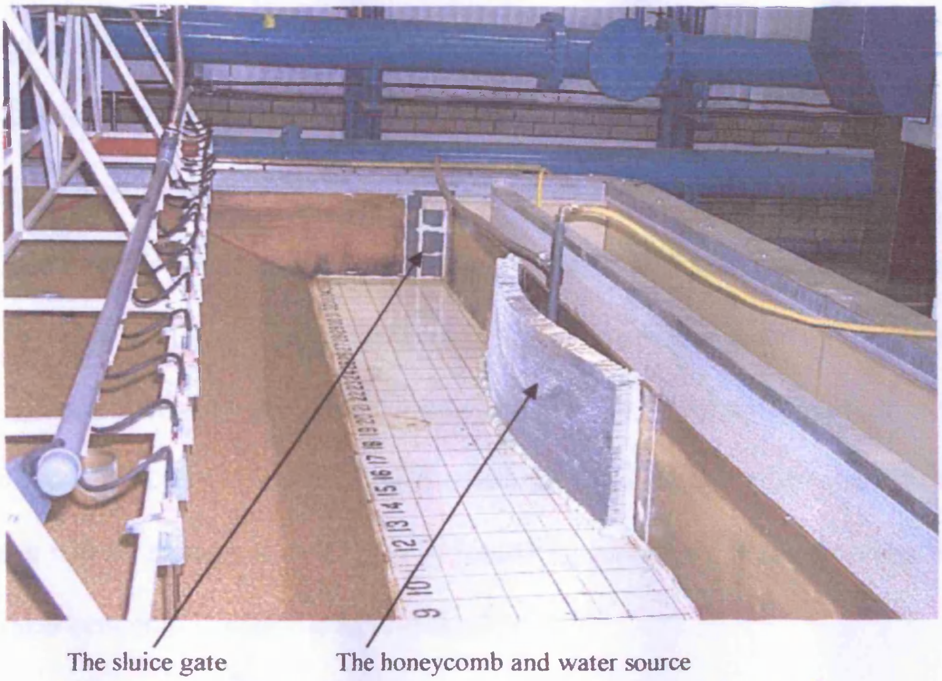

Figure 5.11(a): Sluice gate and water source behind the sand

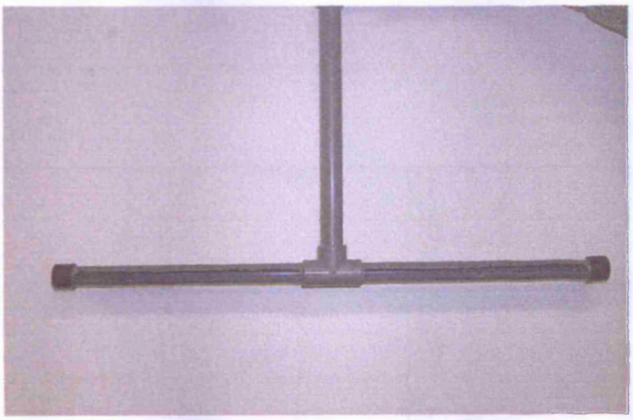

Figure 5.11 (b): Slotted pipe before coverage

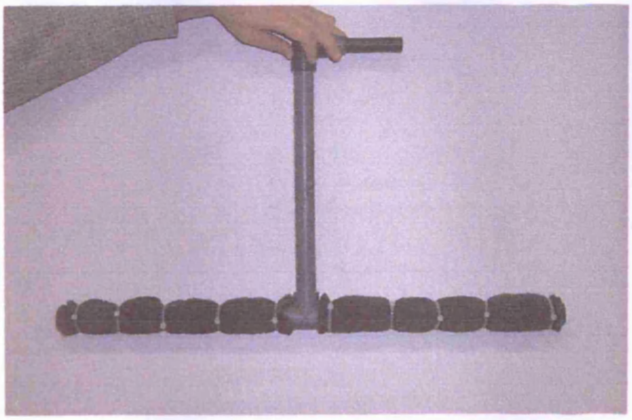

Figure 5.11 (c): Coverage of the slotted pipe

Five observation wells of 0.05m radius were also considered within the sand embankment to provide unpredicted observations within the sand along a cross section. Construction details of the observation wells are shown in Figure 5.12 below and a general view is given in Figure 5.15. It should be noted that, although the observation holes were used for some rough controls during the initial experiments, there were no specific measurements involved in the current research, because it was not planned in the current study to record and concentration data. However, the holes could be used for other purposes in further studies, which will be discussed in chapter 7, regarding recommendation on measurement of the dye tracer concentration in the sand embankment.

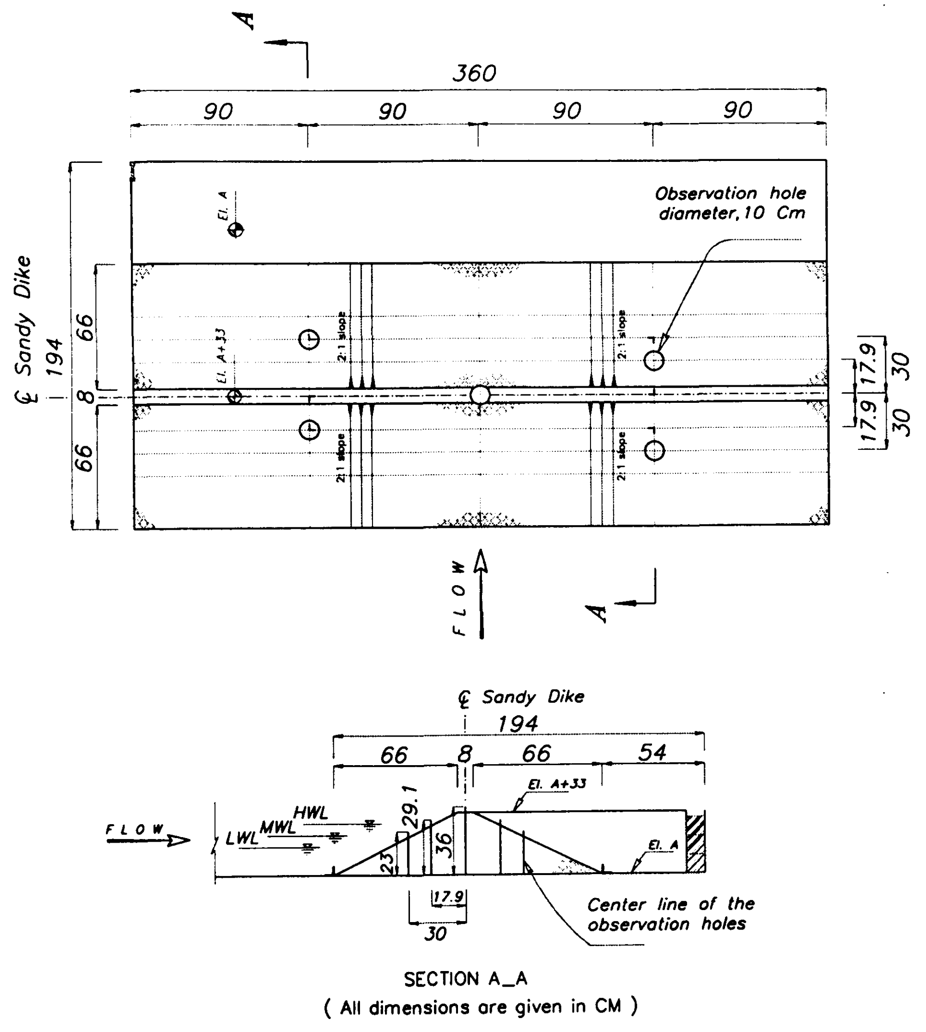

Figure 5.12: Construction details of observation wells

5.2.2.2.1 Sand Embankment Materials

In this study non-cohesive sands were used to create the embankment in the laboratory model. The average grain diameter of the sand was *1* mm. As described earlier in chapter two, section 2.3.2.1.3, it was important to control the validation limits of Darcy's law within the sand embankment. According to Bear (1972) in practically all cases Darcy's law is valid as long as the Reynolds number, based on the average grain diameter, does not exceed a value of between about *1* and *10*. Calculations showed that for the sand used in this study the Reynolds number was about *7*. A series of experiments, according to the British Standard Methods- No.BS 1377: Part 5: 1990, was carried out in the Soil Mechanics Laboratory at Cardiff University to determine the permeability and the specific yield of the sand (Figure 5.13). The results showed that the average value for the sand permeability was 0.995e-3 m/s and also the average value of the specific yield was 29%.

Figure 5.13: Hydraulic conductivity measurement, K_S, constant head method

The bathymetry of the sand embankment was established using the AutoCAD package and according to the construction details of the model, in order to complete the specification of the physical model. It is worth noting that the bathymetry of any application in both the *x* and *y* directions were needed as a part of the free surface numerical model input data, i.e. DIVAST model input data file.

5.2.2.3 Physical Model Construction

The physical model was constructed in the tidal basin. The overall working area of the physical model was about 3m by 4m. The surrounding walls were constructed of plywood and consisted of three vertical sides with angle steel bracket supports, see Figure 5.14. Figure 5.15 shows the installed observation wells before the arrangement of the sand embankment and the grid pattern. It should be noted that the grid pattern (Figure 5.15) was

Figure 5.14: Physical model surrounding walls

Figure 5.15: Physical model observation wells

considered to have an essential scale for recording the dye tracer. The arrangement of the sand embankment is shown in Figure 5.16 and the finished physical model can be seen in Figure 5.17.

Figure 5.16: Physical model, sand arrangement

Figure 5.17: Physical model, finishing

5.2.3 Tidal Specification

A repetitive sinusoidal tide was generated by computer to study the seepage behaviour and solute transport phenomenon in the physical model. For this study the tidal period was taken to be 355 seconds. The mean water level was set at 210mm, with the tidal range being 120mm. All tests were started at high tide, so that the initial depth of water on both sides of the model embankment was 270mm.

5.2.4 Experimental Devices

The main parameters which were investigated in the physical model included: time series water levels of the surface flow domain, point velocity measurements and dye tracers. The Experimental devices used to study the above mentioned parameters are explained below.

5.2.4.1 Tidal Fluctuation Monitoring

The tidal fluctuation data on both sides of the physical model embankment were recorded using a wave probe monitor. The instrument is a simple device for the measurement and recording of water waves in hydraulic models. It works on the principle of measuring the current flowing past a probe, which consists of a pair of parallel stainless steel wires. The probe is energised with a high frequency square wave voltage to avoid polarisation effects at the wire surfaces. The wires dip into the water and the current that flows between them is proportional to the depth of immersion. The current is sensed by an electronic circuit providing an output voltage proportional to the instantaneous depth of immersion, i.e. the output circuitry is suitable for driving both a chart recorder and a data logger. The standard form of probe supplied consists of a pair of stainless steel wires, 1.5mm in diameter and spaced 12.5mm apart, see Figure 5.18 below. However, the flexibility of the drive and sensing circuits enables a very wide variety of probe configurations to be deployed.

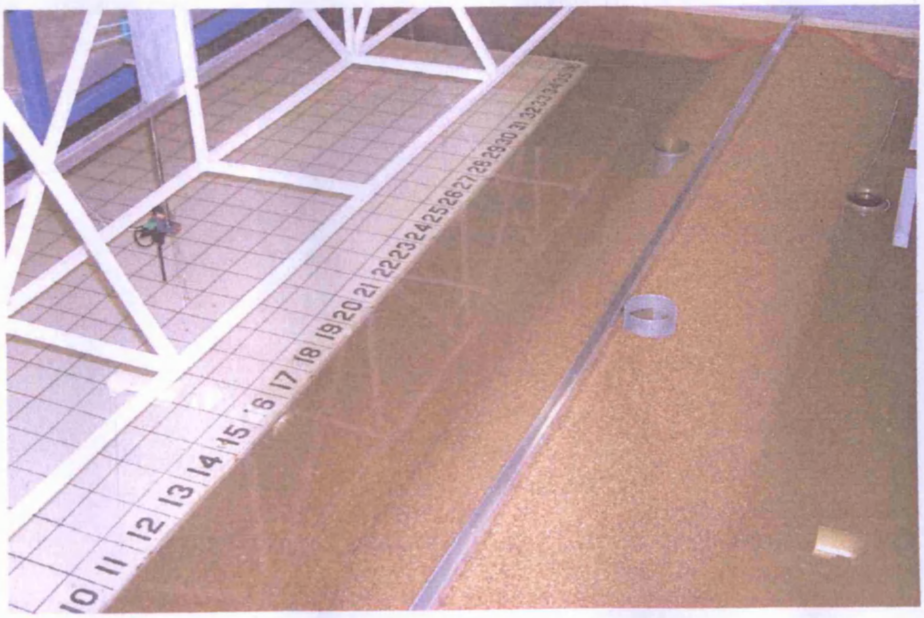

Figure 5.18: Tide monitoring in the physical model

The output voltage was calibrated in terms of wave height by varying the depth of immersion of the probe in still water by a measured amount, and level noting the change in the output signal. A special probe support member with accurately spaced positioning holes was available to facilitate this operation. The calibration stem of the probe had a series of accurately spaced holes that could be used to measure the amount that the probe was raised or lowered. The spacing of the holes was either: 10, 20 or 30mm depending upon the length of probe used. When calibration was complete, the probe was returned to the original datum position. If the electrical conductivity of the water change for any reason (e.g. through changes in temperature) then there was a resultant change in the instrument calibration. This could be re-adjusted by simply checking the setting of the zero point by allowing the water to settle and verifying that the probe's depth of immersion was the same when it was calibrated. If the indicating meter was slightly off zero then the zero can be restored by trimming the *datum adjust* control, with no other adjustments being necessary (Wave Probe Monitor Manual and Operation instructions - Issue 5). The calibration of the probe as used in this study, is shown in Figure 5.19.

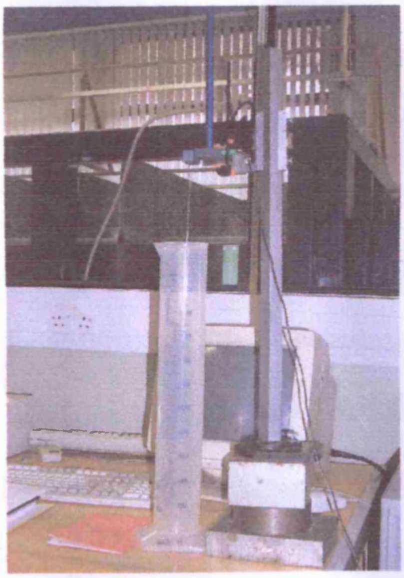

Figure 5.19: Calibration of wave probe monitor

5.2.4.2 Velocity Measurement

The velocity data were acquired using a Nortek Acoustic Doppler Velocimeter (ADV). This type of current meter uses an acoustic pulse, emitted from a central emitter, and then through a configuration of three acoustic sensors collects the reflected doppler shift in the reflected acoustic pulse from a particle within the flow. From these meters the data were transmitted via a conditioning module to the PC, where the data were interpreted to give an instantaneous velocity at a specific point in the flow, specified in Cartesian co-ordinates.

The output from the ADV was via a DOS based platform on a PC, which enabled the user to specify the sampling range, temperature, salinity and other variables for each set of data recorded. The software was automatically adjusted for reflection from any adjacent solid boundaries through the boundary adjustment menu, which could also be used to aid the user in positioning the equipment.

Each ADV enabled readings to be taken at a rate of 25Hz and then the processed data were specified by the user, through the software as values within the range of 0.1 to 25Hz. For the purpose of the experimental data collected in this study, a rate of 1Hz was specified to give data every second. The ADV software also enabled the user to adjust the velocity range to the minimum value expected during sampling and through a Graphical User Interface (GUI) determination of the accuracy of the readings could be made based on the two parameters, namely: Signal to Noise Ration (SNR) and Correlation (Corr). These parameters gave an indication of the scattering of the acoustic signal being received, with a high SNR being favourable, since this ensured that noise due to acoustic damping and deflecting was a minimum. This ensured that the readings taken were as accurate as possible throughout the recording time. The GUI also allowed the user to 'tag' specific data sets, thereby enabling the operator to eliminate incorrect data resulting from a change in position of the ADV, or a lack of coherent data collection due to poor sampling sets when the SNR/Corr values were unacceptable.

Due to the sensitivity of the ADV equipment, which had a manufacturer-specified accuracy of ± 1%, it was important to follow the 'ADV-Check' procedure, which involved using another menu of the software. By following this procedure the user was able to note any disfunction of the apparatus, and consequently make any necessary adjustments to ensure accuracy was maintained in the readings being taken throughout the sampling period. For more details of the ADV equipment, see ADV software Manual version 2.6 (1997) and ADV manual (1997).

Figure 5.20: ADV down-looking probe during operation

5.2.4.3 Dye Tracer Monitoring

As a part of the numerical modelling undertaken, the solute transport module of the DIVAST model was linked to the corresponding module of the GWK model, as described in chapter 3. In investigating the accuracy of this part of the numerical predictions, a comparison between the predictions and a conservative dye tracer was made, with the latter replicating studies in the physical model. The experimental work is described below.

Imaging technologies can be considered as a universal tool for visualizing, digitizing and analyzing phenomena in experimental research (Allersma and Esposito, 2000). In this study the transport processes of a dye tracer were filmed using a digital camcorder, which was equipped with a wide angle lens. The camera was positioned on the ceiling, right over the physical model (Figure 5.21) to provide optical measurements of the tracer migration through the physical model. The use of image processing allowed non-disturbing measurements of the tracer plume migration. A grid pattern was painted over the physical

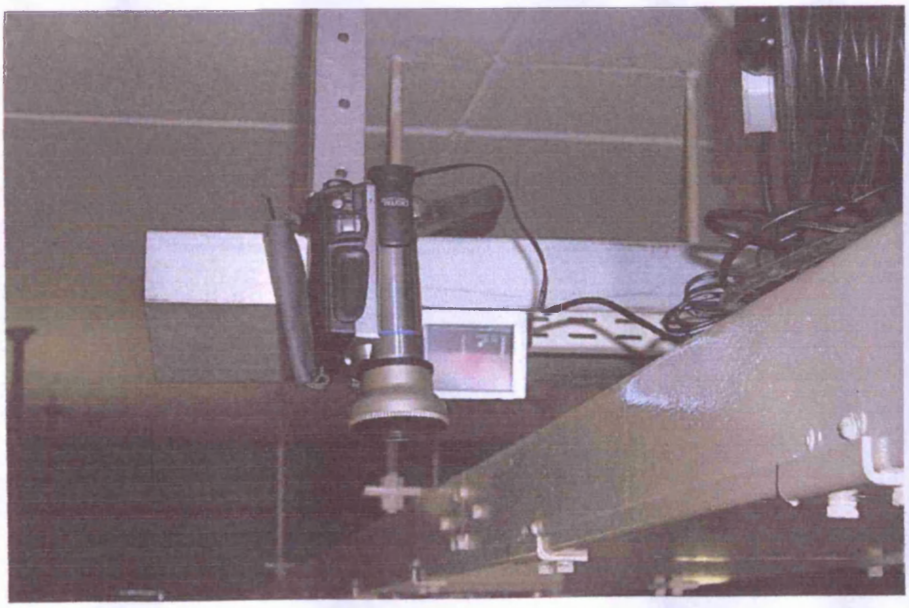

Figure 5.21: Installed camcorder and wide angle lens

model floor to prepare the essential scale for the above mentioned comparison (see Figure 5.17). Figure 5.22 shows the construction details of the tracer device. The apparatus comprised a wide low-depth reservoir, connective flexible tubes and eighteen nozzles. Each nozzle had an independent valve and they were drilled into the main line at 0.20m intervals. A general view of the tracer release device is shown in Figure 5.23. The apparatus was fixed on the instrumentation beam, which could be moved along the model.

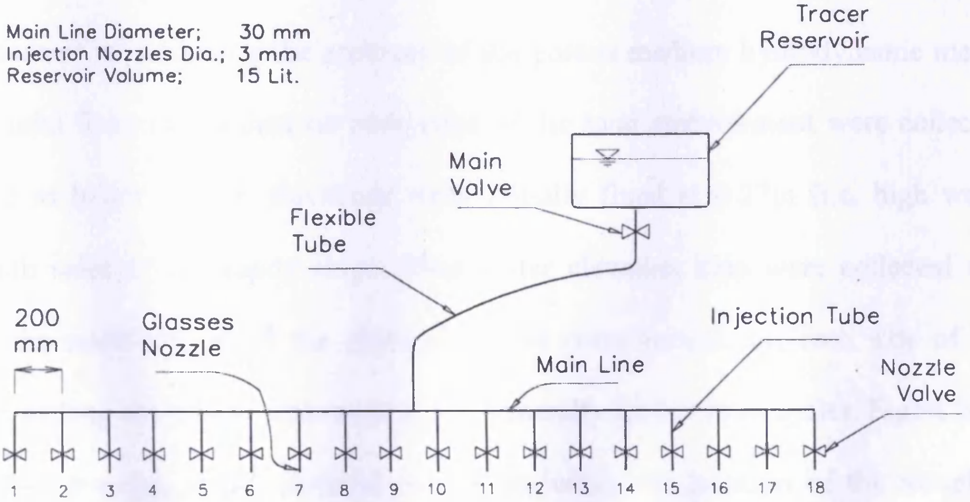

Figure 5.22: Construction details of tracer release device

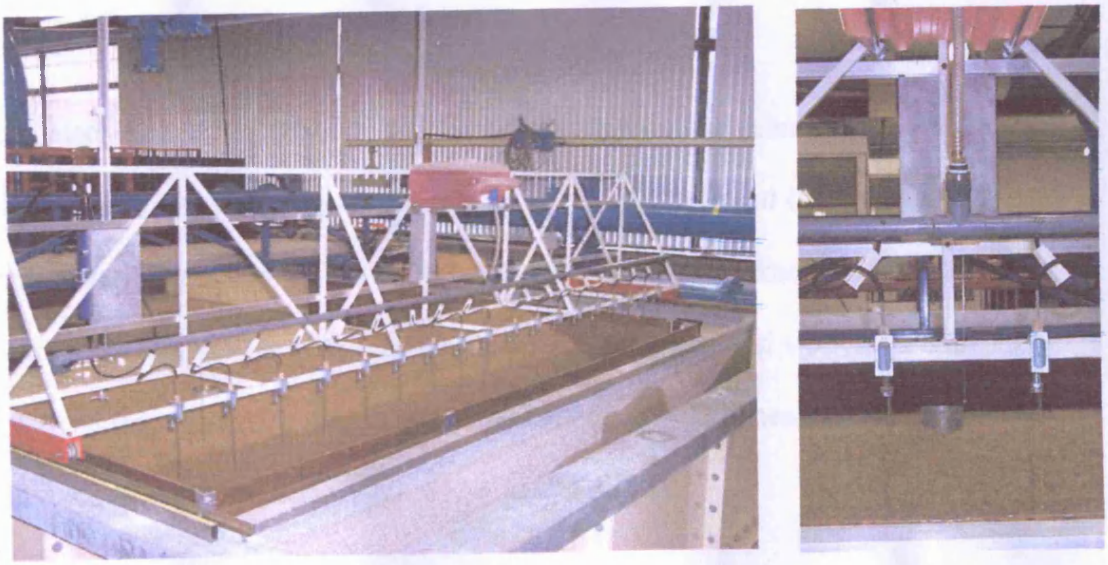

Figure 5.23: General view of dye tracer device and nozzles

5.3 Experimental Procedure

As previously mentioned, in section 5.1.2, one of the main purposes of undertaking the physical model study was to obtain data which for calibration and validation of the integrated model. To achieve this aim an experimental programme was planned and carried out using the laboratory model to study both hydrodynamic and solute transport processes.

For the purpose of investigating the accuracy of the porous medium hydrodynamic model predictions, tidal fluctuations data on both sides of the sand embankment were collected and recorded as below. Water elevations were initially fixed at 0.27m (i.e. high water level) on both sides of the sandy ridge. Then water elevation data were collected and recorded at the middle point of the physical model cross-section on, each side of the embankment as long as the tide was running, i.e. generally for ten tidal cycles. Figure 5.24 shows a scaled drawing of the physical model, including the location of the sampling points. The water elevation data were collected and recorded at the locations *a* and *b* in Figure 5.24.

The figure also shows the locations of the velocity measuring points. The velocity data were collected at 0.40m intervals, starting at an initial point located 0.15m from each side of the longitudinal centre-line of the model and ending at 0.45m from the physical model walls, L1 to L4 on the left-hand side and R1 to R4 on the right-hand side (see Figure 5.24). These positions therefore corresponded to the positions at which these flow characteristics were obstructed from the numerical integrated model output.

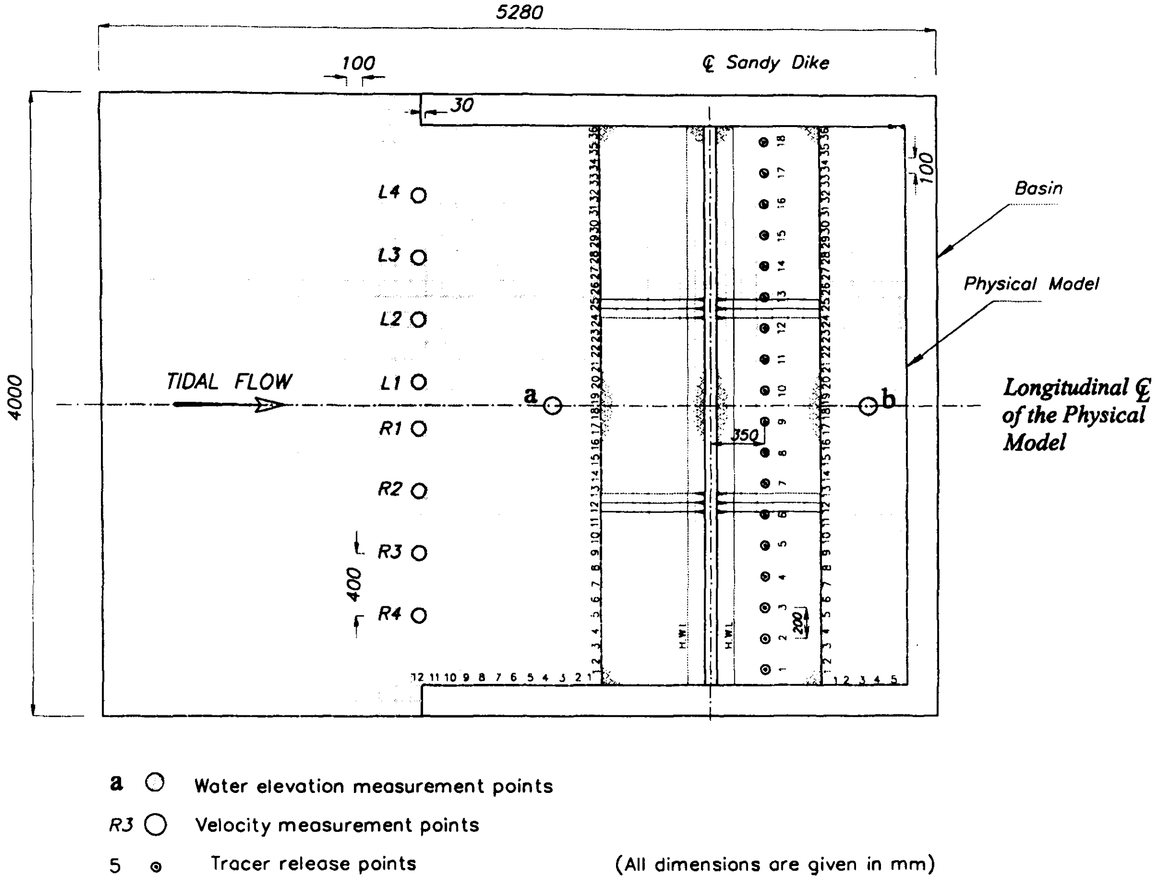

Figure 5.24: Location of measuring points in the physical model

Velocity data were collected and recorded over three tidal periods at each position. To collect data from all points, the probe was moved from each point laterally to the next location using the access platform and the instrumentation beam. The probe was the downward orientation type, and was positioned such that the x-axis was in the direction of flow, Figure 5.20. Data were collected at elevations of 128mm relative to the datum level, i.e. mean water level, Figure 5.25. Based on integrating a logarithmic velocity profile it can be shown that the mean velocity occurs at an elevation of approximately 0.6 of the depth below the free surface (see Chow, 1959). Data processing is explained later in this chapter.

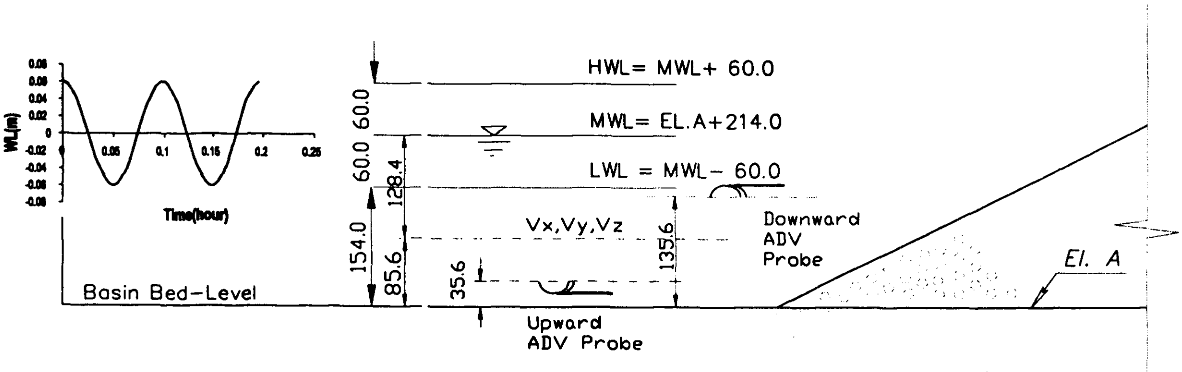

Measurement depth=%60 MWL (from w.s.)

(All dimensions are given in mm)

Figure 5.25: Velocity depth measurement

In order to prepare suitable data regarding the solute transport phenomenon for investigating the validation of the integrated numerical model predictions, the phenomenon was studied through the physical model using a dye tracer, as described earlier. A solute of potassium permanganate, 5g/l concentrations, was used for this purpose. The processes were filmed from the start of each test using the digital camcorder which was installed on the ceiling just over the basin. Dye tracer release experiments were carried out in two different ways. The release apparatus was calibrated before each experiment and the following procedures then adapted:

(i) the tracer was released behind the sand, at the central point of the model cross-section, and at a single point as shown in Figure 5.26, while the water levels on both sides of the embankment were at high water level. The discharge of the nozzle was 1.26E-3 l/min (also see Figure 5.24).

(ii) as can be seen in Figure 5.24 and 5.27 the dye tracer was released behind the sand as mentioned above, but in a line, Figure 5.24 points *1* to *18*.

In both cases the discharges through the nozzles were calibrated using the nozzle valves.

Figure 5.26: Release of dye tracer at a point

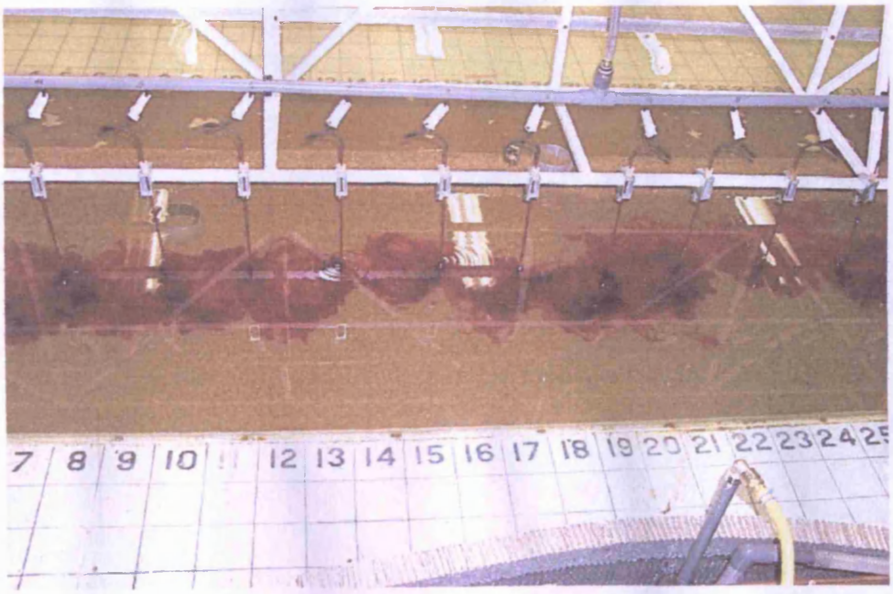

Figure 5.27: Release of dye tracer along a line

Figure 5.28 below illustrates a general view of the one point test after about 30 minutes and Figure 5.29 shows a sample of the tracer plume migration.

Figure 5.28: Overall condition of dye tracer experiment after 30 min., single point test

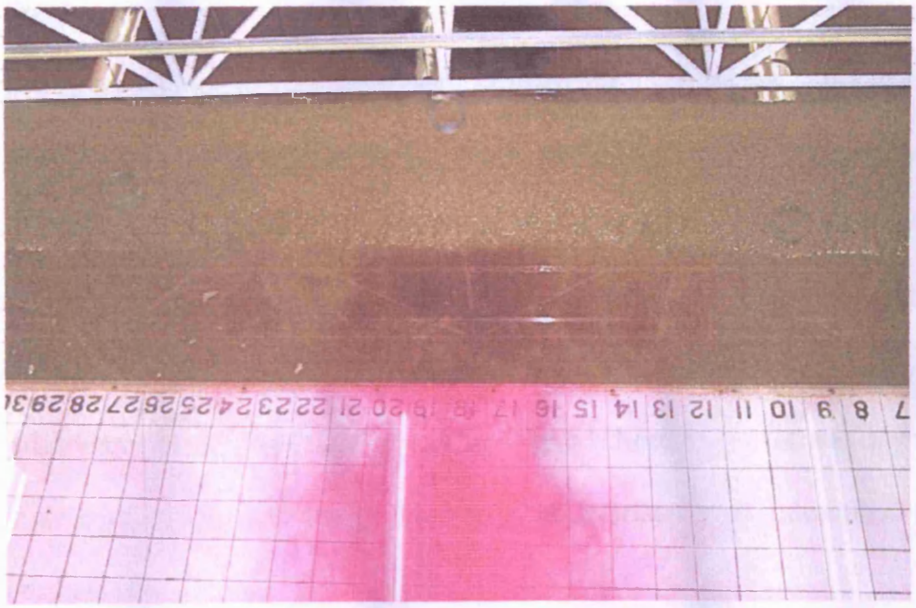

Figure 5.29: Tracer plume migration over different tides

It should be noted that the sand embankment and physical model were flushed after each experiment. For this purpose fresh water was used.

5.3.1 Data Processing

As previously mentioned the tide levels and velocity data were collected and recorded involving a wave probe monitor and an ADV probe and their associated software, respectively. Also, solute transport phenomenon was studied using the dye tracer. The process were filmed and compared with the numerical model predictions as described above. The data processing is now explained briefly.

The time series of water level data were plotted using a spreadsheet to calibrate the hydrodynamic numerical porous medium module. To achieve this aim the recorded data on both sides of the physical model, with the same numerically predicted data, were plotted on the same graph, and will be discussed in more detail in the next chapter.

The velocity data were collected and recorded through the tidal cycles and subsequently the data were time averaged over each 10 second intervals to give an average value of the x-component velocity at each location. However, the raw ADV data and the integrated numerical model output first had to be post-processed, involving two algorithms which were developed for this purpose. The resulting time averaged velocities of the physical and numerical model were then plotted together using a spreadsheet. This plot was then used to calibrate the numerical integrated model, with these comparisons being described in more detail in the next chapter.

The video films of the tracer, which were recorded over the physical model, were transferred to the computer and a set of suitable shots was obtained of them using the Studio DV version 8 package. These shots were subsequently matched and compared with the same time-step prediction plots for the integrated numerical model and the results were used to calibrate and validate the integrated model. These comparisons will be discussed in more detail in chapter 6.

5.4 Summary

In this chapter the main purpose of undertaking the laboratory study was first outlined and subsequently the laboratory set-up and refinement of the tidal basin were described. Then the prototype properties and the physical model specifications were discussed. The construction of the model and material specifications were also outlined, together with details of the experimental apparatus used. The sand embankment characteristics and also the tidal specifications have also been specified. Finally, the methodology for the collection of data and its post processing have been discussed in some detail.

CHAPTER 6

APPLICATION OF LINKED NUMERICAL MODEL TO PHYSICAL MODEL TESTS

6.1 Introduction

In this chapter application of the linked numerical model to a physical model study is given. The numerical model was first set up to simulate the hydrodynamic and solute transport fields for the physical model set up to assess the computational capability of the linked numerical model. Comparisons have been made between the computational predictions, using the linked numerical model, and the laboratory measured results. In these comparisons, different water levels and dye tracer boundary and initial conditions have been used to investigate the validity of the models. Tidal level and velocity measurements were made at various sections corresponding to the same positions where data would be output in the linked model, and thereby enabling a direct comparisons to be made between the numerically predicted and laboratory measured data.

The laboratory experiment results have been divided into three categories, namely:

(i) tide level data, which were used to calibrate and validate the hydrodynamic module of the porous media GWK model as linked to the DIVAST model.

(ii) point velocity data, which were used to verify the hydrodynamic module of the free surface DIVAST module within the linked model, and

(iii) dye tracer observations, which were used to calibrate and validate the solute transport predictions of the linked numerical model, to achieve a wider scientific understanding of the interactions between wetland areas and neighbouring coastal waters and the ground water seepage rates.

As extensive applications have been previously undertaken by other researchers to establish the accuracy of the hydrodynamic parameters for different laboratory models, and because the numerical model DIVAST has been verified against these measurements for hydrodynamic predictions, it was assumed in this research study that the hydrodynamic predictions of the DIVAST model were in accurate in comparison with measured data and this part of the model was assumed to be satisfactory. Furthermore, details of comparisons between the numerical DIVAST model and experimental model results can be found in a variety of scientific publications such as: Lin and Falconer (1997), Hakimzadeh (1997), Li and Falconer (1995), Falconer and Li (1994) etc.

6.2 Numerical Model Application to the Physical Model

Generally, before applying any numerical model to prototype predictions, it should be verified with measurements or other validated numerical models to check its numerical validity. For the verification of the linked numerical model developed in this study, it was applied to a laboratory physical model to simulate both the free surface and porous medium domains, including the recharge/discharge through sand, field velocity and dye tracer predictions, as discussed earlier in Chapter 5.

6.2.1 Model Details

6.2.1.1 Computational Domain

The model has been constructed with a square grid of size 10cm x 10cm, with the longitudinal axis being sited to match the tidal basin and with the origin of the computational domain being located at the point where the tidal basin wall and the weir intersect. Figure 6.1-a shows the origin and the computational domain for the physical model with the grid overlain, and the longitudinal axis of the domain extending 5 m (or 50 grid squares) beyond the sand ridge. The domain includes 50 x 40 grid squares, giving an area of coverage of approximately 20 m^2. The time-step used in the model was 0.2 s and the simulation period was for 5 repetitive tides with a courant number of typically 1.5.

6.2.1.2 Bathymetric data and Bed Roughness

The bathymetric data was obtained from the construction maps, according to the physical model dimensions. The AutoCAD software package was used to convert the data to an appropriate format for the DIVAST model, with depths being specified at the centre of the grid sides in both the x and y directions. A section of the bathymetry of the physical model embankment is illustrated in Figure 6.1-b. The reason for using the AutoCAD software package to prepare the bathymetric data was that the cross-sections of the sandy embankment were symmetric. Also, the bed roughness for the free surface domain, according to previous tests was found to be represented more accurately by an equivalent

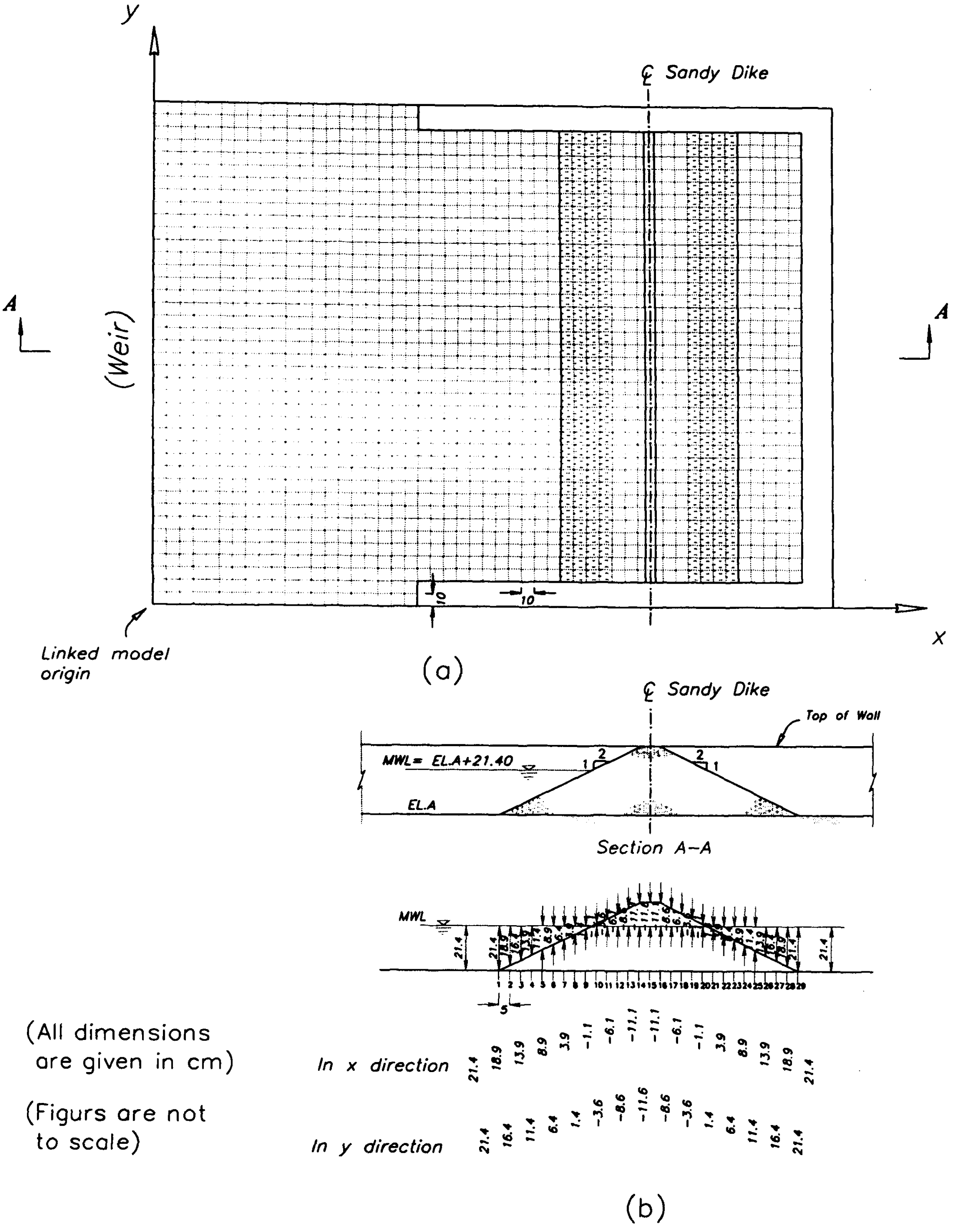

Figure 6.1: (a)-Physical model domain with grid squares overlaid, (b)-bathymetric data

grain roughness of 1mm, for more details see Kocyigit (2003).

6.2.1.3 Open Boundaries

As the numerical linked model was set-up for the whole domain of the physical model, including the free surface and porous medium, it was found necessary to specify the open boundary conditions of the computational domain. The hydrodynamic characteristics of the free surface and porous medium domains were defined within the linked model as follows:

(i): For the free surface domain, *zone A* and *B* – see Figure 3.9 of Chapter 3, the upstream boundary limit of the computational domain was located just along the oscillating weir as a water elevation boundary, zone *A* - boundary I. This open boundary condition was specified via a time-series of tidal elevations, based on the tidal cycle characteristics. Details of the tidal cycle are given in Chapter 5. The second and third open boundaries for the DIVAST model comprised two flow mobile boundaries along the shared lines of this model with the GWK model (Figure 3.9, zone *A* open boundary II and zone *B* boundary III). The GWK model provided both of the above mentioned flow boundaries for the DIVAST model.

It should be noted that as in the investigation of the solute transport modelling the water level behind the sand embankment was kept constant by adding a source-sink of water, as described in Chapter 5. Therefore, the fourth open flow boundary was defined along the end of the computational domain, which will be explained later in this chapter.

(ii): For the GWK model, DIVAST provided two open mobile elevation boundaries, on both sides of the porous medium domain (Figure 3.9, zone *S* open boundary II and III).

6.2.2 Hydrodynamic Modelling

For the purpose of investigating the accuracy of the linked hydrodynamic module predictions, a set of comparisons between the numerical predictions and the laboratory data for the tidal fluctuations and velocities have been made and the results are given herein.

6.2.2.1 Comparison of the Hydrodynamic Data

6.2.2.1.1 Tide Levels Data

In order to investigate the validity of the tidal numerical model predictions, tidal fluctuation data were recorded on both sides of the physical model embankment, as described in Chapter 5. For each individual experiment, the water levels were initially fixed at the approximate high tide water level on both sides of the sandy ridge, at the beginning of the experiment. Therefore, all experiments were started with the same horizontal high water level throughout the model domain, i.e., both for the free surface and porous medium domains. The water elevation data were collected and recorded along the centreline of the laboratory model for each test, and on both sides of the sand embankment, therefore giving a unique set of initial conditions at the beginning of each experiment. The results for each experiment, each side of the sandy ridge, were then compared with one another. It was also intended that the tide elevation data could be used in the calibration of the numerical porous media model through direct comparisons of the data produced by the model with the data collected in the laboratory.

The following comparison, Figure 6.2, illustrates the numerically predicted elevation data on both sides of the sandy embankment with time. It should be noted that, for the front of the sand embankment the numerical model simulated the sinusoidal tide level variations and according to the discharge-recharge calculated during each timestep, the numerical model predicted the water level variations behind the embankment.

As can be seen from Figure 6.2, in front of the embankment the maximum predicted height of the tide was 120mm, varying from a high tide water level of +60mm to a low tide water level of -60mm, with reference to the mean tide water level, over a tide period equal to 355 s. The water elevations behind the sand embankment were initially predicted from +60 mm, at high water level, but the level never fell below -1mm. After three tide cycles the fluctuating water level behind the embankment had stabilized at between +28 mm and -1 mm over the tidal period.

It is worth noting that, as expected, the fluctuations in the predicted water elevations on either side of the physical model embankment did not have similar shapes. According to the results, the high water peaks did not occur simultaneously and the low water levels also did not match each other. This was due to the amplitude of the elevation variations behind the sand embankment being significantly smaller than the amplitude of the tide, which had been simulated in the front of the embankment, and secondly, these water level variations were asymmetric in form due to non-linear effects.

In other words, the following conditions can be seen: when the front of the tide cycle is at high water level, then the tail of the tide is at mid-flood. However, when the tail of the tide

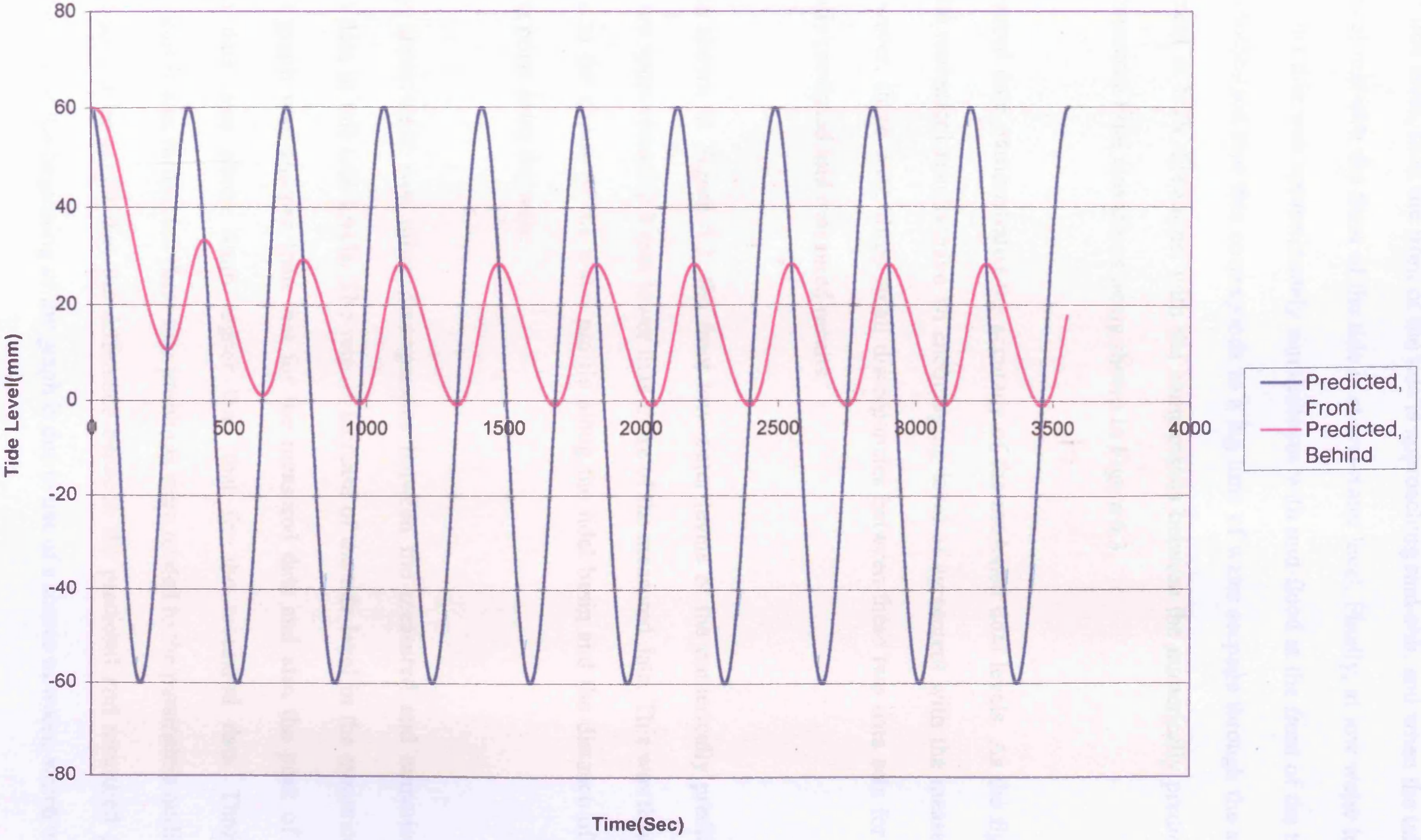

Figure 6.2: Numerically predicted time varying elevations either side of sand embankment

is at high tide level, then the front of the tide is approaching mid-ebb, and when the tail of the tide is at mid-ebb the front of the tide is at low water level. Finally, at low water level the tail of the tide was approximately simultaneous with mid-flood at the front of the tide. It was hypothesised that this corresponds to a lag time of water seepage through the sand embankment in both directions, with the comparisons between the numerically predicted and the measured tidal elevations being shown in Figure 6.3.

The measured data demonstrated the accuracy of the modelled tidal levels. As the figure shows, the numerical results gave an encouraging level of agreement with the measured data. However, there were three small discrepancies between these two data sets for the numerically predicted and measured results.

Firstly, as shown in Figure 6.3, the front low water levels of the numerically predicted results were approximately 3 mm lower than those of the measured data. This was thought to be due to the shape of the water profile along the tidal basin and the distance of the measuring point from the weir.

Secondly, there were two other discrepancies between the measured and numerically predicted data in tail tide levels. The rate of increase of the tide level in the numerically predicted graph was sharper than that for the measured data and also the peak of the predicted data was about 4mm higher than that for the measured data. Through investigations it was found that these two problems were related to the parameters outlined below. It should be noted that the difference between the predicted and measured data behind the sand at the beginning of the graph is due to use of a source of water, which was

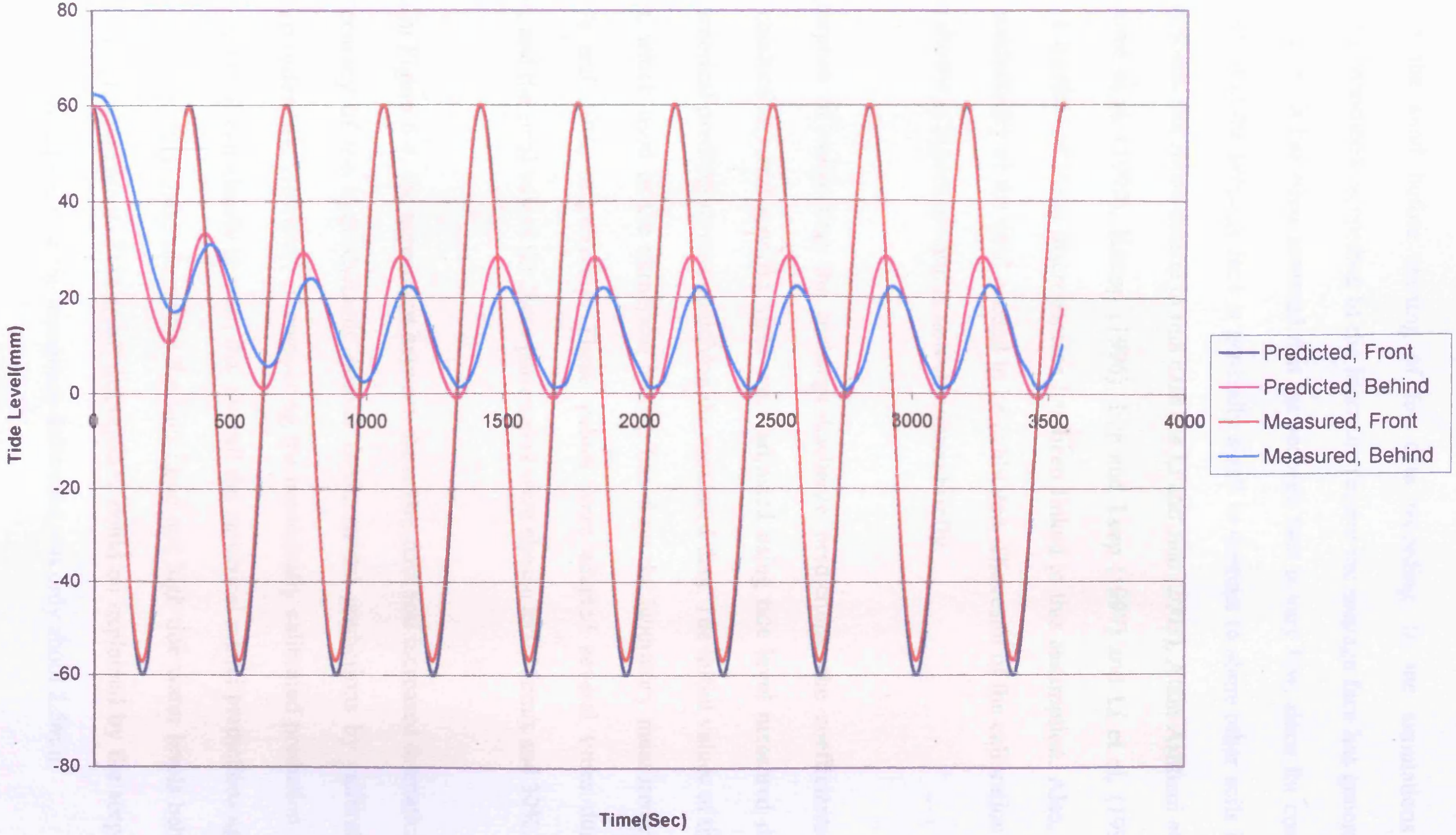

Figure 6.3: Comparison of numerically predicted and measured tide level data

used behind the sand before starting of the data recording. In the simulations of groundwater phenomena, according to the literature review the seepage face has generally been ignored, i.e., it has been assumed that the seepage face is very low, since for coarse materials like sand the seepage face is generally small in contrast to some other soils like clay or clay-loam. For more details in this case see Li and Jiao (2003), Ataie-Ashtiani et al. (1999), Crowe et al. (1999), Knupp (1996), Lee and Leap (1997) and Li et al. (1997). Therefore, a number of these discrepancies has been linked to this assumption. Also, the hydraulic conductivity of the sand needed to be calibrated. The result of the calibration for this case is shown in Figure 6.4 and is now discussed briefly.

For the purpose of calibrating the recharge-discharge predictions, the coefficients of hydraulic conductivity and specific yield were adjusted using tide level measured data, with the numerical predictions now matching the measured data. The initial values of these parameters, which used in the numerical model, based on the laboratory measurements, were 1cm/s and 29%, respectively. These values were adapted several times during calibration, and the final values for these parameters were chosen as 0.95cm/s and 30%.

As shown in Figure 6.4, the agreement between these two data sets increased dramatically and the accuracy of the hydrodynamic porous media model predictions by calibration increased considerably. However, in comparing the numerically calibrated prediction and measured results, it can clearly be seen that overall the numerical model predictions agree well with the laboratory data, except for the mid-flood and high tide water levels behind the model sand embankment. This small discrepancy could be explained by the seepage face, and it was ignored because the maximum difference was only about 2.5mm.

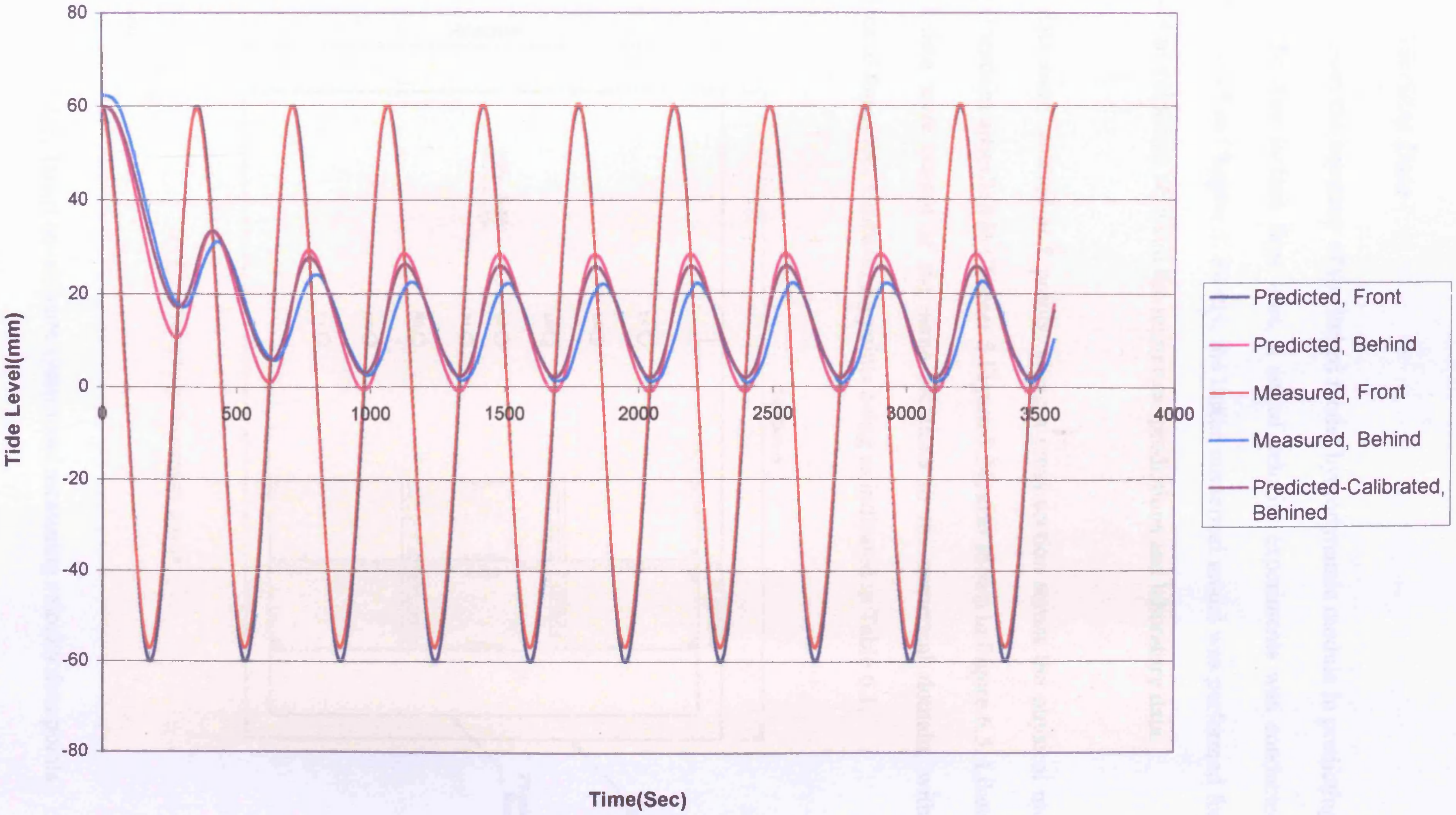

Figure 6.4: Comparison of numerically calibrated predicted and measured tide level data

6.2.2.1.2 Velocities Data

In order to assess the accuracy of the linked model hydrodynamic module in predicting the velocity in the free surface flow area, a set of velocity experiments was conducted as described in detail in Chapter 5. Firstly, the linked numerical model was performed for the comparison of velocities between the numerical predictions and laboratory data.

Velocity data were colleted at 8 points, along a cross-section across the physical model, and at the locations specified in Chapter 5 Figure 5.24, also shown in Figure 6.5. Likewise, numerical data were output at the same locations in the numerical domain, with the co-ordinates of the velocity measuring points being as indicated in Table 6.1.

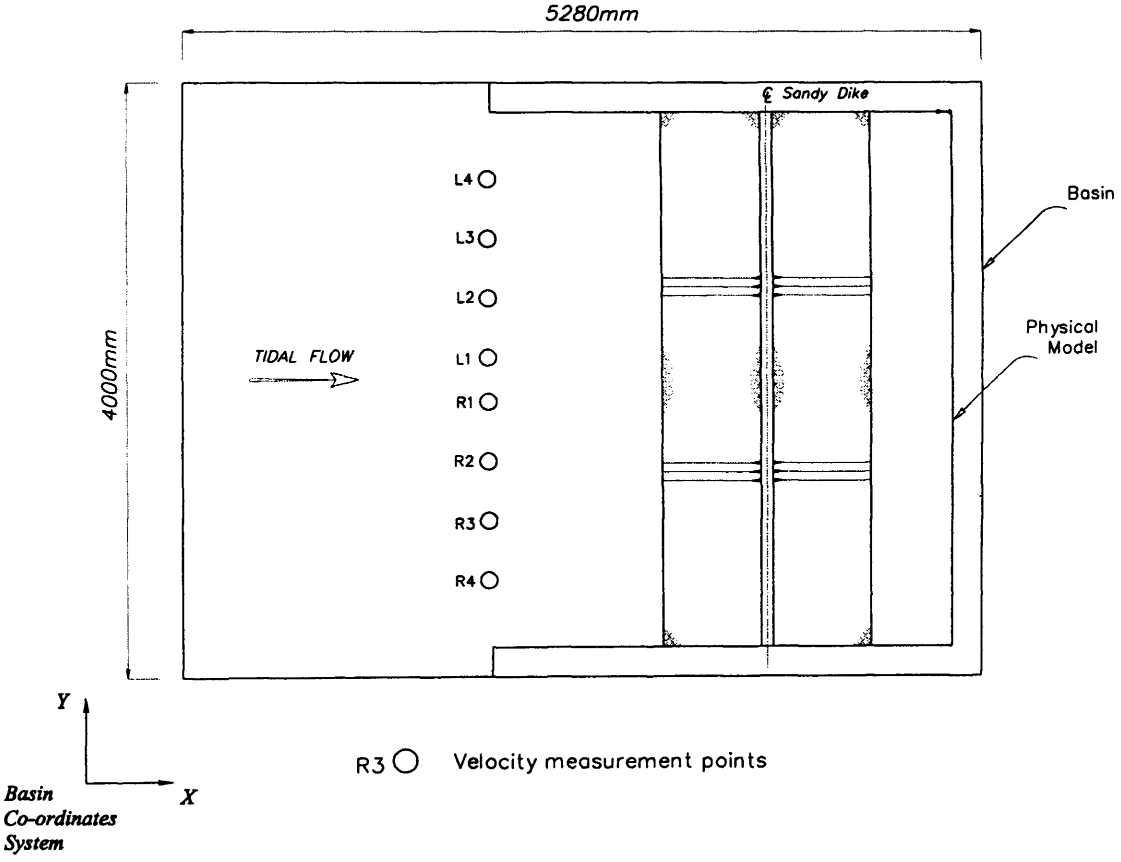

Figure 6.5: Basin co-ordinate system and measuring velocity data points

Table 6.1: Co-ordinate of velocity measurement points in centimetres

Test Point	R1	R2	R3	R4	L1	L2	L3	L4
X	195	195	195	195	195	195	195	195
Y	195	155	115	75	225	265	345	305
I	20	20	20	20	20	20	20	20
J	20	16	12	8	23	27	35	31

In order to compare the *u* velocity components for any test point, the numerical velocity predictions and the measured data are plotted together against time. Firstly, as described previously the velocity data were collected and recorded over a period of 10 tide cycles and subsequently the data were time-averaged over 10s around: high water level, mid-ebb, low water level and mid-flood for the last 3 tides, to give an average value of the velocity component at each location. The resulting time-averaged velocities were then plotted using Excel package, together with the integrated numerical model output.

The results for the test points are shown in Figures 6.6 to 6.13 respectively. As expected, there was close agreement between the measured data and the numerical model predictions using the linked model. As mentioned previously, this was because the numerical model DIVAST has been verified previously against extensive laboratory and field data. However, the level of agreement demonstrated that the DIVAST model is working well in linked phase, integrated with the new porous media sub-model. The maximum measured velocity for these experiments was found to be about 0.92 cm/s when the flow was into the basin and it about 0.89 cm/s when the flow was out of the basin. Both of these values were collected at point L4. However, as can be seen from the figures the variation in the

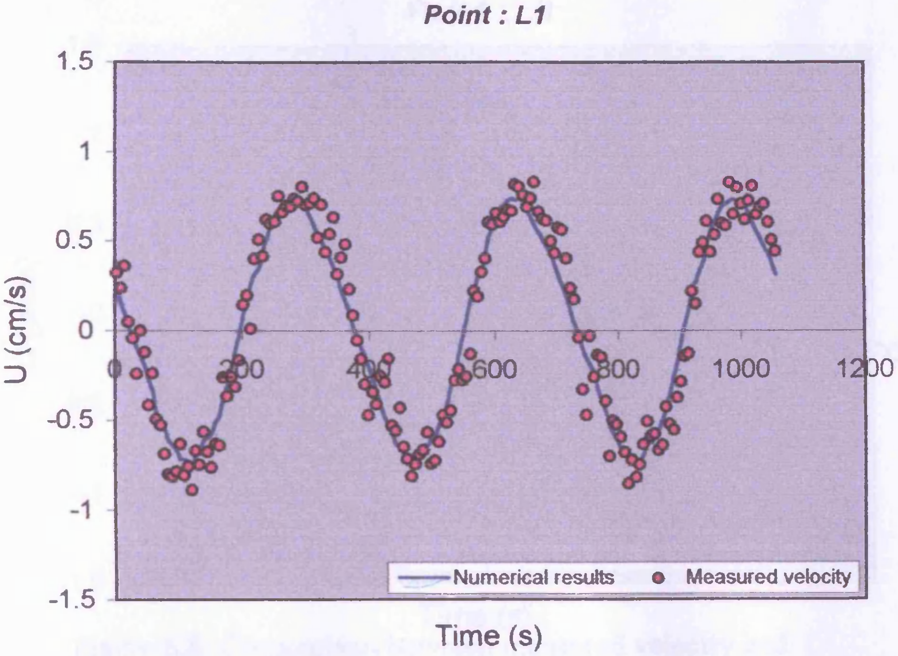

Figure 6.6: Comparison between measured velocity and numerical model predictions, at point L1

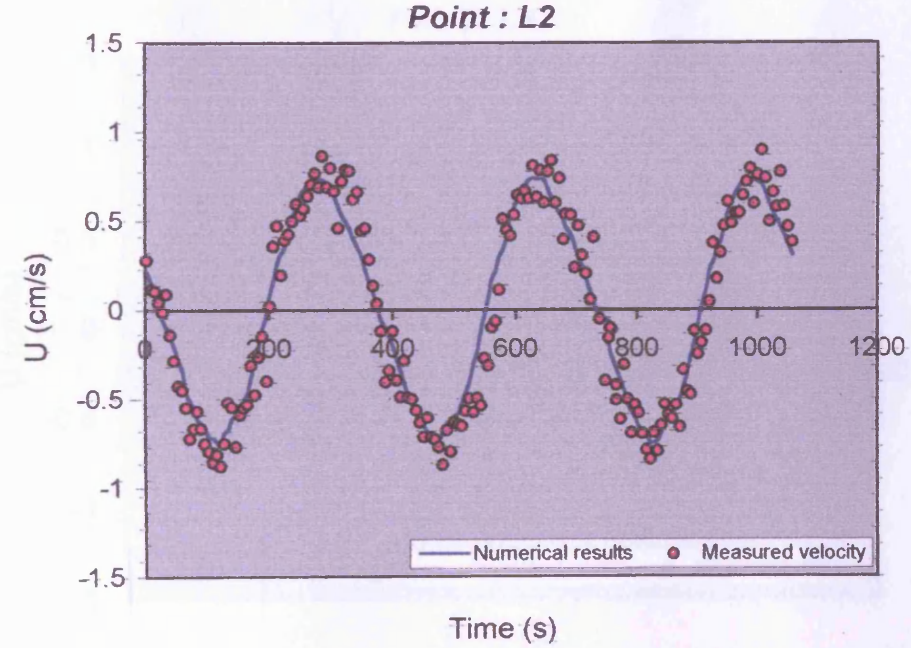

Figure 6.7: Comparison between measured velocity and numerical model predictions, at point L2

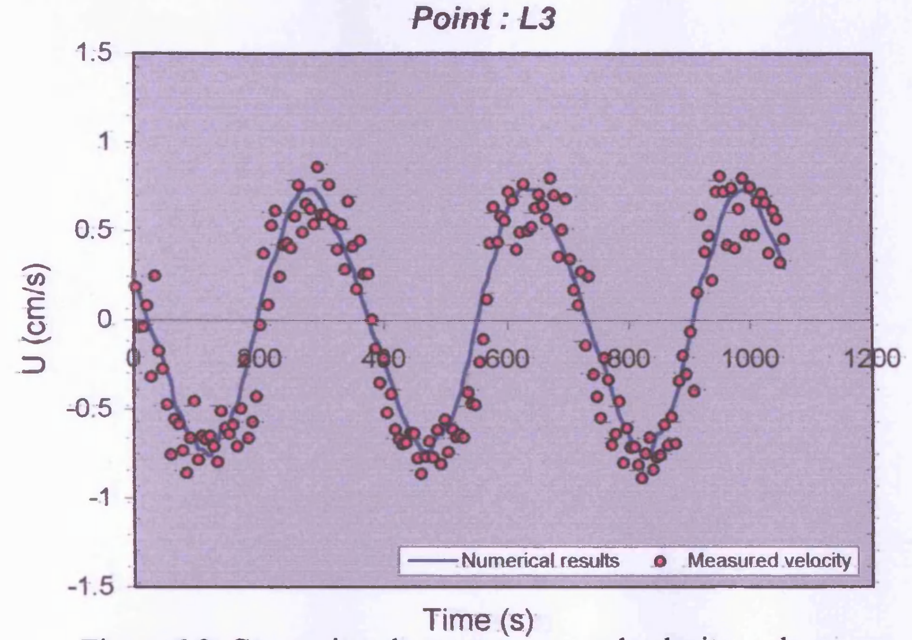

Figure 6.8: Comparison between measured velocity and numerical model predictions, at point L3

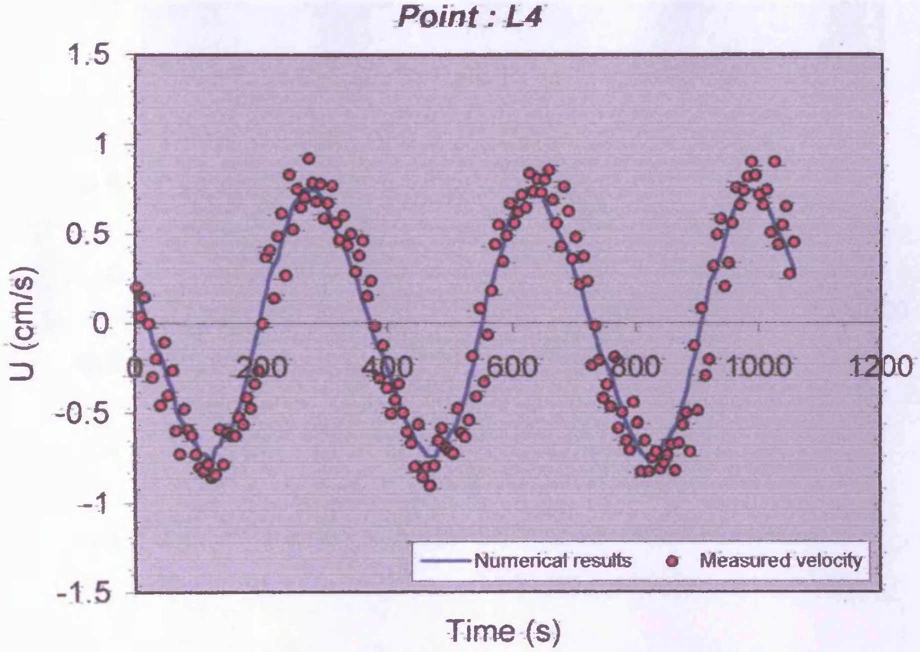

Figure 6.9: Comparison between measured velocity and numerical model predictions, at point L4

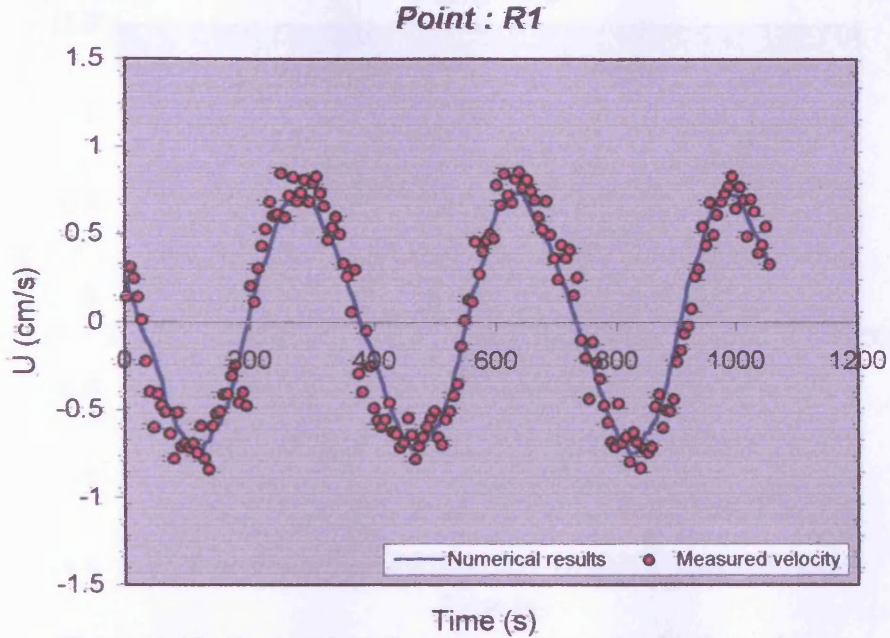

Figure 6.10: Comparison between measured velocity and numerical model predictions, at point R1

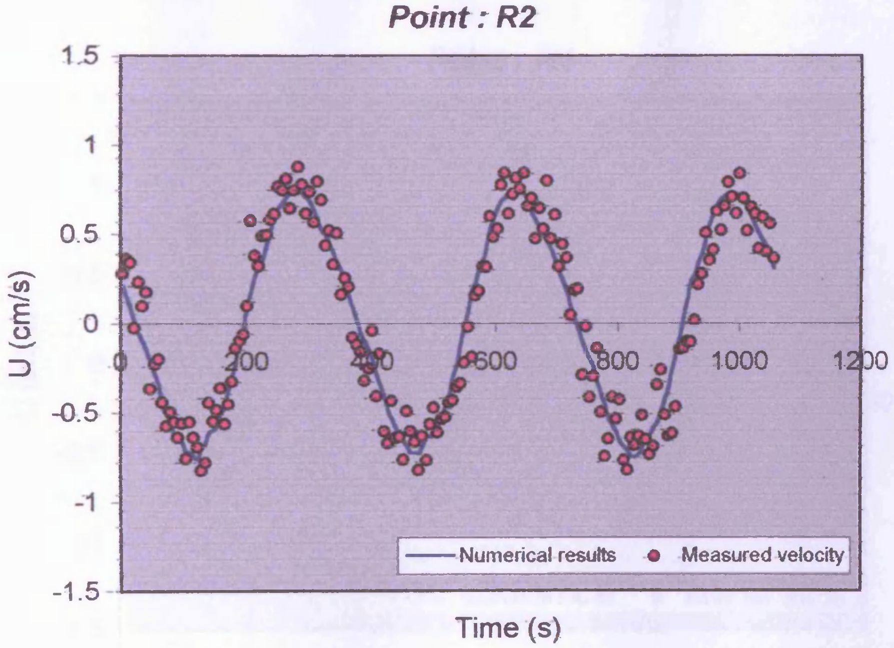

Figure 6.11: Comparison between measured velocity and numerical model predictions, at point R2

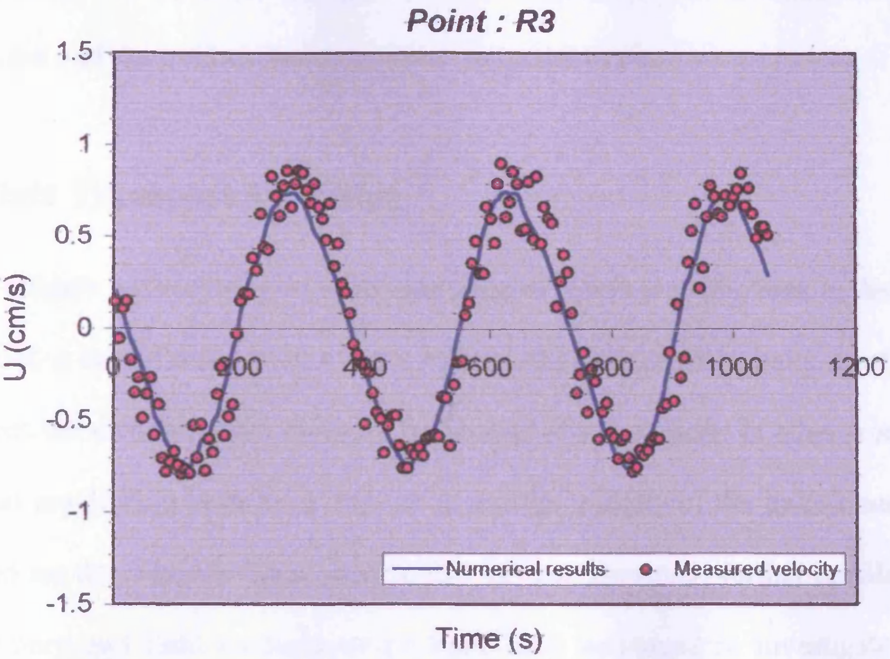

Figure 6.12: Comparison between measured velocity and numerical model predictions, at point R3

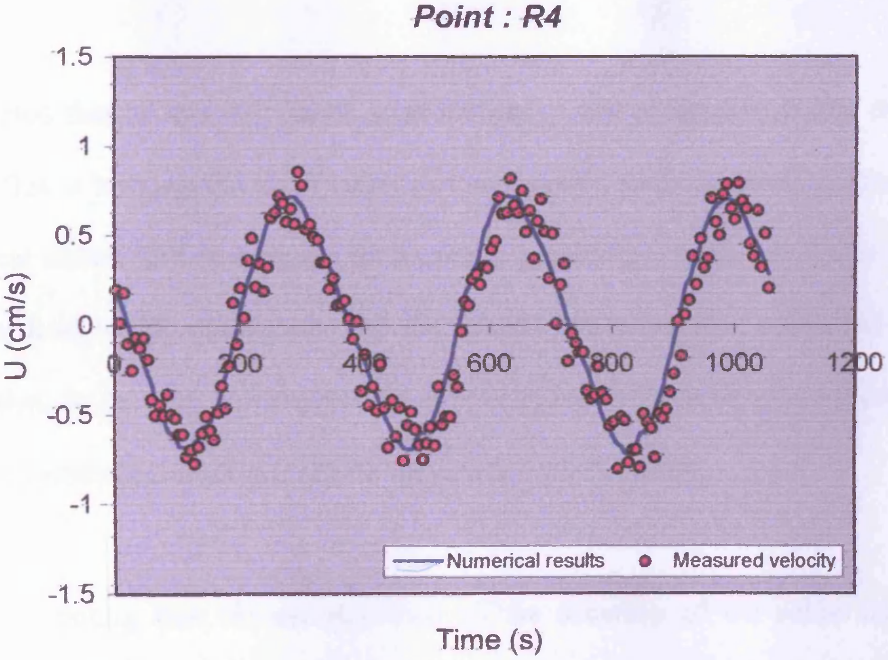

Figure 6.13: Comparison between measured velocity and numerical model predictions, at point R4

velocities in different test points is very limited. This is because of the locations of the test points in the basin and the uniformity of the flow across the basin.

6.2.3 Solute Transport Modelling

In order to investigate the accuracy of the solute transport module predictions in the linked numerical model, a set of comparisons were made using simplified techniques of image analysis between the simulated and observed behaviour of a dye tracer. In other words, the results of visual monitoring have been used to assess the validity of the linked numerical simulations and are described in detail later in this section. However, further details of the different laboratory and field methods which have been employed to investigate solute transport in porous media may be found elsewhere and in a variety of scientific publications, such as Huang et al. (2002), Stern et al. (2001), Harris et al. (2000) and Allersma et al. (2000).

It should be noted that no specific direct measurements were undertaken inside the sand embankment. This is because the main target of this research study has been to develop a linked numerical model and investigate its accuracy involving a physical model and by studying the hydrodynamic parameters and the overall behaviour of a conservative dye tracer distribution. In fact the accuracy of the porous media numerical model predictions was evaluated by studying the effects on the free surface phenomenon.

Also, it is worth noting that the investigations of the accuracy of the solute transport predictions were carried out after obtaining satisfactory agreement in the comparisons of hydrodynamic parameters, velocities and recharge–discharge levels between the linked numerical model predictions and the measured data. These comparisons were discussed earlier in this chapter, but the results and comparisons are presented in more detail below.

6.2.3.1 Comparison of Solute Transport Data

In using the solute transport module of the linked numerical model, similar to that described in Chapter 5, two different tests of conservative tracer simulations were undertaken, using dye concentrations of 5 g/l.

In the first of these simulations the tracer was released uniformly at a point, which was located on the longitudinal centre line of the computational domain and behind the sand embankment (see Figure 5.24) to monitor the spreading of the tracer over different tides in front of the sand embankment, while the depth of water behind the sand embankment was constant. The second simulation was undertaken while a tracer with the same concentration was released along a line across the computational domain and behind the sand embankment.

In both tests the simulations were undertaken for 5 tides and the tracer was released at the beginning of the 4th tide, i.e. exactly when the water elevation behind the sand embankment was at high water level. The same condition was replicated in the laboratory model during the performance of the dye tracer experiments. The model was only run for simulations involving 5 tidal cycles, with the tracer behaviour only being considered over the two last tides, since for longer simulation periods comparisons were found to be difficult. This was because the size of the physical model was not big enough to allow the tracer plume to spread too much. However, during the study it was found that satisfactory results were obtained for these two tides. It is worth highlighting that using a wider physical model with a bigger reservoir will remove the above mentioned problem. However, using a bigger model needs to fix more than one camera to film the whole area of the plume spreading.

6.2.3.1.1 One-Point Tracer Release

Graphical plots of one-point tracer release simulations for different stages of tides 4 and 5 have been produced, involving the Tecplot software package. Also images were processed to estimate the 2-D distribution of the tracer. These two sets of figures were then compared. Table 6.2 represents the characteristics of these plots. In the table the first column represents the time-section number and the second column represents the time-stage of each plot, which is based on the reference time (i.e. the time after release of the tracer). The third column represents the time from the beginning of the video film and the fifth and sixth columns are related to the tidal water levels. Finally, the last column shows any observational notes.

The comparisons of the numerically predicted and monitored tracer behaviour for the different time stages of one-point experiment are presented in Figures 6.14 – 6.22. Figures 6.14 and 6.15 were not included in the laboratory observations because the tracer at these time phases did not appear in the tidal side of the model. However, Figures 6.14 and 6.15 were representative of the velocity fields in the porous medium and the free surface flow domains.

In Figures 6.14 to 6.22 the numerical model results are included for the final calibrated values of the longitudinal and transverse dispersivity coefficients within the porous medium, with the results being 1.5 and 0.1, respectively. It should be noted that before using these values, nominal values of 1.5 and 0.15 were chosen for the coefficients, based on Spitz, and Moreno, (1996). The values were then calibrated, based on trials carried out on the width and length of the predicted plumes for known widths and lengths of those plumes, with the laboratory observations, reducing to 1.5 and 0.12, respectively. However,

Table 6.2: One-Point release tracer characteristics

Time-Stage Number	Time from Start of Releasing of the Tracer (sec)	Time from Beginning of the Video Film (sec)	Tide Level in front of the Dike	Tidal Elevation (mm)	Note
1	0.0	263	High Water Level	+60	*Start of releasing of the tracer*
2	89	352	Mid-Ebb	0.0	
3	197	460	About Low Water Level	- 56	*Appearance of the tracer in the front of the dike*
4	267	530	Mid-flood	0.0	
5	355	618	High Water Level	+60	
6	444	707	Mid-Ebb	0.0	
7	533	796	Low Water Level	-60	
8	622	885	Mid-Flood	0.0	
9	710	973	High Water Level	+60	

after running the model a few times for the line tracer, section *6.2.3.1.2*, it was apparent that it is necessary to re-calibrate these coefficients and the coefficients were again reduced to 1.5 and 0.1, which gave a better agreement with the two data sets. Therefore, the model was re-run for values of 1.5 and 0.1 for the longitudinal and transverse dispersivity coefficients, respectively, yielding the results presented in Figures 6.14 to 6.22.

Figure 6.14

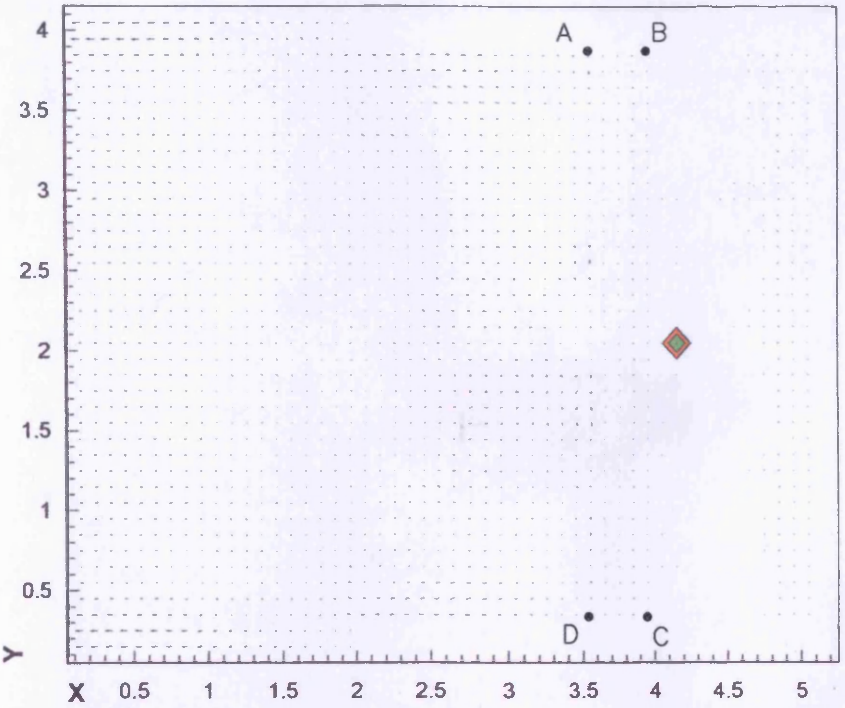

Figure 6.15

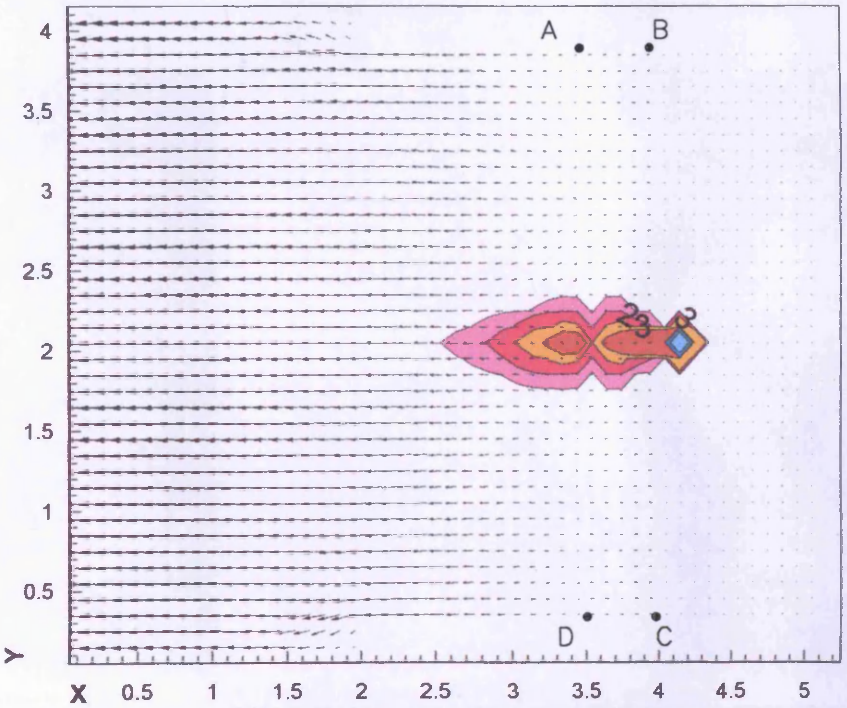

LEGEND

Level	Tracer Dye Concen. (gr/lit.)
7	5
6	1
5	0.1
4	0.01
3	0.001
2	0.0001
1	1E-05

3 cm/sec ←

0.5 1 m

Grid Size 10cm x 10cm

TIDAL DATA

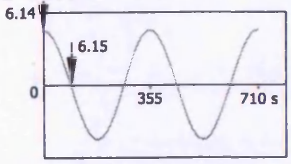

High Water Level & Mid–Ebb
Time = 0.0 & 89 s
Time of Simulation = 30 min

Figures 6.14 and 6.15:

Conservative Tracer Contours and Velocity field Predictions,

Solute Transport Modelling

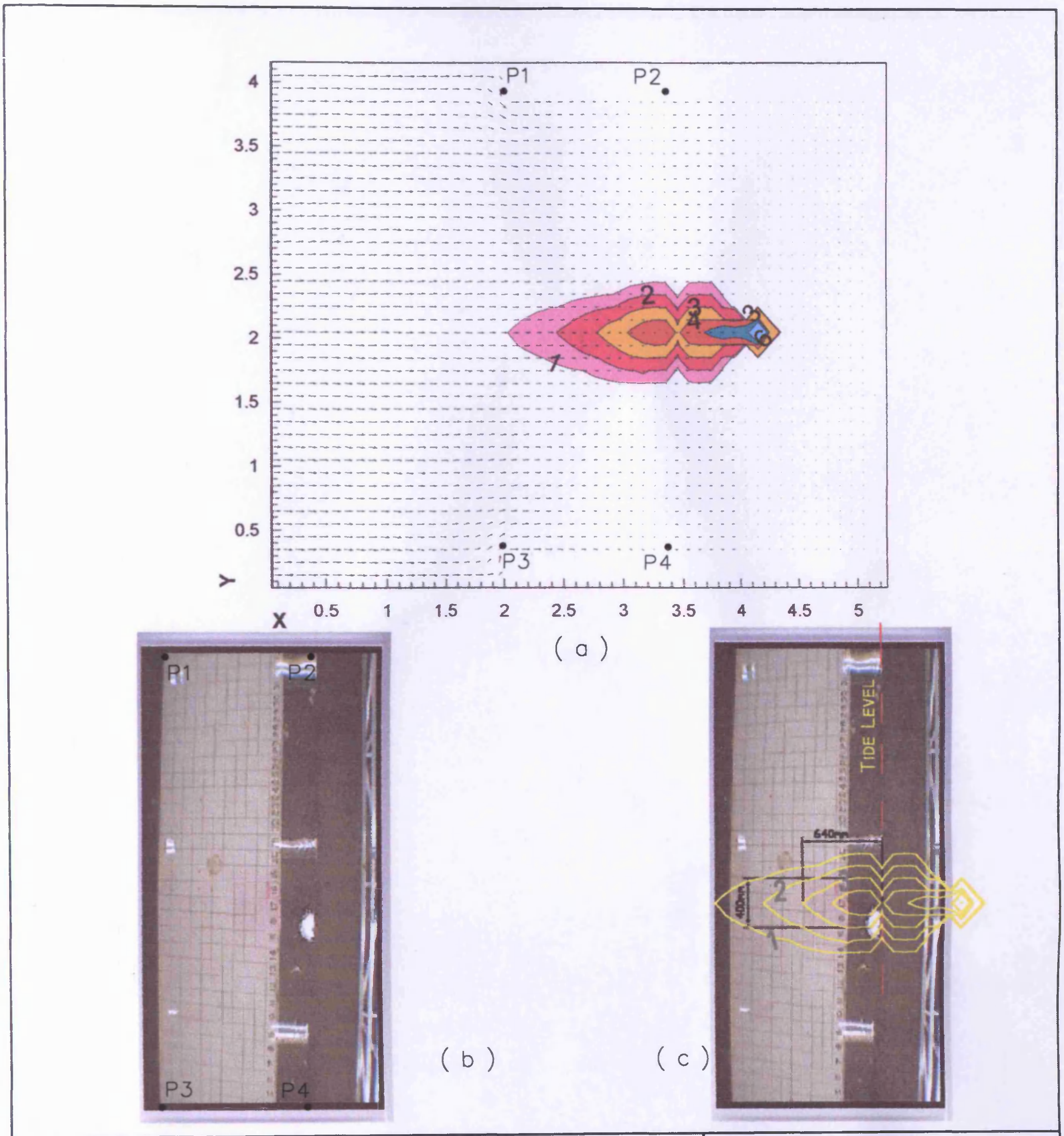

LEGEND

Level	Tracer Dye Concen. (gr/lit.)
7	5
6	1
5	0.1
4	0.01
3	0.001
2	0.0001
1	1E-05

3 cm/sec

0.5 1 m

Grid Size 10cm x 10cm

TIDAL DATA

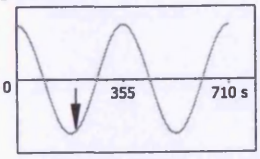

About Low Water Level
Time = 197 s
Time of Simulation = 30 min

Figure 6.16:

Comparison of Numerical Predictions and Laboratory Observation, Solute Transport Modelling

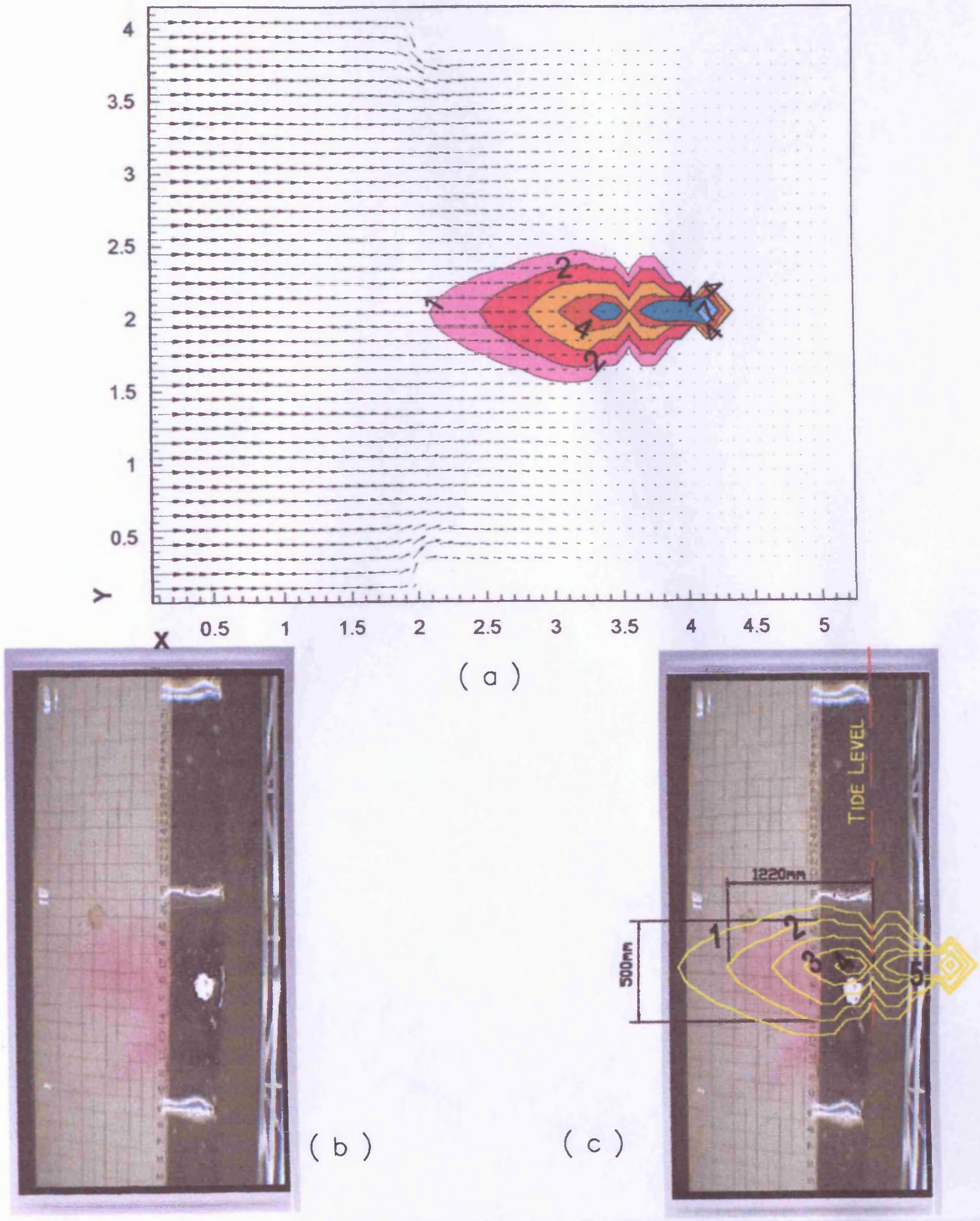

LEGEND

Level	Tracer Dye Concen. (gr/lit.)
7	5
6	1
5	0.1
4	0.01
3	0.001
2	0.0001
1	1E-05

3 cm/sec ← 0.5 1 m

Grid Size 10cm x 10cm

TIDAL DATA

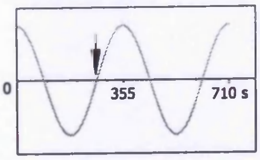

Mid – Flood
Time = 266 s
Time of Simulation = 30 min

Figure 6.17:

Comparison of Numerical Predictions and Laboratory Observation, Solute Transport Modelling

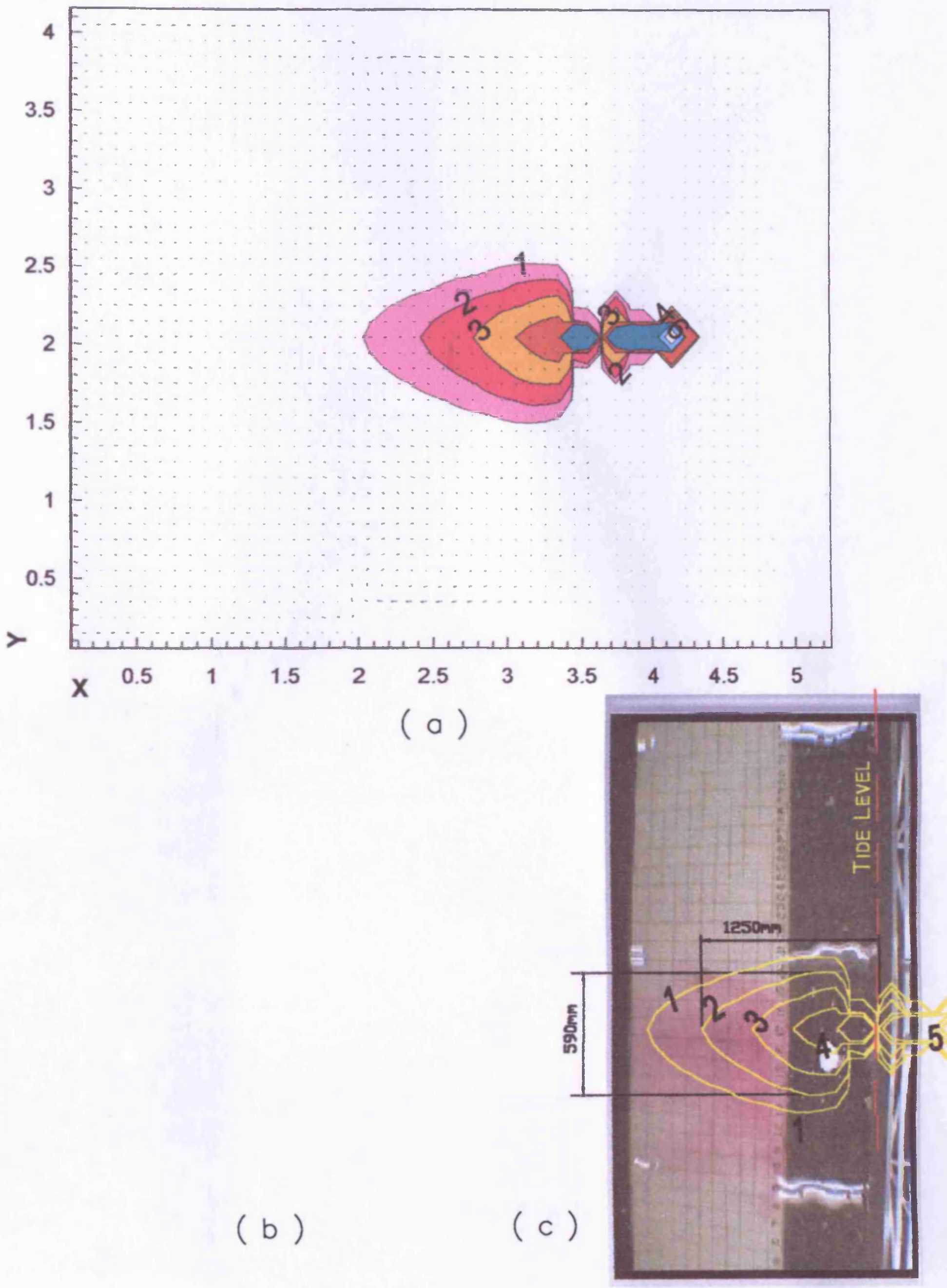

LEGEND

	Level	Tracer Dye Concen. (gr/lit.)
⬜	7	5
🟦	6	1
🟦	5	0.1
🟥	4	0.01
🟧	3	0.001
🟥	2	0.0001
⬜	1	1E-05

3 cm/sec ← 0.5 1 m

Grid Size 10cm x 10cm

TIDAL DATA

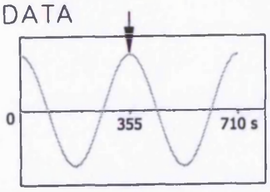

High Water Level
Time = 355 s
Time of Simulation = 30 min

Figure 6.18:

Comparison of Numerical Predictions and Laboratory Observation, Solute Transport Modelling

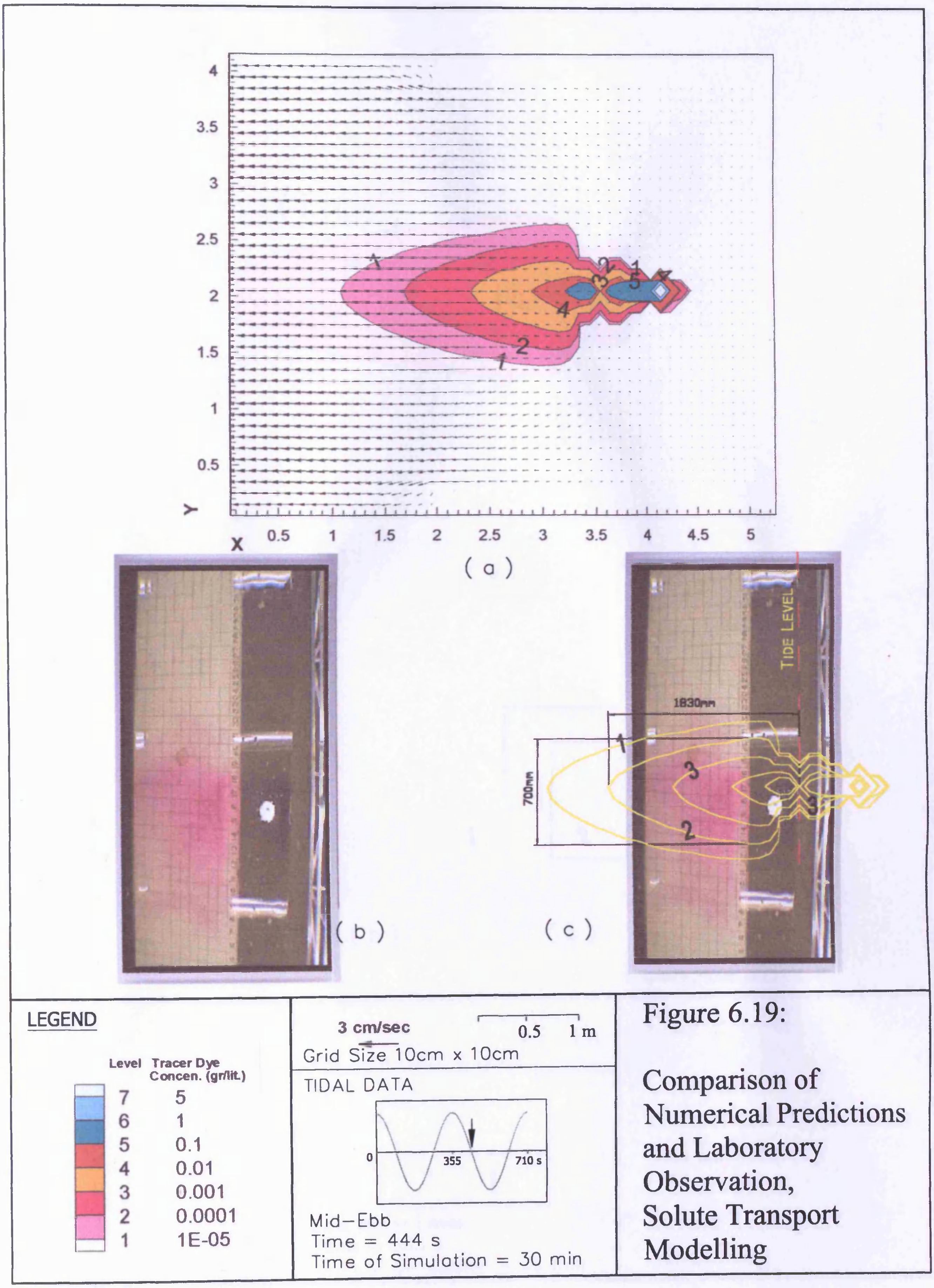

Figure 6.19:

Comparison of Numerical Predictions and Laboratory Observation, Solute Transport Modelling

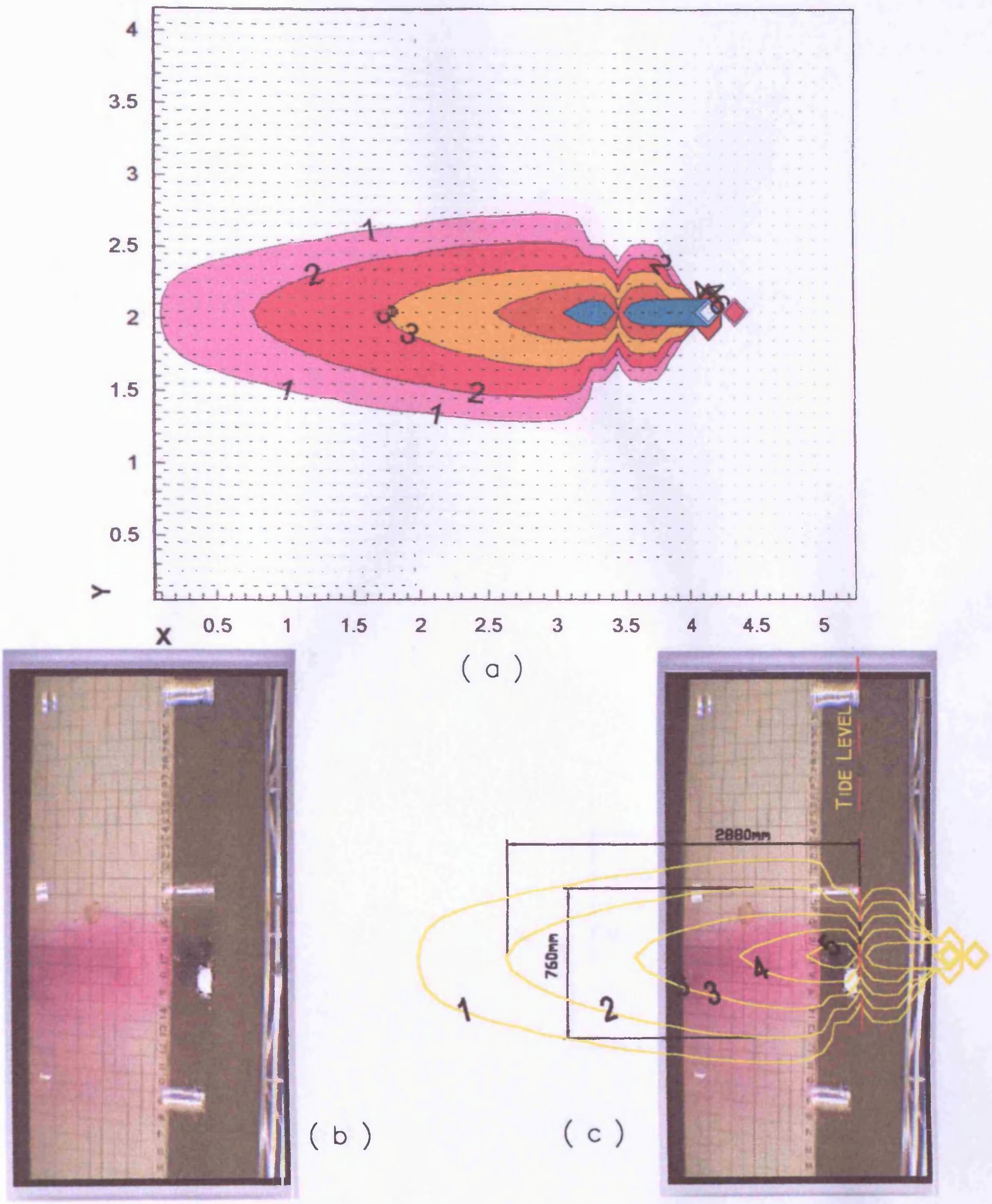

(a)

(b)

(c)

LEGEND

Level	Tracer Dye Concen. (gr/lit.)
7	5
6	1
5	0.1
4	0.01
3	0.001
2	0.0001
1	1E-05

3 cm/sec ←

0.5 1 m

Grid Size 10cm x 10cm

TIDAL DATA

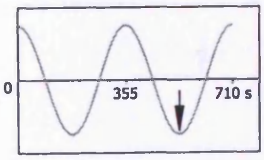

Low Water Level
Time = 533 s
Time of Simulation = 30 min

Figure 6.20:

Comparison of Numerical Predictions and Laboratory Observation, Solute Transport Modelling

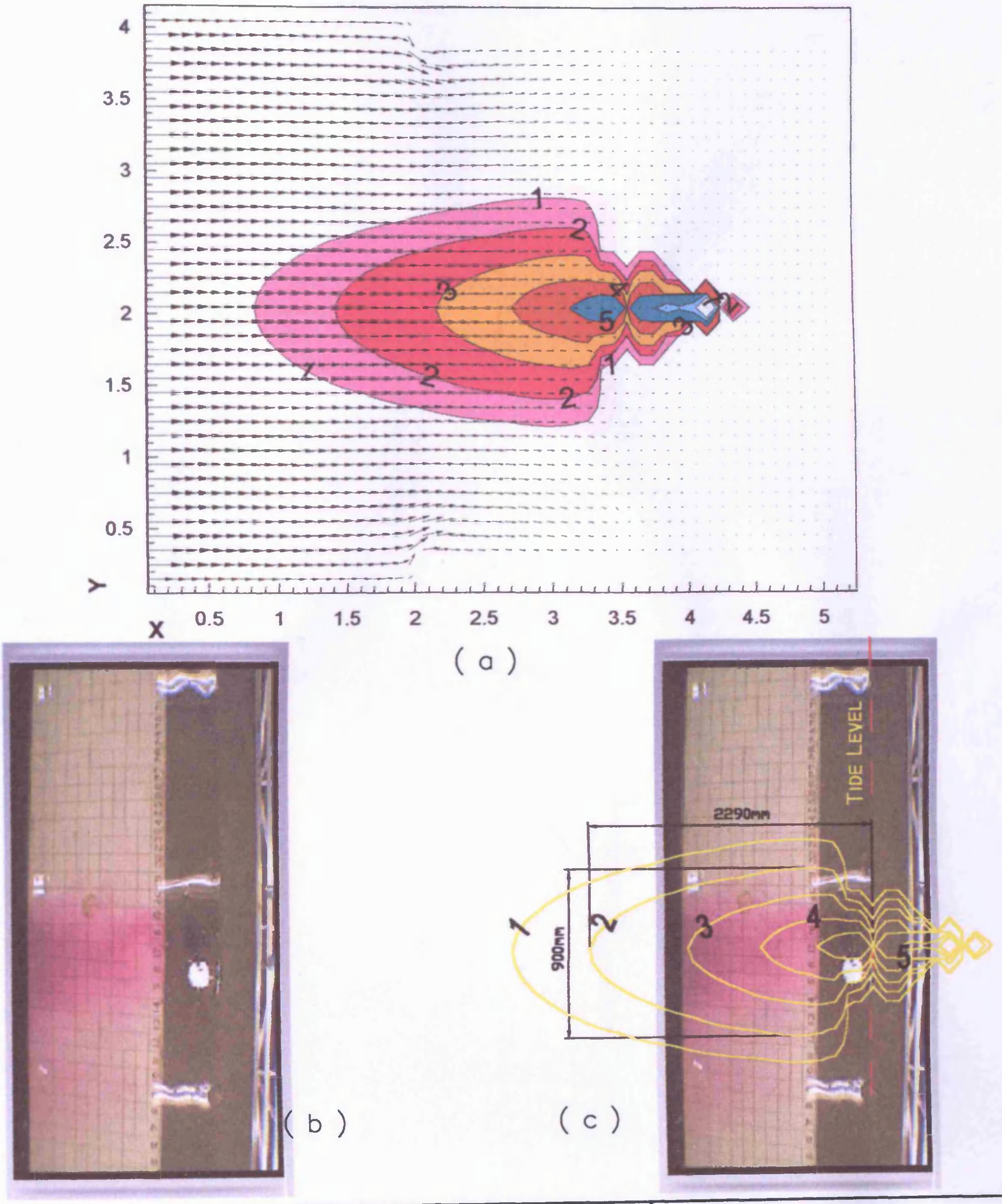

LEGEND

	Level	Tracer Dye Concen. (gr/lit.)
▭	7	5
🟦	6	1
🟦	5	0.1
🟥	4	0.01
🟧	3	0.001
🟥	2	0.0001
🟪	1	1E-05

3 cm/sec ←

0.5 1 m

Grid Size 10cm x 10cm

TIDAL DATA

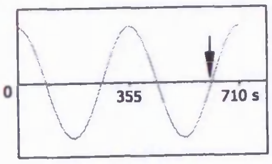

Mid Flood
Time = 621 s
Time of Simulation = 30 min

Figure 6.21:

Comparison of Numerical Predictions and Laboratory Observation, Solute Transport Modelling

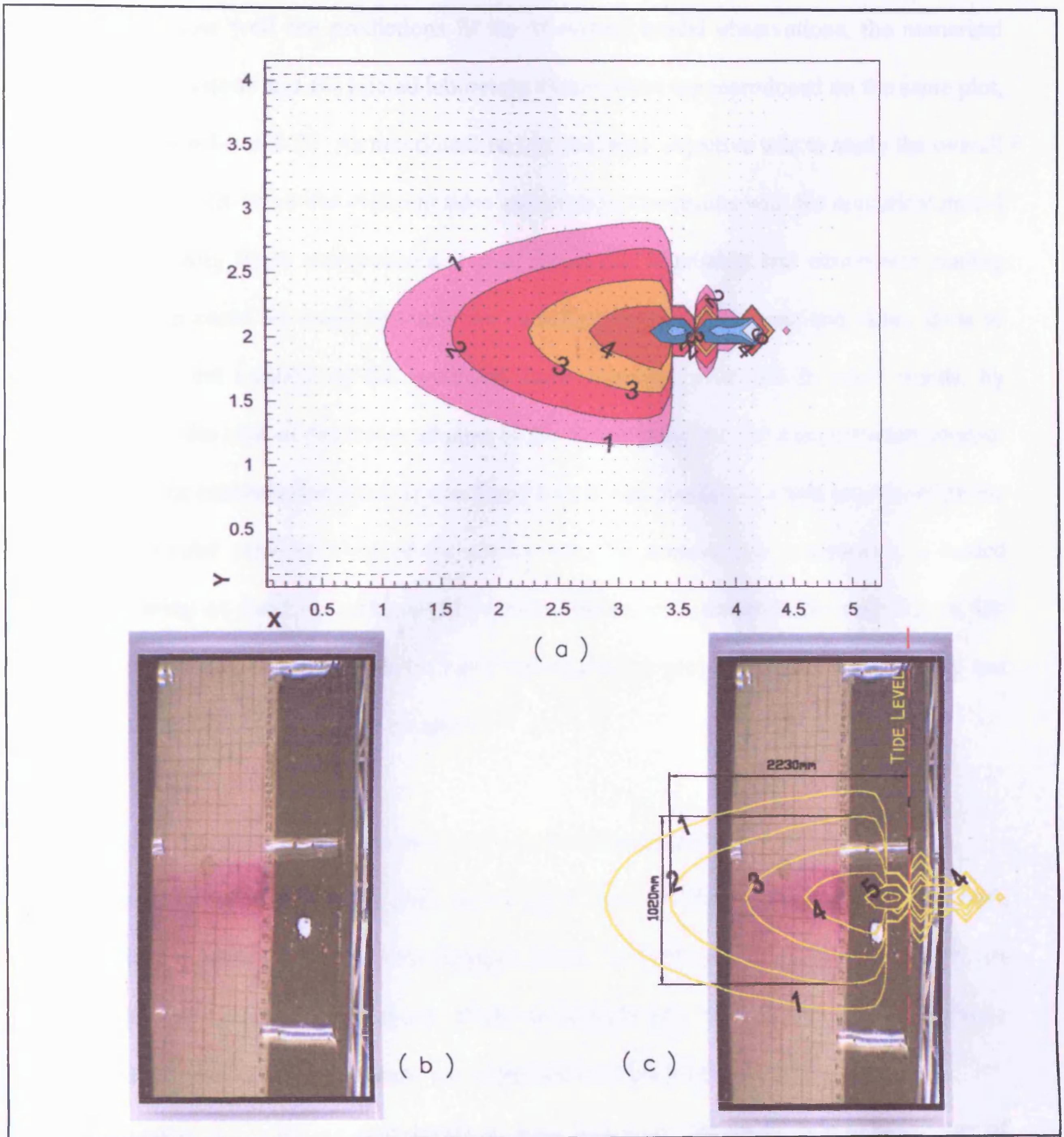

LEGEND

Level	Tracer Dye Concen. (gr/lit.)
🟦 7	5
🟦 6	1
🟦 5	0.1
🟥 4	0.01
🟧 3	0.001
🟥 2	0.0001
🟪 1	1E-05

3 cm/sec ← 0.5 1 m

Grid Size 10cm x 10cm

TIDAL DATA

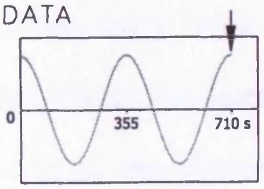

High Water Level
Time = 710 s
Time of Simulation = 30 min

Figure 6.22:

Comparison of Numerical Predictions and Laboratory Observation, Solute Transport Modelling

To assess how well the predictions fit the laboratory model observations, the numerical model simulations and the related laboratory observations are reproduced on the same plot, see Figures 6.14 to 6.22. As mentioned earlier, the main objective was to study the overall behaviour of the tracer for different tides and compare the results with the numerical model results. During these comparisons it was found that a reliable and convenient scaling comparison could be made between the numerical model predictions and video shots to investigate the validity of the predicted flow transport processes. In other words, by comparing the size of the tracer plumes in the video shots and the concentration contour levels in the numerical outputs, it was found that it was possible to relate any tracer plume to a particular contour level of the predictions. To achieve this comparison, a scaled overdrawing of the tracer plume and similar contour was prepared for each figure, i.e. Figures 6.16-c – 6.22-c. However, there were potential problems concerning scaling and these are discussed later in this chapter.

Therefore, the discussion of the results of this part comprised two aspects:

(i) the discussion related to each time-section and (ii) the spreading procedure and, behaviour of the dye tracer in the physical model for different tides. Also, velocity fields were plotted to give an indication of the magnitude and direction of the flow at each plotted time-section. These results are explained in detail herein.

In Figures 6.14 – 6.22, the time-levels go from high water for the 4th tide to high water of the 6th tide. It can be seen from the figures that generally the tracer plume was expanding as time progressed. In comparison the length, width and general shape of the video shot plumes were compared with the related simulated plumes. The experimental results demonstrated that for the majority of the figures the concentration level 2 of the simulations, which represents concentrations in excess of 0.1 mg/l, gave the best agreement with the tracer plume sizes and shapes. As mentioned earlier, the tracer release was started when the water level was at high water. It should be noted that in discussing of these results, high water then was chosen as the time reference.

Figure 6.14 shows the velocity fields through the whole domain. As can be seen from the figure the velocities are approximately equal to zero, since the phase is at a high-water-level. In this figure the porous medium domain limitations are highlighted by points *A, B, C* and *D,* also, see Figure 3.9.

Figure 6.15 illustrates the velocity field at mid-ebb; the field can be distinguished by three separate parts. The first part is to the right of the figure where there is no velocity; this is zone B with a constant water level, see also Figure 3.9. It would appear from this plot, and all of the next plots, that this area is a stagnant zone of velocity because of the constant head level. However, output data demonstrated that the magnitudes of the velocities in this zone were not absolutely zero at all stages, since there was a very low flow in this zone. It should be noted that as mentioned in the explanation for the open boundaries in section 6.2.1.3, i.e. at the far down-stream boundary of the computational domain, in simulating the solute transport this has been set as a flow boundary. This open flow boundary was considered since the source was in this area, see Figure 5.11. The maximum amount of the mentioned flow, through the sand, occurs when the water elevations at the front of the sand embankment were at low-water-level.

The second zone was zone S, with the porous medium domain being defined in Figures 6.14 and 6.15. In this zone the velocities were very low, and with the largest velocities in this domain being predicted to be about 0.17 cm/s, which occurred when the tide in front of the sand embankment was at a low-water-level. The third zone of the velocity domain was zone A, on the left side of the physical model, where the tidal current was active and the magnitude of the velocities in this zone for different stages of a tide cycle can be seen from Figures 6.14 to 6.17. The general behaviour of the dye tracer, established from the video film, is described below in tandem with an explanation of the figures.

The appearance of the tracer in front of the sand embankment is shown in Figure 6.16-b. This occurred around the first low-water-level, i.e. after a time of 197 s. Figure 6.16-a illustrates the numerical simulation at this stage and also Figure 6.16-c shows the scaled over-drawing of Figures 6.16-*a* and *b*. Although in this plot there is no clear agreement between the predicted and observed tracer plume, this is regarded as being quite small and was assumed to be relatively insignificant at this stage, since the overall model provided good predictions when compared with the recorded data.

Better agreement could be found in the next comparison, i.e. Figure 6.17 at mid-ebb, where the concentration level 2 -a concentration bigger than 0.1 mg/l- has been shown to give the best agreement with the observed video data. The dimensions of the tracer plume at this time-section were 1220mm and 500mm. At this stage as the tracer was discharging from the porous medium domain into the front zone, then the tidal flow was pushing the plume back.

Based on the same principles and by following the experimental procedure, Figure 6.18 was produced and can be explained as below. At this stage because there was no gradient in the water elevations then the velocities across the computational domain in Figure 6.18-a were approximately equal to zero. The tracer plume in zone *A*, figure *(a) and (b)*, was pushed back. However, the contour level 2 in this picture was spread more than before, with a length of 1250mm and width 590mm, but it did not cover the whole tracer plume. Several reasons can be considered for this difference. One reason was thought to be that during the experiments the movement of the tracer through the basin was not very uniform and as the shots demonstrated the tracer tended towards the left side of the basin, which had a direct effect on the shape of the plume. This diversion can be described by concept of dispersion of a contaminant in porous media as mentioned by Wang and Anderson (1982). Where they said the dispersion of a contaminant in groundwater is due mainly to heterogeneity of the medium and it is a result of the existence of a statistical distribution of flow paths and of flow velocities around local heterogeneities. However, the small circulation of water behind the sand, which was result of unsymmetrical sink of water during the experiments (see Figures 5.10-a and 5.11-a the location of sink), is not dispensable. The second reason was thought to be that during the experiments it was apparent that the tracer was not distributed uniformly with depth over the water column and it spread and moved close to the basin floor, where the tidal current did not affect it to the same extent. This reason may have a stronger impact.

As mention in Chapter 5 according to Hughes (1995) two good rules are available to help evaluate the physical model results: (i) if there is a discrepancy between a theory and the experiment carried out to verify it, it is likely to be due to inaccuracies in the experiments and (ii) it is far more difficult to undertaken good experiments than it is to develop good theories. Therefore, it is thought that this discrepancy could be a problem related to the performance of the experiments.

As Figure 6.18-(a) shows, because of the no-flow condition the velocity magnitudes are approximately zero. Also, in this figure because of flooding the water levels on both sides of the sand embankment are at the high-water-level and so the sand domain is very narrow. In other words, the width of this domain at this time-section is just 4 grid squires. Therefore, the open boundaries of the porous medium domain are very close together. The same problem could be seen in Figure 6.22. Generally speaking, the small domain of the lab application caused some problems, such as what mentioned above.

Figures 6.19 and 6.20 represent the condition of the tracer and related velocities field at mid-ebb and low-water-level stages of the fifth tide, respectively. Generally speaking, good agreement can be seen in these figures between contour level 2 and the tracer plume. In these pictures the plume is bigger than for other pictures as the longest plume, among all plots, can be seen in Figure 6.20, where the dimensions are 2880mm length and 760mm width. However, there is a discrepancy between the contour level 2 and the tracer on the right side, which could be described by the same reason as mentioned earlier regarding the tendency of the dye tracer to go to the right side of the basin.

The last mid-ebb of the simulation is presented in Figure 6.21, where better agreement can be seen, relative to the recent plots, between the numerical out-put and the laboratory observations, see Figure 6.20. It was found from the video film that the tracer discharge to the front of the model at this stage was at a low level and could be related to the rising tide in font of the embankment.

Figure 6.22 is at last high-water and the dimensions of the plume is approximately twice the dimensions of that shown in Figure 6.18, which was illustrated at high-water-level on the 5th tide. The following conclusions can be stated from the comparisons between the dye tracer and lab observations and also a study of the reference video film.

These experiments proved that as the water elevation in front of the sand embankment was falling from high-water to low-water then the tracer was passing through the sand and moving by advection to the weir at a high rate. The study revealed that the tracer plume developed quickly in a family of approximately ellipses from the point source, through both the porous medium and the free surface domain. Also, as the tide was rising from low water to the next high water, the discharge of the tracer from the back of the basin to the front continued. However, in the first case the plume was longer and the discharge rate was higher than for the second case. Furthermore, the shape of the plume from low water to high water was found to be wider than from high water to low water. For instance, this can be seen in comparing Figure 6.20 with 6.22. The same principle could be used to compare the shape of the plume at mid-ebb with the corresponding shape at mid-flood. For example, as shown by comparing Figures 6.19 and 6.21.

It was also found that the number of tidal cycles was an important parameter concerning the size of the tracer plume. It can be clearly seen from the figures that the concentration of the tracer was increased over the tidal cycles, as the tracer colour changed from a light-red colour to a darked colour.

Finally, it was observed that just when high-water occurred, the shape of the plume changed suddenly and it seemed to be dispersed for a while.

6.2.3.1.2 Line Tracer Release

In a similar procedure to the one-point release, with the same concentration and the same tidal cycle conditions, as described in Chapter 5, a second experiment related to the release of tracer through a line along the cross section of the model, as can be seen in Figures 5.24 and 5.27. This test was undertaken to do more investigations of the overall movement characteristics and the behaviour of the dye tracer and to compare the solute distribution with the numerical linked model predictions.

Firstly, the numerical model was run for the initial calibrated dispersivity coefficients of the porous medium, i.e. 1.5 and 0.12 as mentioned before. However, it was decided to re-calibrate the longitudinal and transverse dispersivity coefficients here again, and the coefficients were reduced to 1.5 and 0.1, respectively. These values showed an improvement in the agreement between the numerical model predictions and the video-shots. Therefore, the model was re-run with the value of these coefficients for the dispersivity, which yielded results which were presented in Figures 6.14 to 6.22 before and also in Figures 6.23 to 6.31 below.

As mentioned above, there was an improvement in the agreement between the two data sets because of the re-calibrating of the coefficients, although the discrepancy between these two data sets was not removed completely. This could be attributed to the numerical model approximations. Moreover, the potential problems related to the performance of the experiments were not negligible.

The comparisons between the numerical model predictions and the laboratory observations involved the same technique and the results presented here in Figures 6.23 to 6.31. It should be noted that the time characteristics of these graphical plots are the same as those shown in Table 6.2, except for the time at which the tracer appeared in front of the sand embankment, and here equal 218 s.

As the velocity field characteristics in the above mentioned figures are the same as those of the one-point tracer plots, the velocities are not discussed here again. The study of the line-tracer video film and the related shots demonstrated good agreement between both data sets and the validity of the numerical model predictions. From the model simulations undertaken and also the laboratory results, i.e. Figures 6.23 to 6.31, it was apparent that the movement and spreading of the line-release tracer was somewhat different from the one-point tracer release. This movement appears to be mostly affected by the presence of the entrance edges of the physical model, see Figure 6.25-(a) points P1 and P3. As the edges created two small local diversions in the flow, the tracer tended to move from the sides of the domain rather than from the centre.

Figures 6.23 and 6.24 indicate the initial stages of the simulation for high water and mid-ebb during the 4th tide, respectively. The initial diffusion of the tracer behind the sand embankment can be seen in Figure 6.23 and the influence of the tracer on the porous

Figure 6.23

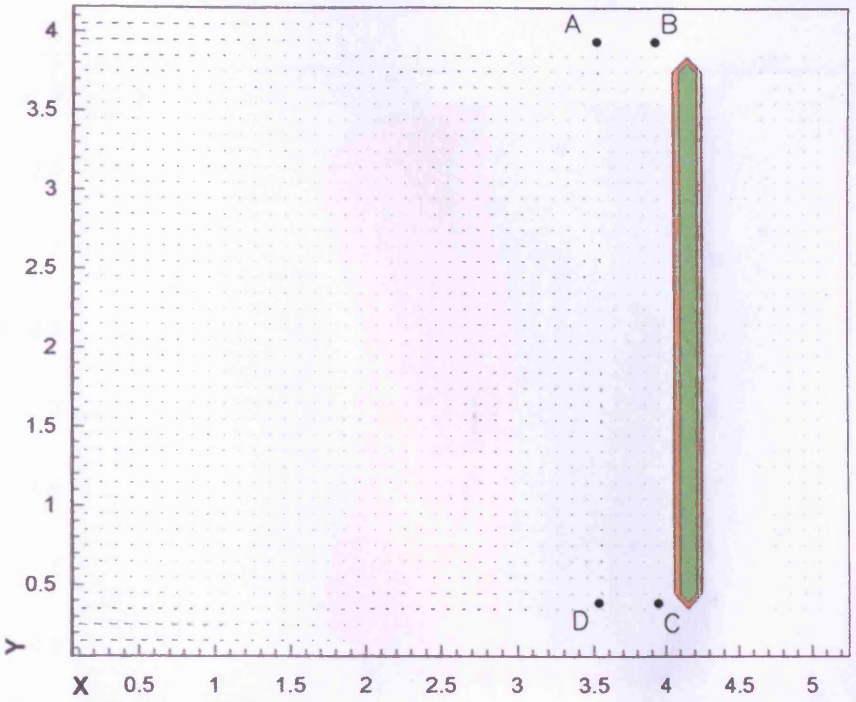

Figure 6.24

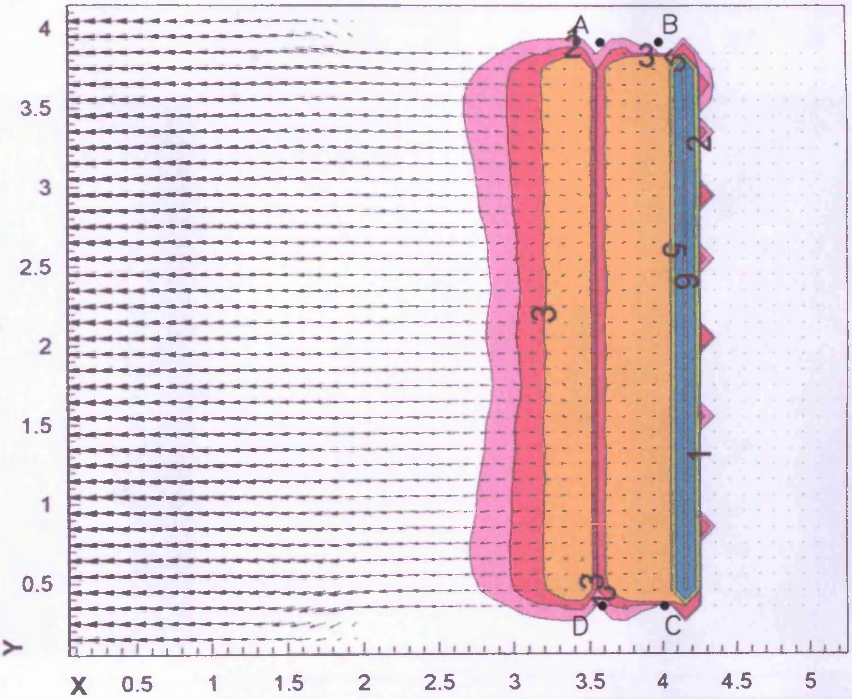

LEGEND

Level	Tracer Dye Concen. (gr/lit.)
7	5
6	2.56503
5	1
4	0.1
3	0.01
2	0.001
1	0.0001

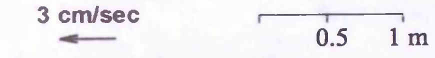

Grid Size 10cm x 10cm

TIDAL DATA

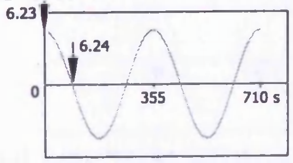

High Water Level & Mid-Ebb
Time = 0.0 & 89 s
Time of Simulation = 30 min

Figures 6.23 and 6.24:

Conservative Tracer Contours and Velocity field Predictions,

Solute Transport Modelling

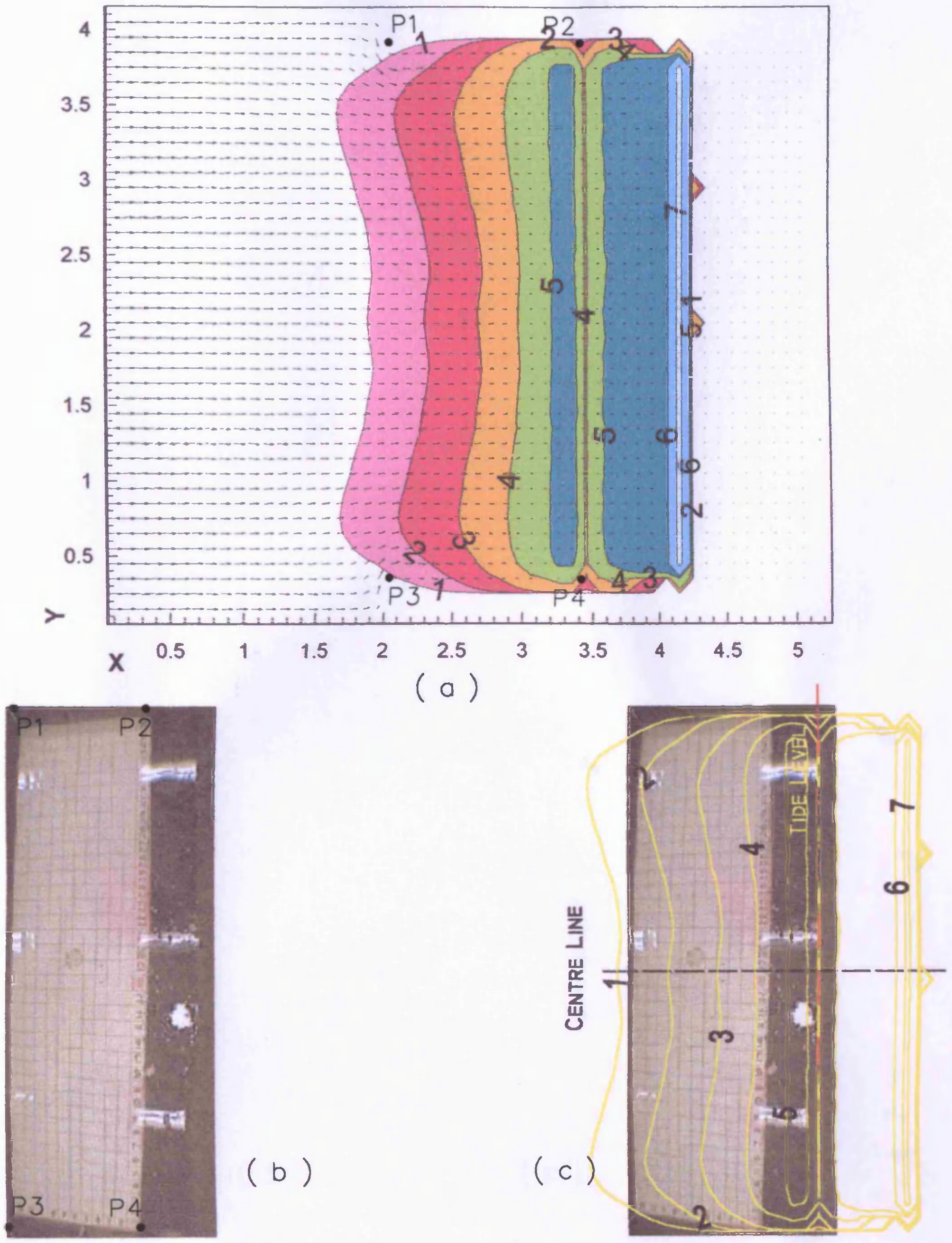

LEGEND

Level	Tracer Dye Concen. (gr/lit.)
7	5
6	1
5	0.1
4	0.01
3	0.001
2	0.0001
1	1E-05

3 cm/sec ←

0.5 1 m

Grid Size 10cm x 10cm

TIDAL DATA

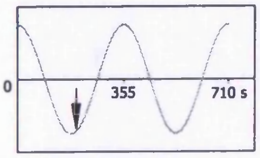

About Low Water Level
Time = 218 s
Time of Simulation = 30 min

Figure 6.25:

Comparison of Numerical Predictions and Laboratory Observation, Solute Transport Modelling

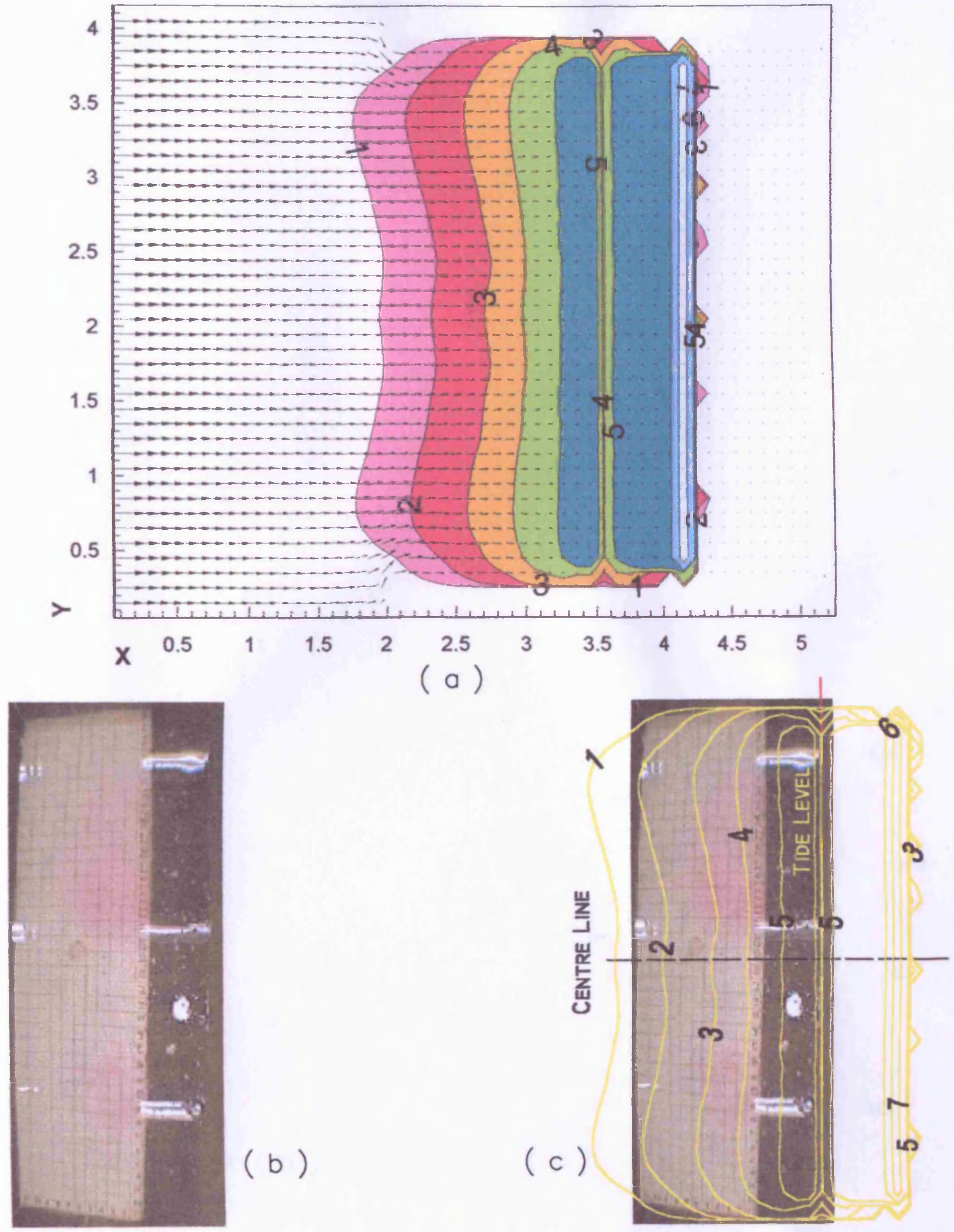

LEGEND

Level	Tracer Dye Concen. (gr/lit.)
7	5
6	1
5	0.1
4	0.01
3	0.001
2	0.0001
1	1E-05

3 cm/sec ⟵ 0.5 1 m

Grid Size 10cm x 10cm

TIDAL DATA

Mid – Flood
Time = 266 s
Time of Simulation = 30 min

Figure 6.26:

Comparison of Numerical Predictions and Laboratory Observation, Solute Transport Modelling

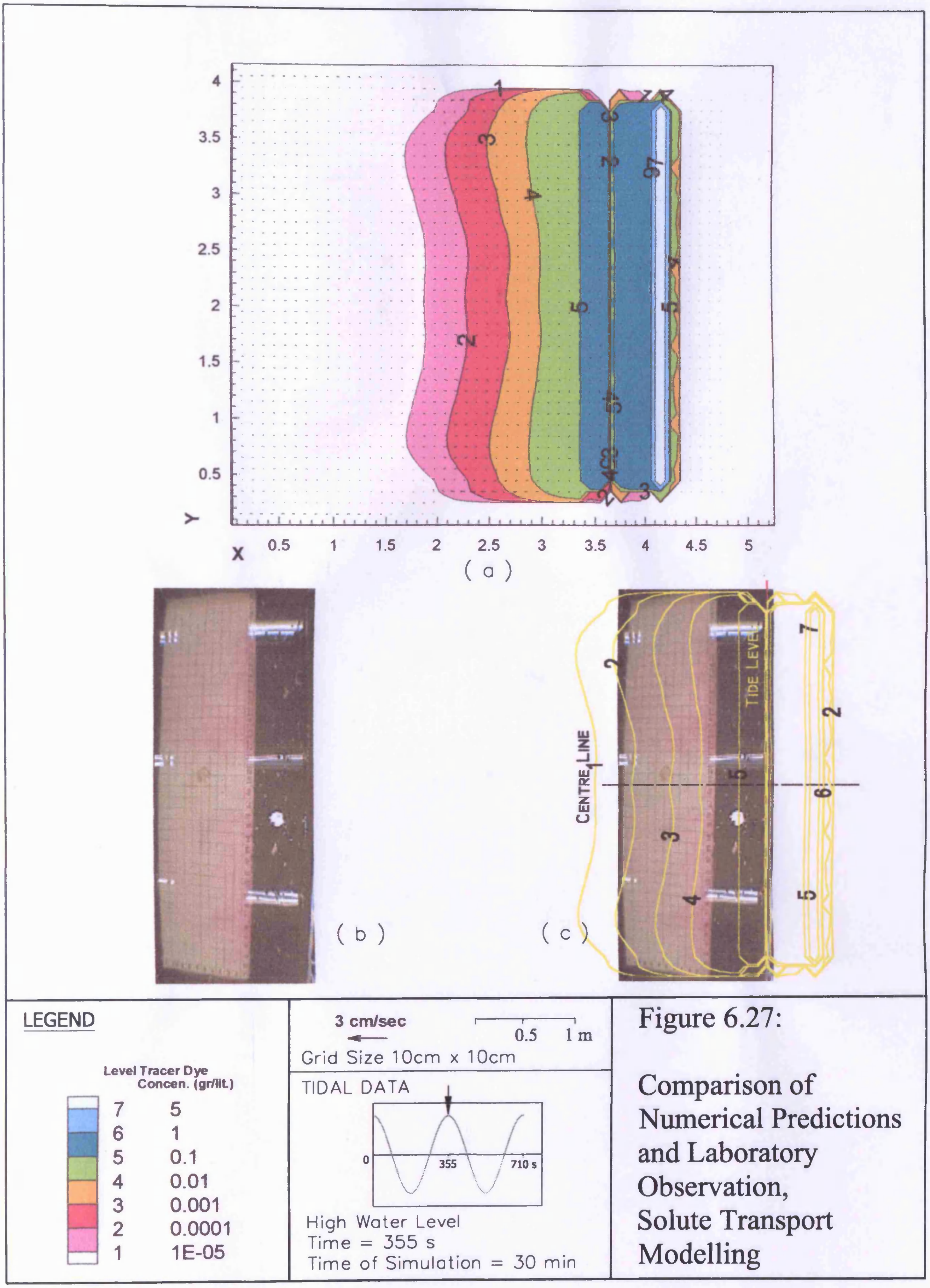

Figure 6.27:

Comparison of Numerical Predictions and Laboratory Observation, Solute Transport Modelling

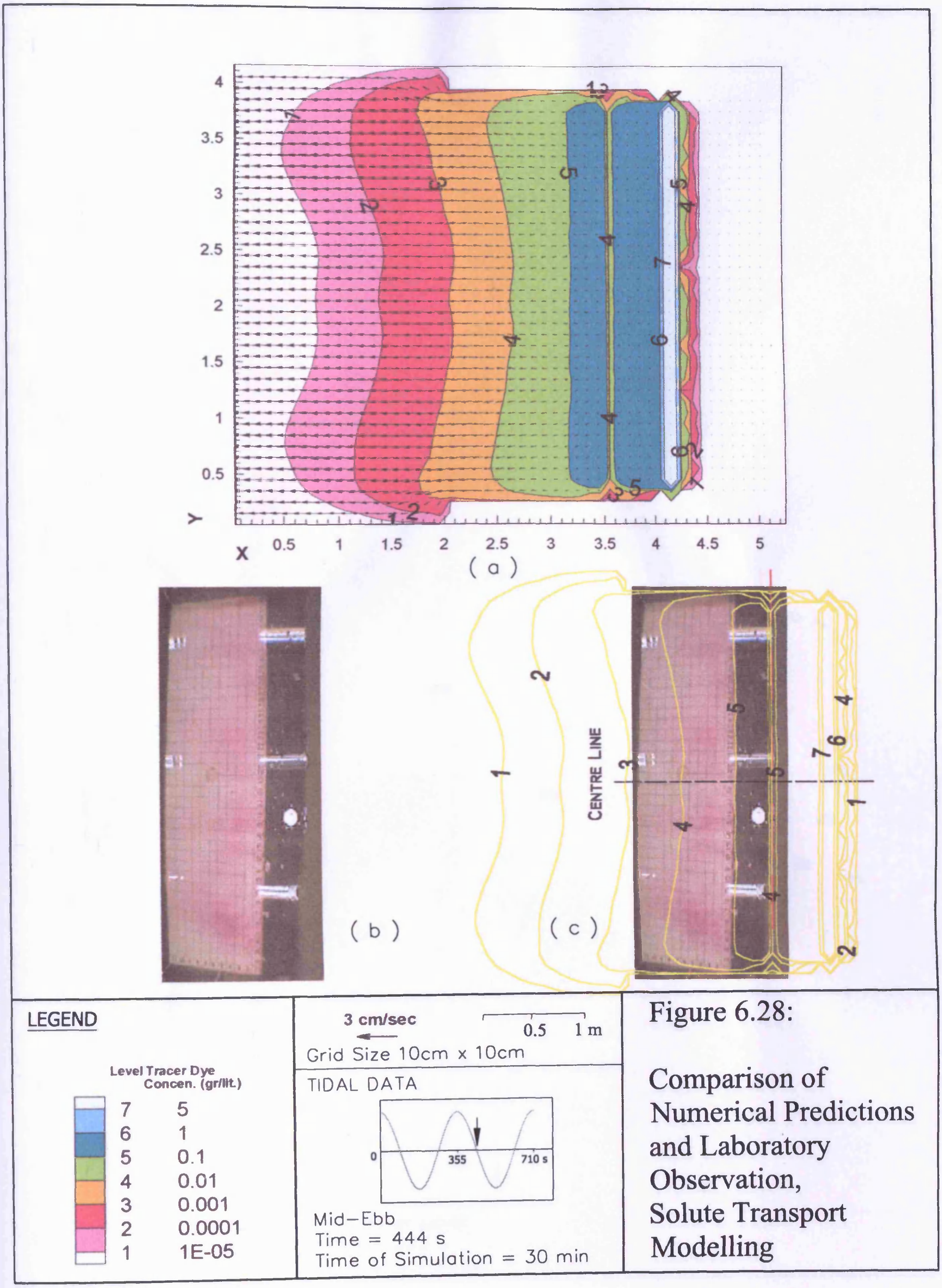

Figure 6.28:

Comparison of Numerical Predictions and Laboratory Observation, Solute Transport Modelling

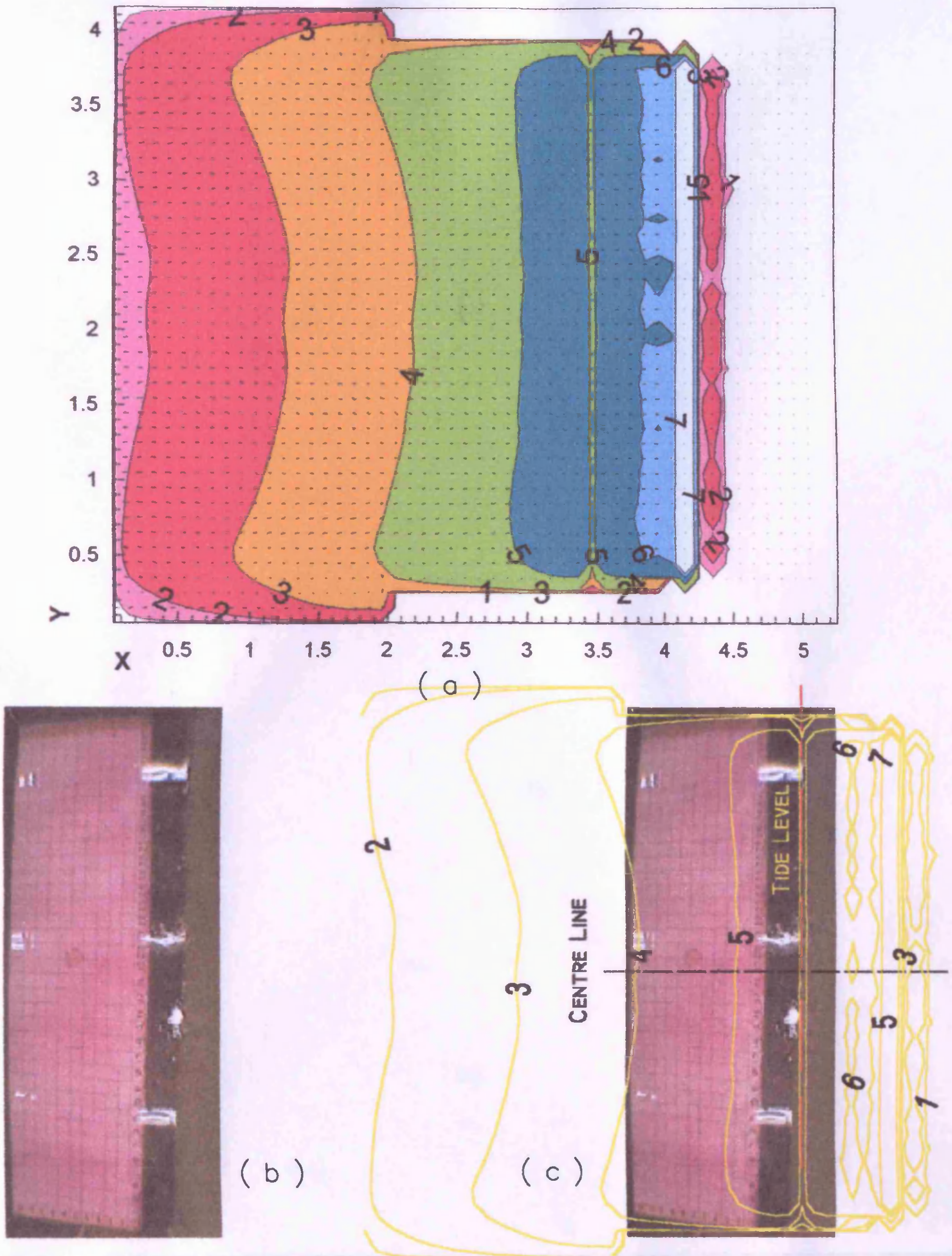

LEGEND

Level	Tracer Dye Concen. (gr/lit.)
7	5
6	1
5	0.1
4	0.01
3	0.001
2	0.0001
1	1E-05

3 cm/sec ←

0.5 1 m

Grid Size 10cm x 10cm

TIDAL DATA

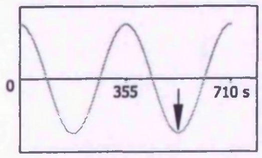

Low Water Level
Time = 533 s
Time of Simulation = 30 min

Figure 6.29:

Comparison of Numerical Predictions and Laboratory Observation, Solute Transport Modelling

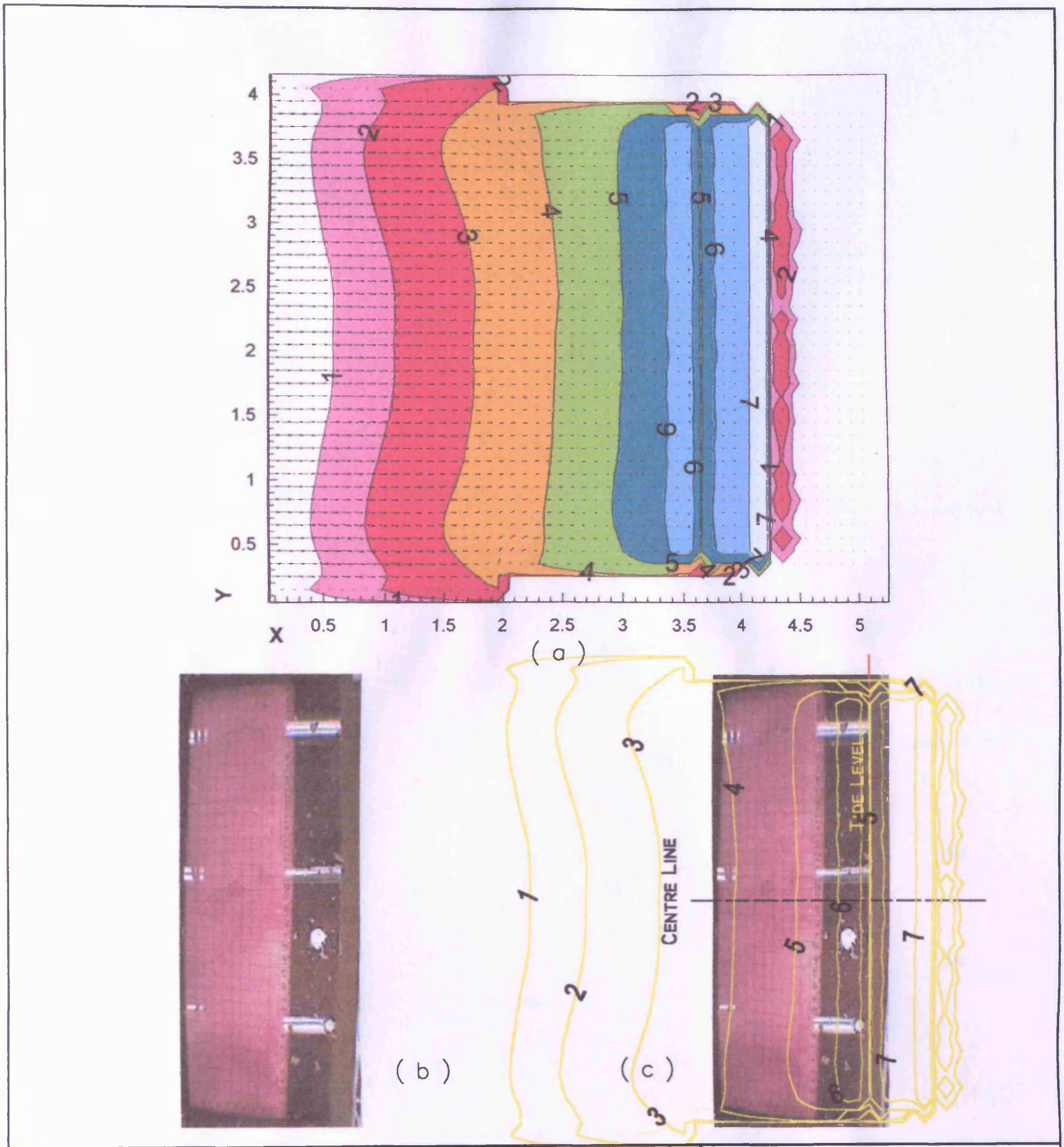

LEGEND

Level	Tracer Dye Concen. (gr/lit.)
7	5
6	1
5	0.1
4	0.01
3	0.001
2	0.0001
1	1E-05

3 cm/sec ← 0.5 1 m

Grid Size 10cm x 10cm

TIDAL DATA

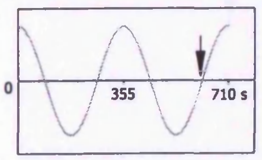

Mid Flood
Time = 621 s
Time of Simulation = 30 min

Figure 6.30:

Comparison of Numerical Predictions and Laboratory Observation, Solute Transport Modelling

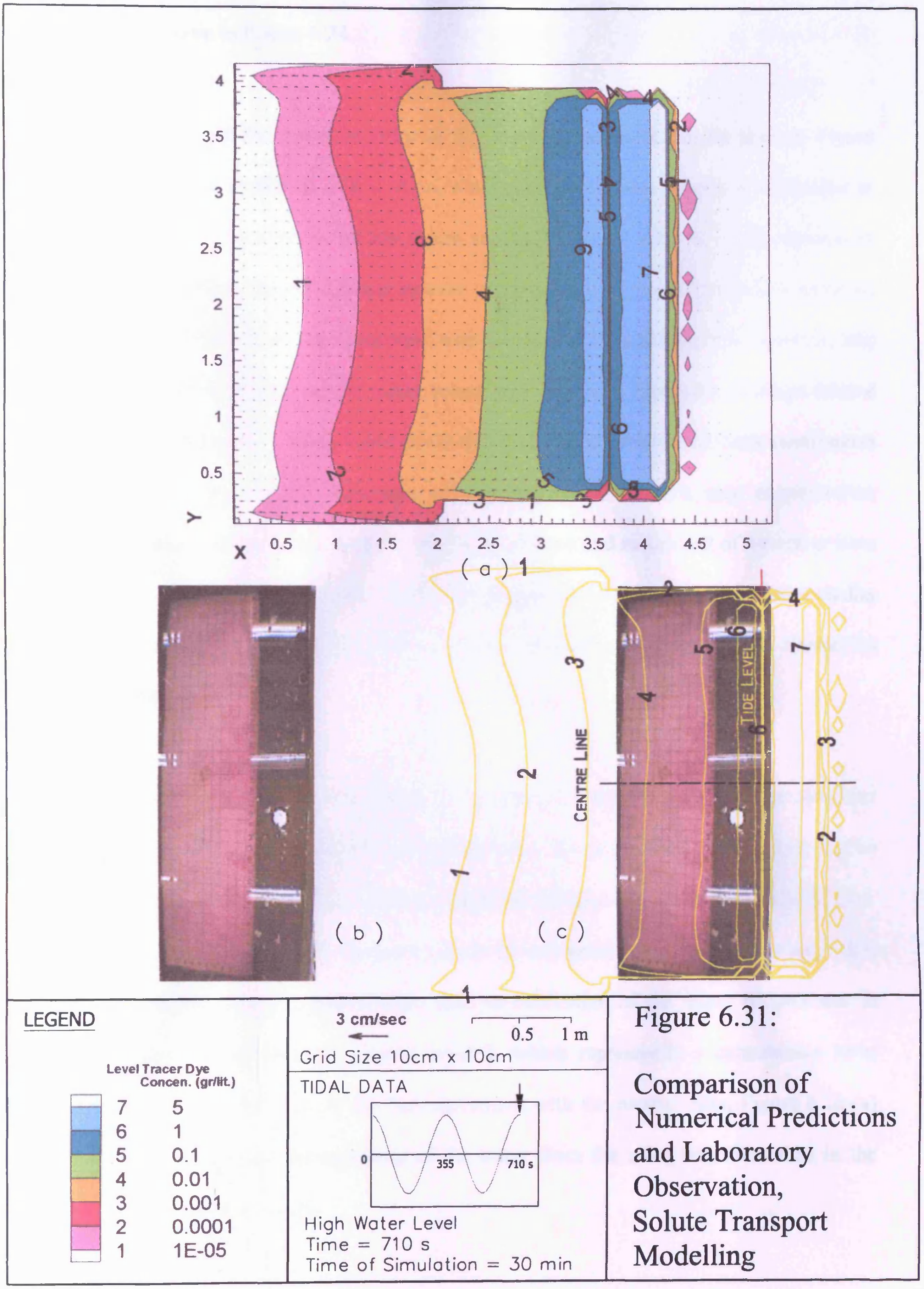

Figure 6.31:

Comparison of Numerical Predictions and Laboratory Observation, Solute Transport Modelling

medium is shown in Figure 6.24.

The appearance of the tracer in front of the sand embankment can be seen in Figure 6.25-(b), again at a time of 218 s. Also, a comparison of these figures is illustrated in Figure 6.25-(c). The pictures in this figure can be compared with the same pictures in Figure 6.16 for the one-point tracer release. According to Figure 6.25 the concentration contour level 3 gave the best agreement with the contaminant distribution, however, this did not seem to be correct as the tracer colour was very light. The same problem existed regarding the one-point tracer release. As in this study the main target of these experiments was to study the overall behaviour of the dye tracer without any concentration measurements, therefore only the predicted tracer plumes and movement of the tracer were compared with the laboratory test results. The suggestions for this case for future studies were based on the results of this study and are given later in this chapter and also in the next chapter.

The next plot, i.e. Figure 6.26, represents the conditions in the comparison of the simulated and the laboratory model results for mid-flood level. As can clearly be seen from Figure 6.26-(b), at this stage the tracer was not completely diffused along the sand embankment, across the model. This could be due to small inhomogeneities in the sand or any other performance errors in the experiments, such as calibration of the tracer nozzles etc. In Figure 6.26-(c) concentration contour level 2, which represented a contaminant level bigger than 0.1gr/l, has shown the best agreement with the plume. Also, Figure 6.26-(a) shows that at this time the spreading of the tracer from the sides was more than in the middle of the physical model.

Figure 6.27 illustrated the conditions of the dye tracer at high-water, in contrast with Figure 6.26. However in this figure time had progressed, but because of the direction of the flow the plume was being pushed back towards the embankment. At this stage, however, the tracer was leaching towards the front of the physical model throughout nearly the whole length of the sand embankment, but it was not uniform.

For the second mid-ebb tidal phase the tracer distribution is presented in Figure 6.28. The main point to note from this figure is the high concentration of tracer on the sides of the model, which can be seen in Figure 6.28-(c) for the contour levels 3 and 4. By this time-phase the tracer had reached the end of the basin and was close to oscillation weir.

A comparison at the last low-water-level of the simulation is shown in Figure 6.29. At this time-phase there was no significant flow. The plume filled the entire front-model, as can be seen in Figure 6.29-(a) and (b). Another point related to this figure is that the spreading of the tracer in the cross-section was approximately uniform.

Figure 6.30-(a) and (b) illustrate the results of the second mid-flood for the numerical model predictions and the laboratory model observations, respectively. The figures show a high concentration of tracer on both sides of the model.

The last comparison between the numerical model results and the laboratory model observations could be found in Figure 6.31. However, it is difficult to obtain satisfactory information regarding the migration of the tracer at this time stage; according to the video film and the numerical model prediction it could be said that at this phase the tracer plume was being pushed back towards the head of the basin. Also in this stage the movement of the tracer along the shared boundary between the sand embankment and the front of the model was temporarily stopped. Moreover, the plume was less diffuse at this stage relative to that shown at the previous stage.

It can therefore be concluded from all of the tracer release results represented herein, that the laboratory model observations generally verified the numerical model predictions and the dye tracer behaviour in both cases. Moreover, both simulations have shown acceptable agreement with the laboratory model results. However, it should be noted that the thoughts and explanations of these results, though based on relevant bases, are perhaps better considered as suggestions for further studies in this case, since they are not direct evidence of the application of the solute transport test data. Therefore, further investigations are strongly encouraged and these comparisons of the dye tracer results should be considered as preliminary in nature.

Also, in the used image method some potential disadvantages, were experienced, such as a diversion in the results due to the large size of the physical model and the usage of a wide angle lens. This was exacerbated further by the inappropriate degree of light and its intensity. Therefore, it is worth suggesting, using of an improved light system in future studies. Also, using more than one camera along the basin could improve the recorded results dramatically.

6.3 Summary

This chapter has considered the application of the numerical linked model to a physical model of tidal oscillating flow through a sand embankment. Comparisons at specific locations between the numerical model predictions and the measured water elevations and velocities were presented for different tidal cycles. A conservative tracer study was carried out to investigate the validation of the numerical linked model predictions. The numerical model predictions and the laboratory model measurements for both the hydrodynamic and solute transport, (i.e. dye tracer) fluxes were compared and the results were generally in good agreement. Although, very encouraging results regarding the hydrodynamic processes were obtained, the solute transport modelling needs to be compared with more field data in future studies. Finally, from the encouraging results of the numerical linked model simulations and its application, it can be concluded that the numerical linked model is appropriate for application to natural combined surface and subsurface environments. Applying the new developed model could be a good opportunity to refine that more than before.

CHAPTER 7

CONCLUSIONS AND RECOMMENDATIONS

7.1 Review and Conclusions

As mentioned in Chapter 1, the main objective of this research study has been to develop and verify an innovative integrated numerical model to achieve a wider scientific understanding of interactions between wetland areas, the neighbouring coastal waters and the groundwater passages. Following a review of previous studies in this field, it was found that most effort has been focused on individual studies of one or two of these phenomena. Hence, the emphasis of this research study has been to study the interaction between these three key water bodies. To achieve this aim, development of a process based generic numerical model has been targeted to gain a more detailed comprehension of water and solute pathways in combined surface (both wetland and coastal waters) and subsurface environments.

Therefore, the main developments and findings from this study can be summarised as follows:

In the first stage of the study a two-dimensional time dependent numerical model, **GWK** (Ground **W**ater **K**ey), based on an alternating direction implicit (ADI) finite difference scheme has been developed. The time variant Boussinesq and continuity equations have been derived, with the relevant assumptions being discussed in detail in Chapter 2.

The finite difference method has been deployed, using a uniform space staggered mesh, and with the discrete equations being solved using the ADI technique. Hence, the numerical scheme remains unconditionally stable. The GWK model has been coded in Fortran 77. Details of derivation of the scheme are outlined in Chapter 3, with the solution procedure of the matrix being given in the same Chapter.

The GWK model is capable of predicting the hydraulic head (i.e. water table), the velocity components in the horizontal plane, the effect of recharges/discharges and sources/sinks, on the water table and solute tracer levels across the domain as functions of time. The structure of the GWK model links well dynamically with the free surface flow model. In the hydrodynamic part of this model, a new technique of using two dependent separate time steps has been deployed, i.e. the main and sub-time steps, thereby enabling the model to predict the water table using both implicit and explicit methods, as described in detail in Chapter 3. However, it is worth noting that the GWK model has been developed in order to be linked to the DIVAST model. It can also be easily applied independently to any kind of porous medium system. In this model, there are no restrictions on the number of sources/sinks and all information may be passed to the model via a data file. The same flexibility can be found in the specification of the open boundary conditions.

However, it should be noted that the GWK model has its own capabilities, as its structure has been organised to be deployed for specific conditions.

Three numerical test cases were carried out to evaluate the accuracy of the GWK porous media numerical model. For this evaluation, the model was applied to an idealized porous media domain with different conditions of dye tracer and sources/sinks of water. It was found from simulation results that the hydrodynamic parameters and the tracer contaminant distribution in the test domains were symmetrical, as to be expected. The graphical results and related discussion of these test cases are given in Chapter 4.

In the second stage of this research study, the GWK numerical model has been dynamically linked to the two-dimensional free surface numerical model, DIVAST, in order to simulate the interaction between wetlands and coastal waters via groundwater flow paths. The dynamic link approach and the related flowcharts are given in detail in Chapter three. The linked numerical model reads the necessary information for each surface/subsurface field, through separate data files. However, it generates both shared and independent output files. The shared output file of the linked numerical model is arranged in an acceptable Tecplot input format file, thereby enabling the user to create both animation/time-stage graphical plots.

In the third stage of the study, in order to calibrate and verify the linked numerical model, a series of experimental tests were undertaken for an *idealized-design* scale physical model. This model was based on a typical prototype example, namely Fleet lagoon and the adjacent coastal waters. In this case previous studies related to the Fleet lagoon have been reviewed and presented. The aim was to study seepage behaviour through a sand embankment by recording the fluctuations in water levels, at either side of the embankment, point velocities and distribution of a conservative tracer. For each case considered there was an oscillating tide on one side of the sand embankment. Velocity components were measured at several points along a cross section within the physical model. Then the measured velocity data were presented graphically over two repetitive tides to be compared with the numerical model results. In order to record the dye tracer behaviour within the physical model, a new release system of dye tracer was constructed and deployed. The dye tracer release system was calibrated and used to study the behaviour of the tracer for two different tracer experiments. Recorded video films were used to extract photographic shots at different tidal phases, to be compared with the numerical linked model predictions. Further details are given in Chapter 5.

The application of the numerical model to the physical model has been given in Chapter 6. The numerical model results have been compared with the laboratory test results. Although, there were slight differences between the numerical model predictions and the laboratory observations in the tracer results, it was generally found that there was good agreement between the predicted and measured data. From the encouraging results of these comparisons, which were made between the linked model predictions and the laboratory results, it was concluded that the linked numerical model was appropriate for application to natural combined surface and subsurface environments.

7.2 Recommendations for Further Study

However, the main aim of this research study, which has been to develop an integrated 2-D numerical model to predict the hydrodynamic and solute transport phenomena in combined subsurface/free surface environments, has been achieved. In order to improve the developed model and also to extend this research study in future, the following aspects are worthy of further consideration:

In numerically modelling the hydrodynamic field of a porous media, three-dimensional simulations may give better results due to the three-dimensional properties of the phenomena. It should be noted that this aspect was ignored in this research study as the seepage face was ignored, for full detail see Chapter 6. However, care should be taken since if a three-dimensional model is to be used, then some difficulties may arise in that insufficient computer capacity may be available or the run-times become unduly long. In turn, this might discourage the use of three-dimensional modelling.

In this research study, the values of the longitudinal and transverse dispersivity coefficients of the porous medium in the advective-diffusion equation were taken as suggested by, Spitz, K., and Moreno, J., (1996). Although the values were then calibrated against the laboratory data for the specific application to this study, it would be useful to investigate the effects of using different coefficients on the predictions of the solute transport levels. However, although the advective term is generally the most significant in predicting the transport of a solute, for low velocity flow conditions such as porous media flows, the dispersion term is generally also dominate. Therefore, it would be useful to investigate the enhanced accuracy of longitudinal dispersion coefficients using in two-dimensional porous media sub-model.

In the context of this study, salinity effects were not investigated. However, this constituent may have an important impact on the solute distribution, as well as on the hydrodynamic parameters. Therefore, the inclusion of salinity in the numerical model and the collection of new laboratory data sets with salinity for validation of the model would be an improvement in the model applicability, especially for practical case study applications.

In the recent years there have been many investigations undertaken to predict the transport of solute particles under tidal current conditions. As in this research study just a fixed tide period has been considered in the simulations. Therefore, it would be useful to study the individual effects of different tide periods and also the interaction of waves and tidal currents on the transport of pollution in combined environments.

It has been well documented that the mortality rate of pathogens is dependent upon many factors in the natural environment. Development of this research study to improve the predictive capability of the linked numerical model by an investigation into the nature of bacterial concentrations and the effect of porous media on these indicators could be undertaken. In this case the linked numerical model should be refined to include predictions of water quality indicators. The recommended investigation with the introduction of formulations to define relationships between these environmental factors and the combined water bodies could give a better understanding of the interaction between subsurface/free surface environments. Therefore, the accuracy of the model may be increased for predicting the quality of groundwater and coastal waters.

The physical model used in this study was an especially appropriate tool for validation and calibration of the hydrodynamic part of the linked numerical model. However, it produced good results in predicting and studying the transport of a conservative dye tracer, but the size of the physical model was not big enough to study the distribution of the tracer as much as would have been preferable. Thus, further laboratory experiments for the solute transport part could be set up by using a bigger tidal basin.

Finally, accommodation of the linked numerical model with a user-friendly interface to formulate it as an integrated hydro-informatics software tool would make it available to a wide group of potential users.

APPENDIX A

MOVING SHORELINE AND THE MOBILE BOUNDARIES OF FREE SURFACE AND GROUNDWATER FLOW

In this Appendix, details are given of numerical representation of flooding and drying and moving shared-line, share mobile boundaries in groundwater and free surface phenomena, to the numerical linked two-dimensional depth average free surface and groundwater model.

As mentioned in Chapter 3, section 3.5 (Dynamic Linked Model Approach), the linked numerical model includes; shared time controller, shared mobile boundaries of flow (water elevation and discharge-recharge), shared mobile boundaries of solute concentrations. Therefore, flow and tracer are able to pass across the shared boundaries in both directions, depending on the relative height of the water table. Here, firstly the details of the flooding and drying approach are given. Then the situation of the free surface and groundwater grids on both sides of a shared-line, neighbouring of mobile boundaries on the both sides of a shared-line, is described.

The flooding and drying approach used in this research study was first developed and refined on the basis of some numerical tests which were undertaken for a series of idealized applications and then has been successfully applied to a number of different sites. A brief description of the above mentioned approach is given herein, however, for more details the reader is referred to Falconer and Chen (1991).

In modelling numerically the flooding and drying of shallow reaches throughout the tidal cycle, considerable numerical problems can arise as a result of the discretized representation of this hydrodynamic process which generally varies in a smooth manner.

The process of the above mentioned approach is outlined as follows:

a. In the free surface module of the numerical linked model, at the end of every half time step, the new total depth of water is calculated first at the *centre of each side* of every wet grid square. For example, using the notation given in Figure A.1 below, the total depth of water at the velocity location *Ui+1/2, j* is defined as

$$HX^n_{i+1/2,j} = h_{i+1/2,j} + \frac{1}{2}(\zeta^n_{i+1,j} + \zeta^n_{i,j}) \tag{A.1}$$

where *HX* is the total depth at the centre of the grid square side in the *x* direction (and similarly for *HY*); *h* is the depth below datum; and *n* is the time step level. Using the Nikuradse parameter *ks* to characterize the bed surface roughness, together with the Colebrook-White equation to evaluate the friction factor *f*, the depth at the centre of all grid square sides is then compared with the corresponding *ks* value. If any side depth becomes less than *ks*, i.e. the bed form height during any half time step, then the corresponding depth (e.g.*HX*) and the corresponding velocity component (e.g. *U*) are both equated to zero.

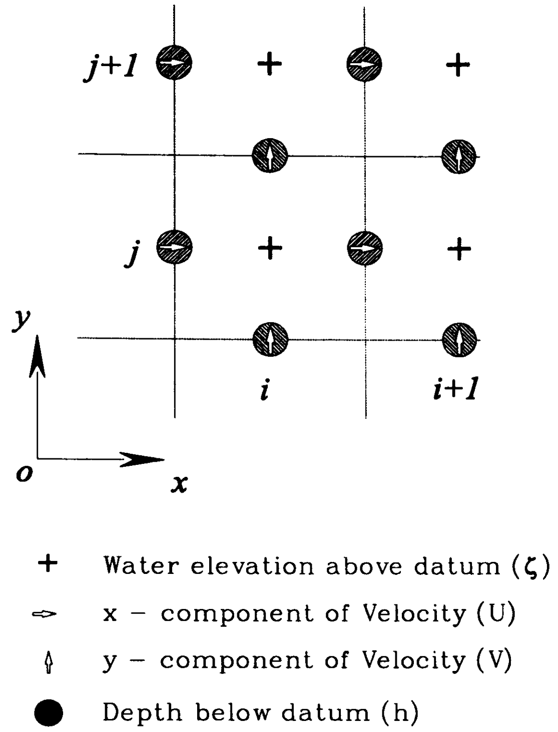

Fig. A.1: Computational space staggered grid

It is worth highlighting at this point that in the modelling of flooding and drying there are two advantages in using the parameter *ks* to represent the bed roughness rather than other friction formulae such as Manning or Chezy. Firstly, for such shallow depths, Reynolds number effects may become significant and these hydrodynamic phenomena can be represented only by using the roughness parameter *ks* and the Colebrook-White equation or the Moody diagram. Secondly, in using *ks* to represent the bed roughness, this can be related directly to the minimum physical depth governed by the bed roughness, e.g. the dune height, rather than the Manning number or Chezy value, neither of which relate directly to a physical depth.

b. If all four side depths for any grid square are less than *ks* (or equate to zero) then the grid square is effectively dry and the cell is removed from the computational domain. The water elevation and the solute concentration levels for the grid square are equated to the corresponding values at the end of the previous half time step when the cell was last wet.

c. In addition to the above checks, the average depth is calculated also at the centre of every wet grid square, for each half time step. Again using the notation given in Figure A.1, the centre depth is defined as

$$HCEN_{i,j}^{n} = \frac{1}{4}(h_{i+1/2,j} + h_{i-1/2,j} + h_{i,j+1/2} + h_{i,j-1/2}) + \zeta_{i,j}^{n} \tag{A.2}$$

where *HCEN* is the depth at the centre of cell *i,j*. If this depth is less than *ks*, then the grid square is also assumed to be dry and the water elevation and solute concentration level set to their previous values as before.

d. For the final drying check, all wet grid squares where the centre depth *(HCEN)* is less than a predetermined value *PRESET* (typically2 ~ 2.5 *ks)* are considered potentially dry. If at least one water depth around the four sides of the grid square is greater than *ks*, and *HCEN* is less than *PRESET* but greater than *ks,* then this grid square will be assumed to be dry unless the flow direction from the adjacent wet grid square-connected by way of the depth greater than *ks*-is towards the potentially dry grid square. If the flow direction is out of the potentially dry grid square then the grid square will be removed, from the free surface domain, as before.

Following these drying checks, all dry grid squares are then considered for possible flooding. In these tests, a currently dry grid square will be returned to the computational domain of free surface phenomenon if *all* of the following conditions are satisfied

(a) any one of the four surrounding grid squares is wet

(b) the water elevation of the surrounding wet grid square(s) is higher than that of the dry grid square i,j

(c) the total depth of the cross section connecting the wet grid square(s) and the dry grid square is greater than *ks*

(d) the depth at the centre of the dry grid square *(HCEN)* is greater than *ks*.

If a dry grid square is assumed to flood and be returned to the computational domain of the free surface phenomenon, then the depths of the four surrounding cross-sections are calculated and the grid square is reintroduced into the calculations at the start of the next half time step.

The plan and vertical section of a shoreline and the location of moving boundaries of combined groundwater-free surface flow are shown in Figure A.2 – *a* and *b*, respectively. As can clearly be seen in Figure (A.2-a), when the water level, in the 2-D depth integrated model, in the free surface area, moves, e.g. going down from positions *1* to *2,* during a half time step, if according to the flooding and drying criteria, which described in this appendix earlier, the cell i is known as a dry grid square. Then the mentioned grid square will be removed from the free surface computational domain and will be added to the groundwater domain.

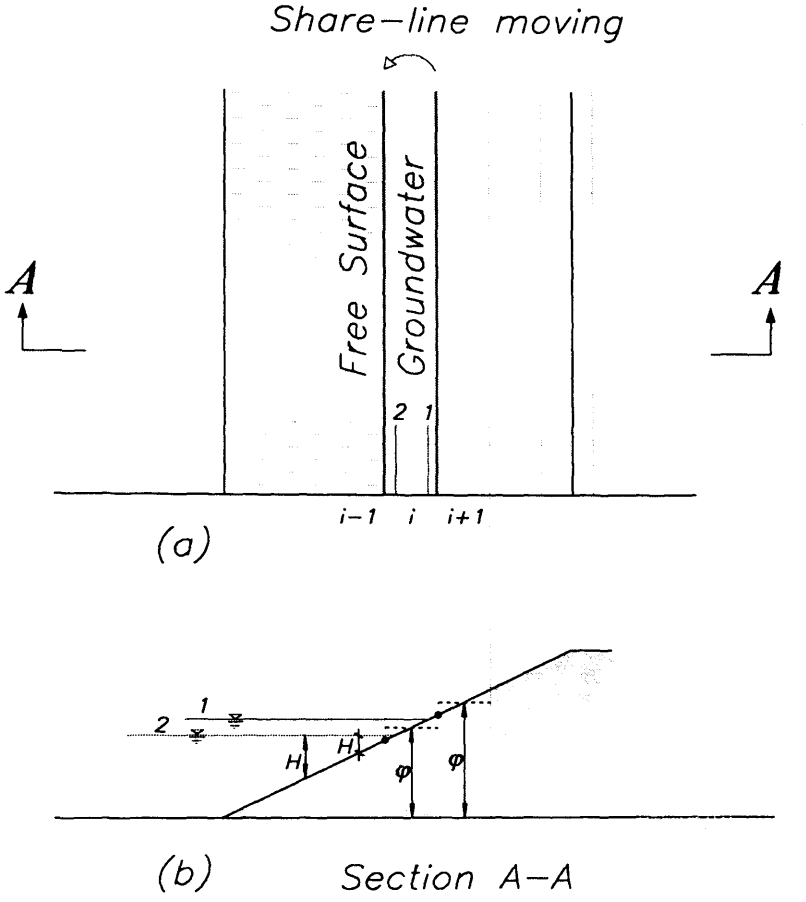

(Pictures are not to scale)

Figure A.2: Moving shoreline and groundwater-free surface grids

This is illustrated in more detail in Figure A.2-*b* where the total head in groundwater and free surface domains are notated by φ *and* H, respectively.

It should be noted that when a grid is included in either free surface or groundwater flow domains, the relevant conservation equations are solving for the hydrodynamic and solute transport modelling for the included cell at each half time step. Hence, flow and tracer are able to pass across the share boundaries in both directions, depending on the relative height of the water table. It should be noted that, the above method contains a small approximation with regard to the conservation of mass at the groundwater-free surface interface.

However, as both computational domains are changing during sequential half time steps along the neighbouring cells, grid by grid not point by point, i.e., along the twin mobile boundaries, and both of the sub models are depth average 2-D model in plan. Therefore, the numerical linked model is capable to simulate a combination of free surface-groundwater flow phenomenon with a high degree of accuracy in a two-dimensional scheme. This is demonstrated by comparing of numerically predicted and laboratory measured data in Chapter 6.

APPENDIX B

TIME VARIATIONS IN WATER LEVELS FOR TEST CASES 1, 2 AND 3

(SEE CHAPTER 4)

Fig. B.1: Time Variations in Water Levels (Test 1- Point 1)

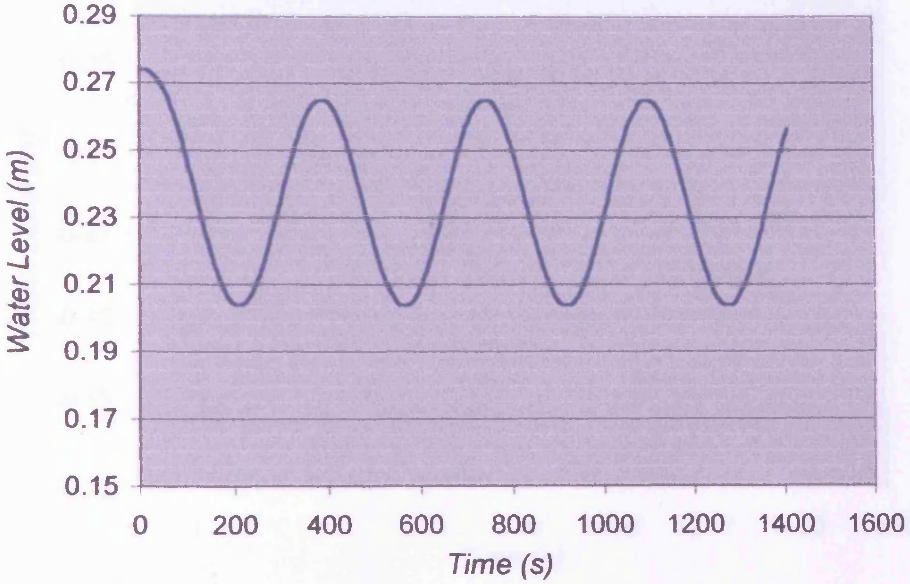

Fig. B2: Time Variations in Water Levels (Test 1-Point 2)

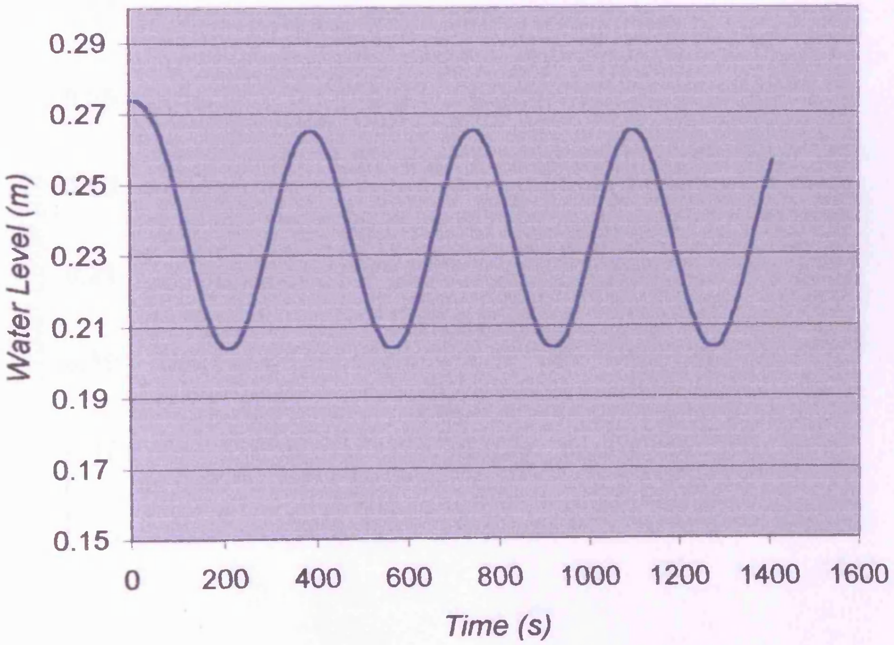

Fig. B.3: Time Variations in Water Levels (Test 2-Point 1)

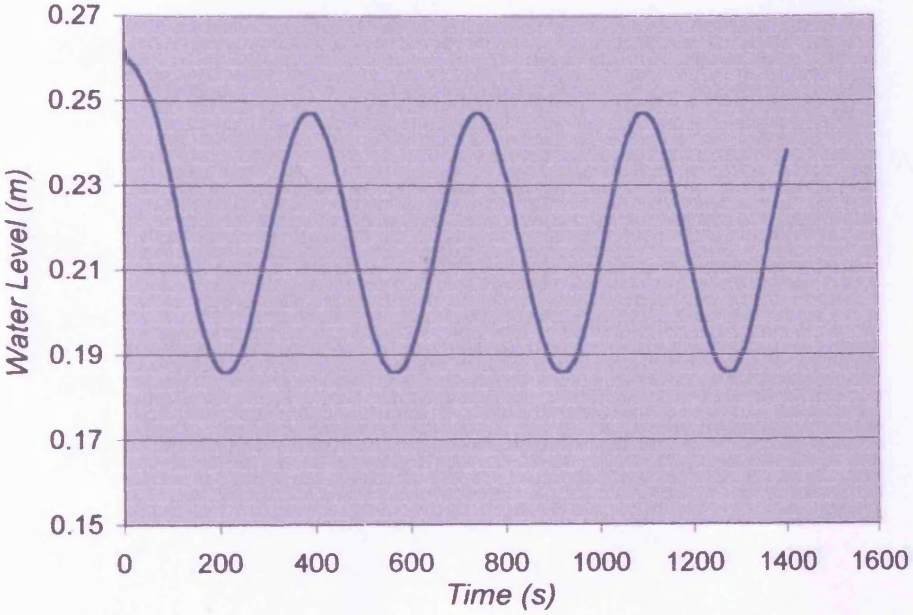

Fig: B.4: Time Variations in Water Levels (Test 2- Point 2)

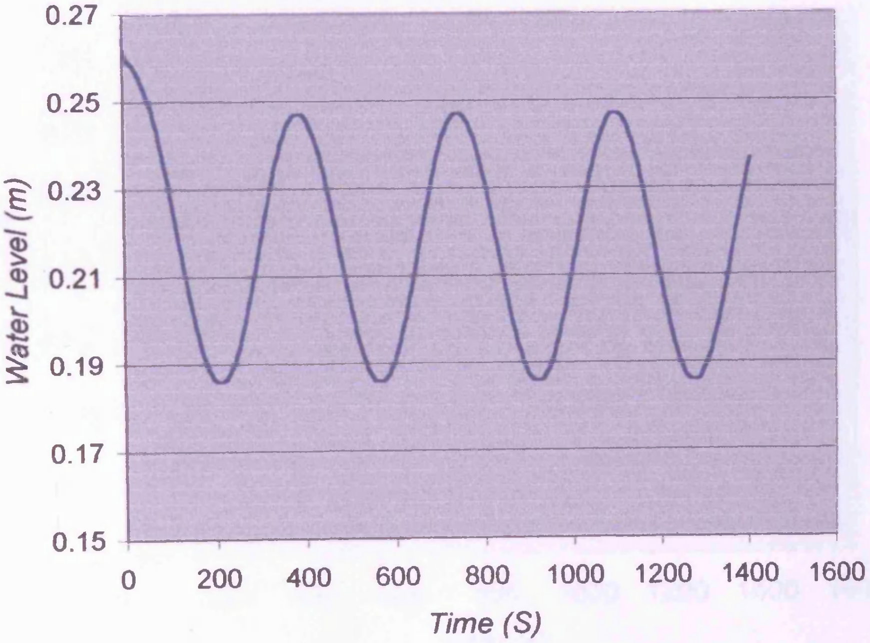

Fig. B.5: Time Variations in Water Levels (Test 3-Point 1)

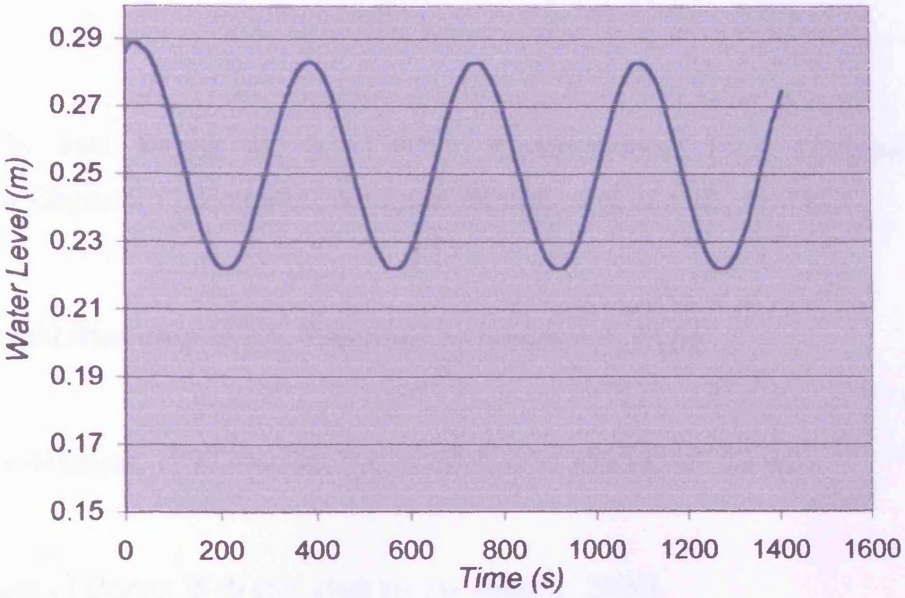

Fig. B.6: Time Variations in Water Levels (Test 3- Point 2)

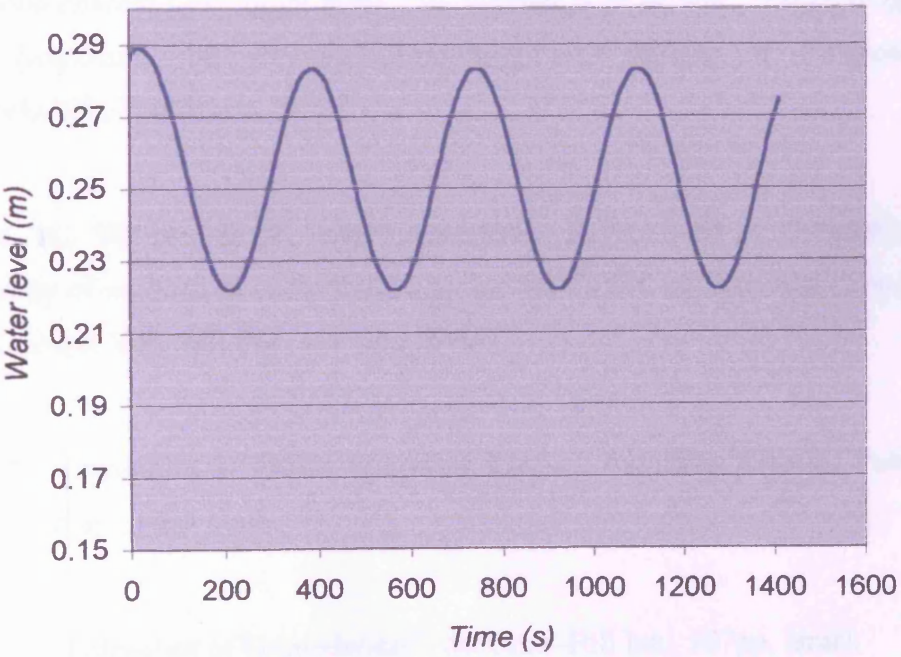

REFERENCES

Abbott, M. B. and Basco, D. R., (1997), "Computational Fluid Dynamics: An Introduction for Engineers" Longman Singapore Publishers (Pte) Ltd., pp. 425.

ADV Operational Manual, (1997), Published by Nortek AS, 33 pp.

ADV Software Manual, 1997, version 2.6, published by Nortek AS, 24 pp.

Allen, J., Images of Dorset Web site, (last access January. 2004), http://www.imagesofdorset.org.uk/Dorset/101/08.htm

Allersma, H. G. B., and Esposito, G. M., (2000), *"Optical Analysis of Pollution Transport in Geotechnical Centrifuge Tests"*, In: Garnier, J. et al. eds., *'Proceeding of the International Symposium on Physical Modelling and Testing in Environmental Geotechnics'*, NECER, France, pp. 3-10.

Ataie-Ashtiani, B., Volker, R. E. and Lockington, D. A., (1999), "Numerical and experimental study of seepage in unconfined aquifers with a periodic boundary condition", *Journal of Hydrology*, Vol. 222, No. 1-4, pp.165-184.

Bear, J., (1972), "Dynamics of Fluids in Porous Media", American Elsevier Publishing Company, Inc., 764 pp., New York.

Bear, J., (1979), "Hydraulics of Groundwater", McGraw-Hill Inc., 567pp, Israel.

Bijker, E. W., (1967), "Some Considerations about Scales for Coastal Models with Moveable Beds", Delft Hydraulics Laboratory, Technical Report No.50, 142pp.

Chen, Y., (1992), "Numerical Modelling of Solute Transport Processes Using Higher Order Accurate Finite Difference Schemes", PhD Thesis, University of Bradford, England.

Chow, V. T., (1973), "Open Channel Hydraulics", McGraw Hill Book Co., 680 pp., Singapore.

Crowe, A. S., Shikaze, S. G., Schwartz, F. W., (1999), "A grid generating algorithm for simulating a fluctuating water table boundary in heterogeneous unconfined aquifers", *Advances in Water Resources*, Vol. 22, No. 6, pp.567-575.

Ebrahimi, K., and Fardad, H., (1999), "Comparison of Some Determination of Hydraulic Conductivity Coefficient in Saturated Soil Condition", *Iranian Journal of Agricultural Sciences,* Vol. 29, No.4, pp.657-666.

Ebrahimi, K., (1994), "Comparison Between four methods of determination of Hydraulic Conductivity Coefficient", M.Sc. Project, University of Tehran, 327 pp.

Edwards, A.C., Heathwaite, A.L. and Dils, R., (2000), "Nitrogen", In: "*Diffuse Pollution Impacts*", D'Arcy, B.J., Ellis, J.B., Ferrier, R.C., Jenkins, A. and Dils, R. (Eds.), Terence Dalton Publishers, Suffolk, pp.61-72.

Elder, J. W., (1959), "The Dispersion of Marked Fluid in Turbulent Shear Flow", *Journal of Fluid Mechanics,* Vol.5, No.4, pp.644-560.

Engelund, F., and Hansen, E., (1967), "A Monograph on Sediment Transport in Alluvial Streams", Teknisk Florlag, Copenhagen.

Esposito, G., Allersma, H. G. B., Soga, K., Kechavarzi, C. and Coumoulos, (2000), "*Centrifuge Simulation of LNAPL Infiltration in Partially Saturated Porous Granular Medium*", In: Garnier, J. et al. eds., '*Proceeding of the International Symposium on Physical Modelling and Testing in Environmental Geotechnics*', NECER, France, pp. 277-284.

Falconer, R. A. and Chen, Y., (1991), "An Improved Representation of Flooding and Drying and Wind Stress Effects in a Two-Dimensional Tidal Numerical Model", '*Proceedings of the Institution of the Civil Engineers,* Part 2, Vol.91, pp.659-678.

Falconer, R. A., (1992), "Coastal Pollution Modelling, Why We Need Modelling: An Introduction", In: '*Proceedings of the Institution of the Civil Engineers, Water Maritime and Energy*', Vol. 96, pp. 121-123.

Falconer, R.A. and Li, G., (1994), "Numerical Modelling of Tidal Eddies in Coastal Basins with Narrow Entrance Using $k-\varepsilon$ Turbulence Model", in Mixing and Transport in the Environment, eds. K.J. Beven, et al., John Wiley & Sons Ltd., London, pp. 325-350.

Falconer, R. A., (1976), "Mathematical Modelling of Jet-Forced Circulation in Reservoirs and Harbours", PhD Thesis, Imperial College, University of London.

Falconer, R. A., Lin, B., Harris, E. and Kashefipour, S. M., (2000), "DIVAST model reference manual", Environmental Water Management Research Centre, Cardiff School of Engineering, Cardiff University.

Fischer, H. B., List, J. E., Koh, R. C. Y., Imberger, J. and Brooks, N. H., (1979), "Mixing in Inland and Coastal Waters", Academic Press, Inc., San Diego, pp.483.

Franks, T. and Falconer, R. A., (1999), "Developing Procedures for the Sustainable Use of Mangrove Systems", *Agricultural Water Management,* Vol. 40, pp.59-64.

Fredericks, J. W., Labadie, J. W. and Altenhofen, J. M., (1998), "Decision Support System For Conjunctive Stream-Aquifer Management", *Journal of Water Resources Planning and Management,* Vol. 124, No.3, pp.69-78.

Freeze, R. A. and Cherry, J. A., (1979), *"Groundwater"*, Prentice-Hall, Inc., Englewood Cliffs, N.J., 604pp.

Hakimzadeh, H., (1997), "Turbulence Modelling of Tidal Currents in Rectangular Harbours", Ph.D. Thesis, University of Bradford, Bradford, UK, 336 pp.

Harris, C., Davies, M. C. R., and Depountis, N., (2000), *"Development of a Miniaturised Electrical Imaging Apparatus for Monitoring Contaminant Plume Evolution During Centrifuge Modelling"*, In: Garnier, J. et al. eds., *'Proceeding of the International Symposium on Physical Modelling and Testing in Environmental Geotechnics'*, NECER, France, pp. 27-34.

Huang, W. E., Smith, C. C., Lerner, D. N., Thornton, S. F. and Oram, A., (2002), "Physical Modelling of Solute Transport in Porous Media: Evaluation of An Imaging Technique Using UV Excited Fluorescent Dye", *Water Research,* Vol. 36, pp. 1843-1853.

Hughes, S. A., (1995), "Physical Modelling and Laboratory Techniques in Coastal Engineering", World Scientific Publishing Co. Pte. Ltd., 568 pp., Singapore.

Holly, F. M. Jr., and Usseglio-Polatera, J. M., (1984), "Dispersion in Two-Dimensional Flow", ASCE, *Journal of Hydraulic Engineering,* Vol.110, pp.905-926.

Hunt, B., (1983), "Mathematical Analysis of Groundwater resources", Butterworth & Co(Publishers) Ltd., pp.271, UK.

Johnston, C. M. and Gilliland P. M., (2000), "Investigation and Managing Water Quality in Saline Lagoons, Based on a Case Study of Nutrients in the Chesil and the Fleet European Marine Site", Report No. ISSN 0967-876X, English Nature, The Environmental Agency and Cardiff University, 134 pp.

Kennedy, K., (2001), "Chesil, the Fleet and the River Wey Farming Integration Study" , UK Marine SACs Project, EC Life-Nature Programme, 65 pp.

Khalifa, A., Garnier, J., Thomas, P. and Rault G., (2000), "*Scaling Laws of Water Flow in Centrifuge Models*", In: Garnier, J. et al. eds., '*Proceeding of the International Symposium on Physical Modelling and Testing in Environmental Geotechnics*', NECER, France, pp. 191-198.

Knupp, P., (1996), "A moving mesh algorithm for 3-D regional groundwater flow with water table and seepage face", *Advances in Water Resources*, Vol. 19, No. 2, pp.83-95.

Kocyigit, O., (2003), "Modelling of Water Quality and Sediment Transport in Aquatic Basins Using an Unstructured Grid System", PhD Thesis, Division of Civil Engineering, Cardiff School of Engineering, Cardiff University.

Larabi, A. and De Smedt, F., (1997), "Numerical Solution of 3-D Groundwater Flow involving Free Boundaries by a Fixed Finite Element Method", *Journal of Hydrology,* Vol. 201, pp.161-182.

Lee, K. K., and Leap, D. I., (1997), "Simulation of a free-surface and seepage face using boundary-fitted coordinate system method", *Journal of Hydrology*, Vol. 196, No. 1-4, pp. 297-309.

Li, C. W. and Falconer, R. A., (1995), "Depth Integrated Modelling of Tidal Induced Circulation in a Square Harbour", *Journal of Hydraulic Research*, IAHR, Vol. 33, No. 3, pp.321-332.

Li, L., Barry, D. A. and Pattiaratchi, C. B., (1997), "Numerical modelling of tide-induced beach water table fluctuations", *Coastal Engineering*, Vol. 30, No. 1-2, pp. 105-123.

Li, L., Barry, D. A., Stagnitti, F., Parlange, J.-Y. and Jeng, D.-S., (2000), "Beach Water Table Fluctuations Due to Spring Tides: Moving Boundary Effects", *Advances in Water Resources,* Vol. 23, pp.817-824.

Li, H. and Jiao, J. J., (2003), "Influence of the tide on the mean watertable in an unconfined, anisotropic, inhomogeneous coastal aquifer", *Advances in Water Resources*, Vol. 26, No. 1, pp.9-16.

Lin, B. and Falconer, R. A., (1997), "Tidal Flow and Transport Modelling Using ULTIMATE QUICKEST Scheme", *Journal of Hydraulic Engineering,* (ASCE), Vol. 123, No. 4, pp.303-314.

Morita, M. and Yen, B. C., (2002), "Modeling of Conjunctive Two-Dimensional Surface-Three-Dimensional Subsurface Flows", *Journal of Hydraulic Engineering,* Vol. 128, No. 2, pp.184-200.

Panigrahi, B. K. (ed), (2001), *"Integrated Surface And Groundwater Management"* ASCE-Conference Proceedings, Virginia, pp. 325.

Pipes, L. A., and Hovanessian, S. A., (1969), "Matrix-Computer Methods in Engineering", John Wiley and Sons, Inc., pp.333, New York.

Polubarinova-Kochina, P. YA., (1962), "Theory of Groundwater Movement", Princeton University Press, pp.613, USA.

Preston, R. W., (1985), "Representation of Dispersion in Two-Dimensional Water Flow", Report No. TPRD/L/2783/N84, Central Electricity Research Laboratories, Leatherhead, England, 1-13.

Robinson I. S., (1983), "A Tidal Flushing Model of the Fleet-an English Tidal Lagoon", *Estuarine, Coastal and Shelf Science,* Vol.16, pp. 669-688.

Robinson I. S., Warren L., and Longbottom J. F., (1983),"Sea-level fluctuations in the Fleet, an English Tidal Lagoon", *Estuarine, Coastal and Shelf Science*, Vol.16, pp. 651-668.

Sellin, R. H. J., Wilson C. A. M. E. and Naish, C. (2001), "Model and Prototype Results for a Sinuous Two-Stage River-Channel Design", Journal of the Chartered Instituation of Water and Environmental Management, Vol. 15, No. 3, pp.207-216.

Smith, G. D., (1985), "Numerical Solution of Partial Differential Equations: Finite Difference Methods" Oxford University Press, pp. 337.

Smith, R., (1992), "Physics of Dispersion in Coastal and Estuarine Pollution: Methods and Solutions", Scottish Hydraulics Study Group, Glasgow.

Spitz, K., and Moreno, J., (1996), "A Practical Guide to Groundwater and Solute Transport Modeling", A Wiley-Interscience Publication, John Wiley & Sons, Inc., pp.461, New York.

Stapleton, C. M., Kay, D., Jackson, G. F. and Wyer, M. D., (2000), "Estimated Inorganic Nutrient Inputs to the Coastal Waters of Jersey from Catchment and Wastewater Sources", *Water Research*, Vol. 34, No. 3, pp.787-796.

Stelling, G. S., et al., (1986), "Practical Aspects of Accurate Tidal Computations", *Journal of Hydraulic Engineering,* Vol.112, pp.802-817.

Stern, D. A., Khanbilvardi, R., Alair, J. C. and Richardson, W., (2001),"Description of Flow Through a Natural Wetland Using Dye Tracer Tests", *Ecological Engineering,* Vol. 18, pp. 173-184.

Tannehill, J. C., Anderson, D. A. and Pletcher, R. H., (1997), "Computational Fluid Mechanics and Heat Transfer", 2th Ed., Taylor and Francis, 792pp, USA.

UK Marine Web site, (last access Nov. 2003), http://www.ukmarinesac.org.uk/activities/lagoons/l4_1_1.htm

Van Rijn, L. C., (1984a), "Sediment Transport Part I: Bed Load Transport", *Journal of Hydraulic Engineering,* ASCE, Vol. 110, pp. 1431-1456.

Van Rijn, L. C., (1984b), "Sediment Transport Part II: Suspended Load Transport", *Journal of Hydraulic Engineering*, ASCE, Vol. 110, pp. 1613-1641.

Wang, H. F., and Anderson, M. P., (1982), "Introduction to Groundwater Modeling: Finite Differences and Finite Element Methods", W.H. Freeman Publisher, pp.237, San Francisco.

Wave Monitor Manual, Published by Churchill Controls Ltd., 26 pp.

Wave Probe Monitor, Operation Instructions – Issue 5, published by HR Wallingford, 15 p.

Weiyan, T., (1992), "Shallow Water Hydrodynamics", Elsevier, Amsterdam.

Westwater, D., Falconer, R. A. and Lin, B., (1999), "Modelling Tidal Currents and Solute Distributions in Fleet Lagoon", Project No. LIF01-06-06, Cardiff School of Engineering, Cardiff, 53 p.

Westwater, D., (2001), "Modelling Hydrodynamic and Shallow Water Processes over Vegetated Floodplains", PhD Thesis, Division of Civil Engineering, Cardiff School of Engineering, Cardiff University.

Relevant Conference Proceedings

Ebrahimi, K., Falconer, R.A. and Lin, B., (2002), "Environmental aspects of polluted wetland areas neighbouring coastal waters", *9th Engineering Seminar of Iranian Student in Europe*, Birmingham, UK

Ebrahimi, K., Falconer, R.A. and Lin, B., (2003), "A Combined Groundwater/Surface Flow and Contaminant Transport Model", *10th Engineering Seminar of Iranian Researchers in Europe,* Glasgow, UK